Exploring transient resonant behaviour over a fringing coral reef

Bernice van der Kooij

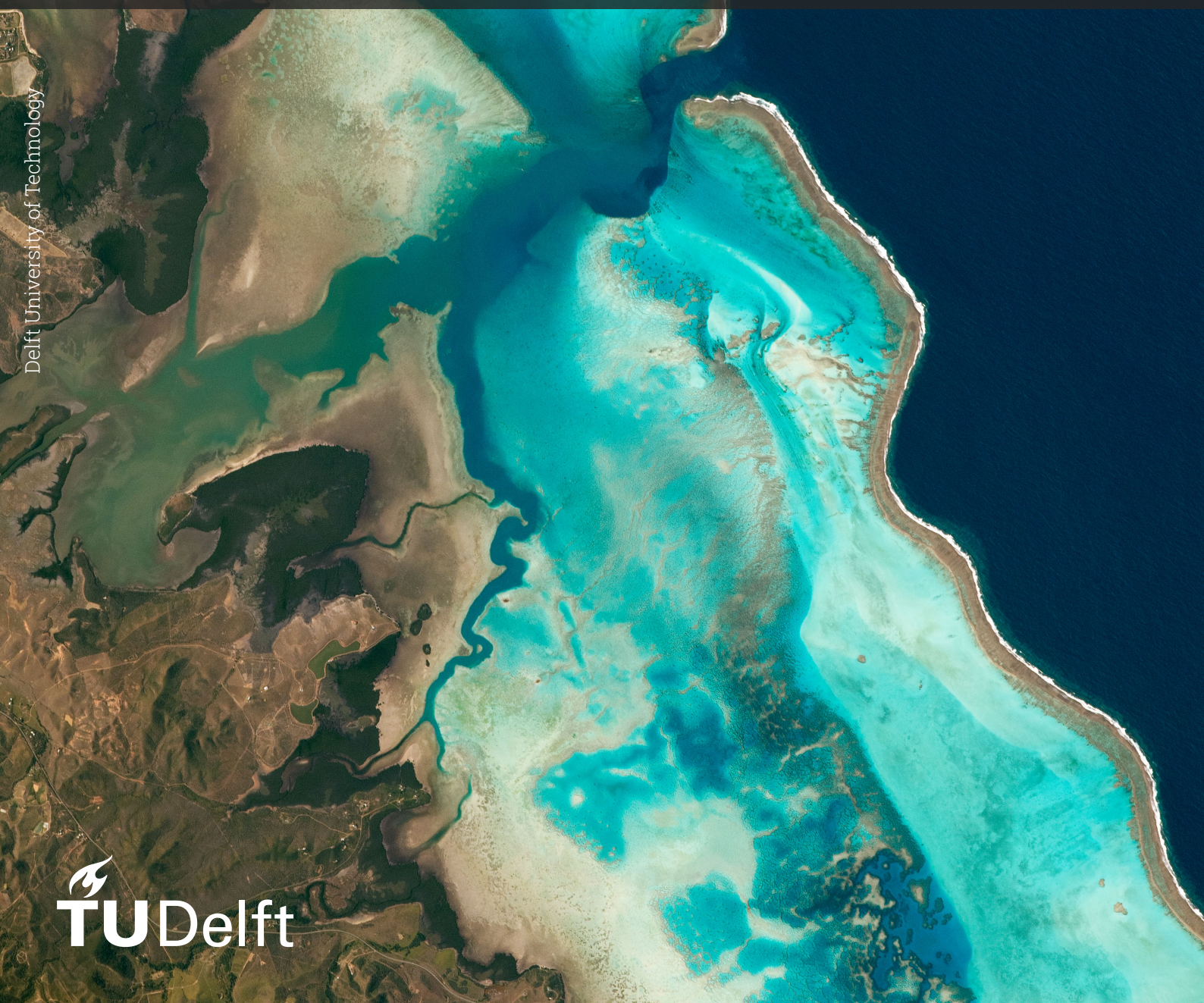

Delft University of Technology

TU Delft

Exploring transient resonant behaviour over a fringing coral reef

by

Bernice van der Kooij

to obtain the degree of Master of Science
at the Delft University of Technology,
to be defended publicly on Wednesday July, 3, 2024 at 16:00.

Student number: 4554671

Thesis committee:		
	Dr. ir. S.G. Pearson,	TU Delft (chair)
	Prof. dr. ir. A.J.H.M. Reniers,	TU Delft
	Dr. M.F.S. Tissier,	TU Delft
	Dr. ir. R.T. McCall,	Deltares
	Ir. F.E. Roelvink,	Deltares

In collaboration with:

TU Delft Delft University of Technology

Deltares

An electronic version of this thesis is available at http://repository.tudelft.nl/.

Cover: Aerial view of a fringing coral reef on the south coast of New Caledonia, photograph taken from the International Space Station (ISS). (ISS Astronaut, 2020)

Preface

Before anything else, I would like to take a moment to mention the people who have helped me throughout the journey of my thesis and whose contribution is greatly appreciated.

First of all, I would like to share my gratitude towards my exam committee. Thank you, Stuart, for your motivating and encouraging words throughout this project. Our discussions were always insightful, leaving me with renewed energy. Marion, thank you for the extensive brainstorming sessions we had together. Your insights were valuable in refining my approach. Thanks to Ad for his helpful feedback, your critical thinking and expertise are greatly appreciated. Thank you, Robert and Floortje for the opportunity to conduct my thesis at Deltares and for giving me the freedom to explore and decide my research path.

To my friends and family, your unwavering support has been invaluable. Mom and Dad, thank you for your unconditional support and always being proud of me.

A special thanks to Sofie. We shared the journey of our theses from start to end. I deeply appreciate your support during both smooth sailing and rough seas. I could not have asked for a better thesis buddy. Nadine, thank you for your readiness to support me, whether it was cooking dinners, editing figures and tables, or simply listening to me talk endlessly. Gina, a coffee with you never failed to brighten my day. Thank you for always being there for me. To all my friends and family, I am grateful for each of you.

Bernice van der Kooij
Delft, July 2024

Abstract

Low-lying reef-lined coasts are vulnerable to coastal flooding. While fringing reefs usually protect coastal communities from moderate storms by dissipating incoming wave energy, they can exacerbate flooding during strong events with energetic waves. Low-frequency waves (0.001-0.04 Hz) play an important role in coastal hazards, dominating nearshore reef flat wave patterns. Furthermore, low-frequency resonance on reef flats has been suggested to exacerbate coastal hazards. Despite expanding knowledge of wave dynamics on coral reefs, the transient characteristics of low-frequency resonant oscillations on reef flats have not been extensively researched, and no methods currently exist for analyzing this phenomenon in field observations.

This thesis introduces a new methodology for assessing transient characteristics of resonant and energetic low-frequency oscillations using the Hilbert-Huang transform. The study is based on a 5-month dataset from a cross-shore transect of a reef at Roi-Namur in the Marshall Islands, where the reef geomorphology corresponds to a natural frequency in the very low-frequency range (VLF, 0.001-0.005 Hz).

The findings indicate that resonance in the dataset typically had a short persistence, with a median and 90^{th} duration of approximately 5 and 10 minutes respectively. Normalised with the period of the oscillations, which have a typical frequency of 0.0035 Hz, these durations are equal to approximately 1 and 2 wave oscillations. While these results are consistent with previous notions about the potentially short durations of resonance for this particular reef and dataset, they contradict suggestions that resonance is associated with a build-up over several wave periods. Comparison of resonance durations with instances of coastal flooding at the site shows that resonance occurred for about 1 hour within a 24-hour recording period during overwash and large runup events, but also at other times. The duration of energetic VLF oscillations, in general, was more closely linked to the severity of coastal flooding events. While resonance did not directly correspond to coastal flooding, it was observed that energetic VLF oscillations persisted for longer durations under (close to) resonant conditions.

These results suggest the critical role of energetic VLF waves in coastal hazards, while resonance may be of secondary importance. However, it is important to acknowledge the limitations of this study, which focused on a single dataset from a specific reef geometry and included short-duration recordings (34 minutes). Moreover, this study demonstrates the application of the Hilbert-Huang transform for analysing sea surface elevation signals recorded at a coral reef.

The insights gained from this research underscore the importance of considering both energetic VLF oscillations and resonance in coastal hazard assessment. Future investigations should explore factors influencing the persistence of such oscillations, like the characteristics of incoming wave forcing, to enhance coastal hazard prediction. Furthermore, the Hilbert-Huang transform offers a versatile framework for exploring more aspects regarding the time-varying and non-linear behaviour of waves on coral reefs.

The methodology framework proposed in this study facilitates the bulk analysis of extensive field data and longer sea surface elevation recordings, enabling further exploration of reef morphology and hydrodynamic controls on the persistence of energetic and resonant VLF oscillations.

List of symbols and abbreviations

Symbols

Symbol	Definition	Unit
α_j	Instantaneous amplitude	[m]
η	Sea surface elevation	[m]
ν	Spectral width	-
ϕ_j	Instantaneous phase	[rad]
ρ	Pearson correlation coefficient	-
τ	Time lag	[s]
θ	Signal energy error by Daqian et al. (2007)	-
ω_j	Instantaneous frequency	[Hz]
$a_{max,error}$	Maximum amplitude error	[m]
c	Wave celerity	[m/s]
c_j	Component or intrinsic mode function	-
$c_{PCC}(\tau)$	Phase cross-correlation	-
d	Duration of (energetic VLF or resonant) event	[s]
D	Duration of (energetic VLF or resonant) oscillation per record	[s]
EI	Time variable error by Veltcheva and Soares (2016)	-
f_{mean}	Mean frequency	[Hz]
$f_{n,th}$	n^{th} mode of eigenfrequency	[Hz]
$f_{overlap}$	Frequency overlap	-
$f_{p,transfer}$	Peak transfer frequency	[Hz]
g	Gravitational acceleration ($= 9.81$ m/s^2)	[m/s^2]
h	Water depth	[m]
$h(\omega)$	Marginal spectrum	[m^2/Hz]
H_s	Significant wave height	[m]
$H_{Axy}(f)$	Transfer function	-
$HS(\omega, t)$	Hilbert spectrum	[m^2]
IO	Index of Orthogonality	-
L	Wave length	[m]
m_k	k^{th} spectral moment	[ms^2]
$normE_{p,transfer}$	Normalised inner reef energy	-
$PMSI$	Pseudo mode splitting index	-
SD	Standard deviation	
T_p	Peak wave period	[s]
t_w	Time window	[s]
$x(t)$	Signal	[m]
z_j	Analytic signal	

Abbreviations

Abbreviation	Definition
CEEMD	Complete Ensemble Empirical Decomposition
EEMD	Ensemble Empirical Decomposition
EMD	Empirical Mode Decomposition
FFT	Fast Fourier Transform
HHT	Hilbert Huang Transform
HHT^{temp}	Temporal HHT approach to resonance analysis
IA	Instantaneous amplitude
IE	Instantaneous energy
IF	Instantaneous frequency
IG	Infragravity (0.005-0.04 Hz)
IMF	Intrinsic Mode Function
IP	Instantaneous phase
iM-EMD	Iterated Masking Ensemble Empirical Decomposition
LF	Low-frequency (0.001-0.04 Hz)
M-EMD	Masking Ensemble Empirical Decomposition
SD	Standard deviation
VLF	Very low frequency (0.001-0.005 Hz)

List of Figures

List of Tables

Contents

1

Introduction

Coral reefs play an essential role in protecting tropical coastlines from the impacts of wave attack and coastal flooding. Spanning over 120 countries and territories, these natural barriers protect more than 230,000 kilometres of coastlines by dissipating wave energy through processes such as wave breaking and bottom friction (Burke and Spalding, 2022; Lowe et al., 2005). This protective function is crucial for safeguarding coastal regions and mitigating wave-driven flooding (Elliff & Silva, 2017).

Climate change increases the pressure on these coastal areas which are home to thousands of vulnerable communities (Ferrario et al., 2014; Storlazzi et al., 2018). Sea level rise exacerbates coastal hazards by increasing water levels, contributing to runup, overwash, and inundation (Cheriton et al., 2016; Péquignet et al., 2009; Merrifield et al., 2014). Furthermore, coral degradation due to climate change and anthropogenic factors further reduces the effectiveness of coral reefs by decreasing bottom friction, thereby impacting the ability of coral reefs to protect coastal areas (Storlazzi et al., 2019; Nwogu and Demirbilek, 2010).

Increasing efforts have been made to understand the hydrodynamics on coral reefs. However, many unknowns still remain. The following two sections will give an overview of the current knowledge about the hydrodynamics on coral reefs and what knowledge gap will be addressed in this thesis.

1.1. Wave dynamics on coral reefs

1.1.1. Low-frequency waves

Coral reefs differ significantly from sandy beaches in terms of their bathymetry. Fringing coral reefs are characterised by a steep fore reef with an abrupt shift at the reef crest to a shallow, gently-sloping reef flat. Figure 1.1 shows a schematised fringing coral reef. These differences in morphology have notable implications for hydrodynamics. The reef flat is typically dominated by low-frequency waves (LF, 0.001-0.04 Hz), which can be divided into very low frequency (VLF, 0.001-0.005 Hz) and infra-gravity (IG, 0.005-0.04 Hz) waves.

Propagating towards a reef-lined coast, high-frequency (sea-swell) waves typically break in a narrow zone on the fore reef. This induces the generation of low-frequency waves through breakpoint forcing (Pomeroy et al., 2012a; Péquignet et al., 2014). After initial dissipation of short waves through wave breaking, further attenuation on the reef flat occurs through bottom frictional dissipation, which is found to be highly frequency dependent (Lowe et al., 2005; Pomeroy et al., 2012a; Van Dongeren et al., 2013). This attenuation is controlled by wave shape, hydraulic roughness, reef flat width and water depth (Péquignet et al., 2009; Pomeroy et al., 2012b).

The water depth on the reef flat influences the propagation behaviour, waveform and amplitude of LF waves (Pomeroy et al., 2012a; Cheriton et al., 2016; Gawehn et al., 2016; Cheriton et al., 2020). At smaller water depths, progressive LF waves dominate observations (Cheriton et al., 2016; Gawehn et al., 2016). Propagating over the reef flat, IG waves can evolve into bore-like waves with steep wave fronts. Cheriton et al. (2016) observed IG wave-wave capture and posit that VLF waves over reef flats may facilitate IG bore merging, leading to larger, more pitched-onshore bores at the shoreline. Additionally, they suggest that greater IG wave heights support the transmission of larger secondary short waves over the reef flat.

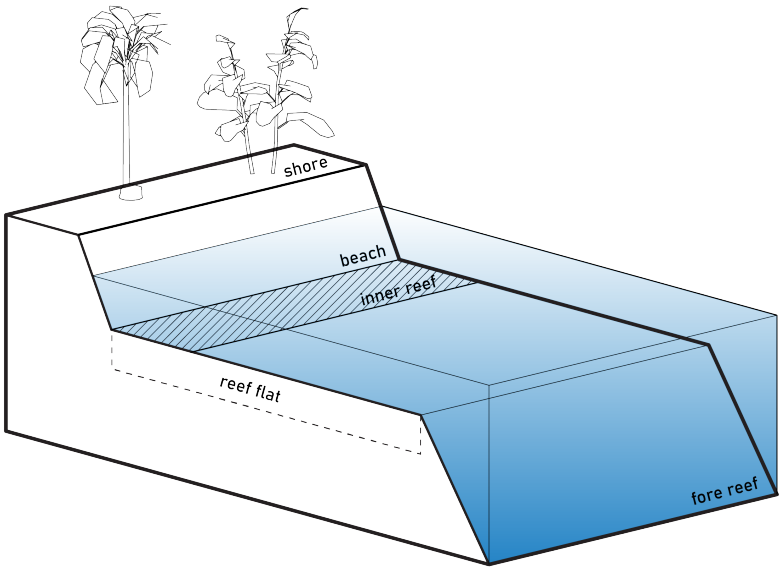

Figure 1.1: Schematised profile of a fringing coral reef. The reef features a shallow, relatively wide reef flat, fronted by a steep fore reef, leading to a steep beach slope. The area of the reef flat closest to the beach is referred to as the inner reef.

1.1.2. Resonance

Depending on their width, reef flats can support standing waves that may be resonantly excited (Péquignet et al., 2009; Pomeroy et al., 2012a; Gawehn et al., 2016; Buckley et al., 2018). Resonance occurs when the forcing frequencies have a similar timescale to the natural frequency of the reef flat and leads to the amplification of this oscillatory component. Resonance has been pointed out to potentially further exacerbate coastal hazards (Gawehn et al., 2016; Shimozono et al., 2015; Roeber and Bricker, 2015).

Therefore, resonance over fringing coral reefs has been subject of research. In the field, the forcing of resonant modes in reef environments has been observed, especially during extreme wave events (Péquignet et al., 2009; Shimozono et al., 2015; Cheriton et al., 2016). Additionally, both numerical and physical experiments have been conducted to increase understanding of the dynamics of this phenomenon (Nwogu and Demirbilek, 2010; Pomeroy et al., 2012a; Gaido, 2019; Van Noort, 2021).

Reef flat resonance is typically most substantial in its fundamental resonant frequency (Gawehn et al., 2016), with a wavelength of four times the reef flat width (Rabinovich, 2010), as shown in Figure 1.2. Depending on the reef flat width and water depth, the natural frequency falls in the VLF or IG domain.

Increased water levels over the reef can raise the resonant frequencies, making them more likely to be excited by incoming waves and leading to amplified resonant responses (Péquignet et al., 2009). The probability of resonance may therefore increase by sea level rise. Additionally, coral reef degradation as a result of climate change and anthropogenic activities reduces the coral roughness, decreasing the bottom friction (Storlazzi et al., 2019), which is regarded as an effective feature in the damping of low-frequency and resonant oscillations (Pomeroy et al., 2012a).

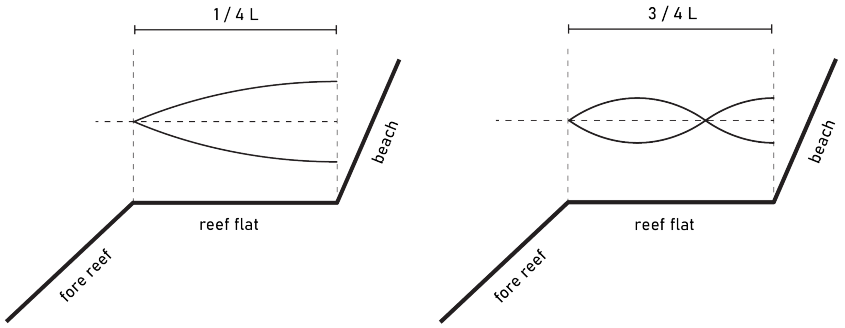

(a) Fundamental mode of resonance. **(b)** First mode of resonance.

Figure 1.2: Profile of a schematised reef flat showing the motion of standing oscillations for (a) the theoretical fundamental mode and (b) the first mode of resonance. The fundamental mode has a wavelength (L) of four times the reef flat width.

1.1.3. Relevance to coastal flooding

Although fringing reefs usually protect coastal communities from moderate storms by dissipating incoming wave energy, they can exacerbate flooding during strong events with energetic waves (Roeber & Bricker, 2015). Low-frequency waves have been shown to play an important role in coastal hazards. Under certain conditions, LF waves can exhibit large amplitudes and bore-like shapes at the shoreline, playing a critical role in extreme shoreline events such as large runup, overwash, and subsequent flooding (e.g., Cheriton et al., 2016; Gawehn et al., 2016, Roeber and Bricker, 2015, Shimozono et al., 2015). Resonant LF waves are suggested to increase the probability and magnitude of coastal flooding (Gawehn et al., 2016). Furthermore, large VLF waves are posited to support IG wave-wave capture, further increasing wave impact on the shore (Cheriton et al., 2020). Therefore, understanding LF wave dynamics over reef flats is imperative.

1.2. Transience of resonance

Despite expanding knowledge, there are still unknowns remaining regarding low-frequency waves and resonance on coral reefs, among which the transient behaviour of such oscillations.

1.2.1. Current knowledge and approaches

The temporal behaviour of reef flat resonance has been studied in a few numerical and physical experiments, specifically regarding the build-up behaviour of resonant amplification. Nwogu and Demirbilek (2010) studied IG motions over a typical reef profile in a combined laboratory and numerical experiment. Bichromatic wave trains were imposed in the physical model to study the resonance response. The results showed a gradual build-up to resonant amplification at the shoreline, reaching maximum amplification after five IG wave periods.

More recently, Gaido (2019) forced resonance over a schematised fringing coral reef by regular small-amplitude long waves in numerical model SWASH (1D). This pointed to a build-up behaviour of resonance as well, though a larger number of twelve IG waves was required as build-up period. Further experiments with SWASH (2DV) were conducted by Van Noort (2021), where a bichromatic wave field was applied to a schematised reef based on the bathymetry of Roi-Namur Island of the Marshall Islands. A lack of build-up was evident from these simulations as maximum amplification was reached within the first wave period.

In these approaches, different methods were used to qualify and quantify resonance. Gaido (2019) identified resonance by forcing the theoretical resonant periods and neighbouring periods. From the computation results, the frequencies leading to the largest resonant amplifications were found. The maximum amplification was identified by comparing the wave height at the beach toe and the maximum runup for each of the periods. Van Noort (2021) distinguished resonance by comparing the incoming energy in the IG wave band between a simulation with a reflective boundary and an absorbing boundary at the beach. Resonance can only occur for the reflective beach, while other complex nearshore processes are accounted for in both simulations. The amplification ratio of resonance is then defined as the ratio of the incoming IG wave energy at the beach toe for the reflective beach over the energy at the beach toe for the absorbing boundary.

Notably, these methods are only applicable in the context of numerical simulations with controlled incoming wave fields. For real-world observations, other approaches are required, which typically rely on spectral analysis. Gawehn et al. (2016) classified VLF oscillations in field observations of Roi-Namur Island into four classes: resonant, (nonresonant) standing, progressive-growing and progressive-dissipative waves. As the first step of this classification, resonance is identified based on a quantification of energy transfer between the incoming wave envelope at the fore reef and the low-frequency energy at the inner reef. First, the frequency with the maximum transfer in the low-frequency band is acquired, referred to as peak transfer frequency ($f_{p,transfer}$). The energy of this harmonic at the inner reef is normalised with the low-frequency energy of the fore reef envelope. A threshold for the normalised energy determines the classification of resonance. This approach assesses the amplification between fore and inner reef wave energy, unlike previously applied methods. Pomeroy et al. (2012a) qualified resonance based on three indicators: between the outer and inner reef signal, there should be a high coherence, a phase difference of 0 or 180 degrees and a certain amplification. However, as this method neglects the incoming forcing, it may identify standing oscillations which are not necessarily resonant (Gawehn et al., 2016).

1.2.2. Knowledge gap

As of yet, the duration and persistence of resonant VLF oscillations in field observations are underdefined. Since these waves may contribute to potential coastal risks, it is worth exploring this topic further. Due

to the non-stationary and irregular nature of wave fields in real-world observations, observing the build-up behaviour of potential resonant oscillations is challenging. Gawehn et al. (2016) note that the resonance identified for the Roi-Namur dataset could be of short duration, suggesting that the resonance may not have been fully developed. However, the method they employed to identify resonance, based on the Fourier analysis, does not allow for analysis of the temporal characteristics.

To the best of the author's knowledge, no method currently exists for assessing the transience of resonance in field observations. This calls for a new approach, which is explored in this thesis.

1.2.3. A new approach for spectral analysis

Although the Fourier transform is widely accepted as a valuable tool in spectral analysis, its underlying assumptions limit its applicability to real-world data. The basic premise of Fourier analysis is that any finite length, infinitely repeated time series can be reproduced by a linear summation of cosines and sines (Fourier, 1888). This mathematical framework assumes stationarity and linearity, conditions which real-world signals generally do not satisfy. Additionally, the time-variant characteristics within a signal are completely lost in the Fourier representation, making it unsuitable for studying transient signals.

In this thesis, the application of another time-series analysis approach is explored: the Hilbert-Huang transform (HHT) (Huang et al., 1998). The HHT combines Empirical Mode Decomposition (EMD) and the Hilbert transform. EMD decomposes a time series signal into several Intrinsic Mode Functions (IMFs), each representing a wave with a specific frequency. The Hilbert transform is then applied to these IMFs and provides the frequency, amplitude and phase information as functions of time. This allows for the analysis of the wave characteristics in both the time and frequency domains.

The HHT has been applied in many research fields, including the analysis of ocean and coastal waves (e.g., Veltcheva and Soares, 2004, Schlurmann et al., 2003, Ortega and Smith, 2009, Senthilkumar et al., 2015). It is a powerful and adaptive method, but lacks a rigorous mathematical framework like the Fourier transform. Therefore, the application of the HHT is not straightforward, and challenges remain. However, the HHT is considered a promising alternative for analysing time-varying characteristics, and it was also proposed by Gawehn et al. (2016) as an alternative technique in the analysis of VLF and resonant waves.

1.3. Research objectives and scope

Resonant and low-frequency waves contribute to wave runup and potential coastal flooding of low-lying islands lined with fringing coral reefs. An underexamined feature of these waves is their transient behaviour, such as the duration and persistence of resonant oscillations observed in the field.

This study aims to explore transient characteristics of resonance and energetic VLF oscillations on a fringing coral reef using the Hilbert-Huang transform. The research questions are as follows:

1. How can the Hilbert-Huang transform effectively decompose a sea surface elevation signal observed at a coral reef into frequency components to extract the dominant VLF component?
2. How can we define and classify standing and energetic VLF oscillations in an inner reef signal using the Hilbert-Huang transform?
3. How can we define and capture the time-varying characteristics of resonant oscillations over a coral reef with the Hilbert-Huang transform?
4. How do the durations of resonant and energetic VLF oscillations vary, and how does this variation relate to coastal flooding of a shore lined with a fringing coral reef?

1.3.1. Approach

The Hilbert-Huang transform (HHT) plays a central role in this thesis. Given its empirical nature, the initial focus of the research is to evaluate its effectiveness. An essential part of the HHT is the Empirical Mode Decomposition (EMD), which involves various algorithms and configurations, as will be discussed later in further detail. This study evaluates their performance and suitability for extracting VLF oscillations from sea surface elevation signals recorded at a reef of Roi-Namur Island in the Marshall Islands, particularly those associated with potential resonant oscillations close to the reef flat's natural frequency.

Once the VLF component of the inner reef signal is extracted using EMD, it undergoes classification based on propagation type and energetic content. This classification utilises outputs of the HHT such as instantaneous amplitude (IA) and instantaneous phase (IP). Separately, the resonance analysis is conducted to identify and characterise resonant oscillations. This analysis aims to determine if the identified resonances

correspond to standing oscillations, as expected in this phenomenon, and to assess whether energetic VLF oscillations align with resonant frequencies. Elements of the resonance analysis method proposed by Gawehn et al. (2016) are utilised, using the HHT for the spectral analysis steps.

Furthermore, VLF components classified as energetic or resonant undergo detailed examination for transient characteristics such as duration. These analyses incorporate elements from classification and resonance identification approaches. The recorded field data includes instances of overwash and significant runup, providing a basis to compare durations of energetic and resonant VLF oscillations with observed coastal flooding events.

1.3.2. Scope of study

Study area and data set: Roi-Namur reef

This study utilises field observations from a coral reef at Roi-Namur Island. The reef features a gently sloping, relatively smooth reef flat, transitioning into a steep (∼1:20) fore reef and a narrow, steep (∼1:6) sandy beach. The reef flat varies in width from 250 to 350 m and has an average water depth of 0.7 m, resulting in a natural frequency within the Very Low Frequency (VLF) bandwidth (0.001-0.005 Hz).

Field data was collected over 5 months (November 2013 to April 2014) along a cross-shore transect of the reef (Figure 1.3). Observations were recorded for 34 minutes each hour, resulting in 3800 time series per observation station. Only sea surface elevation data was recorded; other parameters such as incoming wave angle, velocity and currents are not available. Therefore the investigation focusses on a single cross-shore reef geometry and the study is limited to 1D wave processes. It is also noted that the short duration of the time series is a potential limitation for analysing VLF wave oscillations thoroughly.

Very low frequency waves

This research focusses on VLF waves, as they represent the fundamental resonant mode of the Roi-Namur reef within the VLF bandwidth. The Hilbert-Huang transform enables the analysis of the VLF oscillations separately. While interactions and correlations between VLF and IG waves have been suggested (Cheriton et al., 2020), this study does not investigate these interactions.

Analysis of inner reef oscillations

The study primarily focusses on oscillations on the reef flat, especially at the inner reef. Although incoming wave forcing influences resonant amplification, this study does not link transient characteristics to external forcings.

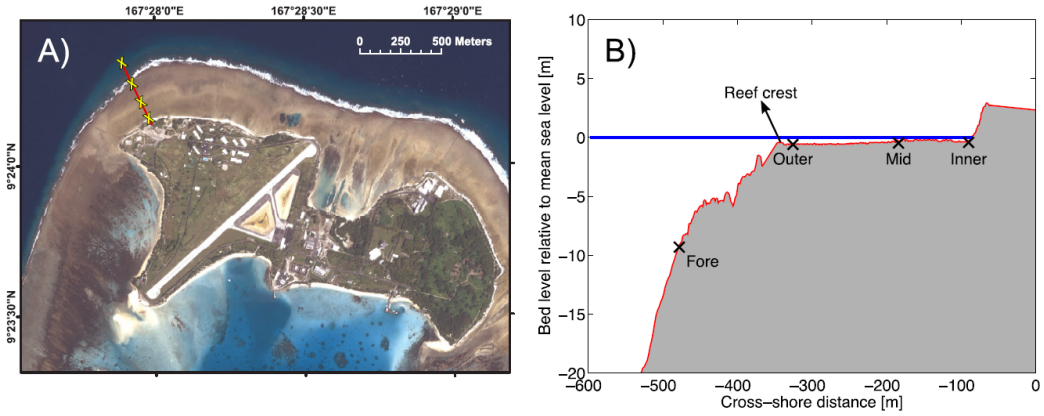

Figure 1.3: Views of the study area on Roi-Namur Island; (a) map view of the site with locations of the instruments on the reef indicated with a yellow cross; (b) bathymetry for cross-reef transect and location of sensors (Gawehn et al., 2016).

1.4. Outline

The outline of this thesis is as follows. Chapter 2 provides relevant background information on coral reef hydrodynamics and spectral analysis approaches. Chapter 3 describes the methodology and the data set that is explored. This is followed by the results in Chapter 4. Next, the discussion is given in Chapter 5, followed the conclusion in Chapter 6. Finally, some recommendations for further research are provided in Chapter 7.

2

Background

2.1. General information about coral reefs

Coral reefs are large underwater structures and ecosystems that are characterised by reef-building animals known as coral polyps. The calcium carbonate skeletons formed by these polyps create the structure of a coral reef. Corals are typically found in tropical and subtropical waters, where light intensities and water temperatures are favourable for their growth (NOAA, 2023). Coral reefs can be categorised based on their geomorphological characteristics into fringing reefs, barrier reefs, and atolls, see Figure 2.2.

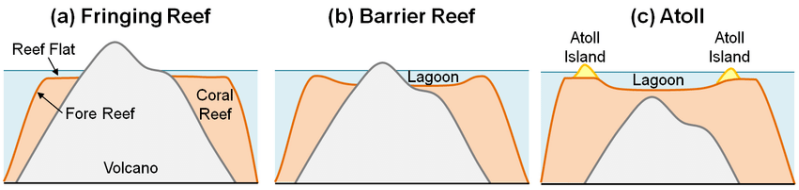

Figure 2.1: Coral reef types based on geomorphological characteristics: (a) fringing reef, (b) barrier reef and (c) atoll (Pearson, 2016).

2.1.1. Fringing coral reefs

Fringing reefs are the most common type of coral reef (NOAA, 2024). They are characterised by a steep fore reef followed by a relatively shallow and wide reef flat. The slope of the fore reef ranges from 1/6 to 1/20, descending into deep water (Quataert et al., 2015). Reef flats have varying widths, typically between 100 and 500 meters, but can be more than 1 km (Quataert et al., 2015). The bottom roughness of the reef flat is relatively high due to the presence of corals. A reef crest, with a slightly higher elevation than the reef flat, is typically located at the interface of the reef flat and the fore reef.

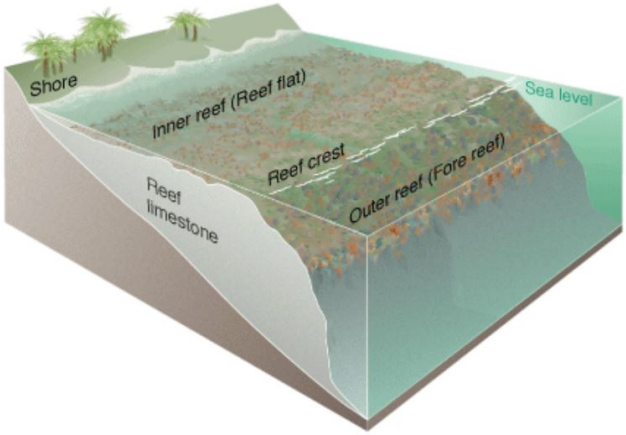

Figure 2.2: Schematised bathymetry of a fringing coral reef (Field et al., 2002).

2.1.2. Hydrodynamic forcing on coral reefs

Coral reefs have proven to be crucial for the protection of tropical shorelines against wind and swell waves (e.g., Ferrario et al., 2014; Lowe et al., 2005). Wind waves are locally generated and are characterised by having higher frequencies and a broad spectrum. Swell consists of wind-generated waves that have travelled a large distance. Through frequency dispersion, swell waves are longer and more regular, resulting in a narrow spectrum (Bosboom & Stive, 2021).

While both locally generated wind waves and swell waves pose flooding threats, swell waves can carry an element of surprise, as they are remotely generated and can arrive unexpectedly. They are therefore also referred to as "blue-sky events".

The reef submergence plays an important role regarding coastal hazards, as a higher reef submergence allows for more wave energy to reach the shoreline. The variation of water levels over coral reefs can be ascribed to local tidal variations and regional and global processes. The tidal range varies among coral reefs. For example, the tidal range is approximately 0.5 m for Ipan (Guam) and 1.0 m for Eastern Samar (Philippines) and Roi Namur (Marshall Islands) (Péquignet et al., 2009; Shimozono et al., 2015; Cheriton et al., 2016). Larger scale water level variations can be attributed to regional sea level fluctuations like El Niño-Southern Oscillation (ENSO), storm surge (including atmospheric pressure changes) and other anomalies (Hoeke et al., 2013). On a global scale, sea level rise contributes to water level variation as well.

Because of their distinct geomorphology, coral reefs are characterised by different cross-shore wave transformations compared to regular sandy coasts. These wave processes will be discussed in the following sections.

2.2. Sea swell waves on coral reefs

The distinctly different bathymetry of fringing coral reefs compared to sandy beaches influences nearshore wave processes that affect the wave transformation of short waves (SS, 0.04-0.2 Hz) as well as long waves (Van Dongeren et al., 2013). This section describes the wave processes regarding sea swell waves on coral reefs.

2.2.1. Shoaling and wave breaking

As waves approach the shoreline, they start shoaling due to a decreasing water depth. Because of the steep fore reef slope of a fringing reef, waves shoal rapidly until they break. Wave breaking effectively dissipates wave energy at the fore reef, but it contributes to wave-induced setup and the generation of long waves, which will be discussed later.

After the reef crest, wave breaking is minimal on the reef flat as there is a limited decrease in water depth. Wave dissipation on the reef flat mainly takes place through bottom friction (Lowe et al., 2005).

2.2.2. Wave-induced setup

The breaking of short waves on the fore reef causes an increase in the mean water level on the reef flat through wave-induced setup (Gerritsen, 1980; Vetter et al., 2010). Wave setup can reach up to 1/3 of the incident wave height along coasts typical of tropical and sub-tropical islands (Tait, 1972; Vetter et al., 2010) and is tidally dependent Becker et al., 2014. Wave setup proves to be an important component contributing to runup at the shoreline (Bruch et al., 2022) as it increases the reef flat water level.

2.3. Low-frequency waves on coral reefs

Low-frequency (LF) waves are defined as waves with a frequency between 0.001-0.04 Hz and can be subdivided into very low-frequency (VLF, 0.001-0.005 Hz) and infragravity (IG, 0.005-0.04 Hz) waves. As mentioned previously, the breaking of short waves is important for the generation of LF waves. After generation, LF waves also undergo wave transformations on the reef flat. These aspects of low-frequency waves are discussed in this section.

2.3.1. Low-frequency wave generation

LF waves are a result of non-linear wave-wave interaction, where energy is transferred from higher frequencies to lower frequencies. Three LF wave generation processes are distinguished: release of the bound long wave, breakpoint forcing and bore merging. The first two are considered here.

Release of the bound long wave

The short waves propagating towards shore often travel in wave groups, in which wave heights vary. These temporal variations in radiation stresses result in a variation of the mean water level on a group scale (Bosboom & Stive, 2021). This low-frequency motion is referred to as the bound long wave. The bound long wave has the same frequency as the wave group approaching the coral reef and is 180 degrees out of phase with the wave group envelope. At first, the celerity of the bound wave is equal to the group velocity. As the wave group propagates into shallower water, the phase difference between the wave group and the bound long wave changes so that the long wave starts to lag behind the wave groups (Bertin et al., 2018). This phase shift allows energy transfer from short waves to the bound long wave (Van Dongeren et al., 2007) causing it to grow and be released from the wave group. The free long wave then travels with the free wave celerity (Janssen et al., 2003). Battjes et al. (2004) found this phenomenon to be dominant for mildly sloping bottoms.

Breakpoint forcing

The breakpoint mechanism generates long waves through a space and time-varying breakpoint which is caused by wave height differences of incoming waves travelling in groups. The resulting water level oscillation on the reef flat has the same period as and is in phase with the wave group. This is also illustrated in Figure 2.3. A narrow surf zone enhances the breakpoint mechanism. Because of the steep bathymetry of the fore reef, the breakpoint mechanism is dominant for coral reef coasts (Pomeroy et al., 2012a). Péquignet et al. (2014) found that breakpoint forcing is a more efficient mechanism for generating LF wave energy than bound long waves. The breakpoint mechanism reduces in efficiency with an increasing water depth on the reef flat, as this decreases the wave breaking of short waves (Pomeroy et al., 2012a).

The reef slope is an important control for the breakpoint forced mechanism, as it influences the width of the surf zone. The most energetic IG waves are associated with steepnesses of $> 1/6$ is associated (Masselink et al., 2019).

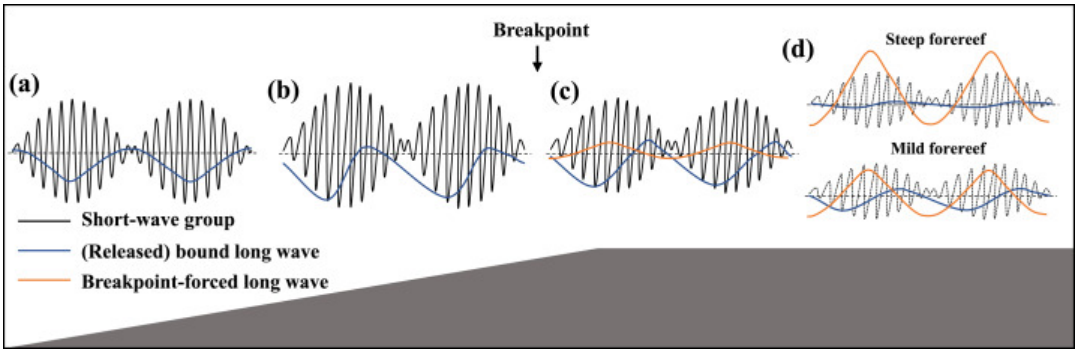

Figure 2.3: Sketches of incoming long waves generated by bound long wave and breakpoint-forced long wave mechanisms. At first, the bound long wave is in anti-phase with the wave group (a), it starts lagging (b) and is released (c). The breakpoint-forced long wave starts growing (c), it is dominant for steep fore reefs or co-exists with the released bound long wave for a mild fore reef. The dotted curve denotes the imaginary short-wave group without significant deformation during breaking (Y. Liu et al., 2023).

Bore merging

The third mechanism for the generation of long waves is the merging of bores. Bore merging takes place in the surf zone and happens when a faster moving bore, that travels on the crest of a LF wave catches up with slower moving bores travelling on the trough. Bore merging is associated with a decrease in the number of waves, and thus a decrease in frequency (Tissier & Bonneton, 2020). The magnitude of LF waves due to bore merging is significantly less than from the other long wave generation mechanisms (Bertin et al., 2018). However, Cheriton et al. (2020) posit VLF waves on the reef flat may facilitate IG bore merging, leading to larger, more pitched-onshore bores at the shoreline.

2.3.2. Low-frequency wave propagation and transformation

Resulting from the short wave breaking and generation of long waves, the reef flat is typically dominated by low-frequency waves. This section will touch upon some aspects of the propagation and wave transformation of low-frequency waves.

Frictional dissipation
Because of the typically high bottom roughness in coral reef environments, bottom friction is an effective mechanism for wave dissipation (Pomeroy et al., 2012a; Van Dongeren et al., 2013). Pomeroy et al. (2015) did laboratory experiments, showing that bottom friction dissipation predominantly affects LF waves, and short waves to a smaller extent. The frictional dissipation character does not only depend on the morphology of a reef, but can also vary as a result of reef water depth variations (Van Dongeren et al., 2013).

Irregular waveforms
Non-linear wave interaction leads to irregular waveforms. It is found that for gentle sloping beaches, where the wave field is dominated by LF wave energy, IG waves exchange energy within the IG frequency band (Bertin et al., 2018). As energy is transferred to higher IG harmonics, the wave shape changes to become skewed (with peaked wave crests and longer wave troughs) and asymmetric (saw-tooth shaped), leading to the steepening of the IG wave (Bertin et al., 2018). The steepening of IG waves can lead to wave breaking near the shoreline (Battjes et al., 2004; Van Dongeren et al., 2007; De Bakker et al., 2014). On steep slopes, IG wave energy is transferred back to short wave frequencies. Chen et al. (2019) note that, while steeper slopes of the fore reef result in more energetic IG waves, they may also act to reduce asymmetry of the reef flat IG waves.

Cheriton et al. (2020) examined IG wave development for different reef geomorphologies and found that IG waves became pitched onshore (negatively asymmetrical) and peaked (positively skewed) primarily for low water levels. They point out that reef flat width and slope are important morphological controls as well, reporting that the most asymmetric, bore-like IG waves occurred on the wider reef flats, and the most skewed IG waves on the steepest reef flat.

Furthermore, Cheriton et al. (2020) suggest that VLF waves may facilitate the development of bore-like IG waves. Larger VLF waves may enhance IG wave-wave capture over reef flats, possibly resulting in more pitched-onshore bores at the shoreline.

VLF waves can display bore-like behaviour as well. Roeber and Bricker (2015) show that during Typhoon Haiyan a tsunami-like wave developed over a fringing reef in the Philippines, causing extensive damage and casualties. In laboratory observations, Nwogu and Demirbilek (2010) observed that resonantly generated VLF waves deformed into bore-like surges. Additionally, Gawehn et al. (2016), who classified VLF waves observed at the Roi-Namur reef, note that resonant VLF waves can display bore-like behaviour.

Reflection
Wave reflection occurs at both the fore reef and the beach due to their steep slopes. The abrupt change in bathymetry at the fore reef acts as a barrier, causing wave reflection in both offshore and onshore directions, as illustrated in Figure 2.4 (Buckley et al., 2018). Consequently, some of the LF wave energy is reflected as it propagates towards the reef flat. The LF wave energy that is not dissipated through bottom friction or wave breaking is reflected seaward at the shoreline. This reflected wave energy is reflected back to the reef flat at the fore reef, creating a trapped wave on the reef flat. Over time, this trapped energy may increase (Péquignet et al., 2011; Pomeroy et al., 2012a).

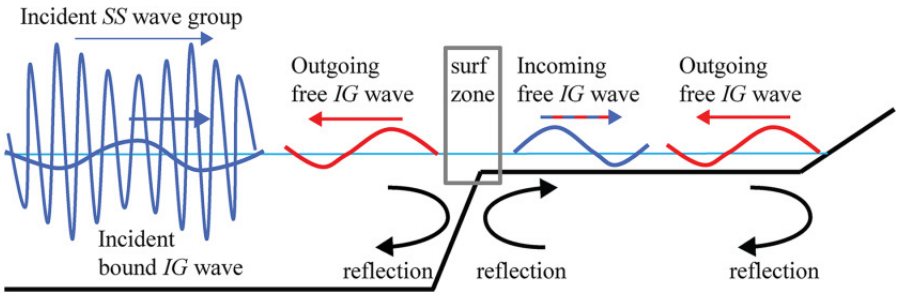

Figure 2.4: Schematic of potential sources and reflection points of IG waves. Reflection occurs at the reef crest and the beach, with trapped waves forming on the reef flat due to these reflections (Buckley et al., 2018).

The interaction between incident and reflected waves results in the development of a standing wave pattern. Wave reflection is frequency dependent and prevails more for lower frequencies, while higher IG frequencies display partial standing or progressive wave patterns (Henderson et al., 2001).

For observations of a fringing reef during a tropical storm, Péquignet et al. (2009) found that, in general, reflection increases with increasing wave period and decreasing offshore wave height. They note that VLF wave reflection is variable during calm and moderate wave conditions, but full reflection was reached during the peak of the storm. Gawehn et al. (2016) found that standing and resonance VLF waves occurred for greater water depth at the reef flat at the Roi-Namur reef, suggesting that larger water depths may allow LF waves to reflect more at the shoreline. They note that progressive VLF waves with steep bore fronts may lack reflection due to their nonlinear shape.

The slope of the beach is an important factor as well. For mild beaches ($< 1/20$), there is little reflection (Pomeroy et al., 2012b), whereas for steep beaches ($> 1/6$) LF waves are fully reflective (Cheriton et al., 2016).

2.3.3. Coastal flooding

The combination of wave-induced setup and low-frequency waves can drive wave runup, the vertical extent of wave uprush on a beach, resulting in coastal flooding (Merrifield et al., 2014; Cheriton et al., 2016; Gawehn et al., 2016; Cheriton et al., 2020).

Bore-like wave shapes are associated with extreme shoreline events during large wave events (Nwogu and Demirbilek, 2010; Roeber and Bricker, 2015; Shimozono et al., 2015; Cheriton et al., 2020). Furthermore, large, resonantly amplified VLF waves can further exacerbate the risk of coastal flooding (Roeber and Bricker, 2015; Gawehn et al., 2016; Cheriton et al., 2020). Resonance is further discussed in the following section.

2.4. Resonance

2.4.1. Theory of reef-flat resonance

A fringing reef can be approximated as an open basin. In open basins, resonant oscillations are typically generated by long waves entering through the open boundary (Rabinovich, 2010). The natural frequencies or eigenfrequencies of an open basin are estimated with: (Wilson, 1953)

$$f_{n,th} = \frac{(2n+1)\sqrt{gh}}{4L} \text{ for n = 0, 1, ...N} \tag{2.1}$$

where n is the mode number, g is the gravitational acceleration, h is the water depth, and L is the length of the basin (in this case, the width of the reef flat). Because of the open end, resonance water level motions have a node at the entrance of the basin (the reef edge) and an antinode at the closed end (the beach), see Figure 2.5. The mode ($n = 0, 1, ...$) determines the wavelength of the oscillation.

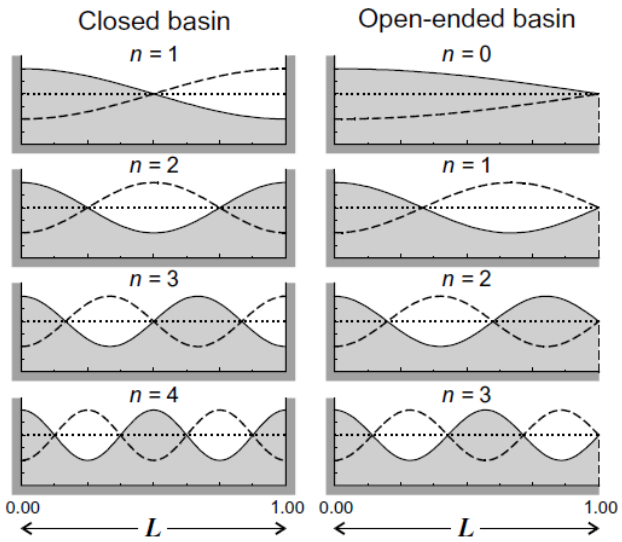

Figure 2.5: Surface profiles for the first four seiche modes in closed and open-ended rectangular basins of uniform depth (Rabinovich, 2010).

Resonance for coral reefs is mostly observed for the fundamental mode (n = 0), which corresponds to a wavelength equal to four times the length of the basin (Rabinovich, 2010). The fundamental mode also typically leads to the largest resonant amplification on coral reefs. Gawehn et al. (2016) notes that reef flats are typically too dissipative to accommodate LF resonance at higher modes.

2.4.2. Resonance controls

The occurrence of resonance is related to hydrodynamic and morphological aspects. The time scale of the forcing, the water depth over the reef and the reef flat width play an important role according to the theory of resonance. The geomorphologic and hydrodynamic controls affecting the occurrence of resonance are explained here.

Resonance frequency

The morphology and water depth over a fringing reef determine the natural frequency of the reef flat. Typical dimensions of the reef flat and reef submergence correspond to resonance periods that are in the order of tens of minutes and fall outside of the energetic part of the wave spectrum (Péquignet et al., 2009). For fringing reefs with a relatively short reef flat and high submergence (for example during extreme weather events), natural frequencies are much higher and may be excited by the incoming forcing, leading to resonant amplification (Pomeroy et al., 2012a). Additionally, waves propagating over a narrow reef experience less frictional dissipation compared to a long reef flat.

Depending on the reef flat width, the natural frequency falls within the IG or VLF frequency range. Reefs with particularly narrow reef flats, such as is the case for the Kwajalein Atoll, can not support VLF motions (Cheriton et al., 2020). The Roi-Namur reef, which is the subject of this study, has a reef flat width of 250 m and has eigenfrequencies in the VLF band.

Pomeroy et al. (2012a) examined the dynamics contributing to resonance on a fringing reef on Guam during a tropical storm and found that wider reefs experience a greater amplification than narrower reefs, although it is recognised that these reefs are characterised by having relatively more frictional dissipation.

As mentioned before, the beach slope influences the ability of the shore to reflect incoming long waves, therefore affecting reef flat resonance, but it may also influence resonance periods. The beach extends the effective basin length and therefore leads to higher resonant periods compared to the theoretical value (Shimozono et al., 2015). Similarly, bottom friction may increase the resonance period as it reduces the wave celerity (Shimozono et al., 2015). Additionally, frictional dissipation is found to effectively reduce resonance magnitude (Pomeroy et al., 2012a).

An increase in water depth results in higher resonant frequencies. Péquignet et al. (2009) conclude that any increase in water level on the reef will potentially allow a wider range of wave conditions to excite reef resonant modes. In addition, an increase in water level over the reef allows more LF wave energy to reach the shore (Péquignet et al., 2009). At the shoreline, LF waves may reflect and increase the possibility of standing and potentially resonating LF oscillations (Gawehn et al., 2016).

Low-frequency wave generation

The occurrence of resonance is also linked to various geomorphological and hydrodynamic controls that affect the generation of low-frequency waves on a reef flat.

The slope of the fore reef is key in controlling the mechanism of LF wave generation. A steeper slope reduces the surf zone width and enhances the generation of LF waves through breakpoint forcing.

Gawehn et al. (2016) concluded that incident wave heights were less important than incident wave peak periods in the generation of resonance and that resonance was preferably induced by swell-dominated offshore wave conditions. Péquignet et al. (2009) found that reflection increases with increasing wave peak period and decreasing offshore wave height.

Gaido (2019), who studied the resonance response of a schematised reef profile to regular small amplitude LF waves using numerical model SWASH (1D), also concluded that the relative resonant amplification was stronger for smaller wave heights than larger wave heights. This is supported by Van Noort (2021), who concludes that the largest resonant amplification occurs for strongly modulated but not overly energetic wave fields.

Directional wave spread of the incident waves has been suggested to cause weak detuning from resonance and reduce the efficiency of energy transfer to low-frequency waves on gently sloping beaches (Herbers & Burton, 1997). Veldt (2019), who researched the effect of wave directional spread for coral reefs, points out that greater wave directional spread leads to lower wave setup and thus to reduced LF wave runup at the

coastline. Furthermore, the incident angle of the incoming wave field influences IG wave generation as well (Herbers et al., 1995).

Other reef configurations
Yao et al. (2019) conducted lab and numerical experiments for different reef structure configurations of a shelf-like reef. They found that the presence of a reef crest increased the IG wave energy at the reef edge through an increase in breakpoint forcing LF wave generation. However, the reef crest also disrupted the cross-shore structure of resonant modes. The relative importance of the breakpoint forcing generation versus the reef structure disruption determined the IG wave at the shoreline.

Studying the effects of excavation pits on coral reef hydrodynamics, Klaver (2018) concluded that wider pits and pits located closer to the reef crest have a larger decrease in resonant amplification and thus IG wave energy.

While fringing coral reefs can exhibit alongshore variability in morphology, which may influence reef hydrodynamics (e.g.,Rey, 2019; Rogers et al., 2013), these are not elaborated here.

2.4.3. Build-up of resonance

In both physical and numerical models, resonance was found to have a period of build-up before reaching maximum amplification (Nwogu and Demirbilek, 2010; Gaido, 2019; Van Noort (2021)). In the analysis of resonance forced by regular, small amplitude IG waves in SWASH (1D), Gaido (2019) found that a number of 12 IG waves was required to reach maximum resonant amplification. Nwogu and Demirbilek (2010) studied the resonance response to a bichromatic wave field in a physical model, and indicated that 5 IG waves were needed for maximum amplification. However, Van Noort (2021), who analysed the resonance response to bichromatic waves in SWASH (2DV), found no build-up behaviour with the maximum amplification being reached within the first wave period.

In the field, the typical irregular and non-stationary wave field makes it challenging to observe and analyse a resonance build-up. Additionally, wave records are typically of relatively short duration, making it difficult to assess potentially long periods of resonance and their build-up. Gawehn et al. (2016) suggested that the resonance at the Roi-Namur reef could be short-lived.

2.4.4. Field observations of resonance on coral reefs

In this section, a few cases where resonance was observed in the field are reviewed.

Ipan (Guam) during typhoon Man-Yi
The Ipan reef in Guam is characterised by a wide fringing reef flat ($\sim$ 450 m) and a very steep forereef slope ($\sim$ 1:11), which results in a narrow wave breaking one around the reef edge. It is a shallow reef with an average water depth over the reef flat of $\sim$ 0.5 m. During typhoon Man-Yi (2007), water levels over the coral reef increased to 2 m and wave conditions were anomalously high ($H_s = 4$ m, $T_p = 12$ s). This led to major wave-driven coastal inundation along the coast.

Péquignet et al. (2009) report field observations of LF, near-resonant oscillations that dominated the variance of sea surface elevation at the shoreline of the Ipan reef at the peak of the typhoon. They note that, while the LF wave amplitude typically decays slightly over a reef (due to frictional effects), anomalous amplification of the longest waves (period 200 to 1000 seconds) is observed during Man-Yi with the largest amplitude occurring at the shore. The increased water level resulted in higher resonance frequencies (falling within the energetic part of the wave spectrum). In combination with the wave group forcing of a similar time scale, this resulted in a resonant response. Resonance modes were not observed during non-storm conditions.

Eastern Samar coast (Philippines) during super typhoon Haiyan
Super typhoon Haiyan (2013), one of the strongest typhoons to make landfall ever recorded, resulted in extreme storm waves ($H_s = 17.3$ m, $T_p = 16.5$ s) that attacked the coast of Eastern Samar in the Philippines. The southeastern coast of Eastern Samar is fronted by shallow fringing reefs with a width of 30-800 m and a depth of 0-1.0 m depending on the tide. The coral reefs in this area are in poor conditions, presumable because of frequent storm damage.

In a field study, Shimozono et al. (2015) confirmed overwash heights of 6-14 m above mean sea level along the southeastern coast which led to extensive inundation in some coastal villages, despite being protected by a wide fringing reef. The steep bathymetry allowed huge waves to develop and propagate to the reef front,

where the rapid decay of wave amplitude induced a significant wave setup over the reef (Shimozono et al., 2015). Again, the larger water depth resulted in a higher resonance mode frequency, which allowed resonant amplification of IG waves.

For a case study on the Eastern Samar coast in the Philippines, Shimozono et al. (2015) found that overwash height rapidly increases for reef widths smaller than 200 m.

Roi-Namur (Marshall Islands) during long-term observations

During a period of 5 months, wave gauges and a current meter were deployed for two shore-normal transects (NW and NE) in Roi-Namur Island in the Republic of the Marshall Islands. The fringing reef at the study site is characterised by a 250 to 350 m wide, gently sloping reef flat. The reef is fronted by a steep fore reef slope ($\sim$1:20) and leads to a narrow and steep ($\sim$ 1:6) sandy beach. The reef is relatively smooth and has an average water depth of 0.7 m. In contrast to the Ipan reef, the narrower reef width may result in resonance under a larger range of water levels (Cheriton et al., 2016). Resonant frequencies may not only be excited during extreme storm events, but also calmer ones. For the NW transect, VLF waves were classified as resonance 3.6% of the study period by Gawehn et al. (2016). Resonance was identified across a range of water levels, but more likely with higher than average water levels (Gawehn et al., 2016; Cheriton et al., 2016). In the observation period, two large wave events were captured with maximum wave heights larger than 6 m and peak periods of 16 s on 19 December 2013 and 2-3 March 2014 (Cheriton et al., 2016). For these two events, Gawehn et al. (2016) suggested percentages of resonance occurrence in 24 hours around the overwash events to be 17% and 33% for the December and March events respectively.

2.4.5. Qualification and identification of resonance

In order to assess whether a wave behaviour is classified as resonance, several methods have been proposed. This section summarises different approaches that have been applied.

Method by Péquignet et al. (2009)

Péquignet et al. (2009) identified resonance for field observations at the Ipan reef collected with various sensors (see Figure 2.6). They start by doing an Empirical Orthogonal Function (EOF) analysis on 2-hour segments of band-pass filtered sea surface elevation time series across the reef to identify dominant modes of variability. The band-pass filter is used to isolate the energy within specific frequency ranges. In this case, the first 3 resonant frequencies (n = 0, 1, 2) are examined. They find that the cross-shore structure of the first two observed modes matches the structure of theoretical resonant modes (Péquignet et al., 2009). Next, coherence spectra analysis is applied to find the degree of correlation between the sea surface elevation at sensors 1 and 2 in the frequency range around the theoretic values of resonant frequencies. The co-spectrum is used to measure the similarity and distribution of frequencies in the two time series. It appears that motions around the resonant frequencies are highly coherent which is particularly pronounced when the absolute value of the co-spectrum between the two sensors is high.

Next, the time scale of the forcing is examined. The time scale of the envelope of the offshore (sensor 6) sea surface elevation seems to be in line with the resonant frequencies. The inshore sea surface elevation in the low-frequency band and the offshore wave envelope show high coherence. To further investigate this relation, a transfer function is estimated as the ratio of the amplitude of the cross-spectrum between the two time series, and the auto-spectra of the wave envelope. The transfer function shows a strong gain of energy near the fundamental resonance mode (Péquignet et al., 2009).

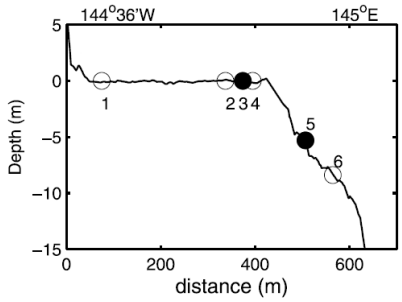

Figure 2.6: Topography along the across-shore transect at Ipan reef with the location and number of the pressure (open circles) and collocated pressure and current-meter (solid circles) sensors (Péquignet et al., 2009).

Pomeroy et al. (2012a) indicators

Pomeroy et al. (2012a) identified resonance for data obtained with numerical model XBeach. Two spatially lagged observation points, x and y, are introduced, as illustrated in Figure 2.7, which are analysed and compared based on three indicators.

The first indicator is a highly coherent variation in water surface elevation. A high coherence characterises a standing wave across a basin, but can also indicate a progressive wave that is consistent in form. The second indicator is used to determine the propagation type of the oscillation by assessing the phase difference between stations x and y. A phase difference of around 180° or 0° indicates a standing motion. The third indicator is the amplification of the wave signal between the x and y. Pomeroy et al. (2012a) determine this with the amplification ratio of the variance density spectra at the shoreline and reef crest.

The coherence, phase and amplification analyses share similarities with the method used by Péquignet et al. (2009) as described before.

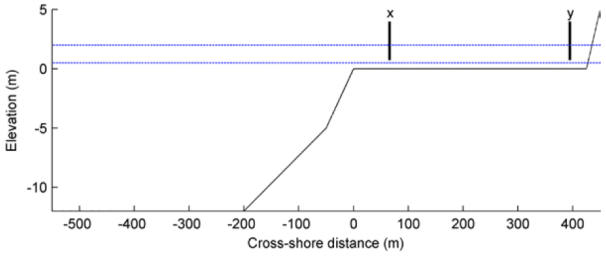

Figure 2.7: Topography along the cross-shore transect at Ipan reef with the location of observation points x and y in the model (Pomeroy et al., 2012a).

Gawehn et al. (2016) classification method

Gawehn et al. (2016) classified VLF waves at the Roi-Namur reef, categorising these waves into four classes: resonant, (nonresonant) standing, progressive-growing and progressive-dissipative waves, see Figure 2.8. The method proposes a sequence of criteria to categorise a VLF motion into one of the classes: resonance, damping and standing criterion.

The criterion for resonance is based on the energy transfer between the incident wave group envelope spectrum and the inner reef flat wave spectrum. Resonance was quantified by normalising the low-frequency energy at the inner reef with the low-frequency energy at the fore reef.

Gawehn et al. (2016) note that the method used by Pomeroy et al. (2012a) potentially incorrectly identifies resonance, as the three criteria are met for both resonant and non-resonant standing waves with an antinode at the shoreline.

The resonance classification by Gawehn et al. (2016) is currently the most suitable option to use as a resonance identification method for various types of observations (field, lab and model). This method will be the starting point of this research and is further explained in the methodology in Chapter 3.

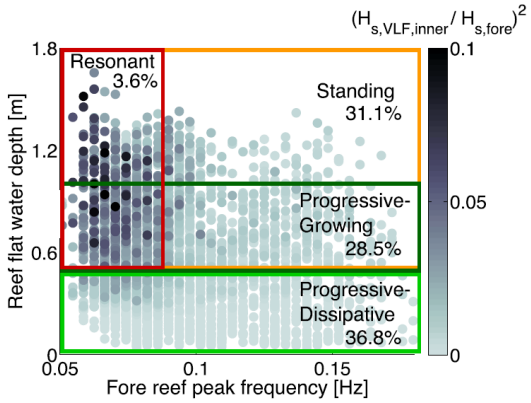

Figure 2.8: Normalised VLF energy at the inner reef flat as a function of the fore reef incident wave peak frequency and time- and spatially averaged reef flat depth. The four VLF wave classes are distinguished in coloured boxes (Gawehn et al., 2016).

2.5. Spectral analysis methods

The analysis of time series plays a central role in the assessment of wave and resonant behaviour. In this section, several methodologies are presented for examining data series in terms of their frequency content. Specifically, the methods of Fourier analysis and Hilbert-Huang transform are explored. The concept of these methods is presented, followed by an overview of the benefits and challenges associated with their application. Particular emphasis is placed on the Hilbert-Huang transform, aligning with the objective of this research.

2.5.1. Fourier analysis

The Fourier analysis is widely accepted as the most useful tool in spectral analysis, so much so that it is almost a synonym of spectral analysis. The basic premise of the Fourier analysis is that any finite length, infinitely repeated time series $x(t)$ can be reproduced by a linear summation of cosines and sines, known as the Fourier Series (Thomson and Emery, 2014; Fourier, 1888):

$$x(t) = \overline{x(t)} + \sum_{p} \left(A_p \cos(\omega_p t) + B_p \sin(\omega_p t)\right) \tag{2.2}$$

Each of the sinusoidal components within this series is characterised by its amplitude and frequency, which are constants. Through the Fourier transform, the data can be converted from the time domain into the frequency domain, revealing the spectral characteristics of the data. An efficient algorithm that enables fast computation of the Fourier transform, and is commonly applied, is the Fast Fourier Transform (FFT) (Thomson & Emery, 2014).

The Fourier analysis provides a simple yet powerful mathematical framework, facilitating energy conservation and the orthogonality of its components. However, there are some restrictions to the methods that are important to recognise.

The underlying assumption of the Fourier analysis is that the data must be stationary and linear (e.g. Titchmarsh, 1948). By definition, each oscillatory component in the Fourier series persists through the entire duration of the data series, implying stationarity. In reality, few data sets of natural phenomena, including sea surface elevation, satisfy this condition. Consequently, when Fourier analysis is applied to such non-stationary data, numerous Fourier components are added to simulate the data's time-varying nature. This generates spurious harmonics and results in the diversion of energy to a much wider frequency domain (Huang et al., 1998). The resulting spectrum fails to accurately capture the true energy density in the frequency space. Thus, while the Fourier components make mathematical sense, they lack physical sense when applied to non-stationary data.

Fourier analysis also requires linearity. This is assumed within the framework of linear wave theory, where the period is constant and the wave height is equal to twice the wave amplitude. However, as waves travel shoreward, asymmetry (sharp crests and flat troughs) increases. Again, additional harmonic components are necessary to simulate the deformed wave profiles (Huang et al., 1998).

As certain features of sea waves are neglected and time-variant characteristics are completely lost in the Fourier representation, this analysis method can lead to misinterpretation of the data and distort the phenomena being investigated (Veltcheva and Soares, 2004; Schlurmann, 2002; Dätig and Schlurmann, 2004).

2.5.2. Hilbert-Huang transform

The Hilbert-Huang transform (HHT) was proposed by Huang et al. (1998) as a new method for analysing nonlinear and non-stationary data and offers a powerful and adaptive tool that preserves the time-varying and local characteristics of the analysed signal. The HHT combines two main techniques: Empirical Mode Decomposition (EMD) and the Hilbert transform. The EMD breaks a signal into components that are called Intrinsic Mode Functions (IMFs), each representing a wave with a specific frequency. The Hilbert transform is then applied to these IMFs and provides the frequency, amplitude and phase information as a function of time. This section describes the HHT approach, its challenges and its applications in ocean and coastal waves research.

The HHT method is motivated based on the assumption that any data consists of different intrinsic mode oscillations (Huang et al., 1999). The EMD is a key element of the HHT and aims to decompose a

given signal into a finite number n of components or IMFs c_j, and a residual r_n.

$$x(t) = \sum_{j=1}^{n} c_j(t) + r_n(t) \tag{2.3}$$

An IMF is defined by two criteria: (i) the number of local extrema and zero-crossings must either be equal or differ by one at most, and (ii) the mean of the envelopes defined by the local maxima and minima must be zero (Huang et al., 1998). Practically, this suggests that within an IMF, the maxima are all positive and the minima are all negative. Consequently, it implies that within an IMF, there are no situations where shorter waves are 'riding' or superimposed on longer waves. The EMD can be implemented with the following algorithm and is illustrated in Figure 2.9

1. identify all local extrema of input $x(t)$
2. interpolate between the maxima (minima) to obtain the upper (lower) envelopes, $e_{max}(t)$ ($e_{min}(t)$)
3. compute the mean of the two envelopes: $m(t) = (e_{max}(t) + e_{min}(t))/2$
4. subtract the mean from the signal to obtain $h_{j,k}(t) = h_{j,k-1}(t) - m(t)$, here: $h_{j,k-1}(t) = x(t)$

This procedure is iterated until a function $h_{j,k}(t)$ is obtained that satisfies the IMF requirements. To guarantee that the IMF components retain enough physical sense of both amplitude and frequency modulations, a stopping criterion is applied to stop the sifting and define an IMF, limiting the number of iterations. Typically, a stopping criterion based on standard deviation (SD) between two consecutive sifting results is used, see equation 2.4. In practice, SD values of 0.2-0.3 have been observed (Zare & Nouri, 2023).

$$SD = \sum_{t=0}^{T} \frac{\left|h_{i,(k-1)}(t) - h_{i,k}(t)\right|^2}{{h^2}_{i,(k-1)}(t)} \tag{2.4}$$

After reaching the stopping criterion, an IMF is obtained: $h_{j,k}(t) = c_j(t)$. The IMF is subtracted from the signal and the process is repeated until all IMFs have been extracted and the remainder of the signal is a constant or monotonic function ($r_n(t)$). In this procedure, the IMF that is extracted first contains the fastest oscillations and, as the number of extracted IMFs increases, the oscillations become slower.

The IMFs derived from the data are complete and practically orthogonal, although the latter is not guaranteed theoretically (Huang et al., 1998).
After obtaining the IMFs, the Hilbert transform is applied. The Hilbert transform is a mathematical operation used to obtain the analytic signal from a real-valued signal by defining its imaginary part. It is important to note that the Hilbert transform is typically applied to "monocomponent" functions, meaning that at any given time, there is one frequency representing the component (Cohen, 1995). This condition is satisfied within an IMF, making it suitable for the application of the Hilbert transform (Huang et al., 1998). After applying the Hilbert transform to every IMF, the data can be expressed as:

$$X(t) = \sum_{j=1}^{n} a_j(t) e^{i\phi_j(t)} = \sum_{j=1}^{n} a_j(t) e^{i\int \omega_j(t)dt} \tag{2.5}$$

The residual r_n is left out in this description since it is either a monotonic function or a constant. The expansion is considered a generalised form of the Fourier expansion with time variable amplitudes and frequencies (Veltcheva, 2002). For comparison, the same data expanded in Fourier representation would be expressed as in equation 2.6, with a_j and ω_j constants.

$$X(t) = \sum_{j=1}^{\infty} a_j e^{i\omega_j} \tag{2.6}$$

From the analytic signal, the instantaneous phase (IP), instantaneous frequency (IF) and instantaneous amplitude (IA) can be computed. Then, a frequency-time distribution of amplitude or squared amplitude can be produced, referred to as the Hilbert amplitude spectrum or Hilbert energy spectrum respectively, see Figure 2.10a. Integration over time in the frequency-time distribution provides the marginal spectrum $h(\omega)$:

$$h(\omega) = \int_0^T HS(\omega, t)dt \tag{2.7}$$

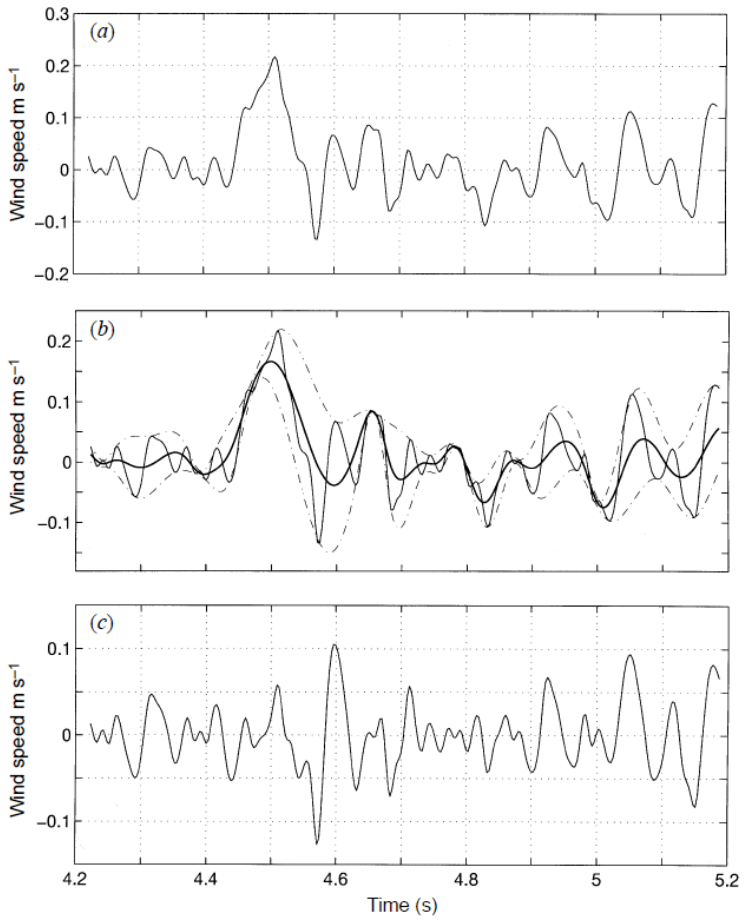

Figure 2.9: Illustration of the sifting process: (a) the original data; (2) the data in a thin solid line with the upper and lower envelopes in dot-dashed lines and the mean in a thick solid line; (c) the difference between the data and the mean of the envelopes (this is not an IMF yet) (Huang et al., 1998).

The marginal spectrum looks more like a traditional Fourier spectrum, see Figure 2.10b, since they are both energy-frequency distributions. However, it is important to note that the y-axis does not represent the same quantity. In the Fourier spectrum, the presence of energy at a given frequency means that a sinusoidal component with this frequency persisted through the entire period of the data. In the marginal spectrum however, the presence of energy at a certain frequency is associated with a likelihood, proportional to the energy amount, of having a component with this frequency and amplitude at any given time during the timespan of the record (Huang et al., 1998). This means that the Fourier and marginal spectra do not share the same interpretation. Only for a stationary process will the marginal spectrum be identical to the Fourier spectrum (Huang et al., 1998).

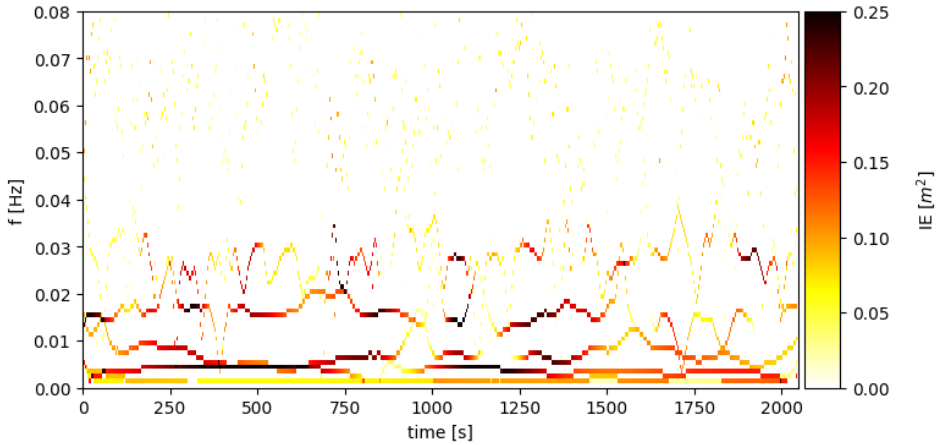

(a) Hilbert spectrum.

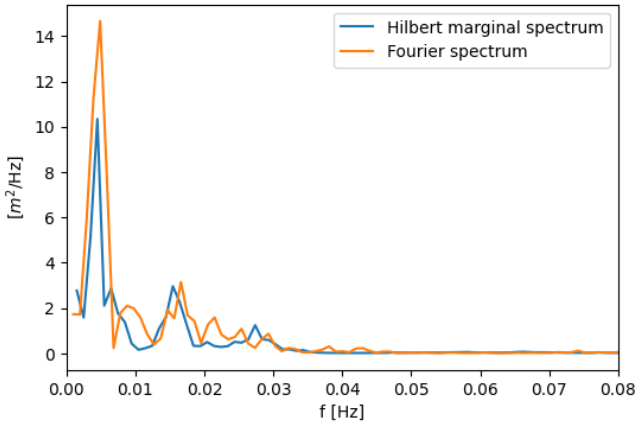

(b) Marginal spectrum.

Figure 2.10: Example of a Hilbert spectrum (a) and corresponding marginal spectrum (b) for an inner reef signal.

Challenges

Although the HHT has great potential and has been applied to an increasing number of fields in recent decades, some challenges related to the mathematical framework of the EMD remain. The main dilemmas belong to five categories: stopping criteria, determination of envelopes, end effects, over/undershoots and mode mixing (de Souza et al., 2022).

The stopping criterion is essential to prevent excessive iteration during the sifting. A high number of iterations may result in an IMF that has little physical meaning. Various stopping criteria are proposed in publications, including the SD criterion as mentioned before.

Interpolation plays a crucial role in the determination of envelopes. Usually, cubic spline is employed for approximating the envelopes due to its stability and smoothness, facilitating the convergence of the method (Huang et al., 1998). However, unwanted effects are common (de Souza et al., 2022). One of the effects originates from the lack of constraints at the end of the data series, which can lead to a big deviation in the numerical envelope compared to the true envelope (see Figure 2.11). These artificial oscillations spread inside and will gradually corrupt the next IMFs. This problem is commonly referred to as the end, edge or boundary effect. Typically, in order to limit the edge effect, the boundaries of the data series are expanded with extra points to interpolate through. Many methods have been proposed to choose these extra boundary points, but so far there is no consensus on which method handles the issue most effectively (Stallone et al., 2020). Some of these methods are addressed in Section 3.

Overshoots and undershoots are another unwanted effect of the envelope interpolations. An overshoot occurs when an extreme of the upper envelope is greater than a signal maximum, see Figure 2.12.

Finally, mode mixing occurs when the decomposition is unable to group signals with similar frequencies in distinct IMFs, resulting in different frequency scales in the same IMF and IMFs with overlapping frequency bands (Huang et al., 1998; Huang et al., 2003).

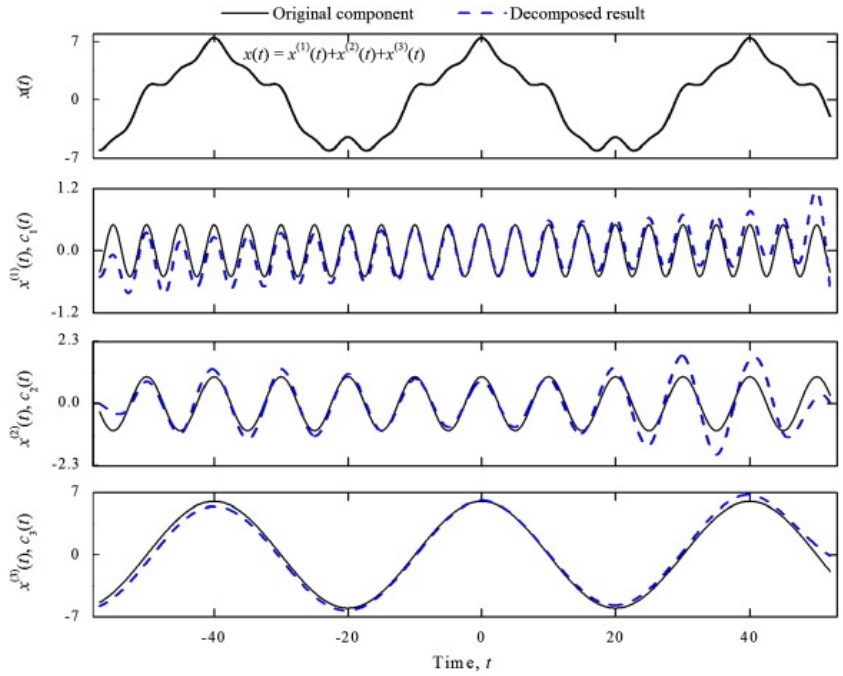

Figure 2.11: A signal $x(t)$ (top panel) and its decomposition by the EMD (bottom 3 panels). The end effect appears at the edges of the record in the first IMF, recognised by the deviation of the decomposed results (dashed line) relative to the original component (solid line). This affects the further decomposition process, where the end effects may spread to the middle of the component. The bottom panel shows that end effects at a higher frequency component may affect the resulting lower frequency IMFs (Lin et al., 2012).

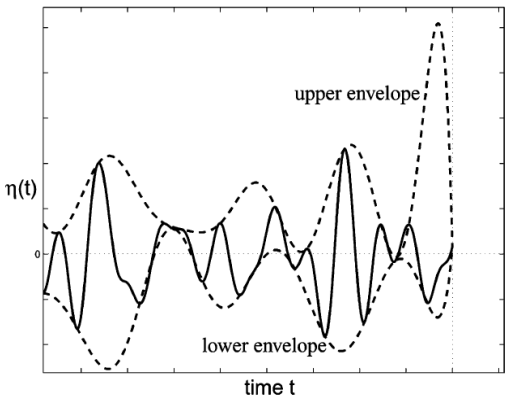

Figure 2.12: An example of a signal (solid line) with upper and lower envelope (dashed lines). A big overshoot of the upper envelope occurs at the end of the record as a result of interpolation (Dätig & Schlurmann, 2004).

Many expansions of the EMD have been proposed to enhance the performance of the sifting procedure. A well-known alternative version is the Ensemble Empirical Mode Decomposition (EEMD) with its closely related Complete Ensemble Empirical Mode Decomposition (CEEMD) (Wu and Huang, 2009; Torres et al., 2011). The EEMD is a noise-assisted sifting procedure in which a white noise signal is added to the data before the EMD is applied. This is performed many times, each with a distinct white noise signal. The final result of the decomposition is given by the set (*ensemble*) of averages of the corresponding IMFs (de Souza et al., 2022). This method requires much more computational power compared to the regular EMD.

Application of the Hilbert-Huang transform in practise

While the EMD lacks a precise mathematical definition, it has proven useful across various research fields. The HHT has been applied in the context of water waves (Huang et al., 2000; Veltcheva, 2002; Schlurmann et al., 2003; Hwang et al., 2003; Ortega and Smith, 2009; Senthilkumar et al., 2015; Veltcheva and Soares,

2016; Mandal et al., 2020; He et al., 2022).

Hwang et al. (2003) applied the HHT to data of wind-generated ocean waves. They found that the HHT method detects more energy in lower frequencies, leading to a lower average frequency in HHT spectra than using the Fourier framework. In further research, Hwang et al. (2005) note that basic statistical measures such as spectral bandwidth or spectral moments yield similar results when computed from both Hilbert and Fourier spectra. This suggests that the study of the statistical properties of ocean waves may not be significantly affected by the choice of spectral technique. Additionally, they find that wave group structures represent low-frequency oscillations. While Fourier analysis may interpret these wave groups as the interaction of two wave components with slight differences in frequencies, the spectral energy does not align with the observed frequency of wave groups. However, the Hilbert analysis accurately places the spectral energy of the wave group within the correct frequency band, provided it is distinct enough from the carrier frequency.

3

Methodology

The methodology of this research is divided into 3 parts. The first part focuses on the evaluation of various sifting configurations for the Empirical Mode Decomposition (EMD). The EMD is the first step of the Hilbert-Huang transform (HHT) and is used to sift a signal to produce components or intrinsic mode functions (IMFs). The performance of the sifting configurations is evaluated through visual inspection and a set of performance metrics. Additionally, some spectral characteristics of the marginal spectra are compared to those of the Fourier spectra. Resulting from this, a choice will be made regarding the EMD technique that will be applied in the HHT for further analyses.

Next, the VLF oscillations at the inner reef are further investigated. The dominant VLF component of the inner reef signal decompositions is identified based on the natural frequency of the reef flat (which is in the VLF range, 0.001-0.005 Hz). The dominant VLF component is classified based on its propagation type (standing or progressive) and amplitude (energetic or non-energetic). Next, the resonance analysis is conducted, of which the method is based on the approach of Gawehn et al. (2016). In this method, resonant oscillations are defined by their frequency being close to the theoretical natural frequency and having a minimum amplification between the fore reef envelope and inner reef signal energy. The original approach is based on spectral analysis using Fourier spectra and disregards non-stationarity within time series. Crucially, the HHT makes a time-varying resonance analysis possible as it facilitates resonant amplification being described over time. Not only does this improve the description and identification of resonance by considering the non-stationarity of signals, it also allows for the investigation of the transient characteristics of resonance. Some resulting patterns from the classification and resonance identification regarding various hydrodynamic factors are analysed.

Following the classification and resonance analysis, some transient characteristics of the energetic and resonant VLF oscillations are further studied. More specifically the duration and intensity of energetic and resonant events are explored, which is possible through the HHT approach. Furthermore, the relation of energetic and resonant oscillations to the instances of coastal flooding is investigated.

An overview of the methodology sections and their purpose is illustrated in Figure 3.1. Additionally, a description of the data that will be analysed is provided in Section 3.1.

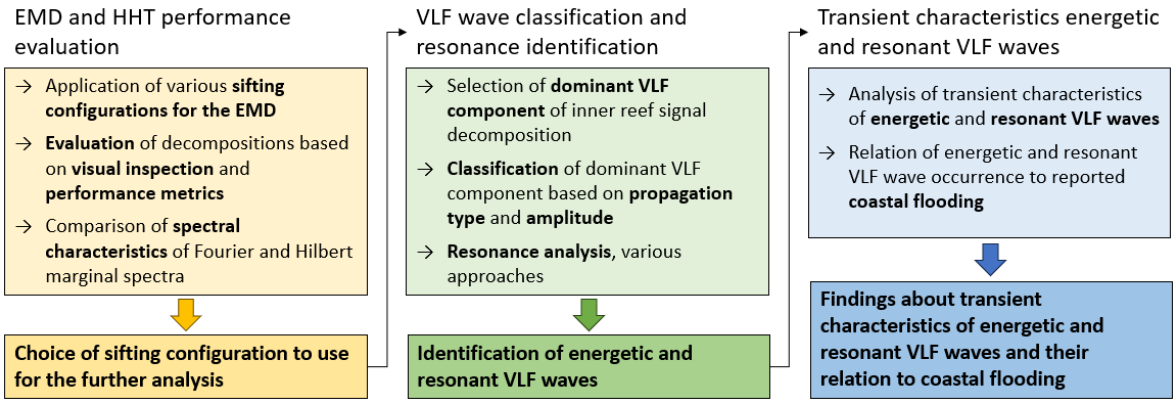

Figure 3.1: Overview of methodology sections. Parts 1 to 3 are displayed from left to right. For each part, from top to bottom, the steps and purpose are highlighted in the coloured boxes.

3.1. Data description

This study utilises field data collected at Roi-Namur Island (Marshall Islands), where observations for a cross-shore transect were recorded from November 3, 2013, to April 13, 2014. Pressure measurements were taken using bottom-mounted pressure sensors at four locations on the reef: the fore reef, outer reef flat, mid reef flat, and inner reef flat. At these locations, pressure was recorded at 2 Hz for 34 minutes every hour, resulting in 4096 samples per recording session. The transect and reef station locations are illustrated in Figure 3.2. This transect includes a reef flat with a width of 250 m, a steep fore reef, and a steep narrow beach, as described previously in Sections 1.3.2 and 2.4.5. The reef geomorphology and average reef flat submergence of 0.7 m lead to natural frequencies in the VLF range.

Additionally, at an offshore location, an Acoustic Wave and Current profiler (AWAC) was deployed at a depth of 21 m to record pressure measurements at 1 Hz for 34 minutes every hour, resulting in 2048 samples per recording session (Quataert et al., 2015). This resulted in a dataset of 3800 records for each station. The pressure data was processed to obtain surface elevation data. No velocity measurements were recorded.

As previously mentioned, Gawehn et al. (2016) also investigated this dataset, classifying VLF waves and identifying resonance through spectral analysis using Fourier analysis. Furthermore, Cheriton et al. (2016) analyzed this dataset and pointed out two overwash events and two high wave runup occurrences during the recording period.

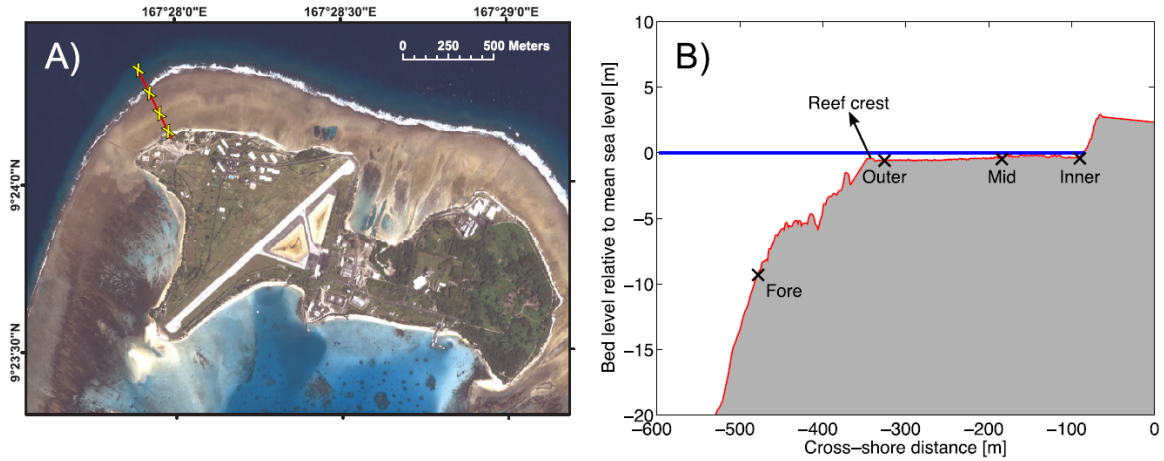

Figure 3.2: Views of the study area on Roi-Namur Island. (a) Map view of the site with locations of the instruments on the reef indicated with a yellow cross; (b) bathymetry for cross-reef transect and location of sensors. (Gawehn et al., 2016)

3.2. Assessing EMD and HHT performance

In this part, the application of the Hilbert-Huang transform is explored, particularly the Empirical Mode Decomposition element. Various EMD configurations are tested and evaluated and the spectral elements resulting from the HHT and the FFT are compared.

This section describes elements of the EMD configuration, indicators that are used to evaluate the performance of various EMD realisations and finally the spectral characteristics that are used for comparison between the HHT and the FFT.

3.2.1. Empirical Mode Decomposition configurations

The HHT is considered a powerful tool because of its adaptability and ability to deal with non-stationary and non-linear data. Although the HHT has great potential, some limitations do exist. Consequently, the method has been subject to research since its introduction (see Section 2.5.2). The evolution of the HHT through research in a wide array of fields has led to many suggestions to improve issues like the end effect and mode mixing. Some of the issues are highlighted in Section 2.5. Some solutions that have been proposed are discussed in this section.

Due to the computational complexity of the HHT, a pre-existing Python package is used in the application. Multiple packages offer a range of configurations and customisation of the HHT, however, there are limitations to the options. Therefore, not all configurations that have shown some success in publications can be applied. In Python, there are several HHT implementations available: `EMD`, `PyEMD`, `PyHHT` and, more recently developed, `AdvEMDpy`. The `EMD` package has been chosen because of its extensive options in configurations, evaluation and comprehensive documentation (Quinn et al., 2021).

The `EMD` package offers a family of sifting algorithms, instantaneous frequency transformations, power spectrum construction and single-cycle feature analysis (Quinn et al., 2021). The sifting procedure that defines the Empirical Mode Decomposition (EMD) is where the algorithm is most customisable. As previously explained, the HHT consists of the EMD, which decomposes a signal into components, referred to as Intrinsic Mode Functions (IMFs). In short, IMFs are extracted from the signal by making an upper and lower envelope through local maxima and minima respectively. The mean of the two envelopes is then subtracted from the signal. This procedure is iterated until some stopping criterion is met. The interpolation technique and stopping criterion are modifiable and the `EMD` package offers various options for these features. Some extensions to the EMD algorithm include the use of a noise or masking signal. These versions of the EMD include the masking EMD (M-EMD), the iterated masking EMD (iM-EMD), the Ensemble EMD (EEMD) and the Complete Ensemble EMD (CEEMD), which are all included in the `EMD` package. For the following aspects of the EMD, various options will be tested and evaluated:

- **Sifting technique**: EMD, M-EMD, iM-EMD, EEMD or CEEMD
- **Interpolation technique**: cubic spline or B-spline
- **Boundary extension**: constant padding or mirroring method by Rilling et al. (2003)
- **Stopping criterion**: standard deviation criterion or stopping criterion by Rilling et al. (2003)

These customisation options are all available in the `EMD` package. The background of the configuration options is discussed below.

Sifting techniques

Various sifting techniques have been developed as extensions to the original EMD procedure. The alternative sifting procedures discussed here are based on a similar concept of introducing a disturbance to the original data in order to have a more uniform distribution of extrema to mitigate mode mixing problems.

The M-EMD makes use of masking signals to improve the extraction of oscillations with a frequency close to the mask signal. It enables the separation of two components that have frequencies within a ratio of 2 of each other (Deering & Kaiser, 2005). By adding a masking signal to the original (or residual) signal, the M-EMD aims to overcome the intermittency of oscillations in a signal and avoid mode mixing (Deering & Kaiser, 2005). The `emd.sift` module of the `EMD` package offers two options for mask-assisted sifting. The `mask_sift` algorithm determines the mask frequencies based on the zero-crossing of the highest frequency component (which is extracted with the regular sift). Subsequent masks are defined by a mask step factor, which is set to 2 as default. The amplitude of the mask is defined by the ratio of the standard deviation of the input signal. The `iterated_mask_sift` algorithm identifies the optimal masks based on the mean of the amplitude-weighted instantaneous frequency (Quinn, 2022; Fabus et al., 2021).

The EEMD and CEEMD are noise-assisted methods. The EEMD sifts an ensemble of signals with white noise added and treats the mean IMFs as the result. This approach relies on the effect of the additive white noise cancelling out across the whole ensemble, whilst the true signal should survive the averaging (Quinn, 2022). The CEEMD is an adjustment to the EEMD, similarly, it sifts an ensemble of signals with white noise added, but a single IMF is taken across all ensembles before moving to the next IMF (Quinn, 2022; Torres et al., 2011).

The `EMD` package features each of these sifting techniques in addition to the EMD, the computation of the masking signals or noise is customisable, but the standard settings will be used in this analysis.

Interpolation techniques

A widely used interpolation technique for obtaining the signal envelopes is cubic spline interpolation. In water wave applications, this technique is often used (Huang et al., 2000; Schlurmann, 2002; Veltcheva and Soares, 2004; Huijsmans et al., 2012; Dehghan et al., 2022). A common alternative to cubic splines is B-spline interpolation (Riemenschneider et al., 2014). The choice of interpolation technique may influence the occurrence of overshoots or undershoots of the envelope, which influences the quality of the decomposition. Both methods will be tested.

Boundary extension techniques

Creating extra boundary data points to the original data set is a key element in mitigating end effects (see Section 2.5.2). The placement of these extra points is based on the original signal and should represent the characteristic behaviour of said signal. Many methods have been proposed to suppress the end effects. A simple method is to extend the data with new maxima and minima that correspond to the maxima and minima nearest to the edges of the record. The data can be padded with these maxima and minima multiple times, resulting in the extrema and interpolation as illustrated in Figure 3.3.

The mirror extension proposed by Rilling et al. (2003) is a popular method due to its excellent performance (Lu et al., 2020). However, performance reduces when the endpoints are not extrema. As the name suggests, the extrema are mirrored in the extreme point closest to the data boundary, see Figure 3.3.

In water wave applications, Dätig and Schlurmann (2004) consider a constant padding approach, but also propose an extended method that includes the slope in the placement of the added boundary points. This method is not commonly applied and is not featured in the Python package, therefore will not be considered.

Stopping criterion

To determine when the iterative procedure of the EMD stops and returns an IMF, a stopping criterion needs to be defined. The stopping criterion that is proposed by Huang et al. (1998) is based on the standard deviation (SD) between two successive sifting results:

$$SD = \sum_{t=0}^{T} \frac{|h_{k-1}(t) - h_k(t)|^2}{h_{k-1}(t)^2} \tag{3.1}$$

Where h_{k-1} and h_k are two successive iterations. Typical values for the SD threshold range between 0.2-0.3. Huang et al. (2003) and Rilling et al. (2003) note that excessive iterations could bias the decomposition process, potentially resulting in uniformity of amplitudes among the IMFs and a larger number of IMFs generated than expected. Rilling et al. (2003) proposed a 2-threshold criterion (TTC) that ensures globally small fluctuations while addressing locally large deviations. This criterion is composed of three inputs θ_1, θ_2 and α, and an evaluation function:

$$\sigma(t) = \left| \frac{m(t)}{d(t)} \right| \tag{3.2}$$

Where $m(t) = [e_{max}(t) + e_{min}(t)]/2$ and $d(t) = [e_{max}(t) - e_{min}(t)]/2$, e_{max} and e_{min} being the upper and lower envelope respectively. The sifting is iterated until $\sigma(t) < \theta_1$, for the fraction $(1-\alpha)$ of total time and $\sigma(t) < \theta_2$ for the remaining part of the time. The default values used by Rilling et al. (2003) are $\alpha = 0.05$, $\theta_1 = 0.05$ and $\theta_2 = 10\theta_1$.

Many more stopping criteria exist, as highlighted by de Souza et al. (2022), however, only the SD and TTC are featured in the `EMD` package.

The different aspects of the EMD configuration as discussed above will be applied for a set of 120 observation records to be evaluated with a set of metrics that are described next.

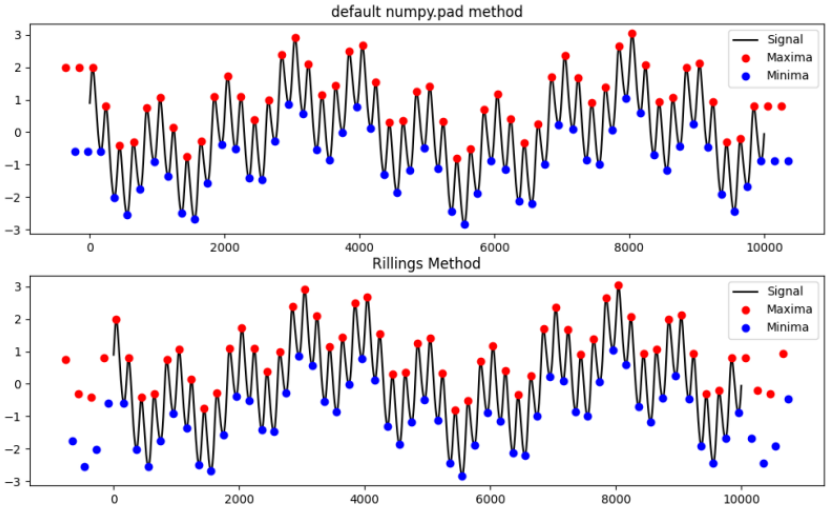

(a) Boundary extensions methods.

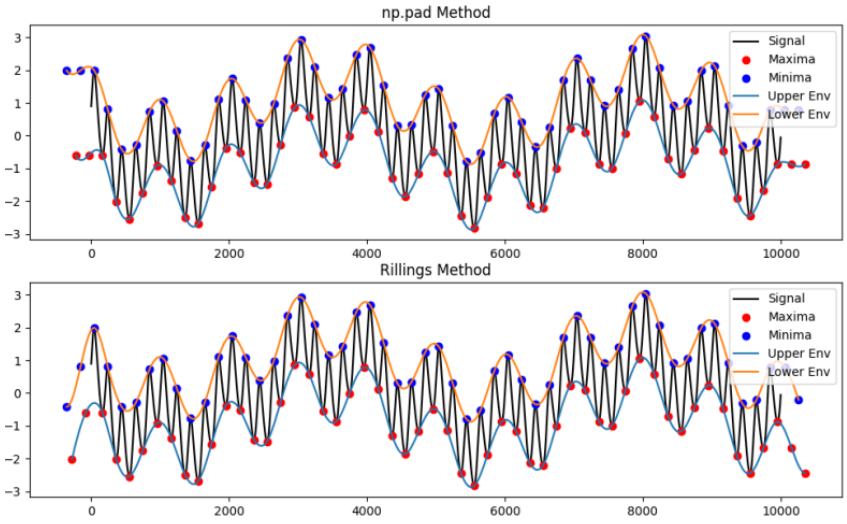

(b) Interpolation through boundary extensions.

Figure 3.3: Illustration of (a) boundary extension methods and (b) resulting envelopes for constant padding and Rilling's mirror extension (Quinn, 2022).

3.2.2. Evaluation metrics

The performance of each configuration will be evaluated through visual inspection and a set of metrics. Visual inspection of a signal and its decomposition is a popular evaluation technique. Although it is not feasible to apply visual inspection to the entire dataset due to its scale, it will be applied to several examples. The evaluation metrics provide a broader, numerical performance assessment. Additionally, the computation time is considered in the evaluation and selection of a sifting configuration.

A multitude of metrics have been suggested to assess the performance of EMD (Huang et al., 1998; Laszuk et al., 2015; de Souza et al., 2022; Zare and Nouri, 2023). An important characteristic of a valid decomposition is orthogonality. While the orthogonality is satisfied in a practical sense, it is not guaranteed theoretically. Therefore orthogonality of a decomposition should also be numerically verified post-decomposition. This is typically done through the overall index of orthogonality (IO), expressed by Huang et al. (1998) as:

$$IO = \frac{1}{\int_0^T x(t)^2\,dt} \cdot \sum_{i=1}^{n+1}\sum_{j=1}^{n+1}\left(\int_0^T c_i(t)\cdot c_j(t)\,dt\right), i \neq j \tag{3.3}$$

where $x(t)$ is the original signal with time length T and $c_{i,j}(t)$ represent IMFs and n is the number of

extracted IMFs. For perfect orthogonality, the IO should be zero. It should be noted that, although the index of orthogonality provides a global assessment, its significance may be limited as orthogonality in the context of the HHT is primarily a local feature, which may affect its accuracy in certain cases.

Daqian et al. (2007) propose a metric, θ, that compares the signal energy of the original and the decomposition of the signal. Mathematically, this criterion can be expressed as:

$$\theta = \frac{1}{RMS_x}\left(\sqrt{\sum_{i=1}^{n+1} RMS_i^2} - RMS_x\right) \tag{3.4}$$

where RMS_x and RMS_i are the root mean squares of the original signal and an IMF respectively. According to the definition, the smaller θ is, the smaller the impact of the end effect.

Other evaluation metrics have been used in ocean or coastal wave research as well. Mandal et al. (2020) use the maximum amplitude error ($a_{max,error}$) indicating the maximum error between the original signal and the sum of the IMFs.

Veltcheva and Soares (2007) propose a time variable error EI, which quantifies the correctness of an extracted IMF based on the normalisation of the IMF with its envelope:

$$EI = (A_j(t) - 1)^2 \tag{3.5}$$

where $A_j(t) = c_j(t)/R_{c_j}(t)$ is the normalised IMF $c_j(t)$ and $R_{c_j}(t)$ is an envelope of IMF $c_j(t)$.

The decomposition can also be evaluated on IMF level, comparing two components specifically instead of the entire set of IMFs. The following metrics are used to evaluate the IMF performance:

1. **Index of orthogonality between components**: in addition to the global IO, the orthogonality between two components can be quantified. The IO_{ij} between two IMFs c_i and c_j is expressed by Huang et al. (1998) as:
$$IO_{ij} = \sum_t \frac{c_i c_j}{c_i^2 c_j^2} \tag{3.6}$$
2. **Correlation**: A low correlation between the IMFs should be ensured as well, especially when applying a masking signal to the signal. The Pearson correlation coefficient (ρ_{ij}) is computed for each pair of IMFs (c_i and c_j):
$$\rho_{ij} = \frac{cov(c_i, c_j)}{\sigma_{c_i}\sigma_{c_j}} \tag{3.7}$$
where cov denotes the covariance and σ the standard deviation.
3. **Pseudo mode splitting index**: Y.-H. Wang et al. (2018) propose an additional metric, the pseudo mode splitting index ($PMSI$). The metric is aimed to quantify the mode mixing between components and is also featured in the `EMD` package. It is expressed as:
$$PMSI_{i,i+1} = max\left(\frac{\vec{c_i}\cdot\vec{c}_{i+1}}{\|\vec{c}_i\|_2^2 + \|\vec{c}_{i+1}\|_2^2 + 10^{-8}}, 0\right) \tag{3.8}$$
4. **Frequency overlap**: the EMD is meant to separate a signal into components with (average) frequencies that decrease as the IMF number increases. A metric to quantify this is proposed by Laszuk et al. (2015). A similar method is featured in the `EMD` package, which calculates the proportion of samples where the instantaneous frequency (IF) of adjacent pairs of IMFs overlaps.

It should be noted that these metrics, although they provide some indication of validity, should not be assumed as objective scores. The (current) absence of an analytical formulation of the EMD, hinders conducting a theoretical analysis and performance evaluation (Deléchelle et al., 2005).

The proposed metrics have in common that a smaller value indicates a better decomposition. However, it is difficult to define a threshold for a good or bad decomposition. In addition to the proposed metrics, computation time also plays an important part in choosing the optimal sifting configuration for this research.

To account for the different wave patterns observed at the fore reef and inner reef, the decomposition performance is evaluated for both of these stations. A selection of 120 time series is made for each of these stations. Based on visual inspection of a few (inner reef) records and the results for the performance indices, the most suitable sifting configuration is selected. An important aspect of a suitable sifting method is that is able to extract the VLF oscillation of the inner reef signal into a single IMF, so that this component can be investigated separately in the following research steps that will be described in Section 3.3 and 3.4.

3.2.3. Spectral analysis

The Hilbert spectrum

After selecting a sifting configuration, all signals are decomposed with this method. A time series $x(t)$ is decomposed into a finite number n of components c_j and a residual r_n, which may be considered as an additional element C_j. *Following equations are from Huang et al. (1998), unless indicated otherwise.*

$$x(t) = \sum_{j=1}^{n} c_j(t) + r_n(t) \tag{3.9}$$

$$= \sum_{j=1}^{n+1} C_j(t) \tag{3.10}$$

After decomposition into components, the Hilbert transform is applied to each IMF, resulting in the analytic signal $z(t)$, which is used to obtain the instantaneous amplitude, phase and frequency.

$$z_j(t) = c_j(t) + iH[c_j(t)] \tag{3.11}$$

Note that the original component $c_j(t)$ is expressed as the real part of the analytic signal and the Hilbert transform $H[..]$ gives the imaginary part of the analytic signal. The instantaneous amplitude (IA, a_j), phase (IP, ϕ_j) and frequency (IF, ω_j) are computed by:

$$a_j(t) = \sqrt{c_j^2(t) + H[c_j(t)]^2} \tag{3.12}$$

$$\phi_j(t) = \arctan \frac{H[c_j(t)]}{c_j(t)} \tag{3.13}$$

$$\omega_j(t) = \frac{d\phi_j(t)}{dt} \tag{3.14}$$

The `EMD` package offers the option to use the Normalised Hilbert Transform (NHT) method. The NHT incorporates amplitude normalisation, making it more robust and accurate in analysing signals with varying amplitudes, and introduces new methods for computing instantaneous frequency to address limitations and improve accuracy compared to the regular Hilbert transform (Huang, 2005). The NHT is used in this analysis, but it will be referred to as the Hilbert transform.

After applying the Hilbert transform to every IMF, the data can then be expressed in (3.15). The residue r_n is left out in this description since it is either a monotonic function or constant.

$$X(t) = \sum_{j=1}^{n} a_j(t) e^{i\phi_j(t)} = \sum_{j=1}^{n} a_j(t) e^{i\int \omega_j(t)dt} \tag{3.15}$$

With the instantaneous quantities, a frequency-time distribution of amplitude or squared amplitude can be produced, referred to as the Hilbert amplitude spectrum or Hilbert energy spectrum respectively. As the energy spectrum is best comparable to the unit of the typical Fourier spectra, this is the spectrum type that will be used in this work. In this report, the Hilbert energy spectrum is denoted as Hilbert spectrum $HS(\omega, t)$. The subscript a will be used when the Hilbert amplitude spectrum is referred to specifically. Integration over time in the frequency-time distribution provides the marginal spectrum $h(\omega)$:

$$h(\omega) = \int_0^T HS(\omega, t)dt \tag{3.16}$$

where T denotes the total duration of the time series. Note that the frequency distribution and resolution of the Hilbert (marginal) spectra can be tailored to the user's preferences or requirements. An example of a Hilbert spectrum and marginal spectrum is given in Figure 2.10. In addition to the instantaneous amplitude, the instantaneous energy IE is defined as the sum of the squared amplitude over all components, which can be written as:

$$IE(t) = \int_\omega HS(\omega, t)d\omega \tag{3.17}$$

Comparison to the Fourier spectra

The Fourier spectra are obtained through the Fast Fourier Transform (FFT). Hanning windows are applied to time segments of 17 minutes (half the duration of a time record) with 50% overlap, resulting in a frequency resolution of 0.001 Hz. The same approach was used by Gawehn et al. (2016). The same bandwidth is applied for the Hilbert (marginal) spectra.

The Hilbert spectrum and Fourier spectrum are compared through spectral characteristics. Various spectral characteristics that are typically obtained from the Fourier spectra are the zeroth moment (m_0), the mean wave frequency (f_{mean}) and the spectral width (ν). These characteristics are calculated from the variance density spectrum according to (e.g., Holthuijsen, 2010):

$$m_k = \int_{f=0}^{\infty} f^k S(f) df \tag{3.18}$$

$$f_{mean} = f_{m01} = \frac{m_1}{m_0} \tag{3.19}$$

$$\nu = \sqrt{\frac{m_2 m_0 - m_1^2}{m_1^2}} \tag{3.20}$$

Similar spectral characteristics can be obtained with the marginal spectrum as well. The zeroth moment of the marginal spectrum is then computed as:

$$m_k = \int_{\omega=0}^{\infty} \omega^k h(\omega) d\omega \tag{3.21}$$

In addition to comparing the spectral characteristics, the resemblance between the marginal spectra and the Fourier spectra is visually inspected. In doing so, it should be noted that these spectra do not share the same interpretation. In the Fourier spectrum, for which stationarity and linearity are assumed, the presence of energy at a given frequency means that a trigonometric component with this frequency and amplitude persisted through the entire period of the data. This does not hold for the marginal spectrum, where the presence of energy at a certain frequency is associated with a likelihood, proportional to the energy amount, of having a component with this frequency and amplitude at any given time during the timespan of the record (Huang et al., 1998).

3.3. VLF wave classification and resonance identification

As the EMD provides the opportunity to separate the VLF oscillation of the inner reef signal, this component can be analysed individually. The objective of this part of the methodology is twofold: first, the inner reef VLF component is classified based on propagation type and energy content and, second, the signal is analysed for resonance, corresponding to research questions 1 and 2 respectively. The methods for these analyses are based on different products of the HHT. The classification relies on the direct instantaneous products of the Hilbert transform, specifically IP and IA. The resonance identification, which is based on the resonance criterion proposed by Gawehn et al. (2016), uses the Hilbert (marginal) spectra in order to capture the time-varying aspect of resonance.

The VLF wave classification and resonance identification are explained in Section 3.3.1 and 3.3.2, and are followed by an investigation of the resulting patterns, which will be described in Section 3.3.3.

3.3.1. Classification of standing and energetic VLF oscillations at the inner reef

After selecting a sifting method in the previous part, the EMD is applied to all field data. The goal of the sifting of the inner reef signal is to isolate the dominant VLF oscillation from the rest of the signal to analyse it separately. After isolating the dominant VLF oscillation the propagation character is assessed through phase comparison to the corresponding mid reef component, this determines whether the oscillation is standing or progressive. Based on an amplitude threshold, the inner reef component is classified as being energetic or not energetic.

Dominant VLF component of the inner reef signal decompostion

To extract the relevant VLF component from the set of IMFs of an inner reef signal decomposition, the frequency and energy content of the IMFs are assessed. First of all, the frequency of the IMF should be close to the natural frequency ($f_{0,th}$). Looking at the resonance diagram by Gawehn et al. (2016) in Figure

3.5, the frequencies of the resonance cases fall in the range of $0.5f_{0,th}$ - $2f_{0,th}$. Therefore, the median instantaneous frequency of an IMF should be within a range of $0.5f_{0,th}$ - $2f_{0,th}$.

The natural frequency or eigenfrequency is based on the reef width and water depth, as explained in Section 2.4.1. The water depth may not be constant along the width of the reef flat because of set-up and (minor) spatial variations of the profile. Therefore, the eigenfrequency is approximated with the following formulation:

$$f_{n,th} = \frac{2n+1}{4}\left(\int_{reefcrest}^{shoreline} \frac{1}{\sqrt{gh(x)}}dx\right)^{-1} \tag{3.22}$$

where n is the mode number, g is the gravitational acceleration and $h(x)$ is the water depth depending on the location on the reef. The reefcrest is located 250 m from the beach toe, as indicated in Figure 3.2. Water level recordings are only available for the reef locations at the outer, mid and inner reef stations, as described in Section 3.1. In between these stations, the water level is linearly interpolated. The water depths at these stations are time-averaged per time record. In reality the water level is changing continuously. Therefore, the time-averageing of water depth may induce an error. However, because a range of $f_{0,th}$ is already considered, potential deviations are accounted for.

Typically, the condition for the median IF to be in the range of $0.5f_{0,th}$ - $2f_{0,th}$ results in the isolation of 1 or 2 components. In the case of multiple remaining components, the energy content is assessed through the instantaneous energy (IE). The component with the larger share of IE is selected.

Propagation type classification

Next, the wave propagation type (standing or progressive) is assessed through a comparison of the instantaneous phase (IP) between two reef flat stations. Pomeroy et al. (2012a) assessed the wave propagation by comparing the signal recorded at two stations on a reef flat. These locations are illustrated in Figure 2.7. This figure shows the proximity of station x to the reef crest, approximately 70 m. Compared to the width of the reef flat ($W = 400$ m), station x is located $0.18W$ from the reef crest.

For this study, data is available for three station on the reef flat (the outer, mid and inner reef station), see Figure 3.2. The outer reef corresponds perhaps most to station x in the study of Pomeroy et al. (2012a), however it is located closer to the reef crest, with a distance of approximately 15 m. Compared to the reef flat width of $W = 250$ m, this equals a fraction of $0.06W$. Assuming a VLF standing motion on the reef flat, a node is expected near the reef crest, suggesting a minimal water level oscillation at this point in space. This lack of a substantial VLF oscillation at the outer reef could also undermine the extraction of this component by the EMD. The mid reef, however, would have a much larger amplitude in case of a standing wave, and is thus considered to be more suitable for the phase comparison. Additionally, the signals recorded at the inner and mid reef are expected to be very similar, resulting in similar frequency bands for the corresponding IMFs of the two signals.

However, to ensure similarity between the two IMFs of the respective reef stations, the coherence is evaluated. In the case of low coherence, no meaningful phase difference can be computed. The instantaneous phase coherence is quantified with the phase cross-correlation via the following equation (Schimmel et al., 2011):

$$c_{PCC}(\tau) = \frac{1}{2t_w}\sum_{t=t_0}^{t_0+t_w}\left(\left|e^{i\phi_1(t+\tau)} + e^{i\phi_2(t)}\right|^{\nu} - \left|e^{i\phi_1(t+\tau)} - e^{i\phi_2(t)}\right|^{\nu}\right) \tag{3.23}$$

where τ is the time lag, t_w is the time window, power ν is a sensitivity coefficient ($\nu = 1$ is used here) and ϕ_1 and ϕ_2 are the instantaneous phases of the components of the inner reef and mid reef respectively. Equation (3.23) is a function of time lag τ. A reasonable range for the time lag of this computation is determined by considering the "theoretical time lag" between the mid and inner reef stations. Because the wavelengths are much greater than the water depth ($L >> h$) at these locations, the shallow water approximation is valid (Bosboom & Stive, 2021), see also Appendix B. Therefore, the time lag is computed through the shallow water phase velocity:

$$c = \sqrt{gh} \tag{3.24}$$

where g is the gravitational acceleration and h is the water depth. Similar to the computation of the eigenfrequency, see (3.22), the water level is time-averaged and interpolated between the stations to compute the time lag.

The maximum theoretical time lag between the mid and inner reef station as computed with this approach is 248.1 seconds. However, the mean and 95th percentile of the time lag between the two stations are 52.9

and 107.7 respectively. To prevent excessive computations, a range of time lags from 0 to 110 seconds is applied in Equation (3.23). This is acceptable because the extremely long time lags indicate an extremely low water level, preventing any significant waves from reaching the shore.

Time window t_w is determined based on the frequency content of the inner reef VLF component. An intial window duration is computed based on the median instantaneous frequency (IF) of the VLF component. However, to have an even distribution of windows over a record, the window duration should divide the time-series evenly. The intial window duration is therefore rounded up to the closest window duration that are presented in Table 3.1. The reason to round up is so that at least one full oscillation is captured in the window.

For each time window in the time series, the maximum coherence is determined. For time windows with a high value of coherence ($>$0.8), the phase difference is assessed. Note that this maximum coherence corresponds to a certain time lag.

Table 3.1: Durations for time window t_w and corresponding number of windows $n_{windows}$. Note that the 110 s is subtracted from the total time series duration of 2048 seconds to allow the time lag.

$n_{windows}$	9	8	7	6	5	4	3	2	1
t_w (s)	215.0	242.0	276.5	323.0	387.5	484.5	646.0	969.0	1938.0

The instantaneous phase of the inner reef and mid reef component are unwrapped within the time window to prevent jumps caused by transitions between waves. This is illustrated in Figure 3.4. Per window, the median instantaneous phase difference between the inner reef and mid reef is computed.

Theoretically, the phase lag is zero for a standing wave. However, a margin should be included to account for minor waveform changes resulting from the EMD and to include near-standing waves as well. The criterion could be an absolute value in seconds or an absolute value for the phase difference in radians. However, since the theoretical time lag of a progressive wave in shallow water depends on the water depth and not the period of the wave, these criteria may not be adequate. Additionally to having a small phase difference in radians, the ratio between the phase difference (in seconds) and the theoretical time lag is used. This ratio should be small for a standing wave. In addition, standing oscillations should make up a minimum part of the time record

The ranges for the phase difference in radians and lag ratio and the minimum occurrence within a time series are determined through an iterative process and visual inspection. This resulted in the following ranges that define the criterion for a standing oscillation:

- Phase difference in radians: -0.25 to 0.25 radians
- Ratio phase difference (in seconds) to theoretical time lag: -0.3 to 0.1
- Minimum occurrence: 25% of the time series (512.0 seconds). This equals a minimum of 3 windows for the two shortest window times, and 2 or 1 windows for the longer window times.

Additionally, the mean amplitude of the VLF component should be at least 0.01 cm to ensure the physical meaning of the component. Including positive values for the phase differences seems odd, as it would mean the mid reef oscillation is ahead of the inner reef oscillation. However, these values are included to account for potential waveform deviations resulting from the EMD sifting. Furthermore, the theoretical time lag may introduce an error since it is based on a theoretical approximation of the propagation velocity ($c = \sqrt{gh}$). As noted before, the time-averaging of the water depth h simplifies the computation of the phase velocity. In further research, the influence of a potential error caused by this simplification may be considered. However, because an error is also introduced by waveform deviations as a result of the EMD, the quantification of a potential error of the theoretical time lag would have limited meaning for the actual error in the lag ratio. Therefore, no attempt to quantify a bandwidth for the theoretical time lag is made here. This approach and its assumptions for defining the propagation type is further discussed in the discussion chapter in Section 5.2.

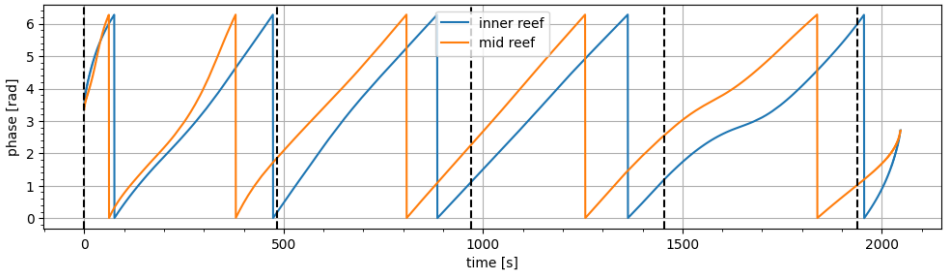

(a) Instantaneous phases for inner and mid reef VLF component.

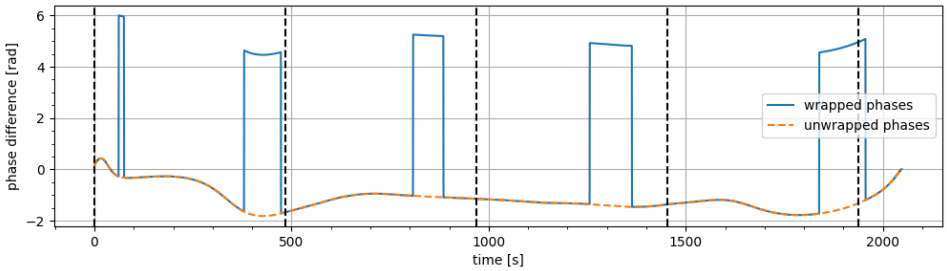

(b) Phase difference based on wrapped and unwrapped phases.

Figure 3.4: Example of (a) instantaneous phases for an inner and mid reef VLF component and (b) the corresponding phase difference computed with the wrapped and unwrapped instantaneous phases. The windows (t_w = 484.5 s) are indicated with the black vertical dashed lines.

Energy classification

After having classified the inner reef component as a standing or progressive oscillation, the components are also classified based on amplitude. The criterion to determine whether an oscillation is 'energetic' or not is based on an amplitude threshold. The maximum peak is taken for each VLF component with a minimum mean amplitude of 0.01 m. Next, the 90$^{\text{th}}$ percentile is used as the amplitude threshold, which is 0.12 m. This equals the 97.5$^{\text{th}}$ percentile when all peaks of all VLF components are considered. An energetic VLF component should have at least a single wave crest that exceeds this amplitude threshold.

3.3.2. Resonance identification

Resonance is associated with a substantial amplification of a certain frequency component. To identify resonance, the energy of the inner reef signal should be related to the incoming forcing. As mentioned in Section 2.4.5, a resonance criterion is proposed by Gawehn et al. (2016) as the first step of their classification method, which they applied to the same Roi-Namur field data as used in this study.

The resonance criterion is based on the energy transfer between the fore reef envelope and inner reef signal and how the energy magnitude of the respective signals relate to each other. First, the envelope $A_x(t)$ of the fore reef signal is produced by applying the Hilbert transform to the detrended zero-mean data. For the fore reef envelope signal and the inner reef signal, the Fourier transform is used to obtain the respective variance density (auto-)spectra ($G_{Ax}(f)$ and $G_y(f)$) and the cross-spectrum. Next, the transfer function is applied to obtain the energy transfer H_{Axy} between these signals:

$$H_{Axy}(f) = \frac{|G_{Ay}(f)|}{G_{AA}(f)} \tag{3.25}$$

Next, the peak transfer frequency $f_{p,transfer}$ is defined as the frequency for which $H_{Axy}(f)$ is maximum. This frequency is considered to be a potential resonance frequency. The variance at the inner reef at $f_{p,transfer}$ is normalised with the sum of variance in the low-frequency range (0.001-0.04 Hz) of the fore reef envelope spectrum, giving the normalised inner reef energy $normE_{p,transfer}$. After normalising $f_{p,transfer}$ with the zeroth mode eigenfrequency $f_{0,th}$, a diagram as shown in Figure 3.5 is constructed. The resonance events are expected to cluster around the frequency ratio $f_{p,transfer}/f_{0,th} = 1$, where the normalised energy (as a measure of amplification) increases significantly, as is illustrated in the Figure 3.5. In the method, resonance events are defined by being close to $f_{p,transfer}/f_{0,th} = 1$ and having a value of $normE_{p,transfer}$ above some threshold. The threshold proposed is based on an optimisation procedure using a Monte-Carlo simulation

and measuring the performance of different threshold values. This approach required several assumptions about the occurrence of resonance. The threshold resulting from this analysis identified a 3.6% occurrence of resonance for the dataset.

Since this resonance analysis depends on Fourier analysis, the energy-time distribution is lost. This section proposed an alternative approach to the resonance criterion by using the Hilbert (marginal) spectra as a replacement for the Fourier spectra. First, the auto-spectra are replaced by the marginal spectra, integrated over the full length of the time record. After that, a windowed integration of the time series is proposed to preserve the time-varying character of the resonant oscillations.

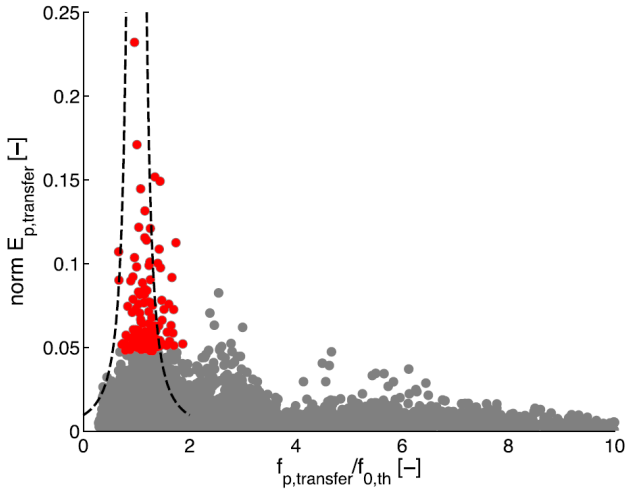

Figure 3.5: Resonance diagram by Gawehn et al. (2016) with normalised energy $normE_{p,transfer}$ of the peak transfer frequency ($f_{p,transfer}$) on the y-axis and frequency ratio between $f_{p,transfer}$ and eigenfrequency $f_{0,th}$. Highlighted in red are the identified VLF resonance events. The resonance events are centred around the frequency ratio of 1 and are above a certain threshold for $normE_{p,transfer}$, resulting in a 3.6% resonance occurrence.

Resonance analysis for full time-series using the HHT

In the approach as explained above, the Fourier auto-spectra can be substituted with the marginal spectra of fore and inner reef signals. The spectral characteristics of marginal spectra are generally consistent with the Fourier spectra, as mentioned in Section 2.5.2 and as will be analysed in Section 4.1.3. While the previous classification steps focused on a single dominant VLF component of the inner reef, this analysis will consider all low-frequency components. This approach aims to mitigate bias toward the selection of specific frequency ranges close to the eigenfrequency.

For the fore reef signal, the envelope is used in the HHT approach as well, although another approach was considered as well, where the frequency and amplitude information wave envelope of the fore reef was approximated through the low-frequency waves of the fore reef signal decomposition, this is further explored in Appendix B.

Next, the cross-spectrum using the HHT approach needs to be considered. The cross-spectrum of the fore reef envelope and inner reef signal is not directly applied, but is used for the transfer function (H_{Axy}) as given in (3.25), where the absolute of the cross-spectrum between the two signals is divided by the auto-spectrum of the fore reef envelope signal.

If we consider two stationary signals $x_1(t)$ (fore reef) and $x_2(t)$ (inner reef) for which the Fourier transform can be expressed in complex values ($X_1(f) = a + ib$ and $X_2(f) = c + id$ respectively), containing the signal information in the frequency domain, the absolute cross-spectrum ($|G_{x1x2}|$) can be decomposed as follows:

$$G_{x1x2} = X_1[X_2]^* \qquad /(2df) \tag{3.26}$$
$$= (a + ib)(c - id) \qquad /(2df) \tag{3.27}$$
$$= (ac + bd) + i(bc - ad) \qquad /(2df) \tag{3.28}$$
$$|G_{x1x2}| = \sqrt{(ac + bd)^2 + (bc - ad)^2} \qquad /(2df) \tag{3.29}$$
$$= \sqrt{a^2 + b^2}\sqrt{c^2 + d^2} \qquad /(2df) \tag{3.30}$$
$$= |X_1||X_2| \qquad /(2df) \tag{3.31}$$

where [..]* denotes the complex conjugate and df is the frequency resolution of the spectrum. The auto-spectrum is defined as:

$$G_{x1x1} = |X1|^2/(2df) \tag{3.32}$$

The transfer function can then be rewritten as:

$$H_{x1x2} = \frac{|G_{x1x2}|}{G_{x1x1}} = \frac{|X_1||X_2|/(2df)}{|X1|^2/(2df)} = \frac{|X_2|}{|X_1|} = \frac{\sqrt{G_{x2}}}{\sqrt{G_{x1}}} \tag{3.33}$$

Consequently, the energy transfer could be approached by using the auto-spectra in the Fourier approach. Note that, in reality, the signals are not stationary and windows are applied to the time-series before performing the Fourier transform. After averaging over the windows, this derivation may not hold anymore.

There is limited research available for the cross-spectrum for the Hilbert-Huang transform, although two approaches have been proposed by Sun et al. (2016) and Shan et al. (2021). Considering these approaches and the aim of this analysis, several approximations for the transfer function have been explored, which is elaborated on in Appendix B. The approach considered most suitable is based on the derivation in (3.33), and is written as:

$$H_{Axy}(\omega) = \frac{\sqrt{h_{inner}(\omega)}}{\sqrt{h_{fore}(\omega)}} \tag{3.34}$$

where $h_{inner}(\omega)$ and $h_{fore}(\omega)$ are the marginal energy spectra for the inner signal and fore reef envelope, respectively.

Additionally, an alternative approach is applied for selecting the $f_{p,transfer}$. Originally, $f_{p,transfer}$ corresponds with the maximum value of the transfer function in the low-frequency domain. A new approach is proposed where the transfer function exceeds its 85$^{\text{th}}$ percentile, and the $f_{p,transfer}$ is then selected from this range based on the maximum inner reef energy. This alternative approach is discussed in more detail in Appendix B.

After implementing these adjustments, the resonance analysis is conducted. The threshold value is determined based on the occurrence of resonance, targeting a 3.6% resonance occurrences ($normE_{p,transfer}$ above the threshold and $f_{p,transfer}/f_{0,th}$ close to 1 in the data set. This occurrence has been identified by Gawehn et al. (2016), who made an effort to optimise the threshold. It is acknowledged that the selection of this threshold may be somewhat arbitrary, however, no additional analysis to define an alternative threshold or resonance occurrence is conducted in this study. The choice for defining resonance through this threshold is further discussed in Chapter 5.

As mentioned before, the frequency resolution of the Hilbert (marginal) spectra is user-defined. For this analysis, a frequency resolution of 0.001 Hz was chosen to maintain consistency with the Fourier analysis. While a finer resolution provides a more precise delineation of exact frequencies, it may compromise the accuracy of the analysis due to the cross-comparison of frequency content between the fore and inner reef. For instance, if the frequencies of the VLF components of the fore reef and inner reef do not align exactly, this can impact the accuracy of the transfer function.

Time-varying resonance analysis using the HHT

One of the most valuable assets of the Hilbert-Huang transform is the ability to retain the time-varying character of the signal. This feature is also relevant for the resonance analysis, because it offers the opportunity to examine the transient character of the phenomenon. Furthermore, the amplification as quantified with $normE_{p,transfer}$ in the previous method, normalises the sum of inner reef energy at $f_{p,transfer}$ with the sum of low-frequency energy of the fore reef envelope over the entire duration of the time-series. It would be more accurate to compare a shorter time duration of the incoming forcing at the fore reef to the corresponding response at the inner reef.

One approach to include the temporal variability of the records is to integrate the Hilbert spectrum over shorter time durations. This will provide a more detailed description of the energy present at a certain moment. As a comparison is made between the signal observed at the fore reef and inner reef, it is important to incorporate a time lag for the inner reef signal. For the computation of the time lag between the fore reef and inner reef station, the shallow water assumption does not hold, considering the water depth of approx. 10 m at the inner reef. Between the fore and outer reef, transitional water depths are assumed for the calculation of the wave group velocity until breaking. An estimation for the breaking point is based on the Miche criterion. After breaking, the shallow water approximation is assumed. This calculation is further described in Appendix B.

As will result from the classification of energetic standing oscillations, these VLF events almost exclusively occur for situations where the eigenfrequency, determined by the reef flat water depth, exceeds 0.0025 Hz. To capture the dynamics adequately, the window duration should be at least as long as the period of this motion, which amounts to 400 seconds. Considering a margin, the window duration is set to 600 seconds (10 minutes), with computations performed at an interval of 100 seconds. A constant time window is used, rather than adjusting it to fit the eigenfrequency of each record. This choice prevents the data distribution from favouring shorter eigenperiods, which would result in more data points being generated for these periods. Shorter eigenperiods have a higher likelihood of enabling resonance, so this approach helps maintain a balanced dataset.

The previously used marginal spectra in the HHT approach are replaced with the marginal spectra integrated over this shorter time window. For the transfer function, several methods are evaluated, see Appendix B. A method similar to the previous approach is used:

$$H_{Axy}(\omega, \tau, t_w) = \frac{\sqrt{\int_{t_0}^{t_0+t_w} HS_{inner}(\omega, t+\tau)}}{\sqrt{\int_{t_0}^{t_0+t_w} HS_{fore}(\omega, t)}} \tag{3.35}$$

where $HS(\omega, t)$ represents the Hilbert spectrum, t_0 is the starting time of the integrating range and t_w is the window duration (600 seconds) and τ is the theoretical time lag between the fore and inner reef station.

With this approach, the resonance diagram similar to the one in Figure 3.5 is produced. Again, there is a need for a threshold, to qualify certain moments as resonance. To be categorised as resonance, a time record needs to contain at least one 600-second time window for which $normE_{p,transfer}$ exceeds the threshold. With this definition, the threshold is iteratively determined until an occurrence of 3.6% is reached. The time-varying resonance analysis is referred to with HHT_{temp} in the further report.

In addition, this analysis is also conducted for the single dominant VLF component that has been distinguished for the VLF wave classification. In doing so, the validity of the VLF component selection is tested, as the resonance is expected to occur in this component. Furthermore, this approach, which is referred to as $\text{HHT}_{\text{temp,VLF}}$, is useful in the analysis of the transient characteristics of resonance occurrences, as will be investigated in Sectio 3.4. For this method, the 85$^{\text{th}}$-percentile frequency selection approach is slightly altered, the frequencies of the 3 maximum energy transfer values are considered instead, since a small number of non-zero values for the inner reef energy-frequency are provided by the marginal spectrum of a single VLF component (with a frequency resolution of 0.001 Hz).

3.3.3. Patterns of VLF wave classification and resonance identification

After having classified the VLF waves based on propagation type and energy content and having identified resonance. It is interesting to look at how these patterns relate to other hydrodynamic factors, such as the amplitude and frequency of the inner reef VLF components, and the water depth and significant wave height on the reef and offshore.

As before, the water depth is averaged per time series. For the reef flat water depth, the time-averaged water depth is interpolated between the outer, mid and inner reef stations. The significant wave height is based on the Fourier spectra and is defined as follows:

$$H_s = H_{m0} = 4\sqrt{m0} \tag{3.36}$$

where m_0 is the zeroth spectral moment, see Equation (3.18).

3.4. Transient characteristics of energetic and resonant VLF waves

Now that the dominant inner reef VLF component is determined and analysed, more characteristics of these oscillations can be explored. Because the Hilbert-Huang approach maintains the time-varying behaviour of oscillations, this is used to the advantage. The objective of this final section of the methodology is to investigate the transient characteristics of energetic and resonant VLF oscillations, corresponding to the fourth and final research question.

A method is proposed to determine the duration of energetic VLF events and resonance events and their corresponding intensity. Furthermore, an attempt is made to relate the inner reef VLF oscillation behaviour to instances of coastal flooding.

3.4.1. Energetic VLF events duration and intensity

For the records that are classified as energetic VLF oscillations, the duration of the energetic VLF "event" is determined based on the instantaneous amplitude (IA). The duration is defined as the time length for which IA is greater than the amplitude threshold. Some time series may contain two (or more) of these energetic VLF events. In the example in Figure 3.6b, at t = 500 s, there is a small decrease of the IA below the threshold, separating the VLF event into two, although it is intuitively a single event. To better describe the duration of a single VLF event, small gaps that are shorter than the median wave period of the VLF component are included in the duration of a single event.

After the energetic VLF events are defined and the duration is determined. The intensity of these events can be assessed through the mean IA and the maximum wave crest of the VLF component within the duration of the energetic VLF event.

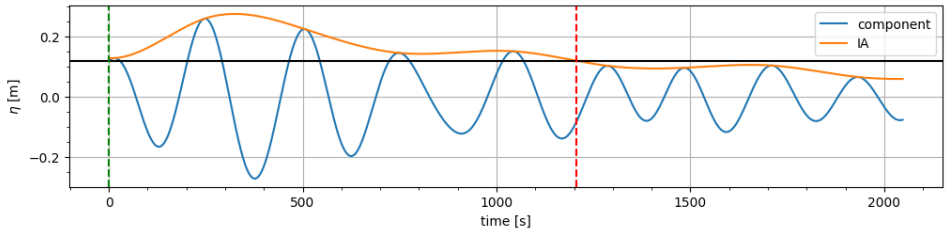

(a) Example 1.

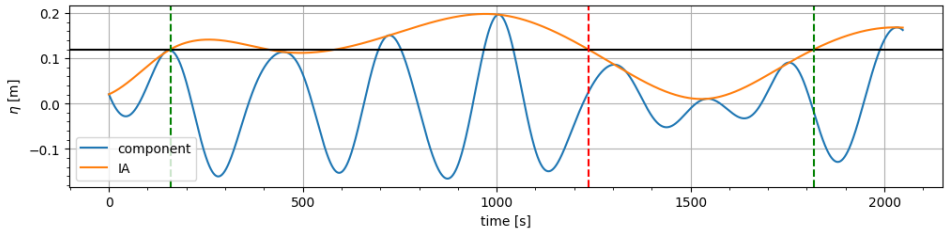

(b) Example 2.

Figure 3.6: Two examples of the dominant VLF inner reef component (blue solid line) and their instantaneous amplitudes (IA, orange solid line), illustrating the duration of a VLF event. The green dashed line indicates the start of an event and the red dashed line the end. The IA should be greater than the amplitude threshold to be considered a energetic VLF event, a small gap is allowed, as illustrated in (b), where a dip below the amplitude threshold around t = 500 s occurs.

3.4.2. Resonance events duration and intensity

In Section 3.3.2 a temporal method for resonance detection is proposed, which will be further capitalised on to evaluate the duration of resonance events. As the $\text{HHT}_{\text{temp,VLF}}$ resonance analysis approach provides $normE_{p,transfer}$ per window for a single VLF component, this parameter can be plotted against the time. Linear interpolation between the 100-second time intervals is applied, after which the upward and downward crossing of the resonance threshold determine the start and end of a resonance event. An example is illustrated in Figure 3.7a. Similarly to the VLF event analysis, the intensity and relation to other inner reef characteristics are investigated.

It is noted that some occurrences of resonance occur at the edges of the time series. The duration for these edge events is difficult to define as no start or end time can be defined, see Figure 3.7b. Also note how the first and final time index of $normE_{p,transfer}$ is around t = 300 and 1700 s, because the mean of the 600-second time window is used. This further complicates defining the duration of edge events. The edge events are therefore not analysed in detail, although they are considered for the total duration of resonance for a time series.

This analysis is also conducted using shorter time windows (300 seconds) to evaluate the sensitivity to the window size.

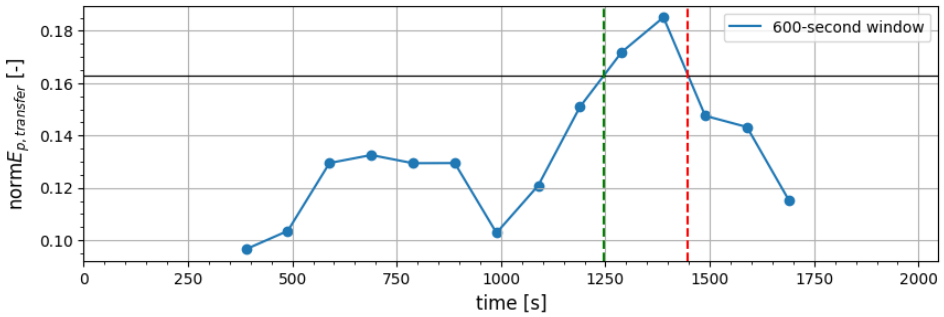

(a) Example resonance event.

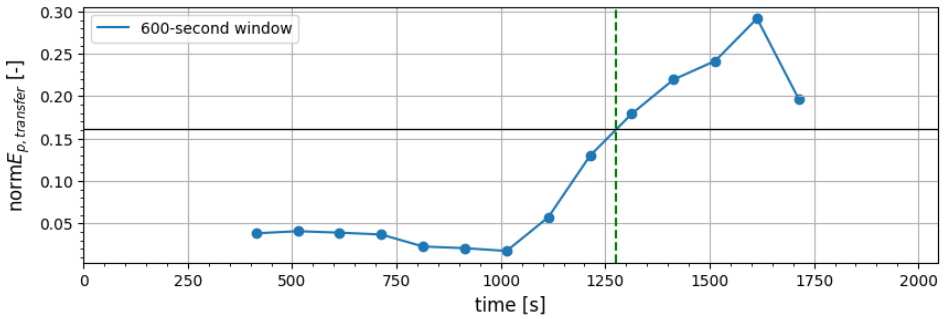

(b) Example edge event.

Figure 3.7: Example of (a) resonance event duration for 600-second window approach. The vertical green and red dashed lines indicate the start and end of the resonance event respectively. An example of an edge event is given in (b).

3.4.3. Coastal flooding events

Lastly, the durations of VLF and resonance events are related to the occurrence of overwash and runup events that have been reported during the field data collection.

As described by Cheriton et al. (2016), two significant overwash events occurred on 18 December 2013 and 2-3 March 2014, the latter being more severe than the first. Additionally, large runup events were reported on 18 November 2013 and 20 February 2014. The duration of the energetic and resonant VLF events is collected per 24 hours and patterns are analysed. In this analysis, it is noted that the time series represent only 34 minutes every hour of recording, as explained in Section 3.1. Additionally, some other factors such as the intensity of the VLF component and the reef water depth are included in this analysis, as well as the offshore tidal level and the incoming significant wave height.

4

Results

In this chapter, the results of the methodology are presented. The results will be presented according to the three sections of the methodology. First, the performance of the EMD and HHT are examined, to find the most suitable method for the extraction of VLF components of the inner reef signal. Next, follows the classification of inner reef VLF waves and the identification of resonance. Different elements of the HHT are used in these analyses. Finally, the duration and intensity of energetic and resonance events and their relation to coastal flooding occurrences are investigated. At the end of each of these sections, a summary of the findings is given to highlight the main takeaways.

4.1. Assesing EMD and HHT performance

This section assesses the performance of various decomposition configurations for the Empirical Mode Decomposition (EMD). The assessment involves computing a set of performance indices and visual inspection of a few examples. Additionally, the Hilbert-Huang Transform (HHT) as a spectral analysis method is compared to the Fast Fourier Transform (FFT). The objective is to determine the most suitable EMD configuration for extracting the VLF oscillation of the inner reef signal, aligning with the first research question. The aspects to consider include having a good visual representation of the VLF oscillation in an IMF, having adequate scores for performance indices and having an acceptable computation time.

The different options for sifting configurations are described in Section 3.2. Five decomposition methods are considered: EMD, M-EMD, iM-EMD, EEMD and CEEMD. Addition settings to the sifting procedure concern the stopping criterion, the interpolation technique and the boundary extension technique. The settings of the default sift and alternatives (in brackets) are:

- Stopping criterion: SD $= 0.2$ (alternative: SD $= 0.3$; Rillings stopping criterion with default settings: $\alpha = 0.05$, $\theta 1 = 0.05$, $\theta 2 = 10\theta 1$)
- Interpolation technique: B-spline (alternative: cubic spline)
- Boundary extension technique: Rilling's mirror extension (alternative: constant padding)

4.1.1. Visual inspection of signal decompositions

Visual inspection is a valuable method for evaluating the decomposition of a signal into IMFs or components. The various modes in a signal can often be visually distinct, although this method is subjective and has limited accuracy. In the inner and mid reef signals, the low-frequency (LF) motion can typically be visually distinguished from high-frequency harmonics.

This section focuses on the visual inspection of the reef station recordings, with emphasis on the inner reef station. The outer reef station has a less essential role in the methodology but will be briefly addressed. The fore reef data is primarily used for the envelope of the signal and will therefore not undergo visual inspection. First, the different decomposition methods with default settings are inspected. The effect of the various sub-settings is briefly inspected as well.

Inner reef

Following are some examples of time series recorded at the inner reef station that show a strong low-frequency

oscillation. Figure 4.1a shows such a signal with IMFs extracted by the EMD, M-EMD, iM-EMD, EEMD and CEEMD in Figures 4.1b to 4.1f. As is clear from the legends for each of these methods, the decompositions result in different numbers of components. For the inner reef decompositions, the following number of IMFs are typical:

- EMD: 5-7 IMFs
- M-EMD: 8 IMFs
- iM-EMD: 5-6 IMFs
- EEMD: 7-8 IMFs
- CEEMD: 15-18 IMFs

In the examples given, some high-frequency components are left out to have a clear vision of the LF components. Looking at the LF oscillation of the inner reef signal given in Figure 4.1a, peaks are estimated to happen around the times 100 s, 350 s, 700 s, 950 s, 1200 s and 1400 s. Note that riding waves with a higher frequency can occur, either increasing or decreasing the water level around the estimated peaks of the LF motion. As LF waves are especially interesting to this research, the sift method should be able to extract a component that adequately represents the dominant LF motion of the signal. IMF 5 in the EMD (Figure 4.1b) corresponds with the estimated peaks at first, but around 1050-1300 s the troughs and peak are captured in IMF 4 while the frequency of IMF 5 decreases. Consequently, IMF 5 shows a trough around 1200 s that is not directly distinguishable in the original signal.

In contrast, the M-EMD and iM-EMD capture most of the LF wave in a single component, IMF 6 and 4 respectively (see Figures 4.1c and 4.1d). The EEMD and CEEMD (Figures 4.1e and 4.1f) perform well, but have similar mode mixing around 1050 s as found in the EMD.

Similar observations are made for other decompositions, of which more examples are given in Figures A.1 and A.2 in Appendix A. In general, the EMD, EEMD and CEEMD seem to be more likely to contain mode mixing, where a wave with a relatively consistent frequency is represented by multiple components over time. In contrast, the M-EMD is more likely to experience mode splitting, where a single oscillation is split into two components. An example of this is illustrated in Figure A.3d at $t = 700$ s. This could lead to an underestimation of the wave amplitude, as is evident when comparing M-EMD to the other decompositions in Figure A.3. The iM-EMD may also experience mode splitting, as illustrated in the example in Figure A.2 in Appendix A.

The masking method is an effective way to overcome intermittency and capture the dominant VLF oscillation consistently in a single component, thus avoiding mode mixing. Extracting the VLF motion into a single IMF enables this component to be investigated separately, which is favourable for this study.

Mid and outer reef

As explained in Section 3.3, the mid reef signal is used in the coherence and phase difference analysis for the VLF wave classification. The decomposition of the mid reef signal should result in a low-frequency IMF that is comparable to its corresponding inner reef component in frequency and waveform, so that coherence is high and a meaningful phase difference can be determined. An example of a mid reef signal decomposition by the M-EMD and iM-EMD is given in Figures A.4 and A.5 in Appendix A. Because the M-EMD mitigates mode mixing, components are extracted to relatively narrow frequency bands that are consistent between the mid and inner reef decompositions. This can be explained by the computation of the masks, which is based on the highest frequency content of the signal. The mid reef and inner reef signals likely have similar high-frequency content, as the reef stations are relatively close to each other. For the iM-EMD, more mode mixing may occur, resulting in non-coherent waveforms between the mid and inner reef.

Figures A.4 and A.5 in Appendix A also contain the outer reef time series and decomposition. At first glance, there are more prominent short waves present in the outer reef signal. Visually, a low-frequency oscillation can be distinguished that is also extracted by the M-EMD in IMF 6 (Figure A.4f) and by the iM-EMD in IMF 4 (Figure A.5f). The coherence of the LF component of the inner reef and outer reef is stronger for the M-EMD compared to the iM-EMD.

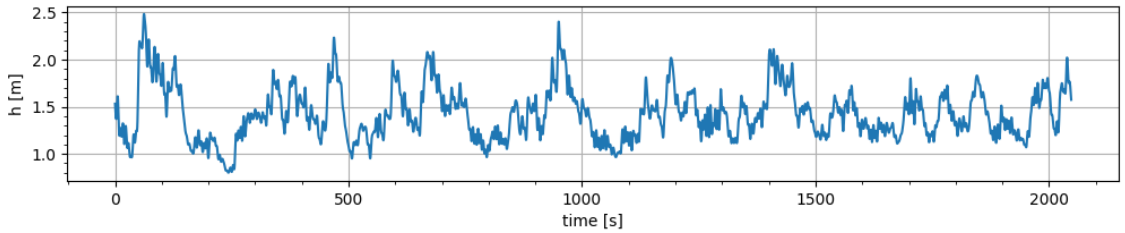

(a) Inner reef signal

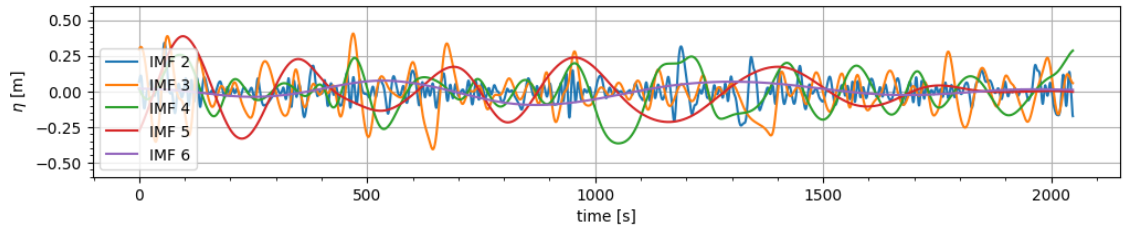

(b) EMD

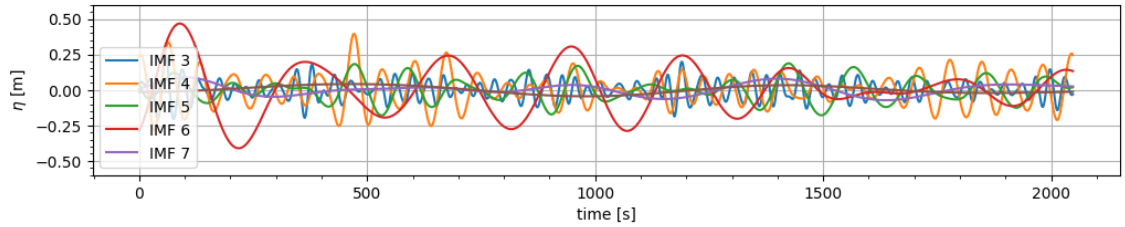

(c) M-EMD

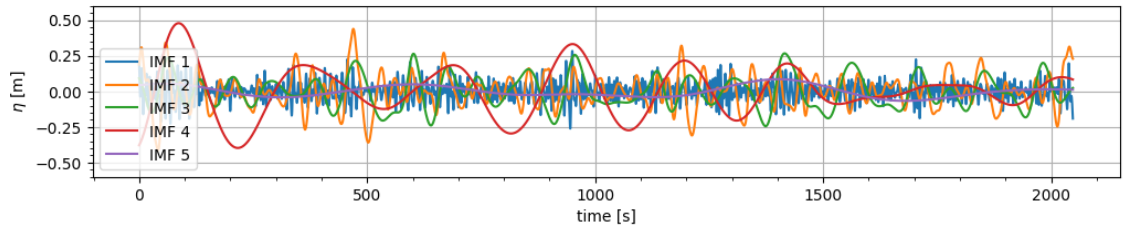

(d) iM-EMD

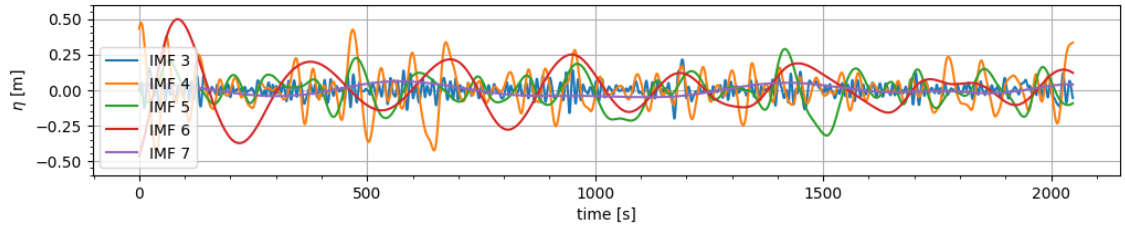

(e) EEMD

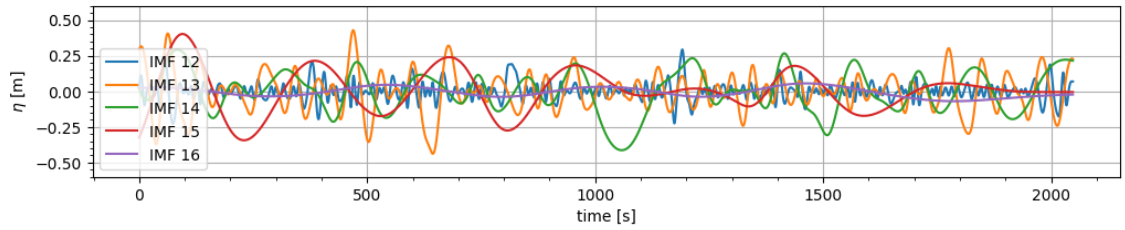

(f) CEEMD

Figure 4.1: Example of an (a) inner reef signal and (b-f) its decomposition by various sifting methods. IMF 5 of the EMD (b) initially corresponds with peaks of the inner reef signal but after t = 1000 s IMF 4 captures part of these peaks. The M-EMD (c) and iM-EMD (d) effectively capture LF oscillations in single components. EEMD (e) and CEEMD (f) exhibit mode splitting around 1050 s similar to EMD.

Alternative configurations
The settings of the configurations have a limited influence on the resulting decomposition compared to the choice of the sift method. In Figures A.6 and A.7 in Appendix A examples are given of an M-EMD decomposition for an inner reef signal with the various configurations as stated before. Between the default stopping criterion (SD $= 0.2$) and SD $= 0.3$, hardly any difference is visible. For the interpolation by cubic splines, again, there is hardly any difference compared to the default configuration. The boundary extension could influence the deviation of the component at the edges. The effect of the choice of boundary extension method is dependent on the signal. In one of the examples given, there is no significant difference between the two boundary extensions (see Figure A.7f). For the other example in Figure A.6f, there is a slight deviation at the starting edge, but it hardly affects the rest of the decomposition.

The performance indices may provide a better overview of the general performance of the different configurations. These are discussed next.

4.1.2. Performance of sifting configurations

To account for the significantly different wave patterns observed at the fore reef and inner reef, the performance is evaluated for both of these stations. The various configurations for the sifting procedure are executed for a set of 120 time series recorded at the fore reef and inner reef stations. A selection was made based on wave characteristics at the offshore station: significant wave height H_s, mean wave period T_{mean} and spectral width ν (computed according to Equations (3.36), (3.19) and (3.20) respectively). The aim is to represent the range of values of these characteristics in the selection of records, to have a reasonable representation of possible signal compositions. Figure A.8 in Appendix A shows these characteristics of the entire record of field observations and for the selection of records. The 5 days (120 time series) that are selected are from 26-02-2014 to 03-03-2014.

Performance metrics
As discussed in Section 3.2, several indices are used to evaluate the performance of the decomposition. Computation time is also considered in the configuration selection. The following five indicators are used to assess the set of IMFs globally:

- Index of Orthogonality (IO, see (3.3))
- Signal energy error (θ, see (3.4))
- Max. amplitude error ($a_{max,error}$)
- Time variable error index (EI, see (3.5))
- Computation time

In addition, four component-specific indicators are computed to assess the relation between individual IMFs:

- Index of Orthogonality between components (IO_{ij}, see (3.6))
- Pearson correlation coefficient (ρ, see (3.7))
- Pseudo mode splitting index ($PMSI$, see (3.8))
- Frequency overlap ($f_{overlap}$)

The decomposition of the selected records is executed for the different configurations, after which the performance indicators can be computed. The median and standard deviation of the indicators are used to represent the performance of a single indicator. It should be noted that no clear references for good or bad scores are available, therefore the evaluation of the performance metrics is comparative. For all indices, a value closer to zero indicates a better performance.

The component-specific indicators consist of multiple values per realisation. For a decomposition with n_{IMF} IMFs, a matrix of $n_{IMF} \times n_{IMF}$ is computed for indices IO_{ij} and ρ. Naturally, these matrices are symmetric and have a value of 1 on the diagonal. To condense the information of the matrix, the mean of each row is computed, excluding value 1 of the diagonal. Of the resulting $n_{IMF} - 1$ elements, the mean is computed again, resulting in a singular value for the index. The computation of the $PMSI$ and frequency overlap results in n_{IMF} values of which the mean is computed.

For the inner reef the performance of the low-frequency components is especially important, therefore, instead of computing the mean over all $n_{IMF} - 1$ or n_{IMF} values, the mean is based only on the components with a median instantaneous frequency equal or smaller than 0.04 Hz.

As with the global indicators, the median and standard deviation of the resulting values are used to represent the performance index. Note that for ρ the absolute correlation values are used to avoid averaging out of positive and negative values.

The results are summarised in Tables 4.1 and 4.2 where a plus sign indicates a good performance and a negative sign a poor performance. Note that for each indicator, a value (of the median) closer to zero suggests a better performance, therefore values closest to zero are assigned a positive sign. Additionally, the standard deviation (SD) is considered in assigning a sign to the numerical score. The performance signs are based on the comparison between scores of the various configurations, as no other numerical reference is available. Table 4.1 presents the global performance indices for both the fore reef and inner reef, and Table 4.2 presents the IMF-specific performance indices. The full results of the performance indices are presented in Tables A.1, A.2, A.3 and A.4 in Appendix A.

From Table 4.1 and 4.2 it can be concluded that there is not a single sifting method that performs well in all aspects. On global orthogonality, the fore reef decompositions score worse for the EMD, M-EMD and iM-EMD than the inner reef, but similar or better for EEMD and CEEMD. However, on IMF-specific orthogonality, the scores are generally better and fore reef and inner reef scores similar. The EEMD and CEEMD score better on orthogonality than the non-ensemble methods.

For θ the EMD and M-EMD score worse compared to the other methods, especially the EMD has a large θ for both the fore and inner reef. All methods perform well for the maximum error, the error generally having a median in the order of magnitude 10^{-16}, only the EEMD has poor performance for this indicator. This finding is consistent with findings by Mandal et al. (2020). For the EI, only the M-EMD and the CEEMD perform well (on the fore reef).

Next are the IMF-specific indicators. Again, the orthogonality typically performs well, except for the iM-EMD. The correlation coefficient also seems to perform well for most decompositions. This is especially important to consider when using a masking method, such as the M-EMD and the iM-EMD. The mode splitting indicator $PMSI$ does not perform well for the masking methods. This is consistent with the findings in the examples, where mode splitting occurred for the M-EMD and iM-EMD, while mode mixing occurred predominantly for the EMD and to some extent for the EEMD and CEEMD to. The M-EMD performs well for frequency overlap, as is consistent with the visual inspection of the examples.

Finally, the computation time of the iM-EMD, EEMD and CEEMD is significantly longer, by a factor of 2 for the EEMD and a factor of at least 10 for the iM-EMD and CEEMD. Since many records need to be processed, such a long computation time is undesirable.

From the visual inspection, it appeared that the decomposition by the M-EMD is most favourable for the further analysis of the VLF components. For most indicators, the M-EMD scores reasonably and it has good performance for the IMF-specific orthogonality and correlation, which are important aspects to consider for a masking method (Quinn, 2022). Furthermore, the computation time is relatively short. For the additional configurations, the default settings are chosen. The application of manual masks was considered, but was eventually decided against. This analysis is briefly discussed in Appendix A.

4.1.3. Comparison of spectral characteristics between the HHT and FFT

After the decomposition of a signal into components, the Hilbert transform is applied to each component resulting in the instantaneous phase (IP), frequency (IF) and amplitude (IA). The instantaneous energy (IE) is the squared IA. The energy spectrum can be produced with the desired frequency resolution. The Hilbert spectrum is a representation of the energy over time and frequency, whereas the marginal spectrum is the time-integrated version of the Hilbert spectrum, resembling the traditional Fourier spectrum. The spectral analysis methods of the HHT and the FFT are compared through spectral characteristics and visual inspection of energy-frequency spectra.

The Fourier spectra have a resolution of 0.001 Hz, which is obtained by applying Hanning windows to time segments of 17 minutes (half the duration of a time record) with 50% overlap.

Comparison of spectra

Figure 4.2 is an example of marginal and Fourier spectra for an inner reef signal. Note that, although the unit of spectra are the same, the interpretation of these values is not, this was highlighted before in Section 3.2. In marginal spectra of various decompositions, the peak frequencies shift around depending on the decomposition method. The separation of frequency bands is most pronounced for the M-EMD, although also evident for the iM-EMD. More frequency overlap occurs for the EMD and CEEMD, see Figures A.10 and 4.2. Figure 4.2 in Appendix A provides an example of fore reef signal spectra.

Table 4.1: Performance of the fore and inner reef decomposition of various configurations. Global performance indices.If there are two values, the first value is for the fore reef, the second for the inner reef. If there is one value, fore and inner reef scored the same.

Method	Configuration		Evaluation metrics				
	Aspect	Detail	IO	θ	$a_{max,error}$	EI	Comp. time (s)
EMD	*default*		$-/+$	$-$	$+$	$--$	$++$
	Stopping criterion	SD = 0.3	$-/+$	$-$	$+$	$--$	$++$
	Stopping criterion	Rilling	$+/++$	$+/-$	$+$	$--$	$+$
	Interpolation	Cubic spline	$-/+$	$++/+$	$++$	$--$	$++$
	Boundary extension	Constant	$-/+$	$-$	$+$	$--$	$++$
M-EMD	*default*		$--/+$	$-/+$	$++$	$++/-$	$+$
	Stopping criterion	SD = 0.3	$--/+$	$-/+$	$++$	$++/-$	$+$
	Stopping criterion	Rilling	$--/+$	$+/+$	$++$	$++/-$	$+/-$
	Interpolation	Cubic spline	$--/+$	$--$	$+$	$+/-$	$+$
	Boundary extension	Constant	$--/++$	$-/+$	$+/++$	$+/-$	$+$
iM-EMD	*default*		$-/+$	$++/+$	$++$	$-$	$--$
	Stopping criterion	SD = 0.3	$-$	$++/+$	$++$	$-$	$--$
	Boundary extension	Constant	$-/+$	$++/+$	$-/++$	$-$	$--$
EEMD	*default*		$++/+$	$+$	$--$	$-$	$-$
	Stopping criterion	SD = 0.3	$++/+$	$+$	$--$	$-$	$-$
	Boundary extension	Constant	$+$	$+$	$--$	$-$	$-$
CEEMD	*default*		$+$	$+$	$+$	$+/-$	$--$
	Stopping criterion	SD = 0.3	$+$	$+$	$+$	$+/-$	$--$
	Boundary extension	Constant	$+$	$+/++$	$+/++$	$+/-$	$--$

Table 4.2: Performance of the fore and inner reef decomposition of various configurations. IMF-specific performance indices (all components for fore reef and LF components for inner reef). If there are two values, the first value is for the fore reef, the second for the inner reef. If there is one value, fore and inner reef scored the same.

Method	Configuration		Evaluation metrics			
	Aspect	Detail	IO	ρ	$PMSI$	$f_{overlap}$
EMD	*default*		$+$	$++/+$	$+$	$++/+$
	Stopping criterion	SD = 0.3	$+$	$++/+$	$+$	$++/+$
	Stopping criterion	Rilling	$++$	$++/+$	$+$	$+$
	Interpolation	Cubic spline	$-$	$-$	$-$	$-$
	Boundary extension	Constant	$+$	$++/+$	$+$	$++/+$
M-EMD	*default*		$+$	$++/+$	$-$	$++/+$
	Stopping criterion	SD = 0.3	$+$	$++/+$	$-$	$++/+$
	Stopping criterion	Rilling	$++/+$	$++/+$	$-$	$++/+$
	Interpolation	Cubic spline	$--$	$--$	$--$	$--/-$
	Boundary extension	Constant	$+$	$+$	$-$	$+$
iM-EMD	*default*		$-$	$+$	$-$	$+$
	Stopping criterion	SD = 0.3	$-$	$+$	$-$	$+$
	Boundary extension	Constant	$-$	$+$	$-$	$+$
EEMD	*default*		$+$	$++/+$	$+$	$-$
	Stopping criterion	SD = 0.3	$+$	$++/+$	$+$	$-$
	Boundary extension	Constant	$+$	$++/+$	$+$	$-$
CEEMD	*default*		$+/++$	$++$	$++/+$	$--/+$
	Stopping criterion	SD = 0.3	$+/++$	$++$	$++/+$	$--/+$
	Boundary extension	Constant	$+/++$	$++$	$++/+$	$--/+$

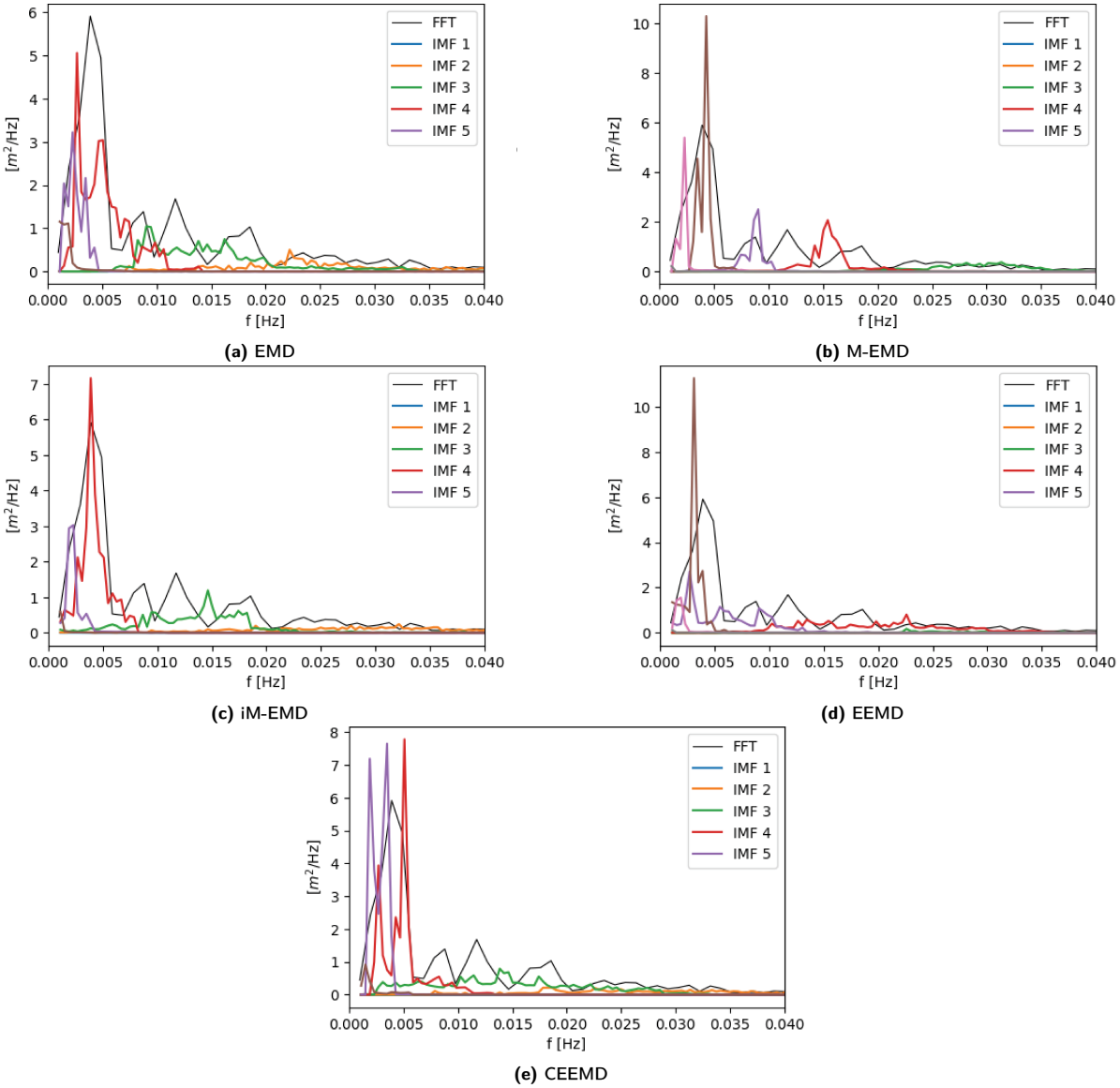

Figure 4.2: Marginal spectra with bandwidth 0.0004 Hz per IMF (coloured solid lines) for the different sifting methods and Fourier spectra with bandwidth 0.001 Hz (black solid one) for an inner reef signal. The M-EMD (b) has very little frequency overlap compared to the other decompositions.

Spectral characteristics

Because the interpretation of the variance density spectrum and the marginal spectrum is not the same, it is interesting to analyse how the several spectral characteristics compare. The spectral characteristics that are computed are the zeroth moment (m_0), mean frequency (f_{mean}) and spectral width (ν). The equations to compute these values are given in Equations (3.18), (3.19) and (3.20) respectively.

The distribution of zeroth moments of the EMD and M-EMD compared to the Fourier is given in Figures 4.3a and 4.3b. For both the fore reef and the inner reef the M-EMD gives lower values for m_0 compared to the Fourier, this is especially noticeable for the higher values of m_0. The EMD has a similar pattern for the inner reef signals, but slightly overestimates m_0 compared to FFT.

Figures 4.3c and 4.3d illustrate how the mean frequency compares for the different methods. The M-EMD is very comparable to the FFT for this spectral characteristic for both the fore and inner reef. This is consistent with the energy-frequency distributions given in Figure A.10 and 4.2. The EMD consistently estimates lower mean frequencies compared to the FFT for the fore reef.

The distribution of spectral widths is given in Figures 4.3e and 4.3f. The M-EMD is most comparable to the FFT for these values compared to the EMD, especially for the fore reef. These distributions are also consistent with the examples of spectra given before (Figure 4.2 and Figure A.10 in Appendix A).

These comparisons give insight into how the marginal and Fourier relate in spectral information. However, which method is more 'correct' remains a question. While the Fourier spectra have a strong mathematical foundation, the physical meaning reduces when dealing with real-world non-stationary and nonlinear signals. Therefore, which one of the sifting approaches best describes the physical signal is difficult to judge based on the comparison with Fourier spectra, as these spectra also may not accurately represent the 'truth'. The interpretation of the EMD and HHT will be further discussed in Chapter 5.

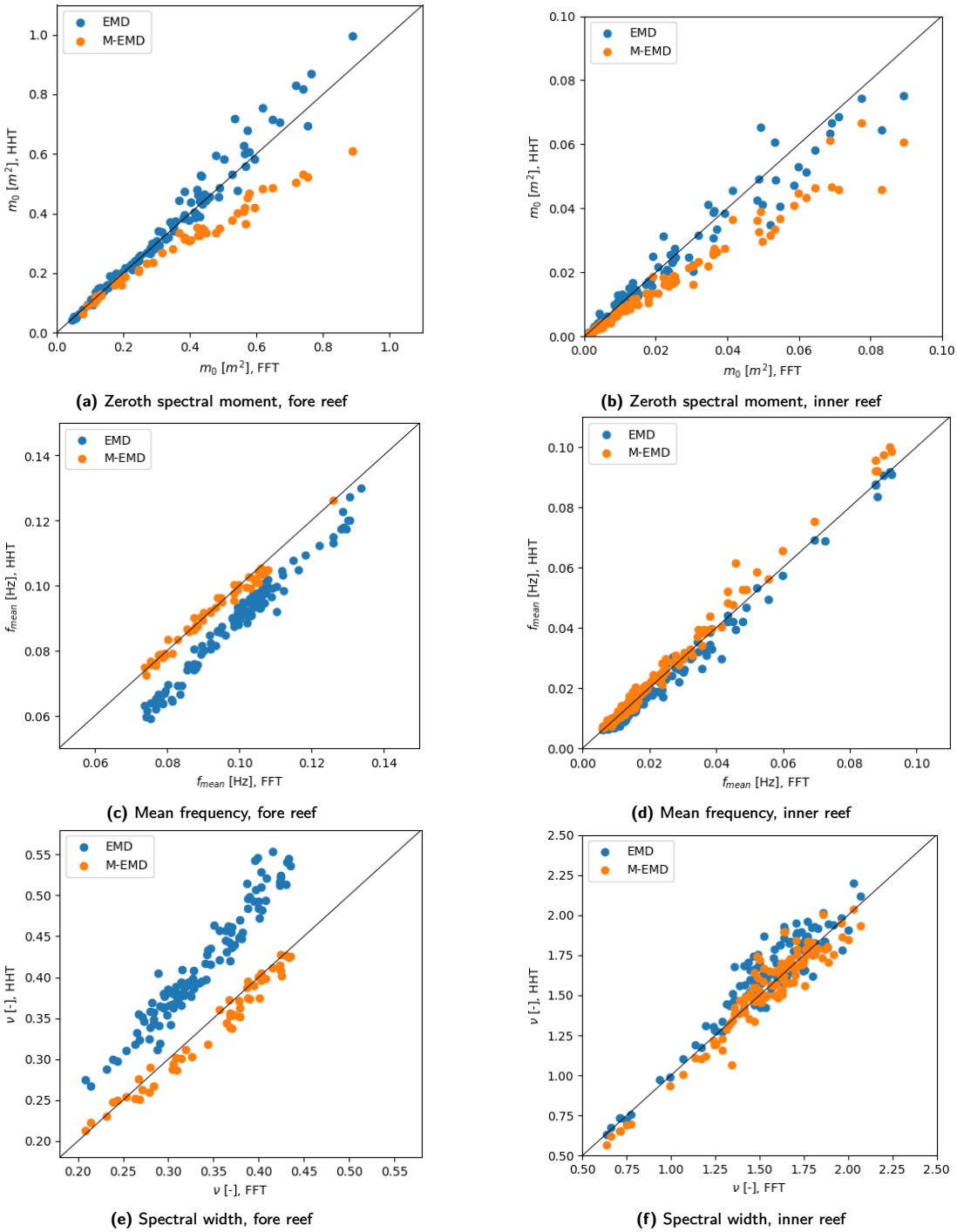

(a) Zeroth spectral moment, fore reef

(b) Zeroth spectral moment, inner reef

(c) Mean frequency, fore reef

(d) Mean frequency, inner reef

(e) Spectral width, fore reef

(f) Spectral width, inner reef

Figure 4.3: Spectral characteristics of the M-EMD and EMD techniques for the Hilbert spectra (y-axes) compared to the Fourier spectra (x-axes) for fore reef and inner reef signals: (a) and (b) the zeroth spectral moment m_0, (c) and (d) the mean frequency f_{mean}, and (e) and (f) the spectral width ν.

Section summary

Various sifting configurations have been evaluated through visual inspection and a set of performance indices. Visual inspection shows that the various oscillations in an inner reef signal are captured by the decomposed components, although some challenges associated with the EMD and its variants are recognised, particularly **mode mixing** and its opposite **mode splitting**.

The **M-EMD** is able to most consistently capture the visually dominant low-frequency oscillation in a single component. Because of this, the M-EMD is the most suitable option considering the following analyses of the VLF component. To ensure the quality of the IMFs of the M-EMD, the **correlation** (ρ) and **orthogonality** between components (IO_{ij}) are evaluated, both of which score adequately. Additionally, the **marginal spectra** and **frequency overlap index** ($f_{overlap}$) illustrate that the frequency content of the IMFs is well separated for the M-EMD, indicating the absence of mode mixing.

Comparing the marginal spectra to the Fourier spectrum, it is clear that the two bear similarities in spectral shape and spectral characteristics, even though the interpretation of the spectra is not the same.

4.2. VLF wave classification and resonance identification

After the M-EMD is chosen as the most suitable sifting method, all signals are processed with this decomposition method. As explained in Section 3.3, in this part, the VLF waves at the inner reef are classified and analysed for resonance. The classification of the inner reef VLF oscillations based on their propagation character and energy content corresponds to the objective of research question 2. The resonance identification is based on a new approach which includes the time-varying character, aligning with research question 3.

This section starts with the VLF wave classification step, which consists of selecting the dominant VLF component, and the assessment of its propagation type and energy content. Secondly, various approaches for resonance identification are applied and compared. Finally, the patterns regarding the classification and resonance analysis related to various hydrodynamic factors are investigated.

4.2.1. Classification of standing and energetic VLF oscillations at the inner reef

Dominant VLF component of the inner reef signal decomposition

The dominant VLF component of the inner reef is selected based on the median instantaneous frequency (IF) and the energy content. First of all, the median IF should be within $0.5 f_{0,th}$ and $2 f_{0,th}$. If more than one component satisfies this condition, the IMF with the highest energy fraction is selected. Typically IMF 6 is selected, but the selection of IMF 7 or 8 occurs as well. The range of median IFs of the selected VLF components is illustrated in Figure 4.4a, which also contains the distribution of theoretical eigenfrequencies. There is a clear distinction between the frequencies of IMF 6 and 7, which is expected considering the M-EMD approach, which uses a factor 2 between masking signal frequencies for the extraction of two consecutive IMFs. Although it seems that the frequency 0.003 Hz is underrepresented in the IMFs, this is not necessarily the case. Figures 4.5a and 4.5b display the distribution of the 50% (25^{th}-75^{th} percentile) and 95% (2.5^{th}-97.5^{th} percentile) ranges of the instantaneous frequencies respectively. These figures indicate that a range of frequencies is observed within the VLF components. Furthermore, considering the bandwidth for the spectra (0.001 Hz for both Fourier and Hilbert spectra) for the resonance analysis, the median frequencies would be distributed as in Figure 4.4b.

In the M-EMD, the separation of frequency components is forced through masking signals, which not only results in the distribution of IMF frequencies as displayed in Figure 4.4a, but can also cause mode splitting, as has been reported in Section 4.1. During the analysis, it was noted that because of mode splitting, a part of the amplitude that intuitively belongs to the dominant VLF component could end up in another IMF. This leads to underestimation of the amplitude and sometimes to the wrongful selection of the 'dominant' VLF component. Although this observation outlines the limitations of the current M-EMD approach, this issue is not further addressed in this research. Further discussion of the limitations and challenges of the M-EMD follows in Chapter 5.

In the rest of this section, the IMF with the dominant VLF oscillation at the inner reef will be referred to as the (inner reef) VLF component.

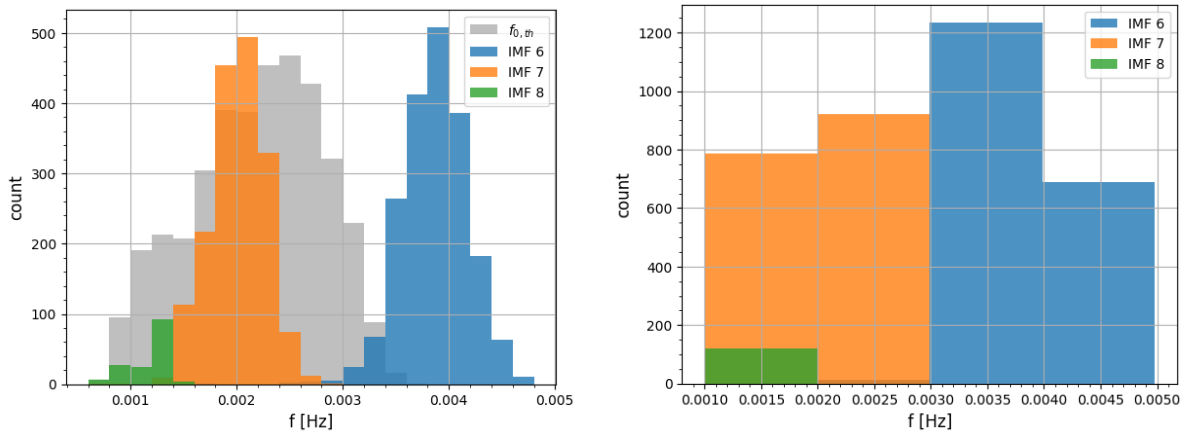

(a) Distribution with bin width 0.0002 Hz.

(b) Distribution with bin width 0.001 Hz.

Figure 4.4: Distribution of median instantaneous frequencies for the dominant inner reef VLF components. The bin widths are 0.0002 Hz and 0.001 Hz for (a) and (b) respectively. The distribution of eigenfrequencies is displayed in (a) as well.

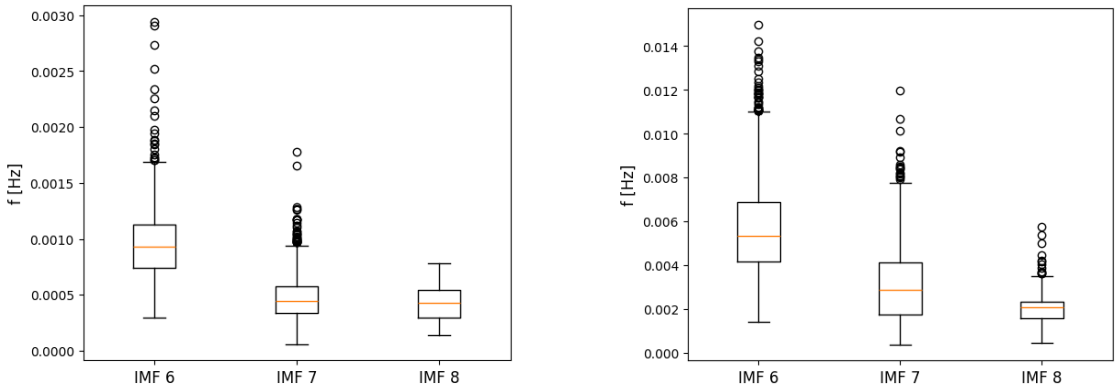

(a) 25^{th}-75^{th} percentile range.

(b) 2.5^{th}-97.5^{th} percentile range.

Figure 4.5: Distribution of the (a) 50% and(b) 95% ranges for the median instantaneous frequencies for the dominant inner reef VLF components.

Propagation type classification

The wave propagation character is assessed by comparing the phase difference between the inner reef VLF component and its corresponding mid reef component. The phase difference is determined for time windows in the same order of duration as the period of the component. Only if the coherence between the mid and inner reef components is high (>0.8), can the phase difference be compared meaningfully. Through Equation (3.23) the phase coherence of two components is computed based on their instantaneous phase (IP) information. This equation is a function of time lag and therefore also provides the lag corresponding to the maximum coherence. Comparing this time lag to the phase difference by subtracting the instantaneous phases of the inner and mid reef components and converting this to seconds, this results in Figure 4.6. This figure illustrates that for high coherence (>0.8), these two approaches for defining the time lag agree well with a Pearson correlation coefficient of -0.97.

As explained in Section 3.3.1, there are several criteria for defining a standing wave. Firstly, the ratio between the mid-to-inner reef phase difference (in seconds) to the theoretical phase lag (determined with $c = \sqrt{gh}$) should be in the range of -0.3 to 0.1. Secondly, the phase difference in radians should be between -0.25 and 0.25. These two conditions must be satisfied for a minimum of a quarter of the time series, corresponding to 1-3 time windows, depending on the window duration, see Table 3.1. Figure 4.7 shows the lag ratio plotted against the phase difference in radians, where the grey areas represent the two criteria. The dots in the area where the two grey ranges overlap are considered to be standing VLF waves. With these criteria, 43.1% of the VLF components are classified as standing waves.

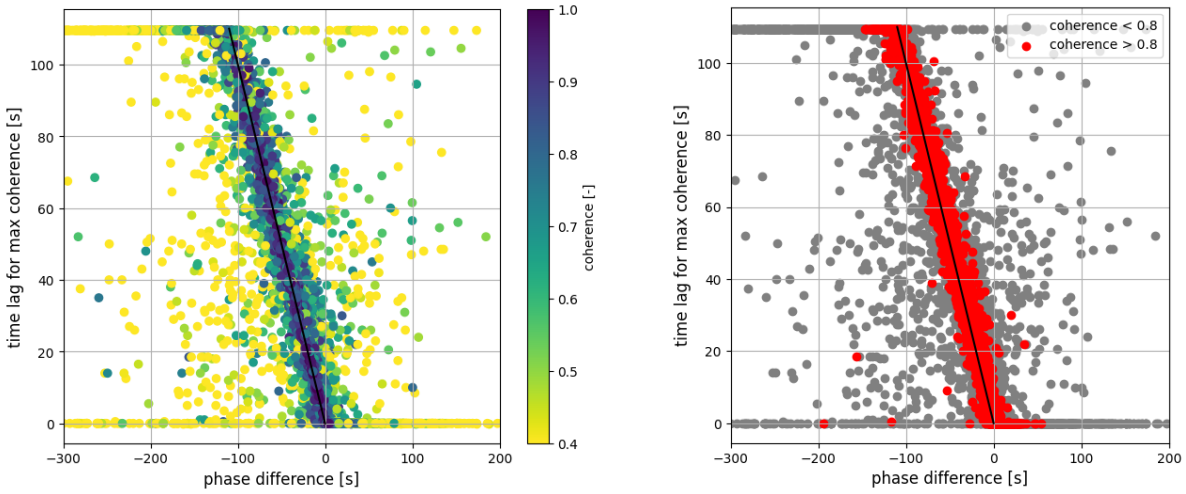

Figure 4.6: The time lag of the maximum coherence (determined with Equation (3.23)) versus the phase difference in seconds, between the inner and mid reef VLF component. There is a strong inverse linear relation between these two parameters when the coherence is high (Pearson correlation coefficient -0.97). A similar distribution as in (a) with the phase difference in radians on the x-axis is shown in Figure B.15 in Appendix B.

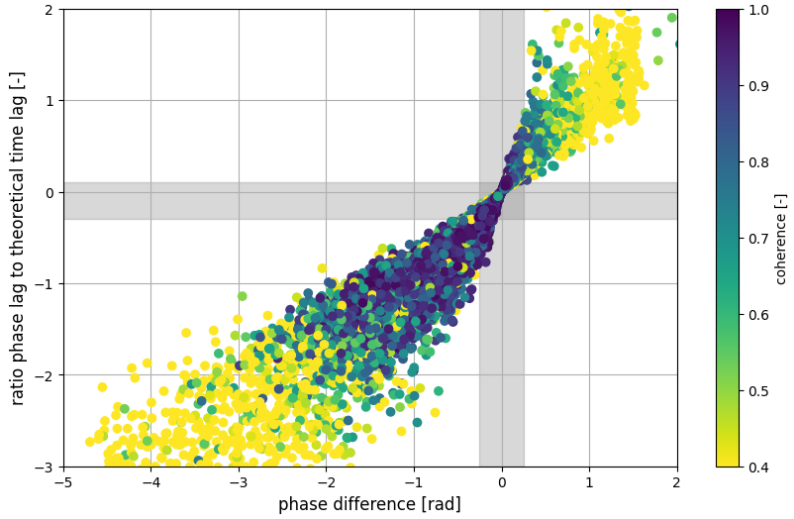

Figure 4.7: Distribution of the ratio between the phase lag in seconds and the theoretical time lag based on phase velocity $\sqrt{gh}$, to phase difference in radians. The phase differences in radians and seconds are based on the subtraction of the instantaneous phases for the inner and mid VLF components. Every point represents a time window containing at least one full wave oscillation. The grey areas illustrate the ranges for the phase difference ([-0.25,0.25]) and the lag ratio ([-0.3,0.1]) for a standing oscillation.

Energy classification

An amplitude threshold of 0.12 m for the inner reef component is used to distinguish energetic components from non-energetic components. The basis of the amplitude threshold is explained in Section 3.3.1. A VLF component is considered energetic if it contains at least one wave crest above this threshold. This results in 7.2% energetic VLF components.

Combining the two steps of the classification, the occurrence of each wave class is presented in Table 4.3. In case of a low coherence between the inner and mid reef components (< 0.8), the propagation type is not determined. It is assumed that these components are progressive. The time series that are classified as non-energetic and non-standing are referred to as one class (which is given the name 'other' in figures in the following sections).

It should be noted that from this classification, no definite conclusions can be made about resonance occurrence. While there may be an overlap between resonance and energetic standing oscillations, this is not necessarily true, as a certain amplification is typically associated with resonant oscillations. Therefore resonance occurrence is investigated separately in the next section. For the resonance analysis, the classification will be referred to to get a better insight into how the propagation and energy content of the VLF component relate to the resonance identification.

Table 4.3: Classification of dominant VLF inner reef components.

VLF component classification	Energetic	Non-energetic
Standing	6.1%	37.0%
Progressive	1.1%	55.8%
Undefined (coherence < 0.8)	0%	

4.2.2. Resonance identification

In this section, the various resonance analyses as explained in Section 3.3.2 are conducted. The 'resonance diagram' is important in this analysis, showing the distribution of the normalised peak transfer energy ($normE_{p,transfer}$) for the ratio between the peak transfer frequency ($f_{p,transfer}$) and the theoretical eigenfrequency ($f_{0,th}$), which will be referred to as the frequency ratio axis.

In combination with the classification of the previous section, this results in the distribution illustrated in Figure 4.9a. From this figure, the energetic standing wave class appears to be distributed randomly across the x-axis. Through visual inspection of the Fourier spectra and corresponding transfer function, the peak transfer frequency selection based on the maximum value of $H_{Axy}(f)$ seems to be arbitrary on multiple occasions. This is illustrated for an example in Figure B.9 in Appendix B. As further explained in Appendix B, an alternative frequency selection method is proposed. The alternative method considers the frequencies where H_{Axy} exceeds its 85$^{\text{th}}$ percentile, and selects $f_{p,transfer}$ within this range, based on the maximum inner reef energy. The 85$^{\text{th}}$-percentile method results in a distribution with a similar overall outline, but the energetic standing waves are centred close to a value of 1 for the frequency ratio, which is a more intuitive distribution. This is illustrated in Figure 4.9b. Additionally, the 85$^{\text{th}}$-percentile method also leads to a denser distribution close to the frequency ratio of 1, which is illustrated in Figure B.16 in Appendix B. Between the two frequency selection methods, there is an agreement of 61.3% of resonance cases, as is also visualised in the diagram in Figure 4.8a.

Since the occurrence of resonance of 3.6% is assumed, the denser distribution results in a higher resonance threshold, see Table 4.4. As a result of the increased threshold, there is some disagreement between the resonance identification between the two frequency selection approaches. This is illustrated in Figure B.17 in Appendix B. Would the resonance threshold remain equal to the original approach, the new method would result in a resonance occurrence of 6.6%, almost double the original percentage of 3.6%. For this analysis, the occurrence of 3.6% is maintained for the threshold assumption, as has been explained in Section 3.3.2.

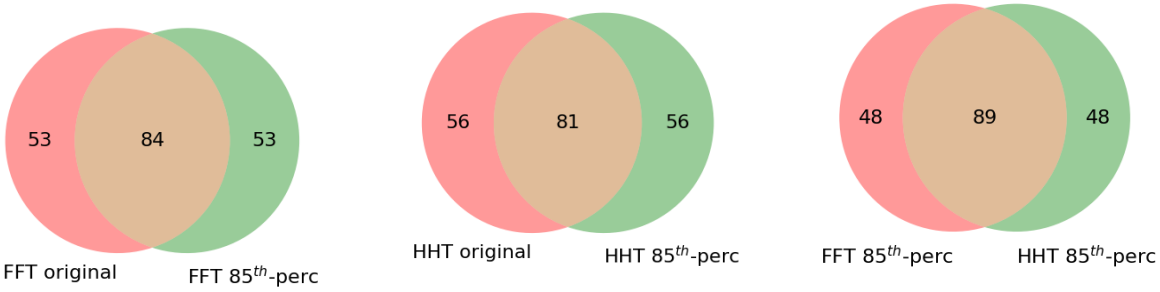

(a) FFT method. Overlap of 61.3%.

(b) HHT method. Overlap of 58.1% overlap.

(c) FFT and HHT method, overlap of 65.0%.

Figure 4.8: Venn diagrams illustrating the number of resonance cases identified by various resonance analysis approaches. The total number of resonance occurrences is 137, as the occurrence of 3.6% is maintained for the various approaches.

Table 4.4: The values indicate the threshold for $normE_{p,transfer}$, to ensure a resonance occurrence of 3.6% for the different resonance analysis approaches using the Fourier spectra (denoted with FFT) and Hilbert spectra (denoted with HHT).

	Original frequency selection	85th-percentile frequency selection
FFT	0.0467	0.0583
HHT	0.0575	0.0713

Table 4.5: Distribution of resonance cases over VLF wave classes for the different resonance analysis approaches.

	Energetic standing	Standing	Energetic progressive	Other
FFT original	57.7%	37.2%	2.9%	2.2 %
FFT 85th-percentile	65.7%	30.7%	1.5%	2.2%
HHT original	53.3%	38.0%	2.2%	6.6%
HHT 85th-percentile	66.4%	26.3%	2.9%	4.4%

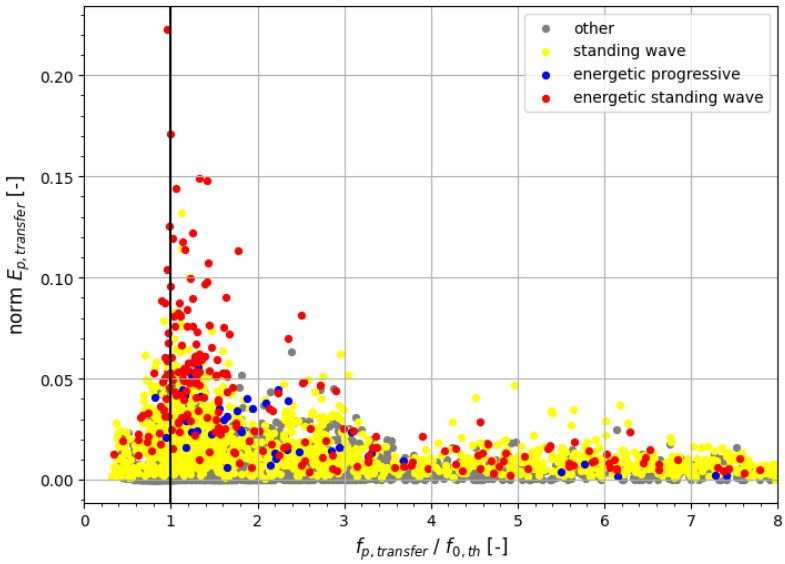

(a) Original frequency selection method

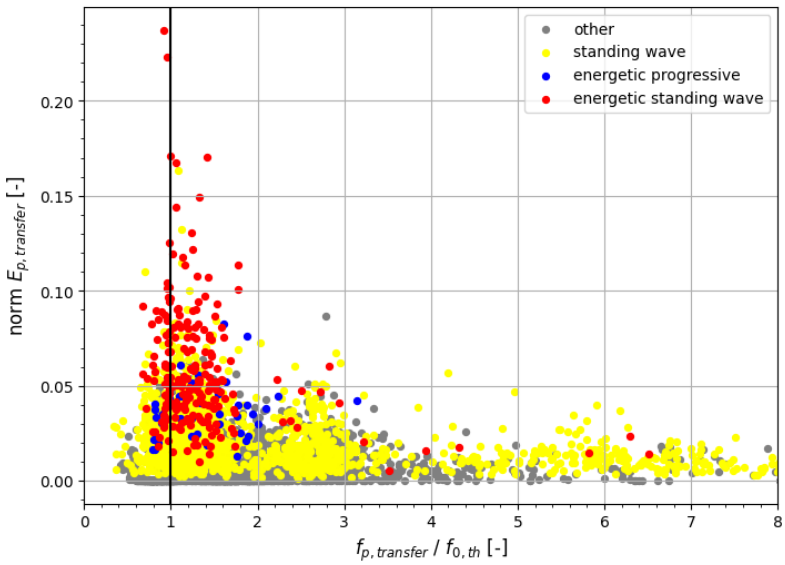

(b) 85th-percentile frequency selection method

Figure 4.9: Resonance diagrams based on the Fourier spectra approach. The two frequency selection methods, the (a) original and (b) 85th-percentile method, are compared. The colour indicates the inner reef VLF wave class. Note that the energetic standing waves are centred more around 1 on the x-axis for the 85th-percentile frequency selection method. The scatter densities of these diagrams are indicated in Figure B.16 in Appendix B.

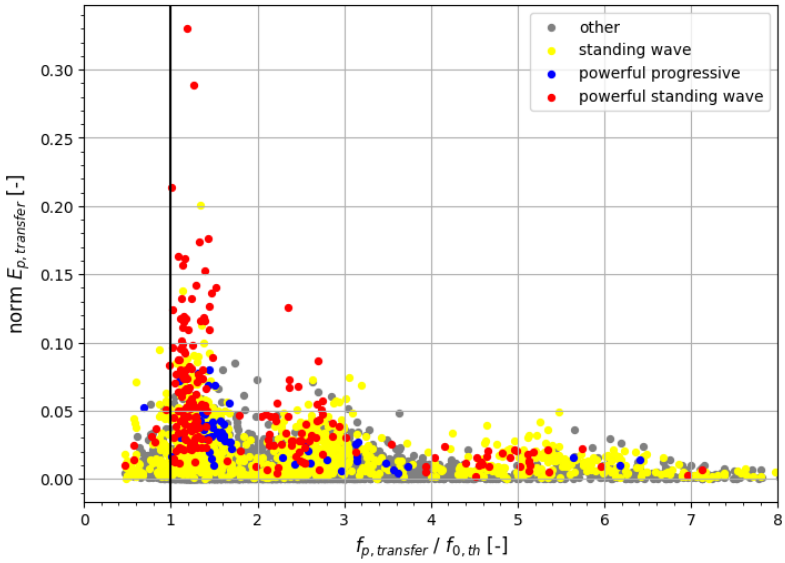

(a) Original frequency selection method

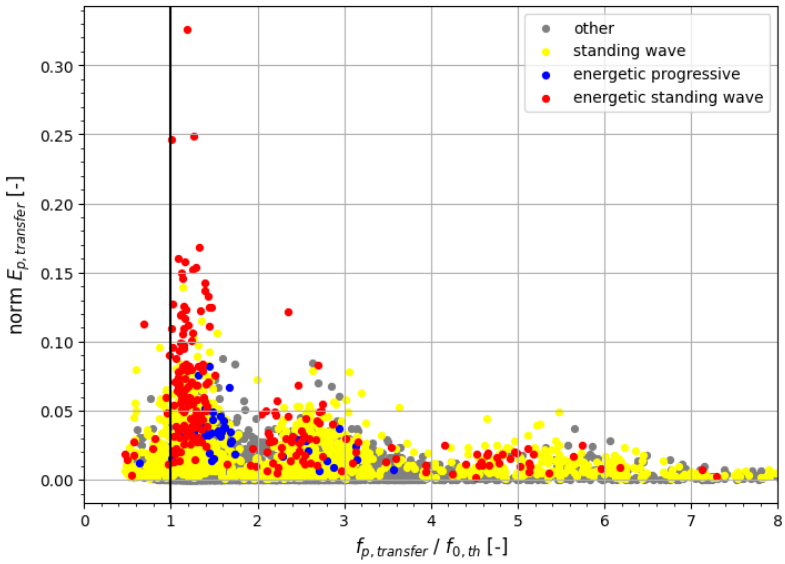

(b) 85th-percentile frequency selection method

Figure 4.10: Resonance diagrams based on the full-time-integrated marginal spectra approach with the two frequency selection methods, the (a) original and (b) 85th-percentile method. The colour indicates the inner reef VLF wave class. The scatter densities of these diagrams are indicated in Figure B.18 in Appendix B.

Resonance analysis for full time-series using HHT

When replacing the Fourier spectra with marginal spectra, the resonance diagram shows a similar distribution as was obtained with the previous approach, which is illustrated in Figure 4.10. Regarding the distribution of wave classes in the resonance diagrams, the two frequency selection methods result in similar patterns. The agreement between the two frequency selection methods is similar for the HHT as it was for the FFT approach, see Figure 4.8b. Furthermore, identification of resonance has an overlap of 65% (89 out of 137) between the FFT and HHT with the 85th-percentile frequency selection, as is illustrated in Figure 4.8c. Comparing the resonance cases identified by these two approaches further, the peak transfer frequencies are similar, but the magnitude for the corresponding normalised energy $normE_{p,transfer}$ is different for the two approaches. This is illustrated in Figure B.20 in Appendix B.

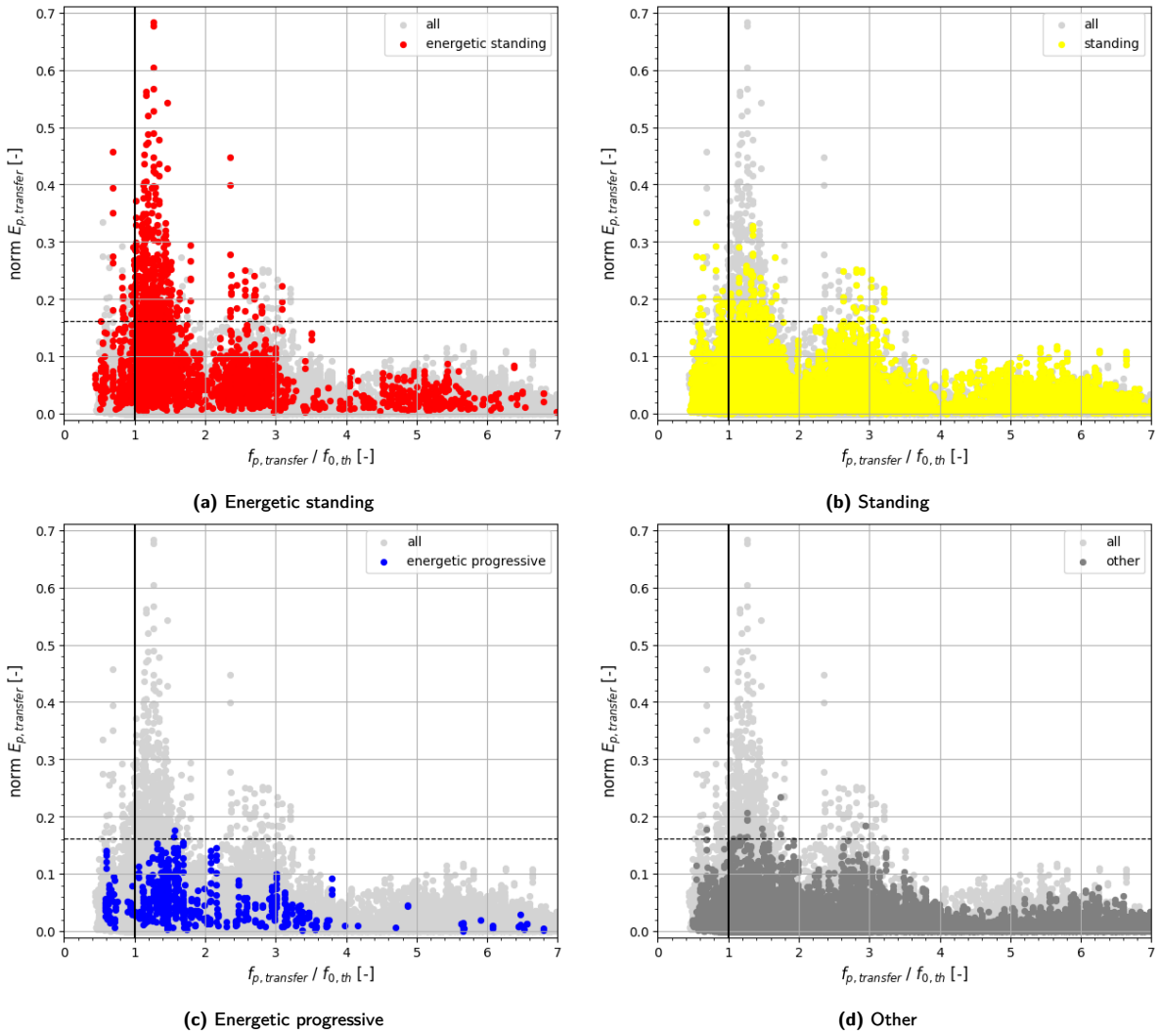

(a) Energetic standing

(b) Standing

(c) Energetic progressive

(d) Other

Figure 4.11: Resonance diagram based on the time-varying HHT approach (HHT_{temp}) with the 85th-percentile frequency selection method. The Hilbert spectra are integrated over 600-second time windows with a 100-second interval. The colour indicates the inner reef VLF wave class. The horizontal dashed black line indicates the resonance threshold. The scatter densities of these diagrams are indicated in Figures B.21 and B.22 in Appendix B.

Time-varying resonance analysis

Including the time-varying character could provide a more accurate approximation of the amplification between the incoming forcing and the corresponding response at the inner reef. For this approach, only the 85th-percentile method is used for the frequency selection. Figure 4.11 shows the distribution of the wave classes in the resonance diagram with the time-varying approach. In this approach, the marginal spectra are computed through time-integration of 600-second windows with a 100-second interval, as explained in Section 3.3.2. The figure shows similarities with the earlier figures, although the number of scatter points has naturally increased. Note that the VLF wave classification is defined per wave record and not per time window. To illustrate how the amplification $normE_{p,transfer}$ varies over time as a result of the fore reef envelope and inner reef signal energy, two examples are presented in Figures B.24 and B.25 in Appendix B.

The standing wave classes (Figures 4.11a and 4.11b) both show a pattern of peaks of $normE_{p,transfer}$ around the frequency ratios of approximately 1, 3 and 5, indicating the different modes for standing oscillations (see Figure 2.5). This pattern is considerably less pronounced for the progressive wave classes (Figures 4.11c and 4.11d). The similar pattern between the two standing wave classes indicates that, although standing VLF oscillations at the inner reef may be less energetic, they can still be the result of considerable amplification of the incoming energy. Likewise, the energetic standing VLF oscillations are not always the result of resonant amplification.

The resonance threshold is determined based on the criterion that a time series should contain at least one 600-second time window for which $normE_{p,transfer}$ exceeds the threshold. Maintaining the resonance occurrence of 3.6%, a threshold value of 0.1617 is obtained. This results in the distribution of resonance over the wave classes as presented in Table 4.6, showing that 93.4% of resonance are classified as standing oscillations, the majority of which is energetic. For a small number of cases, resonance is identified for VLF components that are classified as progressive oscillations. This is odd considering that resonance should be a standing wave. The 'resonant' progressive waves in Figures 4.11c and 4.11d hardly exceed the resonance threshold (indicated with the dashed line), which may suggest the resonance threshold should be higher. Upon further inspection of these cases, it appears that the VLF wave appears to be standing at moments of resonance. These VLF components are classified as progressive either because the standing oscillation is of too short duration (less than a quarter of the time series) or there are discrepancies in the waveform of the mid and/or inner reef VLF components. This highlights the limitation of the current classification approach, which will be further discussed in Chapter 5.

Comparing the time-varying resonance identification to the HHT method, there is an agreement of 73.0%, see Figure 4.12a. The differences are illustrated in Figure B.23 in Appendix B. Figure 4.13 illustrated how many 600-second windows of a single time series are categorised as resonance for the resonance diagram of the fully time-integrated HHT method. There are typically more 'resonant windows' for higher values of $normE_{p,transfer}$ in this diagram, which aligns with the expectation.

To assess whether the dominant VLF oscillations selected as the first step of the VLF wave classification are representative of the VLF resonant oscillations, the time-varying resonance analysis is executed using only the dominant VLF component of the inner reef signal instead of the complete set of components. This method is referred to as $HHT_{temp,VLF}$. The same value for the resonance threshold (0.1617) is maintained. As illustrated in Figure 4.14, the $HHT_{temp,VLF}$ approach corresponds very well with the first peak in the resonance diagram of the HHT_{temp} approach. Indeed, Figure 4.12c shows that there is a 100% agreement between the cases selected by the original HHT_{temp} approach and the $HHT_{temp,VLF}$ approach. This confirms that the inner reef energetic VLF oscillations selected for the VLF classification are indeed the most prone to resonance (in the fundamental mode).

However, 15 extra resonance cases are identified through $HHT_{temp,VLF}$ approach. This suggests that, in the energy-frequency spectrum, the frequency with maximum energy does not necessarily correspond to the frequency with the higher energy transfer H_{Axy}. An example of such a case is given in Figure B.27 in Appendix B.

For further analysis, the resonance criterion is based on the HHT_{temp} approach, the extra 15 cases from $HHT_{temp,VLF}$ approach are thus not included. Additionally, 'potential resonance' cases are considered in the next section, where patterns of resonance occurrence are analysed. These are defined as records for which resonance is identified by at least two of the full-record resonance analyses (FFT or HHT, with original or 85^{th}-percentile frequency selection method).

Table 4.6: Percentage of resonance per wave class for the temporal HHT resonance analysis.

	Energetic standing	Standing	Energetic progressive	Other
HHT_{temp}	67.9%	25.5%	1.5%	5.1%

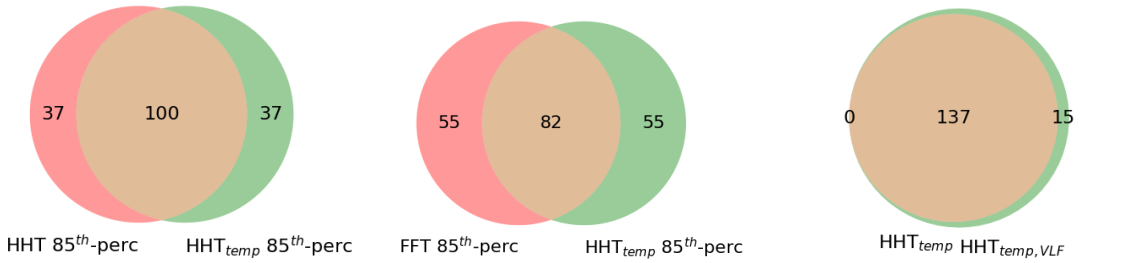

(a) HHT and HHT_{temp} method. Overlap of 73.0%.

(b) FFT and HHT_{temp} method. Overlap of 59.9%.

(c) HHT_{temp} and $HHT_{temp,VLF}$. Overlap of 100%.

Figure 4.12: Venn diagrams illustrating the number of resonance cases identified by various resonance analysis approaches. The total number of resonance occurrences is 137, as the occurrence of 3.6% is maintained for the various approaches.

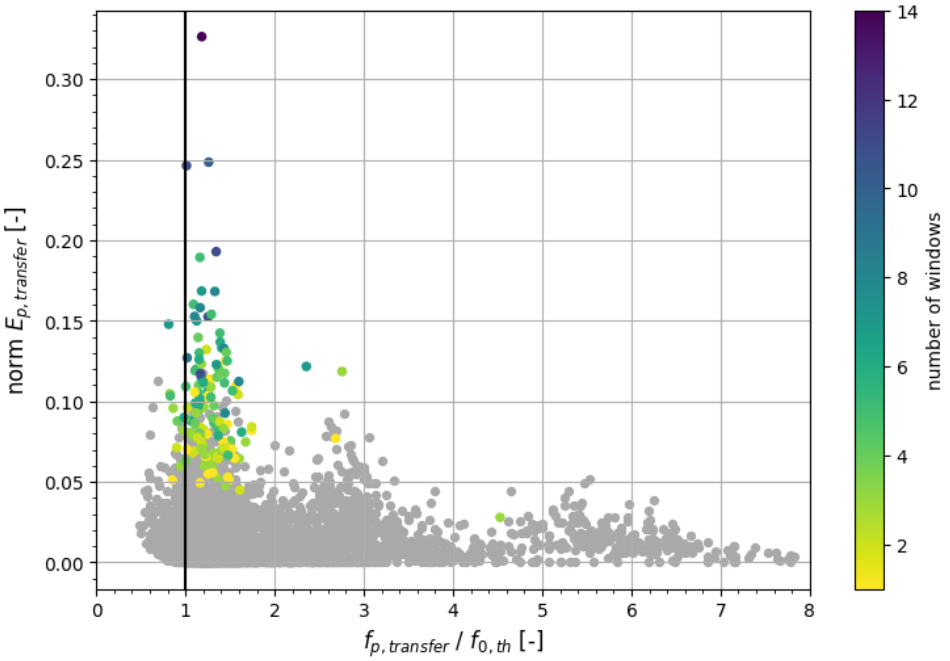

Figure 4.13: Resonance diagram based on the HHT approach with the 85th-percentile frequency selection method. The colour indicates the number 600-second windows above the resonance threshold in the HHT_{temp} analysis. Because the 100-second interval for the windows, there is a maximum of 14 windows per time series.

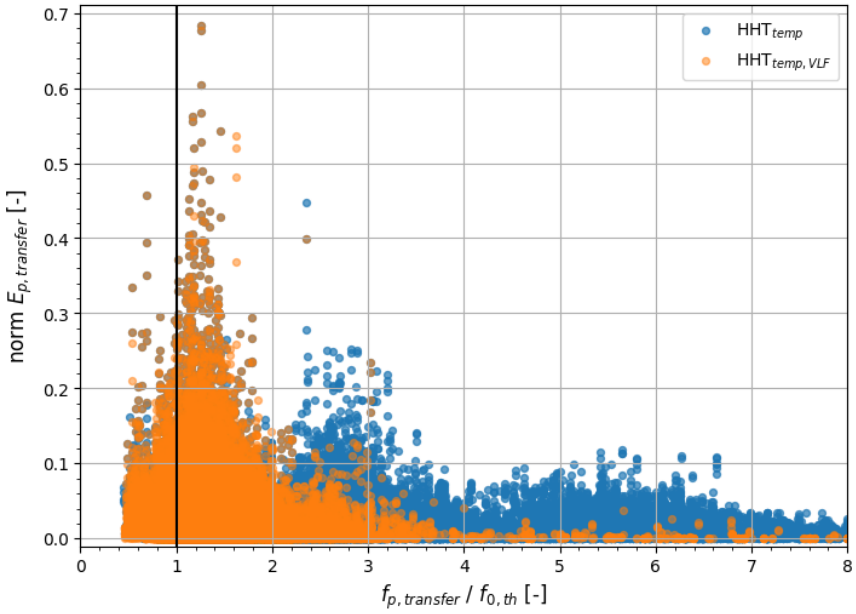

Figure 4.14: Resonance diagrams based on the time-varying HHT approach (HHT_{temp}) and HHT approach only using the dominant VLF component of the inner reef signal ($HHT_{temp,VLF}$), with the 85th-percentile frequency selection method. 600-second time windows are used. The scatter density of this diagram is indicated in Figure B.26 in Appendix B.

4.2.3. Patterns of VLF wave classification and resonance identification

After the classification and resonance identification, the results are investigated to reveal patterns related to some hydrodynamics factors, such as eigenfrequency, water depth and wave height.

Resulting from the classification of the VLF components, the mean instantaneous amplitude (IA) and median instantaneous frequency (IF) are computed and plotted against each other. Figure 4.15 shows the distribution for the VLF wave classes and the resonance cases. The same distribution of the median IF as illustrated in Figure 4.4 is recognised in these figures. It appears that both the energetic and resonant oscillations typically have median IFs of 0.003 to 0.0045 Hz, corresponding to IMF 6. Regarding the resonance occurence, another important frequency to consider is the $f_{p,transfer}$. Because of the bandwidth of 0.001 Hz, the $f_{p,transfer}$ is 0.0035 Hz (meaning 0.003-0.004 Hz) for the majority of resonance cases, and sometimes 0.0025 and 0.0045 Hz. This finding corresponds fairly well with the distribution indicated in Figure 4.15b.

Additionally, Figure 4.16 displays the distribution of the mean IA and the theoretical eigenfrequency $f_{0,th}$. While f_{0th} does not equal the VLF oscillation frequency, it is related to the reef water depth. Energetic standing VLF oscillations occur almost exclusively for eigenfrequencies exceeding 0.0025 Hz, while the majority of energetic progressive oscillations occur for eigenfrequencies below this threshold, as illustrated in Figure 4.16a. Figure 4.16b indicates that resonance tends to occur at higher eigenfrequencies as well, mostly exceeding 0.0025 Hz.

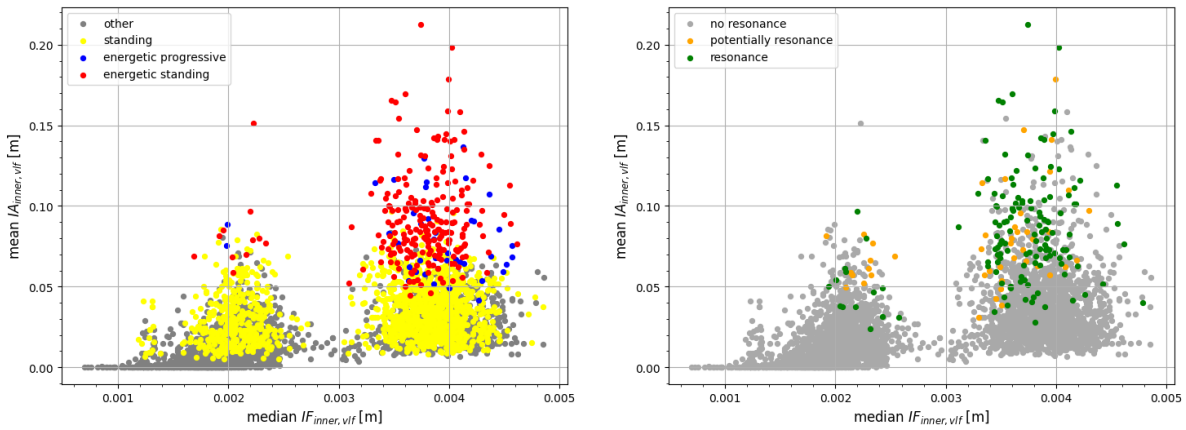

(a) Distribution of VLF wave classification.

(b) Distribution of resonance identification.

Figure 4.15: The mean instantaneous amplitude of the inner reef VLF component ($IA_{inner,vlf}$) plotted against the median instantaneous frequency of the VLF component ($IF_{inner,vlf}$), with colour indicating the (a) VLF wave classes and (b) resonance. The scatter density of this diagram is indicated in Figure B.28 in Appendix C.

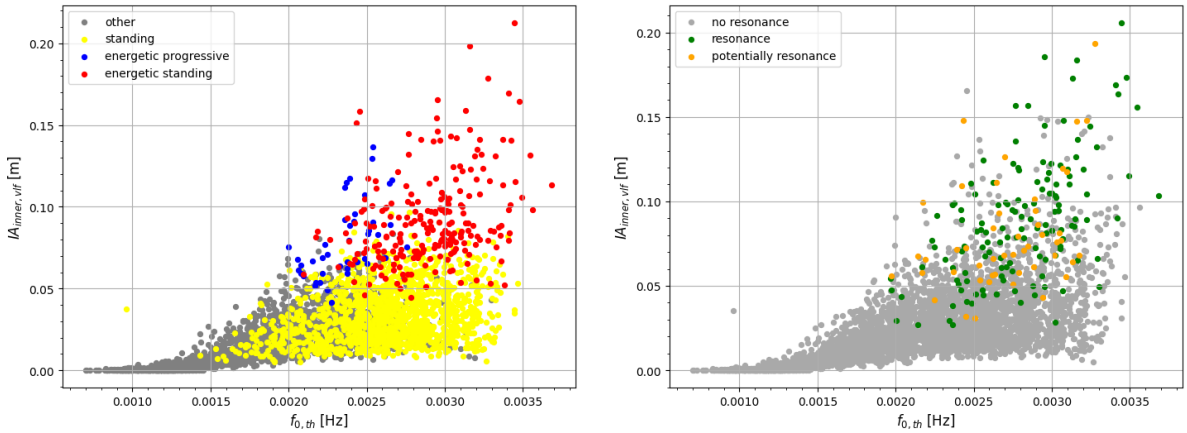

(a) Distribution of VLF wave classification.

(b) Distribution of resonance identification.

Figure 4.16: The mean instantaneous amplitude of the inner reef VLF component ($IA_{inner,vlf}$) plotted against the eigenfrequency ($f_{0,th}$), with colour indicating the (a) VLF wave classes and (b) resonance. The scatter density of this diagram is indicated in Figure B.29 in Appendix C.

Furthermore, the patterns are investigated for other hydrodynamic parameters. Figure 4.17 shows the relation of the reef flat water depth (h_{reef}) to the significant wave height at the inner reef ($H_{s,inner}$). Figure 4.17a illustrates that the energetic (standing) VLF oscillations correspond with high wave heights at the inner reef. In more than half of the cases where the $H_{s,inner}$ exceeds its 90th percentile (0.5 m), there is an energetic standing VLF oscillation, see Table 4.7. This is not necessarily the case for resonant oscillations, which seem to be spread out over the $H_{s,inner}$-axis. However, 65.0% of the resonance cases do take place concurrently with a high significant wave height at the inner reef, as indicated in Table 4.8. These findings outline the importance of understanding the occurrence and characteristics of energetic standing and resonant VLF oscillations, as they are related to the occurrence of larger waves at the inner reef. The positive relation between the IA of the VLF wave and $H_{s,inner}$ is not surprising, as these parameters are not independent, although they are computed with different methods. Correlating the $H_{s,inner}$ and $IA_{inner,vlf}$ reveals a strong linear correlation with a correlation coefficient of 0.93. Furthermore, the correlation between the $H_{s,inner}$ of the VLF range and the $IA_{inner,vlf}$ is even more evident with a correlation coefficient of 0.97. These relations are visualised in B.31 in Appendix B.

Figure 4.17b also illustrates that resonance mostly occurs for higher reef flat water depths, the mean $\pm$ one standard deviation being 0.94 ± 0.25m, while the reef flat water depth 0.59 ± 0.31m.

Additional figures are provided in Appendix B illustrating the relationships between reef flat water depth, and external factors such as tide levels and incident wave heights at the fore reef.

Table 4.7: Percentage of each wave class for the significant wave height at the inner reef $H_{s,inner}$ exceeding its 90th percentile (0.5 m).

	Energetic standing	Standing	Energetic progressive	Other
$>$ 90% $H_{s,inner}$	53.2%	38.7%	5.3%	2.9 %

Table 4.8: Occurence of each resonance class in combination with the significant wave height at the inner reef $H_{s,inner}$ exceeding its 90th percentile (0.5 m).

	Resonance	Potential resonance	No resonance
$>$ 90% $H_{s,inner}$	65.0%	55.6%	7.4%
total cases (100%)	137	45	3618

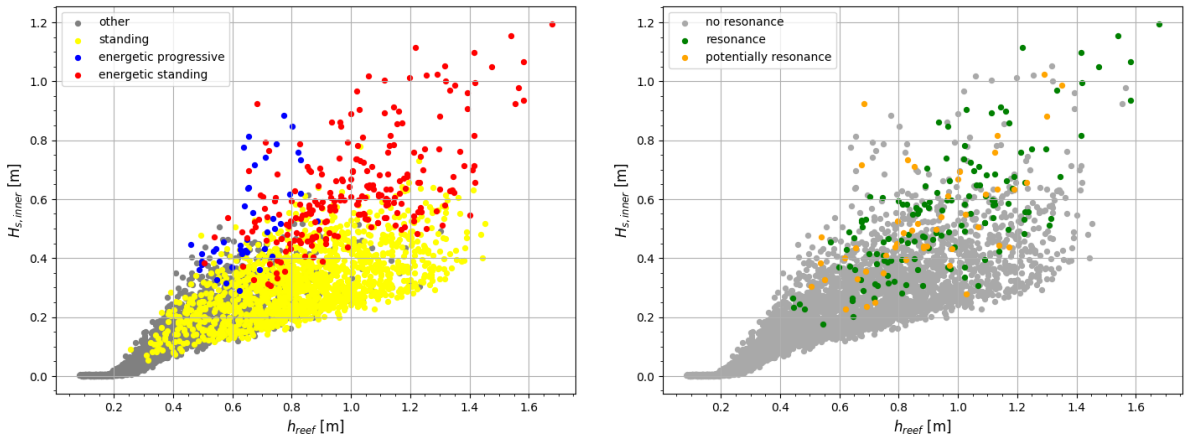

(a) Distribution of VLF wave classification.

(b) Distribution of resonance identification.

Figure 4.17: The inner reef significant wave height ($H_{s,inner}$) plotted against the reef flat width (h_{reef}), with colour indicating the (a) VLF wave classes and (b) resonance. The scatter density of this diagram is indicated in Figure B.30 in Appendix C.

Section summary

The dominant VLF component of the inner reef is classified based on propagation type and amplitude. The propagation type is determined through the phase difference between the mid and inner reef VLF components. Energetic VLF oscillations are defined by containing at least one wave crest above 0.12 m. Results show **6.1% and 1.1% of the inner reef VLF components in the dataset exhibit energetic standing and progressive VLF oscillations** respectively.

To assess inner reef resonance, the inner reef energy is related to the fore reef envelope signal using the criterion proposed by Gawehn et al. (2016). A 3.6% resonance occurrence is maintained across analyses via the threshold for $normE_{p,transfer}$. Comparison of FFT and HHT approaches reveals 65% overlap in resonance cases. While the methods show similar distributions of $f_{p,transfer}/f_{0,th}$ for resonance cases, they differ in values for $normE_{p,transfer}$.

The **time-varying resonance analysis** (HHT_{temp}) utilises 600-second windows with a rolling interval of 100 seconds for the time-integration of the Hilbert spectrum, and a time lag between the fore and inner reef stations is included. Comparing HHT_{temp} and HHT approach shows that typically more 'resonant segments' occur for higher values of $normE_{p,transfer}$ for the HHT approach. These two methods agree on resonance identification for 73% of the cases.

Furthermore, the $HHT_{temp,VLF}$ approach, similar to the time-varying resonance approach but **using only the dominant VLF component** of the inner reef decomposition, shows 100% agreement with HHT_{temp} in selecting resonance cases. **This demonstrates the efficacy of the selected dominant VLF components in capturing oscillations containing the zeroth resonance mode**.

Combining the classification and resonance identification, **more than 90% of the identified resonant oscillations are classified as standing oscillations**. This finding supports the definition of resonance, which is a type of standing oscillation. Both energetic standing and resonant oscillations typically have a frequency of around **0.003-0.0045 Hz**, corresponding to the higher end of the VLF range. Additionally, energetic standing oscillations were found to occur mostly for higher reef water depths ($>$ 0.7 m) and correspond to high significant wave height at the inner reef oscillations.

4.3. Transient characteristics of energetic and resonant VLF waves

Now that the inner reef oscillations have been classified into wave classes and examined for resonance, some transient characteristics are investigated. This part will concentrate on analysing the duration and intensity of energetic VLF events occurring at the inner reef. Furthermore, a method to assess the duration of resonance events is applied. Subsequently, these findings are evaluated in the context of overwash events observed during the field data collection period. This section aims to answer the fourth and final research objective.

4.3.1. Energetic VLF events duration and intensity

An energetic VLF event is defined by the IA exceeding the energetic threshold of 0.12 m. By defining the upward and downward crossing of this threshold, the duration and corresponding intensity of these events are quantified, as is explained in Section 3.4.

The durations of the determined energetic VLF events are shown in Figure 4.18. For both the standing and progressive oscillations, the majority of energetic VLF events have a duration between 200-500 seconds. The standing oscillations show the potential for longer durations, 10% of these oscillations persist longer than 844.6 s (14.1 minutes), while the 90th percentile for the progressive oscillations is 617.9 s (10.3 minutes).

The relation between the duration ($d_{vlf,event}$) and the intensity of the energetic VLF events is assessed with two parameters: the maximum peak of the VLF component ($c_{max,vlf,event}$) and the mean instantaneous amplitude (IA) of the energetic VLF event ($IA_{vlf,event}$). The results are presented in Figure 4.19. A general trend is observed that higher peaks and amplitudes occur for longer VLF events, although the correlation coefficients (0.50-0.66) indicate a moderate correlation. It should be noted that these figures visualise the individual energetic VLF events. The sum of VLF event durations per track ($D_{vlf,events}$) is also analysed which results in much stronger correlations (0.62-0.89) between the VLF event durations and intensity, especially for the mean amplitude of the VLF oscillation ($IA_{inner,vlf}$), as is illustrated in Figure 4.20.

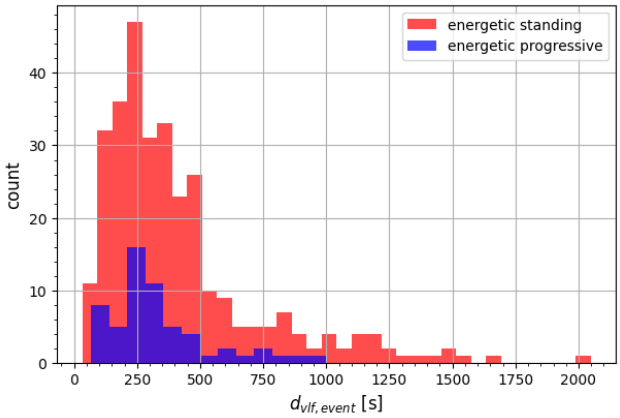

Figure 4.18: Distribution of energetic VLF event durations. The median duration of the standing and progressive oscillations is 326.3 seconds (5.4 minutes) and 285.0 seconds (4.8 minutes) respectively. The bin width of the histogram is 60 seconds.

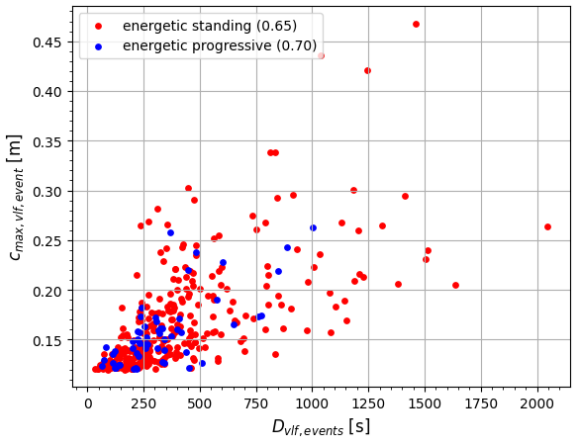

(a) Maximum peak of the energetic VLF event.

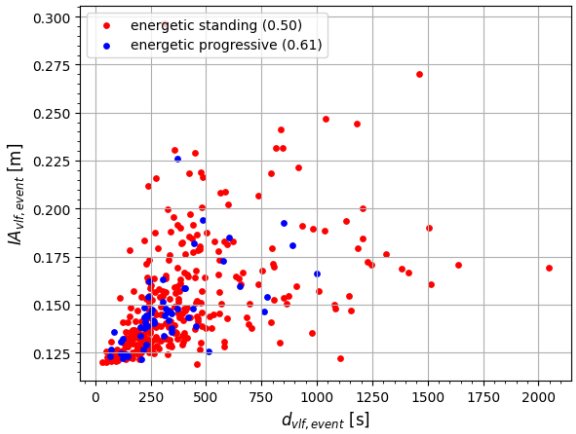

(b) Mean IA of the energetic VLF event.

Figure 4.19: (a) The maximum peak ($c_{max,vlf,event}$) and (b) the mean instantaneous amplitude ($IA_{vlf,event}$) of the energetic VLF event plotted against the energetic VLF event duration, with the Pearson correlation coefficient given in brackets in the legend. The scatter density of the diagrams is indicated in Figures C.2 in Appendix C.

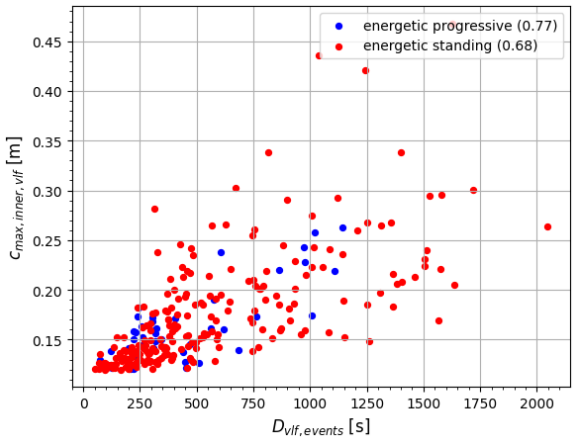

(a) Maximum peak of the VLF component.

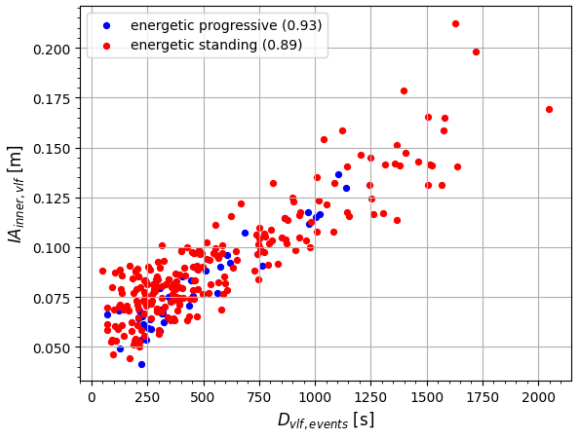

(b) Mean IA of the VLF component.

Figure 4.20: (a) The maximum peak ($c_{max,inner,vlf}$) and (b) the mean instantaneous amplitude ($IA_{inner,vlf}$) of the inner reef VLF component plotted against the sum of the duration of energetic VLF events per record, with the Pearson correlation coefficient given in brackets in the legend. The scatter density of the diagrams is indicated in Figures C.3 in Appendix C.

Comparing the VLF event duration to $H_{s,inner}$, this results in strong positive correlations (0.78-0.81) for both the progressive and standing energetic oscillations, as illustrated in Figure 4.21a.

Notably, the mean $IA_{inner,vlf}$ is not independent of the (total) duration of the energetic VLF events, as the duration is defined by the crossing of the amplitude threshold. Likewise, this implies a dependence between $H_{s,inner}$ and $D_{vlf,events}$, as a strong correlation between the mean $IA_{inner,vlf}$ and $H_{s,inner}$ was suggested before in Section 4.2.3.

Figure 4.21b indicates a weak correlation between the duration and the reef flat water depth h_{reef}. However, the figure does indicate that progressive oscillations largely occur for smaller water depths compared to standing oscillations, which was suggested earlier in Figure 4.17a. This sharp delineation between progressive and standing energetic oscillations is further interpreted and discussed in Chapter 5.

The occurrence of the energetic VLF oscillations over the 5 months of measurements is provided in Figure 4.22, illustrating that the energetic standing and progressive oscillations often coincide and alternate depending on the reef flat water depth. The VLF event occurrences are further investigated in Section 4.3.3.

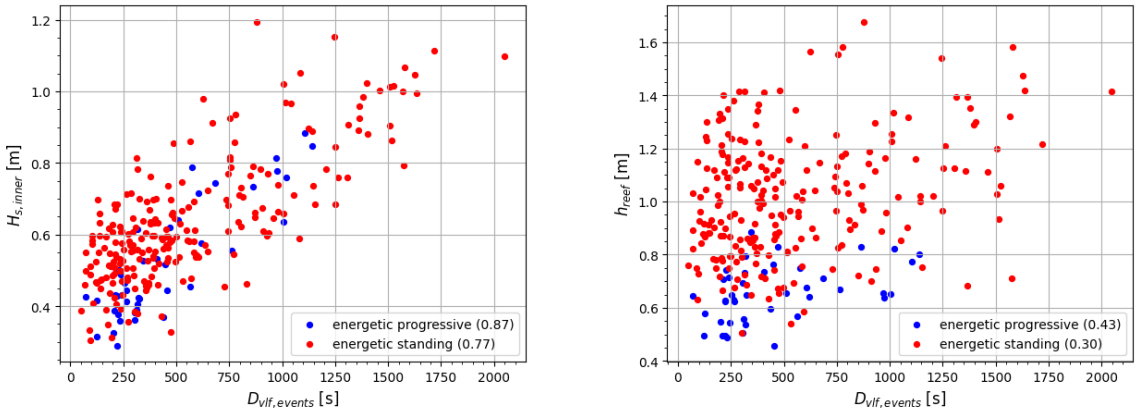

(a) Inner reef significant wave height.

(b) Reef flat water depth.

Figure 4.21: The (a) inner reef significant wave height and (a) reef flat water depth plotted against the sum of the duration of energetic VLF events per record ($D_{vlf,events}$), with the Pearson correlation coefficient given in brackets in the legend. The scatter density of the diagrams is indicated in Figures C.4 in Appendix C.

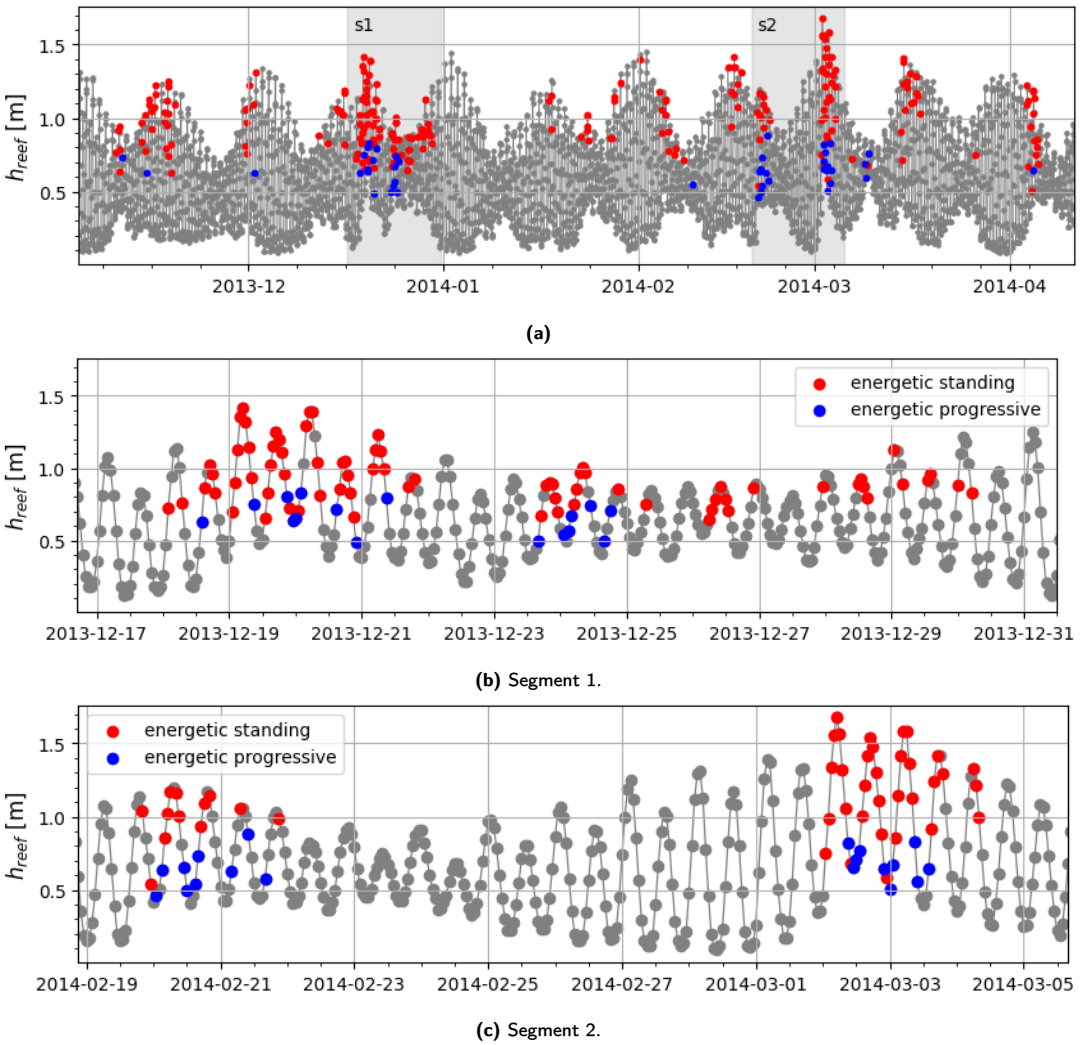

(a)

(b) Segment 1.

(c) Segment 2.

Figure 4.22: The energetic VLF events are displayed in based on the inner reef water depth. The grey areas in (a) represent segments 1 and 2 (s1 and s2) and are magnified and displayed in (b) and (c) respectively.

As noted before, an energetic (standing) oscillation, does not imply resonance necessarily. If we combine the classification of the VLF oscillation and the resonance criterion, the energetic VLF events can be distinguished as being resonant or not. Figure 4.23 shows the distribution of energetic VLF event durations for the resonance categories. For resonant oscillations, the energetic VLF events is longer on average, with a median duration of 391.5 seconds (6.5 minutes) compared to the median duration of 267.5 seconds (4.5 minutes) for non-resonant oscillations, as is indicated in Table 4.9.

Additionally, Figure 4.24 shows the resonance diagram with the duration of energetic VLF events within the 600-second windows illustrated with colour. This figure suggests that higher values for $normE_{p,transfer}$ (indicating greater amplification), typically have a longer duration.

Table 4.9: Energetic VLF event duration and intensity. Values for the median and 90 percentile of different resonance categories. The definition of resonance and potential resonance are explained in Section 4.2.2.

	Duration [s]		Max. peak [m]		Mean amplitude [m]	
	50%	90%	50%	90%	50%	90%
Non-resonant	267.5	672.3	0.14	0.21	0.14	0.18
Resonant	391.5	915.5	0.16	0.25	0.15	0.20
Potential resonance	383.5	849.2	0.16	0.24	0.15	0.20

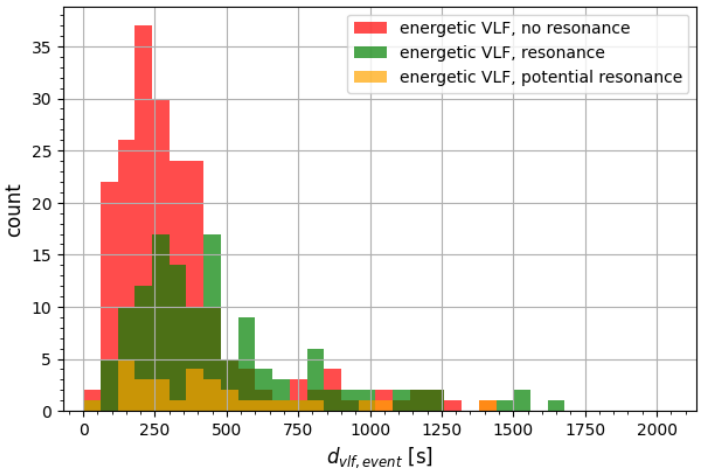

Figure 4.23: Duration of energetic VLF events for resonance identification. The bin width of the histogram is 60 seconds. The median and 90th percentile values are presented in Table 4.9.

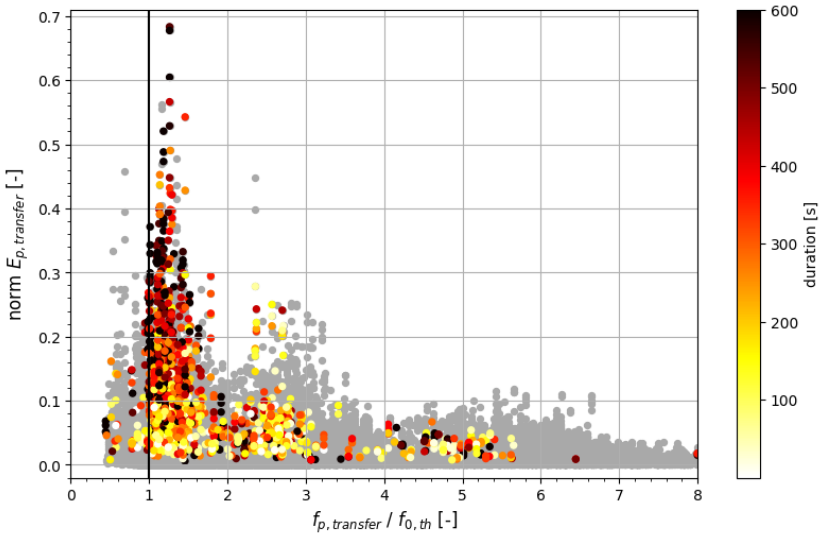

Figure 4.24: Resonance diagram based on the time-varying HHT approach (HHT$_{temp}$) with the 85th-percentile frequency selection method. Time windows of 600 seconds are used. The colour indicates the duration of an energetic VLF event in the 600-second windows. The scatter density of this diagram weighted with the VLF event duration is indicated in Figure C.1 in Appendix C.

4.3.2. Resonance events duration and intensity

The last section focused on the duration of energetic VLF events, also touching upon the difference between the duration of resonant and non-resonant energetic VLF oscillations. However, the span of resonance itself is not addressed through that analysis. A new method is applied to analyse the duration of resonance events. This method is based on the temporal resonance analysis as applied in Section 4.2.2. For this analysis the variation of $normE_{p,transfer}$ over time is described by the HHT$_{temp,VLF}$ resonance analysis, since this ensures that the $normE_{p,transfer}$ is computed for the VLF component. A resonance event is defined by the upward and consecutive downward crossing of the resonance threshold ($normE_{p,transfer} = 0.1617$). This way 89 records remain for this analysis, containing a total number of 96 resonance events. However, through visual inspection, it was noted that numerous instances of resonance durations are restrained by the limited time series length. These edge events, lack an upward or downward crossing of the resonance threshold (or both). Because the complete durations of the edge events are not known, a distinction is made between these and 'complete' resonance events.

Figures 4.25a and 4.25b show the distribution of resonance durations for resonance events and edge

events respectively. The median durations are approximately 400 seconds (6.7 minutes). Note that the longer resonance events are identified for the edge events. This outlines the constraints of the time series in this analysis. Furthermore, the duration of the edge events is defined by the mean of the first or final time window, being approximately 300 and 1700 s. The longest resonance duration is 1300.5 seconds, for which $normE_{p,transfer}$ is above the threshold for all windows. In this case, some 700 seconds are not included in the resonance durations because no extrapolation beyond the mean of the window is applied. This is not an issue for the defined resonance events.

The durations of the complete resonance events are normalised with the period corresponding to the $f_{p,transfer}$ of the events, resulting in the distribution displayed in Figure 4.26a, which also shows the normalised total duration of resonance per time series. The median and 90th percentile of the distributions are given in Table 4.10. Although the majority of resonance events have a normalised duration of 1 to 3, a third of the events have a value below 1. A normalised duration of below 1 is peculiar as one would expect resonance to persist at least for one duration of the wave period, considering its standing propagation character. 24.2% and 53.3% of resonance events had a normalised duration below 1 for energetic and non-energetic VLF oscillations respectively. The normalised total duration of resonance per time series is longer on average, although values below 1 still occur.

The shorter (normalised) resonance event durations correspond to lower values of the peak $normE_{p,transfer}$ of the event, as is illustrated in Figure 4.27. This suggests that the $normE_{p,transfer}$ threshold for resonance should be higher. On the other hand, perhaps the threshold should be lower, thereby increasing the duration of resonance events. Further discussion of these results follows in Chapter 5.

Table 4.10: Values for resonance events and total resonance per time series. Resonance events are instances of resonance where there is an upward and downward crossing of the resonance threshold. The durations are defined by these threshold crossings and are normalised with the peak transfer period ($T_{p,transfer}$). The maximum peak and mean amplitude are defined for the extent of a resonance event. The total duration of resonance also includes edge events. These durations are normalised with the median $T_{p,transfer}$ and the maximum peak and mean amplitude are defined for the time series duration of the VLF component. Values for the median and 90th percentile of the energetic and non-energetic wave classes are given.

	Duration [s]		Norm. duration [-]		Max. peak [m]		Mean amplitude [m]	
	50%	90%	50%	90%	50%	90%	50%	90%
Energetic, event	375.0	689.0	1.4	2.4	0.16	0.24	0.14	0.19
Non-energetic, event	251.8	508.0	0.9	1.8	0.08	0.11	0.08	0.11
Energetic, total	420.0	778.5	1.7	3.2	0.18	0.27	0.09	0.14
Non-energetic, total	251.0	564.0	1.0	2.5	0.09	0.12	0.05	0.07

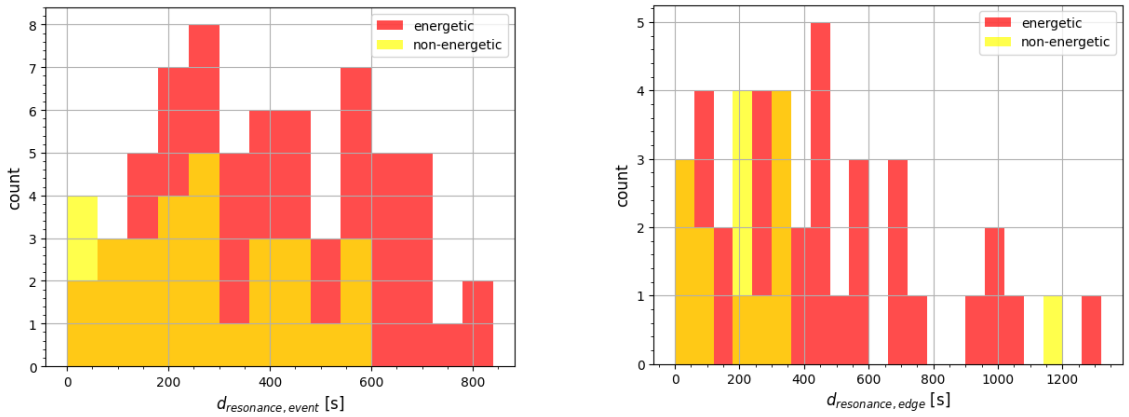

(a) Resonance events.

(b) Edge events.

Figure 4.25: Distribution of resonance duration for (a) resonance events with a defined start and end (by the upward and downward crossing of the resonance threshold) and (b) edge events, that lack a downward and/or upward crossing of the resonance threshold. The bin width of the histogram is 60 seconds.

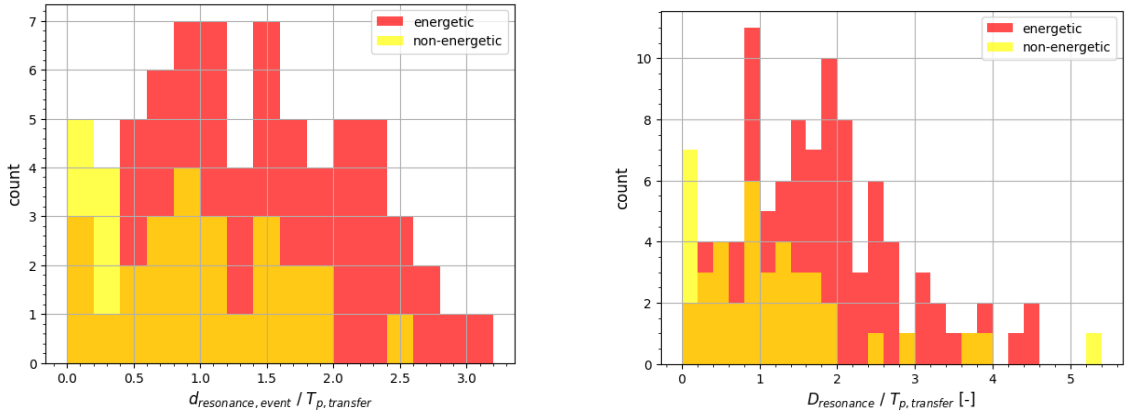

(a) Resonance events.

(b) Total resonance durations.

Figure 4.26: Distribution of (a) complete resonance events, and (b) total resonance duration per time series that include edge events. The bin width of the histogram is 60 seconds.

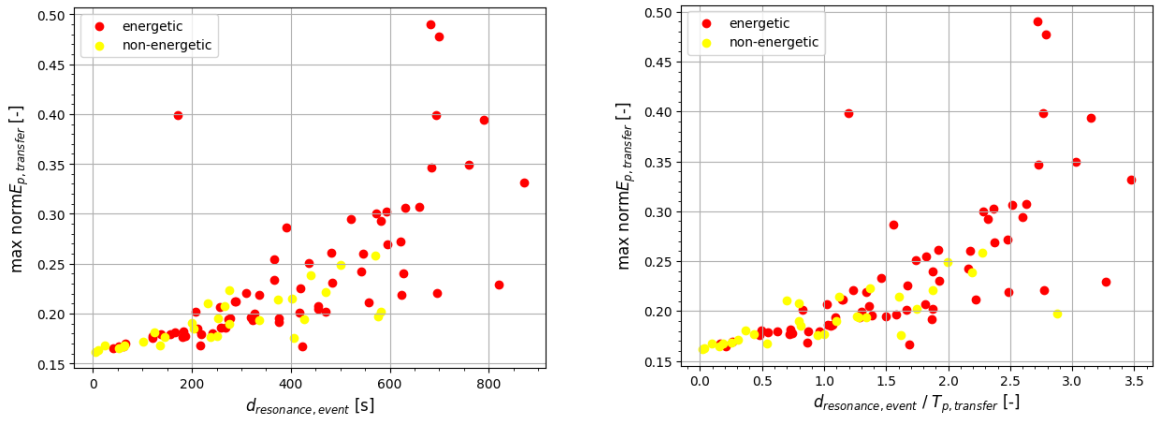

(a) Resonance event duration.

(b) Normalised resonance event duration.

Figure 4.27: The maximum $normE_{p,transfer}$ of a resonance event plotted against the (a) duration and (b) normalised duration of resonance event. 33% of resonance events (energetic and non-energetic combined) have a normalised duration below 1.

The relation between the resonance event durations and corresponding maximum peaks and mean amplitudes are correlated weakly, with a correlation coefficient of 0.52 and 0.32 respectively. Additionally, the total duration of resonance is compared to the maximum peak and mean amplitude of the inner reef VLF component, and to the inner reef significant wave height and reef flat water depth. These relations also show weak correlations with correlation coefficients between 0.25-0.44. Figures of these relations are displayed in Figures C.5 and C.6 in Appendix C. The median and 90th percentile values for the intensities are shown in Table 4.10.

To assess the sensitivity of resonance event detection and the resulting outcomes to the window duration for the resonance analysis, the analysis is also performed using 300-second windows. According to the resonance analysis with 600-second windows, the median value for the peak transfer frequency was determined to be 0.0035 Hz, equivalent to a period of 285.7 seconds. Hence the choice of 300-second windows. This approach yielded fewer resonance events with a normalised duration below 1. Regarding the total duration of resonance per time series, the 300-second window approach yielded a longer median duration although the 90th percentile durations are similar. Further details on these findings are provided in Appendix C.

4.3.3. Coastal flooding events

After having determined the durations of energetic and resonant VLF events, the occurrence of these events over the 5-month survey is analysed. Especially the relation of these events to the observed coastal flooding

is investigated.

Coastal flooding events were documented on four occasions during the survey. Severe overwash was observed on December 19, 2013, and March 2-3, 2014. Additionally, large runup events were reported on November 18, 2013, and February 20, 2014 (Cheriton et al., 2016).

Figures 4.29 and 4.30 show the occurrence of energetic and resonant oscillations respectively. In these figures, the overwash (o1 and o2) and runup (r1 and r2) occurrences are displayed with grey areas, which have a width of 48 hours. The exact occurrence of the overwash and runup is not known, therefore the timing of the the VLF oscillations is not analysed on a more detailed time scale. Additionally, Figures 4.31 and 4.32 show the reef flat width and VLF oscillation intensity and the offshore tidal level and fore reef significant wave height.

Generally, the occurrence of resonance seems to co-occur with the occurrence of energetic VLF events. On days when energetic VLF events occur, there is always a moment where resonance occurs. Vice versa, most resonance events occur together with energetic VLF events, except for a few non-energetic resonance events.

The substantial overwash events (o1 and o2 in Figure 4.29b) coincided with long periods of energetic VLF oscillations, lasting approximately 5 hours within a 24-hour recording period. The runup events in November and February (r1 and r2 in Figure 4.29b) were associated with shorter durations of energetic VLF oscillations, approximately 1.5 hours. Notably, for the November event, these energetic VLF oscillations occurred before the runup was observed. The total duration of resonance was approximately 0.6 and 1 hour for the December and March overwash events respectively. For the runup in November and February, the duration of resonance was of comparable duration.

The March event was reportedly more severe than the December event, the durations of both energetic VLF and resonance events are comparable but slightly longer for the March event. The increased severity of the March event could be attributed to higher reef flat water depths, as was also suggested by Cheriton et al. (2016). The boxplots in Figure 4.28 show how the two overwash events compare for the duration of VLF events, mean IA and maximum peak of the VLF components. The distributions are relatively similar, although the March overwash event (o2) shows a slightly higher maxima for the mean IA.

Interestingly, while substantial resonance durations were recorded on December 23, 2013, and April 3, 2014, no substantial wave runup was reported for these dates. The overall energetic VLF durations for these dates were approximately 1 hour respectively, which is much shorter than the VLF event durations for the December and March overwash events. On December 23, tidal levels were lower due to neap tide (see Figure 4.32a), but the reef water depth on April 3 was similar to February 20, when large runup was reported. The VLF oscillation was of shorter duration and slightly lower intensity on April 3, which could explain the absence of substantial (reported) runup.

These distributions of the duration of energetic and resonant VLF oscillations suggest that the durations of VLF events may be a more relevant indicator for (the severity of) coastal flooding events than the duration of resonance. This notion is further discussed in Chapter 5.

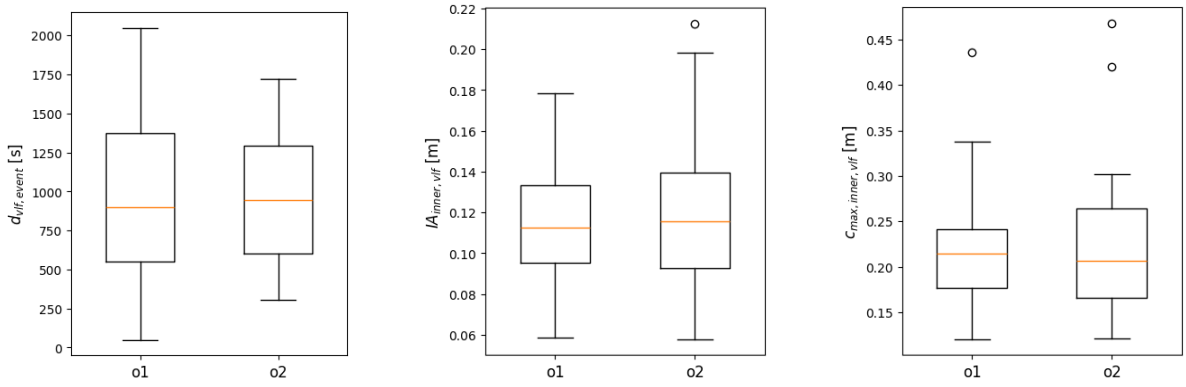

(a) Duration of VLF events. **(b)** Mean IA of VLF component. **(c)** Maximum peak of VLF component.

Figure 4.28: Boxplots representing the (a) duration of VLF events, (b) mean IA of the VLF component and (c) maximum peak of the VLF component for tracks with energetic VLF oscillations in a 48-hour period around the overwash (o1, o1) events. The total VLF event durations within these 48-hour periods are 7.9 and 8.8 hours for o1 and o2 respectively.

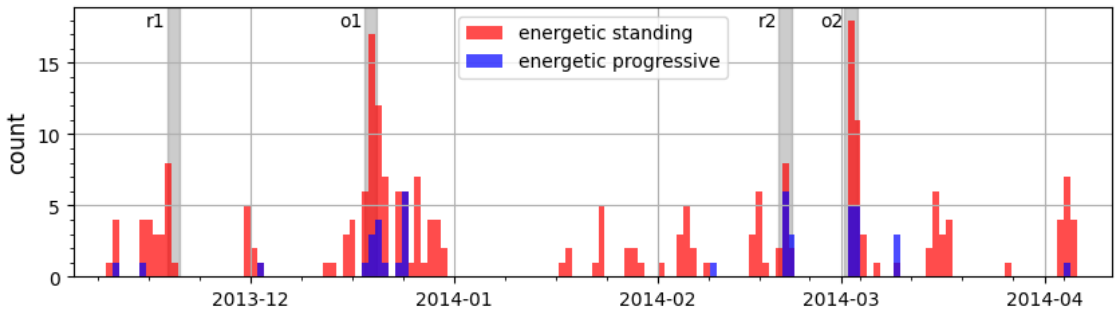

(a) Unweighted occurrence of VLF events.

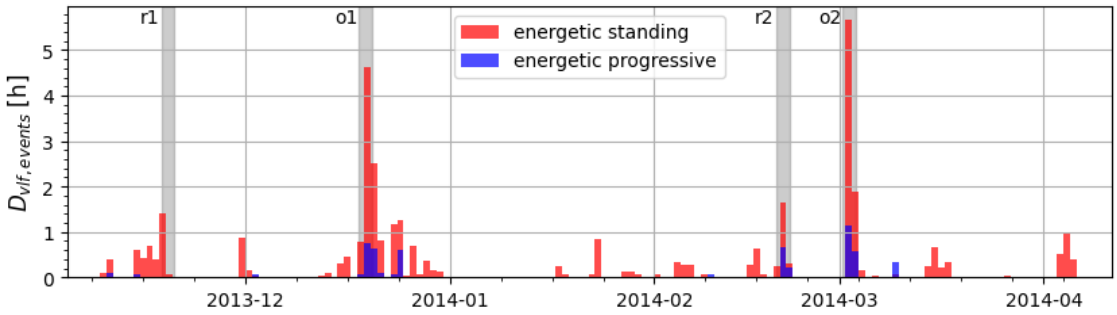

(b) Occurence of VLF events weighted with their duration.

Figure 4.29: Occurence of standing and progressive energetic VLF oscillations. The histograms have a bin width of 24 hours. (a) shows the number of VLF events, which are weighted with the duration of the VLF events in (b). Multiple 48-hour segments are marked in light grey, indicating periods of overwash (o1, o2) or large runup (r1, r2).

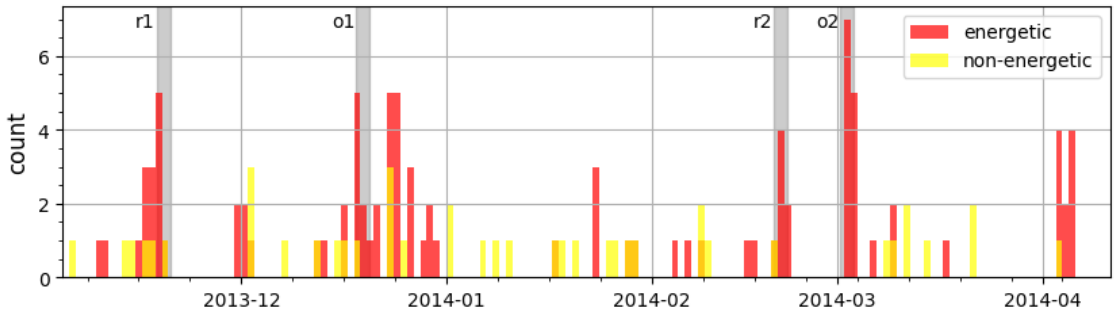

(a) Occurrence of resonance.

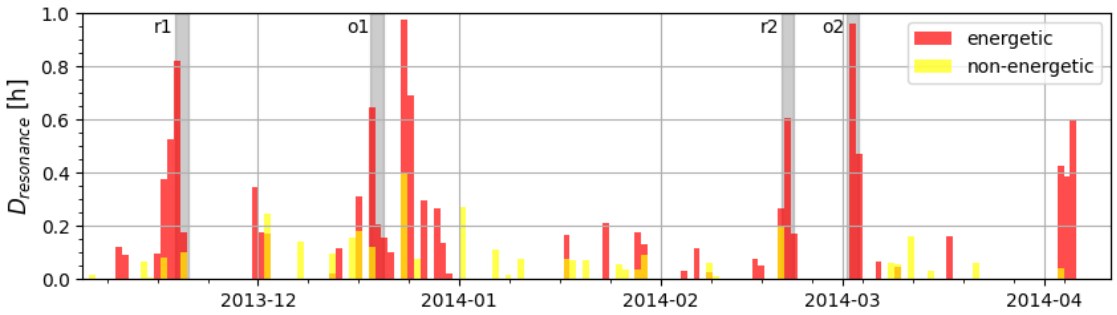

(b) Resonance duration.

Figure 4.30: Occurence of energetic and non-energetic resonant VLF oscillations. The histograms have a bin width of 24 hours. (a) shows the number of VLF events, which are weighted with the duration of the VLF events in (b). Multiple 48-hour segments are marked in light grey, indicating periods of overwash (o1, o2) or large runup (r1, r2).

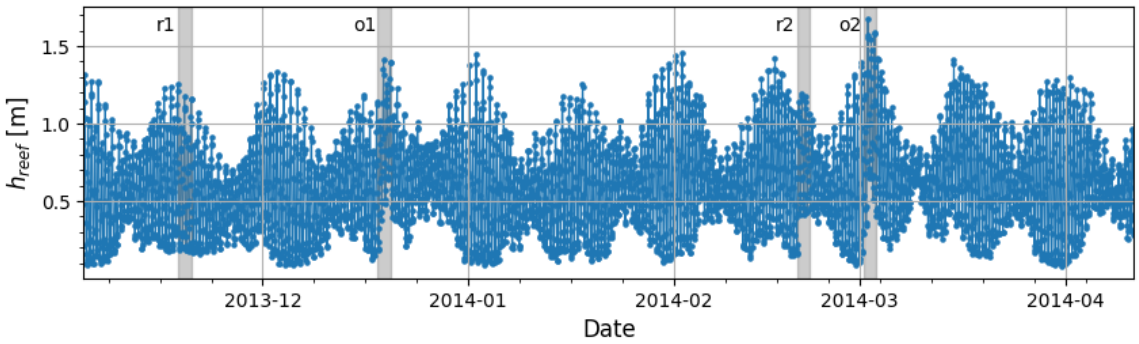

(a) Tidal levels.

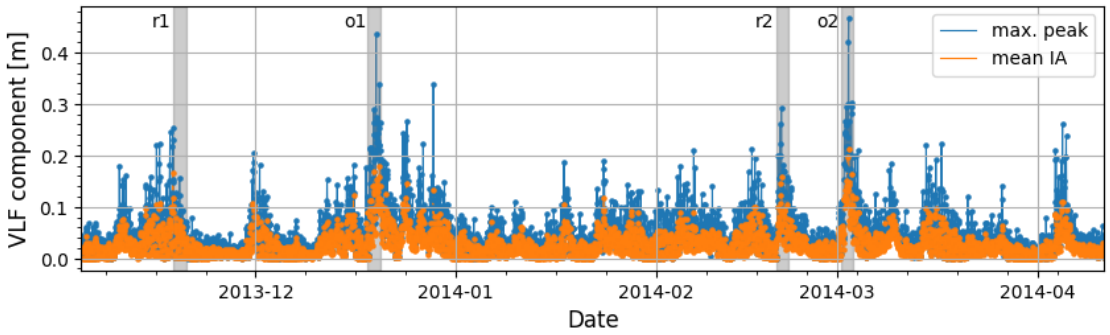

(b) Significant wave height at fore reef.

Figure 4.31: The (a) reef flat water depth and (b) intensity of inner reef VLF component. Multiple 48-hour segments are marked in light grey, indicating periods of overwash (o1, o2) or large runup (r1, r2).

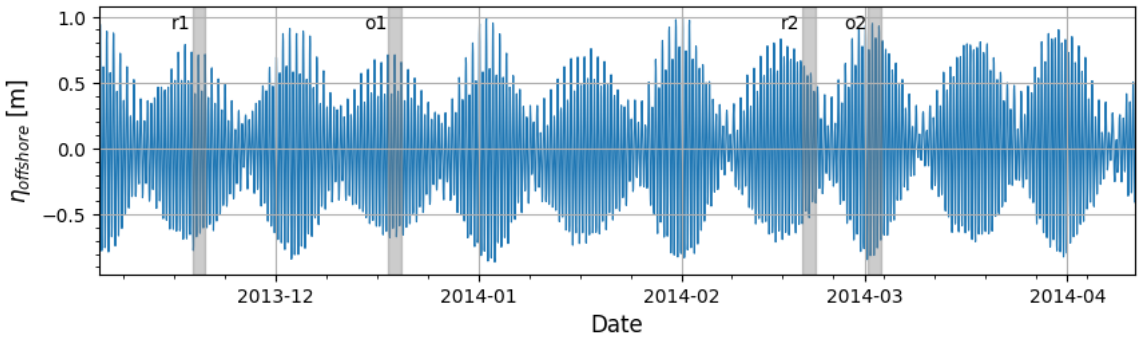

(a) Tidal levels.

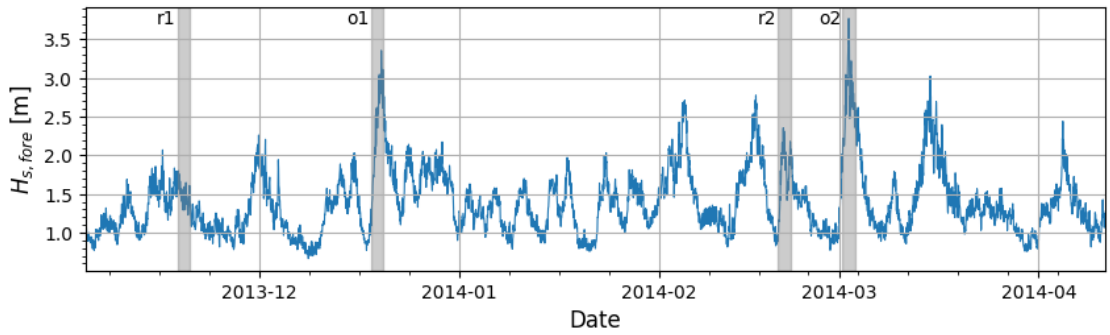

(b) Significant wave height at fore reef.

Figure 4.32: (a) Tidal level ($\eta_{offshore}$) and (b) significant wave height at fore reef ($H_{s,inner}$). Multiple 48-hour segments are marked in light grey, indicating periods of overwash (o1, o2) or large runup (r1, r2).

Section summary

The duration and intensity of energetic (amplitude $>$ 0.12 m) VLF events were analysed, showing median **durations of 5.4 and 4.8 minutes** for standing and progressive oscillations respectively. **Some standing oscillations reached much longer durations** with a 90th percentile duration of 14.1 minutes, whereas the 90th percentile duration for progressive oscillations was 10.3 minutes. Furthermore, **the energetic VLF events were found to have longer durations under resonant conditions**.

The duration of resonance events was in a similar range as the duration of VLF events, with a maximum duration of around 800 seconds (13.3 minutes). Normalising the resonance event durations with the period corresponding to $f_{p,transfer}$ shows that the resonance events had a duration of **up to 3 times the wave period**. Some events exhibited a **resonance duration shorter than one wave period**, which is an unexpected result. The shorter durations of resonance are associated with lower values of $normE_{p,transfer}$.

Relation of VLF and resonance event durations to reported overwash and runup events showed that **the two overwash events corresponded with a duration of approximately 5 hours of VLF events and more than 0.6 hours of resonance** within a recording period of 24 hours. Two anomalies were observed when a significant duration of resonance events did not result in substantial runup (at least, not reported). **The distributions of the duration of energetic and resonant VLF oscillations suggest that the durations of VLF events may be a more relevant indicator for (the severity of) coastal flooding events than the duration of resonance**.

Additionally, the **water level appears to be an important factor**, as water levels were higher for the more severe March overwash event compared to the December overwash event.

5 Discussion

In this section, the limitations and challenges of the methodologies are discussed, as well as the significance of the results. Furthermore, the findings of this study will be discussed in light of the bigger picture of coral reefs and their challenges regarding coastal hazards.

5.1. Empirical Mode Decomposition

The application of the Hilbert-Huang transform is what sets this study apart from most other research that has been conducted regarding coral reef hydrodynamics and resonance specifically. Contrary to the traditional Fourier analysis, the HHT can capture non-stationarity and nonlinearity by preserving the time-variability of a wave signal. This makes it possible to obtain valuable information about the transience of various processes such as coral reef resonance. However, there are limitations to the HHT, which should be considered when applying this method. Most of these limitations are a result of the lack of a rigorous mathematical foundation for the Empirical Mode Decomposition compared to other signal processing techniques.

5.1.1. Orthogonality and performance indices

Orthogonality is an important characteristic of an accurate and useful decomposition, as it implies the independence between extracted components. While the orthogonality of intrinsic mode functions is fulfilled in the practical sense, it is not guaranteed theoretically (Huang et al., 1998). The absence of an orthogonal decomposition theory poses a significant challenge and constraints for the applicability of the EMD (Niu et al., 2021).

To assess the orthogonality of decompositions, various metrics have been used. Because there is an absence of a comprehensive theoretical foundation for EMD, this hinders a theoretical analysis and performance evaluation (Deléchelle et al., 2005). However, some metrics are commonly applied in research, namely the Index of Orthogonality (IO), and measures of orthogonality (IO_{ij}) and correlation (ρ) between IMFs. Higher values of these indices suggest a lower degree of orthogonality.

It is important to note that orthogonality is inherently a local quality and should ideally be evaluated using local and scale-dependent metrics (Mandic et al., 2013). The performance indices employed here are defined globally and may thus offer limited insights. These limitations should be considered for the interpretation of the performance scores. Moreover, the absence of defined thresholds discerning good or bad decomposition performances calls for a comparative assessment between the different configurations.

5.1.2. Mode mixing and the masking EMD

The edge effects and mode mixing are two main challenges of the EMD, both of which have been observed through visual inspection of decompositions, see Section 4.1. Mode mixing occurs when the decomposition is unable to group signals with similar frequencies in distinct components (de Souza et al., 2022). The original EMD is found to result in distorted IMFs caused by mode mixing, making it difficult to interpret the results accurately. Despite this issue being recognised by numerous studies (de Souza et al., 2022), the original EMD is a common decomposition approach used in ocean and coastal wave research (e.g., Senthilkumar et al., 2015; Veltcheva and Soares, 2016; He et al., 2022). Others have considered the Ensemble EMD (EEMD) or Complete Ensemble EMD (CEEMD) as well (Yin et al., 2014; Mandal et al., 2020). The EEMD and CEEMD

are noise-assisted decomposition methods and were proposed to reduce mode mixing (de Souza et al., 2022). Another extended version of the EMD is the masking EMD (M-EMD) which mitigates mode mixing by adding a masking signal with a similar frequency to the component targeted for extraction, to overcome intermittency. A comparative study for the decomposition of an electroencephalogram signal concluded that the M-EMD performs better than the EEMD and EMD regarding mode mixing (Ho & Hung, 2020).

Mode mixing poses limitations for several methods used in this study, particularly regarding the extraction of the dominant VLF oscillation component and its subsequent analyses. Extensive analysis was conducted, via both case-specific and general evaluation, to assess the performance of various EMD configurations and suitability within the scope of this study. Subsequently, the M-EMD method emerged as the most appropriate choice, because of its effective mitigation of mode mixing.

However, it is important to acknowledge some drawbacks of M-EMD. One challenge arises from the fact that the target frequency is often not known beforehand. When the masking signal and the input signal share similar frequency scales, their interaction may induce mode splitting, potentially resulting in residual noise (Y.-H. Wang et al., 2018).

Mode splitting has been quantified using the pseudo-mode splitting index (PMSI). Evaluation of this metric revealed that M-EMD showed relatively poorer performance compared to other sifting configurations. However, there is no definitive threshold to discern good or bad scores for the PMSI. For instance, Y.-H. Wang et al. (2018) reported PMSI values as high as 0.3, indicating more severe mode splitting, whereas this study found median PMSI values for the default M-EMD configuration of 0.053 and 0.079 for the fore and inner reef signal decompositions, respectively (see Tables A.3 and A.4 in Appendix A).

Visual inspection revealed the occurrence of both mode mixing and mode splitting. While mode mixing results in frequency overlap of components, mode splitting refers to the splitting of a single oscillation over multiple components, potentially leading to underestimation of oscillation amplitudes. Given that extracting the complete VLF oscillation into a single component is a crucial aspect of this study, it is essential to minimise mode mixing. While the M-EMD may display mode splitting, mode mixing is dominant for the EMD. Both have been observed for the EEMD and CEEMD decompositions.

Although the M-EMD produces IMFs with narrow-band frequencies, being comparable to Fourier decomposition in this regard, this characteristic may not always represent the physical oscillations accurately. Additionally, the introduction of masking signals (which are linear harmonics) can influence the extracted waveform. Consequently, the M-EMD would perform relatively poorer in waveform analysis compared to methods such as the iM-EMD. However, visual inspection suggests that M-EMD most consistently captures the visually identifiable continuous VLF oscillation in a single component, which is the most relevant feature for this study. Furthermore, the scores of orthogonality and correlation between IMFs were examined to evaluate the quality of the decomposition, especially when applying the M-EMD. Performance values indicated a comparable performance to other sifting approaches, as indicated in Table 4.2.

5.1.3. Suggestions for further research and application

Numerous additions to the EMD have been proposed to improve its accuracy and applicability. Some recent developments are discussed briefly.

The iterated masking EMD (iM-EMD), introduced by Fabus et al. (2021), extends the M-EMD approach by optimising masking signal frequencies based on oscillation amplitudes. The iM-EMD allows for a varying phase in the masking signal, which could potentially enhance the extraction of nonlinear waveforms. The iM-EMD has been applied in this study, showing promising results. However, the computational demands formed an obstacle in applying this sifting procedure to all data.

Additionally, there are other proposed extensions that have not been assessed in this study, due to their absence in the `EMD` Python package. In the integral mean mode decomposition (IMMD) by Niu et al. (2021), the mean value of the envelopes of the signal is replaced by the mean value of the definite integral. This substitution allows for a mathematically precise expression of the mean value, theoretically implying decomposition orthogonality.

Additionally, methods have been suggested to address other challenges. For example, Zare and Nouri (2023) proposed the correlation-based expansion model to mitigate end-effects. This model predicts data beyond the signal boundaries by assessing the similarity between the signal's initial and final segments with its inner segment. Furthermore, various approaches utilising machine learning techniques have been proposed. These techniques include Support Vector Regression Machines (SVRM) with Particle Swarm Optimization (PSO) (W. Wang et al., 2007), SVR to predict two points, a maximum and a minimum at each end for determining the envelopes (Xue et al., 2013), Generalised Regression Neural Network (GRNN) (Lv et al.,

2017), SVR combined with EEMD (G. Liu et al., 2019), and many more (de Souza et al., 2022).

In a comprehensive review of the evolution, challenges and limitations of the HHT, de Souza et al. (2022) highlight the increasing popularity of the HHT and the substantial research efforts dedicated to its theoretical development and practical applications. While progress has been made in addressing limitations such as mode mixing and determination of envelopes, challenges remain, including the need for a rigorous mathematical framework and improved algorithmic adaptability (de Souza et al., 2022).

5.2. VLF wave classification and resonance identification

Following the assessment of the EMD configurations, the M-EMD is employed to separate the various frequency components in the reef signals. Therefore, the challenges addressed in the previous section are relevant to the further methodology steps as well. This section discussed the impact of these limitations on the VLF oscillation classification approach. Furthermore, the methodology of resonance identification is discussed.

5.2.1. Classification of standing and energetic VLF oscillations at the inner reef

Extraction of VLF component

As previously mentioned, the M-EMD exhibits mode splitting where the amplitude of a single oscillation is spread across multiple components. Given that the classification of inner reef signals relies heavily on the oscillation information of the dominant VLF oscillation, mode splitting could potentially affect the resulting classification by underestimating the amplitude of the dominant VLF oscillation. While this issue is acknowledged, no specific measures are taken to evaluate the VLF component in detail. However, visual inspection suggests that the VLF component often aligns well with the inner reef signal.

In the analysis of the VLF wave classification in Section 4.2.3, it was observed that energetic VLF oscillations, particularly standing ones, result in higher significant wave heights at the inner reef ($H_{s,inner}$). Furthermore, a strong linear relation between the mean instantaneous amplitude of the VLF components and the significant wave height of the VLF bandwidth was found, as illustrated in Figure B.31. Although this does not conclusively demonstrate an accurate estimation of the VLF components by the M-EMD, this correlation confirms that higher VLF component amplitudes correspond to higher significant wave heights at the inner reef. To further investigate the accuracy of the VLF components, the correlation between the original signal and the VLF component could be incorporated into the current approach, where the energy content of the components is assessed. When the correlation and energy content are comparable between multiple low-frequency components, additional evaluation should be applied to verify the quality of component separation of the decomposition.

The effect of the M-EMD is evident in the distribution of the median instantaneous frequencies of the dominant VLF components, as illustrated in Figure 4.4a. The mask frequencies of the M-EMD are determined by the highest frequency component in the signals and subsequent mask frequencies are a factor 2 apart. This results in a normal distribution of frequencies of IMF 6 and IMF 7 VLF components around 0.004 Hz and 0.002 Hz respectively. The frequency information is primarily used for spectral analysis through the Hilbert spectrum, where a bandwidth of 0.001 Hz is applied. Figure 4.4b illustrates that the frequency distribution for this resolution is more uniform.

Classification of propagation type

The classification method used to distinguish between progressive and standing oscillations relies on the quality of the selected dominant VLF components, as this ensures an accurate representation of the oscillation waveforms. Phase differences close to $+/-$ 2π are observed, indicating a phase difference of a complete wave oscillation, despite using the unwrapped phase. This highlights waveform inconsistencies between mid reef and inner reef VLF components. Although phase difference "jumps" can be easily addressed, other waveform inconsistencies may go unnoticed due to the bulk analysis nature of the method.

Additionally, the threshold for discerning standing and progressive waves is relatively arbitrary. However, the distinction between propagation types appears satisfactory based on visual inspection and aligns with expectations for the patterns observed in subsequent research steps, as will be discussed later. A 34.7% occurrence of standing VLF oscillations was found by Gawehn et al. (2016) (standing plus resonance wave class), comparable to the 43.1% found in this study.

Through visual inspection, it appears that the distinction between standing and progressive waves is not necessarily binary, but rather shows a transition. For further refinement, the classification of propagation

types may be divided into three categories, discerning a category between standing and progressive waves for a transitional propagation type.

It is also noted that the propagation type of a wave signal may not be constant over a time series. The classification did not account for this aspect because the accuracy of the phase difference per time window may not always be satisfactory due to waveform inaccuracies. Another EMD algorithm, such as the iM-EMD, could perform better in this regard.

The propagation type classification results could be compared to those obtained using the method of Pomeroy et al. (2012a) (see Section 2.4.5) on a time series-specific level. This method, however, does not account for variations in propagation type within a time series, as it is based on Fourier analysis.

Classification of energetic VLF waves

Regarding the distinction between energetic and non-energetic oscillations, the choice of threshold is highly influential on the classification. Alternative thresholds or the distinction of multiple power levels could be explored in future investigations. Furthermore, the choice of threshold influences the resulting energetic VLF event durations.

5.2.2. Resonance identification

The resonance analysis primarily follows the method proposed by Gawehn et al. (2016). This method, while effective, has its challenges, particularly concerning the transfer function and selecting the peak transfer frequency ($f_{p,transfer}$).

Selection of peak transfer frequency

The original Fourier-based approach assumes that the most relevant oscillation has the highest energy transfer. However, this assumption can be inadequate, as shown in Figure B.9 in Appendix B, where two distinct frequencies have similar energy transfers, making the frequency selection arbitrary.

To address this, an alternative method was developed, considering the magnitude of the inner reef energy in addition to a high energy transfer value (defined by the 85th percentile). This approach assumes that a higher inner reef energy is more relevant for assessing resonance, which may not always be accurate. However, more energetic VLF oscillations arguably are physically more relevant since these oscillations pose a higher threat to the shore (as has been demonstrated on several occasions in this and other studies) and still correspond to high energy transfer values.

When comparing the records identified by the original and 85th-percentile approaches, differences stem from the re-evaluated threshold for $normE_{p,transfer}$, based on a resonance occurrence of 3.6%. Maintaining the original threshold value, the 85th-percentile approach would still capture all originally identified resonance cases (Figure B.17a in Appendix B).

The HHT approach also benefits from the 85th-percentile frequency selection. As described in Appendix B, defining the cross-spectrum for computing the transfer function is challenging with the HHT. Unlike Fourier analysis, which provides amplitude and phase information per frequency component, the HHT provides this information per time index for each IMF. This difference requires considering a time lag between the fore and inner reef stations. Additionally, the extracted components from the fore reef envelope and inner reef signal may not contain identical frequency oscillations but rather similar narrow-band frequency ranges. This is crucial when comparing short time windows, as energy might not be 'collected' for each frequency. This is especially relevant for the fore reef envelope, as it potentially leads to zero-division. The 85th-percentile frequency selection helps bypass these inaccuracies by emphasising inner reef energy content, which holds more physical meaning than the cross-spectrum or its derivatives in context of the HHT.

Investigating differences in identified resonance cases by the HHT and FFT approaches (with the 85th-percentile frequency selection), the HHT generally estimates the resonance cases which are identified by FFT but not HHT, to have lower $normE_{p,transfer}$ values, though with similar frequency ratios (Figure B.20b in Appendix B).

Normalisation of inner reef energy

Although selecting $f_{p,transfer}$ through the transfer function approach remains debatable, the normalising of the inner reef and fore reef energy aligns well with the definition of resonance. Particularly, the HHT_{temp} approach, considering short period fore reef energy and subsequent inner reef response, may better describe the amplification between the fore reef envelope and its subsequent inner reef response. The HHT offers new opportunities for a refined approach to the resonance analysis, relating more specific time instances of

inner reef energy to preceding fore reef forcing, making the amplification measure $normE_{p,transfer}$ more meaningful. A potential error in the time lag estimation is expected to have minimal impact on the HHT_{temp} analysis, as the error is expected to be of smaller magnitude than the window size.

Resonance identification for dominant VLF component
As a modification of the HHT_{temp} approach to the resonance analysis, the analysis is conducted for only the inner reef VLF component, referred to with $HHT_{temp,VLF}$. This analysis showed a full agreement of identified resonance compared to the HHT^{temp}. This illustrates that the VLF component indeed represents the fundamental mode of resonance. This result also indicates that there is limited frequency overlap between the low-frequency IMFs, even when using a 0.001 Hz bandwidth, as values for $normE_{p,transfer}$ were mostly the same.

Resonance identification and propagation type
When comparing the results of the resonance identification and propagation type classification, most of the resonance cases correspond to standing oscillations (93.4%). This agrees with the definition of resonance. The few 'progressive' resonant oscillations hardly exceed the resonance threshold and are often found to be standing at the moment of resonance. This indicates that the resonance threshold is at a good location, where virtually all the oscillations are classified as standing.

Suggestions for further research and application
Various choices for aspects of the resonance analysis approach may be revisited for further application. First of all, a sensitivity analysis of the choice of time integration window duration may be conducted. The sensitivity of the frequency bandwidth (0.001 Hz) for the Hilbert spectra may also be investigated. This study used the same bandwidth for the HHT and FFT for consistency. It is pointed out that a finer resolution (perhaps with a logarithmic scale), while providing more detailed frequency information, might pose issues for the current transfer energy computation method. The frequency range of fore reef envelope spectrum used for normalisation for $normE_{p,transfer}$ could be reconsidered. Now, the low-frequency range (0.001-0.04 Hz) is used rather than the VLF range (0.001-0.005 Hz).

Additionally, attempting to identify resonance raises questions about its definition regarding the magnitude and duration of amplification. This study used a practical threshold for $normE_{p,transfer}$, based on the previously suggested resonance occurrence of 3.6% for this dataset. This resonance occurrence was defined by Gawehn et al. (2016) through an extensive sensitivity analysis. This process is not repeated in this study, which is why the 3.6% occurrence is maintained. When the analysis is applied to other data sets and other reef geometries, the resonance occurrence needs to be revisited. Furthermore, in the case of complex reef geometries, unlike the one analysed in this study, the theoretical natural frequency may be challenging to determine. For example, Yao et al. (2019) found that the presence of lagoons influenced the cross-shore free surface elevation of the fundamental resonant mode.

For future research, exploring different methods to determine energy transfer within HHT is recommended. Despite extensive efforts to find alternative approaches defining energy transfer as a function of frequency, these attempts were unsuccessful. A different approach may shift away from spectral analysis and focus more on wave group definition and characterisation, such as the approach proposed by Veltcheva and Soares (2016).

Lastly, it is noted that the performance of different approaches applied for the resonance analysis is difficult to assess, as no ground truth data is defined for the occurrence of resonance. In conclusion, defining and identifying resonance over a fringing coral reef remains challenging.

5.3. Transient characteristics of energetic and resonant VLF waves

Having discussed the opportunities, challenges, and limitations of the HHT framework for VLF wave classification and resonance identification, this section provides context for interpreting the findings about the transient characteristics of energetic and resonant VLF waves.

The inspection of VLF components of the inner reef signals through the M-EMD and time-frequency analysis via the Hilbert transform enables the exploration of the time-varying behaviour of these oscillations. Energetic VLF events have been identified, of which durations and intensities are analysed. Additionally, a method to specifically assess the duration of resonant VLF oscillations has been proposed.

5.3.1. Energetic VLF events

An energetic VLF event is defined as a VLF oscillation with an amplitude greater than 0.12 m, which corresponds to the 97.5th percentile of all peaks in the inner reef VLF components of the entire dataset. It has been shown that these energetic VLF events are more likely to result in high significant wave heights at the inner reef (see Figure 4.17a), highlighting the importance of understanding their characteristics. Analysis of the observed durations for these energetic VLF events indicates that most events last between 200 and 500 seconds, with some extending to much longer durations. Especially the standing energetics VLF events showed the potential for much longer durations, with a 90th percentile of 14 minutes.

Correlation analysis between the duration and intensity of these VLF events reveals a positive linear relationship, although the correlation is not strong (Pearson correlation coefficient < 0.7), as shown in Figure 4.19. This may be influenced by the event definition, which allows for brief drops below the 0.12 m threshold as long as the duration of these drops is shorter than one wave period of the oscillation. This approach can result in lower mean amplitudes for longer durations but does not affect the maximum peak observed within the VLF event. The sensitivity to the allowable gap between energetic amplitudes may be assessed in further investigations.

The mean instantaneous amplitude shows a stronger correlation (Pearson correlation coefficient of 0.89) with the sum of the duration of VLF events per record, as shown in Figure 4.20. It should be considered that these two variables are not independent, as the VLF duration is defined based on the instantaneous amplitude. Additionally, the sum of VLF event durations shows a strong correlation with the significant wave height at the inner reef, as shown in Figure 4.21a, suggesting that longer energetic VLF events may potentially lead to larger significant wave heights, though, again, this relationship is not independent.

Energetic VLF oscillations and propagation behaviour

Although the reef flat water depth does not seem to be related to the duration of VLF events, there is a distinction between progressive and standing oscillations, as illustrated in Figure 4.21b. This distinction becomes more apparent when analysing the occurrence of energetic VLF events. As can be expected, these VLF events often occur for multiple consecutive hours, potentially provoked by large incoming waves. Moreover, progressive and standing VLF events are not independent events, they often succeed each other. The previously identified relation - that progressive oscillations tend to occur at lower reef water depths - is evident in the occurrence patterns of progressive and standing oscillations, as visualised in Figure 4.22.

The alternating pattern of progressive and standing oscillations may be explained by factors such as increased frictional dissipation at smaller water depths or different reflective behaviours (Gawehn et al., 2016). Greater water depths may allow VLF waves to reflect more, leading to standing oscillations. Furthermore, Gawehn et al. (2016) found that shoreline reflection rarely occurred for progressive-growing VLF waves, attributing this to the nonlinear bore-like shape of the progressive VLF waves. Another reason for the progressive propagative character at smaller water depths could be that the natural frequency of the reef is not reached under these conditions. In the current classification, just two categories for propagation are used, while a transition between standing and progressive oscillations is expected in reality. This may be resolved by introducing an intermediate propagation class.

Regarding the relation between the propagation behaviour of the VLF wave and its intensity and significant wave height at the inner reef, both progressive and standing energetic VLF oscillations display similar trends, with standing VLF oscillations being more energetic on average. The most apparent difference between progressive and standing VLF oscillations is their duration, which tends to be longer for the latter.

Energetic VLF oscillations under resonant conditions

A difference was observed in the duration of VLF events under resonant and non-resonant conditions (for standing VLF waves). Resonant energetic VLF oscillations exhibit longer average and maximum durations, as shown in Figures 4.23 and 4.24 and Table 4.9.

5.3.2. Resonance events

The duration of resonance events has been assessed through the upward and downward crossing of the $normE_{p,transfer}$-threshold. As explained in Section 4.3.2, this led to some resonance edge events being missed as they lacked an upward or downward crossing. The definition of resonance events through crossings of the threshold creates a bias towards shorter durations, as the longest durations were found for edge events, as shown in Figure 4.25b. The edge events durations could also be of very short duration, being cut off by the time series. Because of this, the edge events are not analysed in detail, as they are incomplete. They are

however included in the total duration of resonance per record, primarily for the comparison of the durations to coastal flooding.

Short duration of resonance

The duration of the resonance is relatively short on average, with a median duration of 420 and 251 seconds for energetic and non-energetic resonant oscillations respectively. These are equivalent to 1.7 and 1.0 the duration normalised with $T_{p,transfer}$. Gawehn et al. (2016) pointed out that the resonance for these field observations could indeed be of short duration. Most field data studies do not include notions about the persistence of resonance. However, physical and numerical experiments have suggested a typical build-up behaviour for resonant amplification, see also Section 2.4.3. Nwogu and Demirbilek (2010) and Gaido (2019) observed that 5 and 12 wave periods respectively were needed to reach maximum amplification. Van Noort (2021) however, did not observe this behaviour and maximum amplification was reached within the first wave period.

The shorter durations of resonance observed in this study can be attributed to several factors. Firstly, the method used relies on the inner reef VLF components and the fore reef LF components of the envelope. The IMFs might be influenced by mode-mixing or other EMD-related issues, affecting their accuracy. The choices for resonance identification, e.g., threshold, window durations, and window intervals, also significantly impact the $normE_{p,transfer}$ values over time. A finer spectral bandwidth might more accurately define the peak frequency, though this approach has its own disadvantages, which have been discussed in Section 5.2.2.

Apart from methodological artefacts, the shorter durations could also result from changing conditions at the fore reef. It has been observed in some cases that the inner reef VLF component has a longer duration of an energetic amplitude than the resonance duration, suggesting that changes in the fore reef envelope might influence the resulting resonance duration. If the fore reef envelope remained constant, the resonance might be detected for a longer period. Furthermore, resonance may not have been fully developed because of changing wave forcings at the fore reef, explaining the short duration and lack of build-up. However, this is speculative and requires further investigation into the fore reef forcing to better understand this relationship.

As discussed before, the resonance threshold led to virtually only standing resonant oscillations, thereby separating standing and progressive oscillations effectively. While this threshold may be effective for identifying resonance, it may not accurately reflect the duration of resonance. The initial build-up phase is likely excluded from the duration defined by this threshold. A minimum threshold could be considered to investigate the growth from small to large amplification, although this was not done in this study due to the variability of the cases. Regarding the choice for the resonance threshold, the shorter durations (normalised duration < 1) of resonance corresponded to lower values of the peak $normE_{p,transfer}$, as shown in Figure 4.27.

Final remarks

Although this method depends on various choices, such as the resonance threshold, the 600-second window duration, and the 100-second window interval, it demonstrates the possibility of assigning a duration to resonance events. This feature is highlighted in Figure 4.30, where the unweighted occurrence of resonance per 24 hours of recordings may be up to 7 "hours", while the determined total resonance duration for the same 24 hours is only 1 hour. For further studies, the settings of the resonance analysis may be refined.

One of the significant limitations in studying the build-up and persistence of resonance is the duration of the time series, which is only 34 minutes. As was evident from the analysis, many resonance events were not captured completely, as they were cut off by the length of the time series.

Lastly, the observed durations raise questions about the definition of resonance. Even if a resonant magnitude of amplification is reached, should it be considered resonance if it is highly transient? Further research is needed to investigate how the forcing and conditions differ between long and short durations of resonance.

5.3.3. Relation to coastal flooding

Overwash events

The VLF and resonant event durations were related to observed runup and overwash events. During the December and March overwash events, standing VLF event durations were around 5 hours in 24 hours of recordings, with 0.6 to 1 hour of resonance identified for both cases. Cheriton et al. (2016) noted that reef flat water depth plays an important role in coastal hazards. The March overwash event may have been more severe because of the higher water depths. Additionally, the intensity of the VLF oscillations was slightly

greater for the March overwash events, although not significantly according to Figure 4.28.

Durations of energetic and resonance VLF oscillations as indicators for coastal flooding
The duration of energetic VLF events appears to be a good indicator of the severity of the overwash events, in combination with the reef water depth. For the overwash events, the duration of energetic VLF events was the longest, while there was a much shorter duration for the large runup instances, approximately 1.5 hours.

It is noted that long durations of VLF oscillations are consistent with larger amplitudes, which may be responsible for coastal flooding as much as the duration. Whether the duration or amplitude of energetic VLF oscillations is more responsible for overwash events is difficult to determine as these two quantities are dependent on each other through their definition.

The duration of resonance events does not always indicate coastal flooding. Two anomalies were observed with relatively long durations of resonance but no record of overwash or runup.

While resonance duration itself is not necessarily linked to the severity or occurrence of coastal flooding according to Figure 4.30, it is noted that energetic VLF oscillations are found to have a longer duration (and higher intensity) during resonant conditions, as shown in Figure 4.23 and Table 4.9.

Suggestions for further research and application
The current investigation was conducted for a relatively coarse time scale, with the durations accumulated per 24 hours and the coastal flooding events approximated through a 48-hour time window. The reason for this approach is the unknown details of the occurrence of the reported overwash and runup events.

It would also be interesting to look at the durations of the energetic and resonant oscillations on a more detailed timescale, perhaps looking at the consecutive duration of resonant and energetic VLF oscillations. This may also reveal the contribution of energetic progressive waves to coastal flooding, which have a much shorter duration.

Furthermore, the emphasis in the current analysis was to link duration to coastal flooding, while the magnitude of the VLF oscillations plays a vital role as well. The overwash event showed similar distributions of mean instantaneous amplitude and maximum peak of the VLF component, with the more severe overwash event in March having slightly higher values for the higher percentiles, as illustrated in Figure 4.28. Again, these characteristics may be investigated for a smaller timescale.

Finally, it should be taken into account that only 34 minutes for every hour are recorded, which is why this analysis does not provide a full picture of the waves that occurred.

5.4. Significance of research

Low-lying reef-lined coasts are vulnerable to coastal flooding. Although fringing reefs usually protect coastal communities from moderate storms by dissipating incoming wave energy, they have been documented to exacerbate flooding during strong events with energetic waves (e.g., Roeber and Bricker, 2015). Low-frequency waves play an important role in coastal hazards and tend to dominate nearshore reef flat wave patterns, as demonstrated in this thesis and supported by previous research (e.g., Péquignet et al., 2011; Pomeroy et al., 2012a; Cheriton et al., 2016). Furthermore, low-frequency resonance has been suggested to further exacerbate coastal hazards (e.g., Nwogu and Demirbilek, 2010; Gawehn et al., 2016). Therefore, it is crucial to understand the characteristics of LF oscillations on reef flats.

While many studies have analysed wave transformation and low-frequency waves on fringing coral reefs, few have addressed the transient aspects of these waves. This study explores a previously under-examined characteristic: the duration of energetic VLF and resonant oscillations.

5.4.1. Resonance duration

This research has quantified the duration of resonance, which is new information as no previous studies have indicated the duration of resonance over coral reefs observed in the field. The results suggested a generally short persistence of resonance with a duration of a maximum of 3 wave periods for a resonance event or 5 wave periods per 34-minute time series. A third of resonance events had a duration normalised with its wave period of below 1. This poses a question about the definition of resonance: should a certain amplification be of a minimal duration to be considered resonance? The short durations of resonance may indicate that maximum amplification was not reached.

When relating resonance duration to overwash and runup events, it was observed that long durations of

resonance may have contributed to overwash events. However, resonance was also present at times without significant runup or overwash (at least not reported). Resonance appears to be most relevant during high water levels on the reef flat, combined with long durations of energetic VLF oscillations at the inner reef. Furthermore, no substantial difference in inner reef significant wave height was found for resonance compared to other energetic VLF oscillations.

Despite the constraints of this study, these findings raise the question of whether there is too much emphasis on resonance as non-resonant VLF oscillations may be equally important to coastal hazards. However, if maximum resonant amplification was not reached due to changing wave forcing at the fore reef, more severe amplification of VLF oscillations might be possible.

5.4.2. Coastal hazards and prediction

This research illustrates that reef flat water depth is an important factor in determining whether VLF oscillations are standing or progressive. It was observed that progressive oscillations are typically shorter in duration and of lower intensity. While further investigation into the behaviour of progressive waves is needed, such as the impact of their waveform, their shorter duration and lower amplitude suggest they may be less harmful than longer-duration standing oscillations.

In light of the importance of water level for the occurrence of energetic standing oscillations, sea level rise (SLR) poses an increasing threat. SLR may allow for more forcings to excite resonance by increasing the natural frequency of the reef, as noted before (e.g., Beetham and Kench (2018); Cheriton et al. (2016); Grady et al. (2013)). This study illustrates the contribution of reef flat water depth to standing energetic VLF oscillations (whether resonant or not). Therefore, an increase in water level due to SLR may increase flood risk by promoting the standing wave pattern associated with higher significant wave heights at the inner reef.

Combined with water depth, energetic VLF oscillations seem to be related to flood risk, as they correspond to high inner reef significant wave height. The duration of energetic VLF oscillation appears to be correlated to the occurence and severity of coastal flooding, whereas the duration of resonant oscillations seems to be correlated to a lesser extent. To further improve the prediction of coastal hazards, understanding the factors that influence the duration of energetic (resonant) VLF oscillations is valuable.

5.4.3. The Hilbert-Huang transform

Beyond the results of this research, the Hilbert-Huang transform (HHT) has proven to be valuable for distinguishing the VLF oscillation component, allowing for an in-depth evaluation of this component. It has been used to characterise the duration of VLF and resonant oscillations but may be considered for more applications and research regarding the nonlinear and non-stationary elements of coral reef hydrodynamics. Some recommendations are provided in Chapter 7.

5.4.4. Limitations

Several aspects result in a limitation of the applicability of the results of this study. First of all, the relatively short duration of the time series makes it challenging to capture the full extent of resonance events, which has been demonstrated in Section 4.3.2. The Hilbert-Huang provides the possibility to analyse much longer time series, as no stationarity is required for this approach.

Additionally, it is recognised that the dataset studied is of limited duration, with 5 months of recording during which only two substantial overwash events occurred. Furthermore, the data only concerns one reef geometry. Various geomorphologic controls have been identified in previous research, which may result in different transient behaviours for different reef geomorphologies.

Finally, no 2D aspects of geomorphology or wave processes were considered in this study. The Roi-Namur reef is characterised by a slightly curving coastline and has some variations in reef flat width, but is otherwise relatively alongshore uniform, as shown in Figure 3.2. However, many reefs show a lot of alongshore variation. For example, paleo-stream channels are found to play a role in the locally increased vulnerability of the coast for high runup (Rey, 2019).

Additionally, the angle of incidence and wave directional spread potentially influence the wave dynamics and runup on coral reefs (Veldt, 2019). These aspects may also have contributed to wave dynamics in the current field observation. However, because of the lack of data for these parameters, this has not been included in this study.

6

Conclusion

The aim of this research was to explore the transient characteristics of resonance and energetic VLF oscillations on a fringing coral reef using the Hilbert-Huang transform. This chapter presents the key findings to the research questions listed in Chapter 1. Additionally, the implications and next steps are highlighted.

6.1. Research questions and findings

How can the Hilbert-Huang transform effectively decompose a sea surface elevation signal observed at a coral reef into frequency components to extract the dominant VLF component?
Various Empirical Mode Decomposition approaches have been investigated in this research, illustrating their respective ability to separate frequency components. Although no optimal configuration of the sifting procedure was identified, the masking EMD (M-EMD) proved to be a promising method and most suitable for this research. The main limitation of this approach is the potential for mode splitting, as was described in Chapter 5. However, the VLF component extracted by the M-EMD has proven to represent the dominant VLF oscillation of the inner reef signal well, as was demonstrated through multiple analyses.

How can we define and classify standing and energetic VLF oscillations in an inner reef signal using the Hilbert-Huang transform?
A distinction between standing and progressive VLF oscillations was made to further analyse the difference in their behaviour and occurrence, but also to use this classification as a verification for the resonance identification, as resonance is a type of standing wave. Additionally, the agreement between energetic and resonant oscillations can also be evaluated through this approach.

After the dominant VLF component of the inner reef signal was determined based on its frequency content, its propagation behaviour was defined through the instantaneous phase information provided by the HHT. A combination of a small phase difference between mid and inner reef VLF components in addition to high coherence determined standing oscillations. A combination of various criteria for the phase difference was formed through visual inspection of components and signals. This resulted in 43.1% standing VLF components in the dataset. The distinction between progressive and standing oscillations was consistent with the findings for reef water depths, as standing waves were found to occur for higher water depths while progressive waves were more common during smaller water depths. Energetic oscillations were defined by the exceedance of an amplitude threshold by the instantaneous amplitude, resulting in 6.1% and 1.1% of standing and progressive energetic VLF oscillations in the dataset respectively. The energetic oscillations were shown to be consistent with higher inner reef significant wave heights, making them relevant to investigate further.

How can we define and capture the time-varying characteristics of resonant oscillations over a coral reef with the Hilbert-Huang transform?
The HHT has been applied as a replacement for Fourier spectra to identify resonance. The HHT provided new opportunities to assess resonance for a smaller time window. In this study, windows of 600 seconds (10 minutes) were used to produce marginal spectra for the fore reef envelope and inner reef signal. The time lag between the fore reef and inner reef stations was included to ensure a realistic comparison of the energy-time content of the respective signals. Through this approach, it was possible to assess the duration

of resonance events.

Furthermore, this approach to the resonance analysis was conducted using only the dominant VLF component of the inner reef signal, thereby forcing the peak transfer frequency to be in the frequency range of this component. This modified approach to the time-varying resonance analysis was shown to be consistent in recognising resonant VLF oscillations with the approach using the full set of components. This highlights the efficacy of the selected dominant VLF components in capturing the oscillations containing the fundamental resonance mode.

Through a previously defined resonance occurrence, a threshold for amplification between the inner reef signal and fore reef envelope was determined. Combining the resonance identification with the VLF wave classification, 93.4% of resonance corresponded to a standing oscillation, of which the majority was energetic. Both energetic and resonant oscillations typically have a frequency of around 0.003-0.0045 Hz, corresponding to the higher end of the VLF range.

How do the durations of resonant and energetic VLF oscillations vary, and how does this variation relate to coastal flooding of a shore lined with a fringing coral reef?

Through the instantaneous amplitude and the time-varying resonance analysis of the VLF component, the HHT offered the opportunity to define the duration of energetic and resonant VLF oscillations. The resonance durations and energetic VLF event durations observed in this dataset had an average duration in the order of hundreds of seconds. The median of energetic VLF event durations was 5.4 and 4.8 minutes for standing and progressive oscillations respectively. Additionally, energetic standing VLF oscillations showed longer durations during resonant conditions.

For resonance events, which were defined by the upward and downward crossing of the resonance threshold, the median duration was 6.3 and 4.2 minutes for energetic and non-energetic oscillations respectively. These are normalised with the wave period, resulting in a median of 1.4 and 0.9 normalised duration. It is noted that the shorter (normalised) durations of resonance correspond to a lower value of amplification.

The duration of energetic and resonant VLF oscillations has been compared to the severity of reported overwash and runup events in the period of observations. The standing energetic VLF event durations were especially long (approximately 5 hours) for the December and March overwash events. For these events, the resonance durations were also significant, approximately 1 hour, although similar resonant durations were observed on other occasions for which no significant runup was reported. These observations highlight the importance of the durations of energetic VLF oscillations to coastal hazards, while the durations of resonance events could be less critical. However, these findings could be site-specific or specific for the limited measurement period of 5 months.

6.2. Implications and next steps

The Hilbert-Huang transform proves to be a useful tool in the analysis of time-varying characteristics of VLF oscillations in a sea surface signal recorded on a reef flat. This study demonstrated the possibility of defining standing and resonant oscillations through the products of the HHT. Through the time-varying approach to resonance identification, the persistence of these oscillations could be quantified, which was not done before for field observations where irregular wave fields are typical. Furthermore, this approach provides the possibility to extend the definition of resonance to have a certain duration in addition to having a certain amplification around the natural frequency. While there are limitations to this approach, it offers new insights.

Regarding the occurrence of coastal flooding, a stronger link is made to the duration of energetic VLF oscillations compared to resonant oscillations. However, resonance may contribute to the durations of energetic VLF oscillations. Additionally, it is possible that no maximum resonant amplification was reached in this field data. Analysis of more data and more reef geometries may reveal if longer and/or stronger amplified resonant oscillations occur under different conditions. In this sense, the HHT with the M-EMD and the further methodology used in this study provide a good framework for bulk analysis of field data.

7

Recommendations

In this chapter, some recommendations are given regarding the application of the methodology framework of this study. Some suggestions for modifications and refinements of the current approach were already proposed in the Discussion in Chapter 5. These recommendations included the evaluation of the quality of the extracted VLF components, the addition of a transitional propagation type category, sensitivity analyses to spectral resolution, thresholds and window durations applied in the methodology. This chapter provides several specific recommendations for further research. These recommendations mainly concern subjects where the Hilbert-Huang methodology can be applied.

7.1. Waveform analysis

Gawehn et al. (2016) propose that the shape of VLF waves can impact their reflective behaviour. They suggest using the HHT to investigate these nonlinear wave shapes, as the Fourier Transform is not suitable for this purpose. While the M-EMD method proved effective for the goals of this study, it may be less suitable for capturing non-linearity. For waveform analysis, other EMD approaches, such as the EEMD recommended by Gawehn et al. (2016) or the iterated Masking EMD, which allows for phase shifts in the masking signal, could be considered. These methods may better capture wave asymmetries, as demonstrated in Section 4.1. However, computational periods may be long. Alternatively, more recently developed EMD algorithms, e.g., the ones mentioned in Section 5.1, may be considered.

Investigating wave shape could reveal more characteristics of progressive and bore-like VLF waves and their differing behaviours from standing waves. A bore-like LF waves have been suggested to cause severe impact at the shoreline (e.g., Roeber and Bricker, 2015; Shimozono et al., 2015; Cheriton et al., 2020). The HHT could be used to investigate the development of these waves over time. Additionally, the HHT is more suitable for analysing non-linear signals than the FFT.

7.2. VLF and IG waves

Building on this, the relationship between VLF and IG wave energies could be further explored using the Hilbert-Huang approach. Large VLF waves have been posited to support IG bore merging over a reef flat, exacerbating coastal hazards further (Cheriton et al., 2020), which they also observed for the Roi-Namur reef that has been the subject of this study. Furthermore, the relation between the fundamental and first mode of resonance may be investigated. From the patterns of the resonance diagram for the temporal analysis, illustrated in Figure B.23, it appears that the modes of resonance both occur for energetic standing VLF oscillations and perhaps alternate within a time series.

If both the VLF and IG wave oscillations are successfully extracted from the signal, their interactions could be analysed. The HHT may reveal the variation of this interaction over time, and can capture non-linearity within the frequency components.

7.3. Fore reef forcing analysis

The relationship between the durations of VLF events and incident forcing should be further investigated in order to improve the prediction of their occurrence. The wave envelope method using the Hilbert Transform

or other wave group methodologies utilising the HHT could be useful for this. Veltcheva and Soares (2016) propose a method for identifying wave groups using an energy threshold to mark the start of a new wave group. Previous research by Van Noort (2021) suggested the importance of wave group modulation of the incident forcing, revealing that greater modulation is a key factor in low-frequency wave energy generation at the fore reef. While this study focused on bichromatic waves, distinguishing wave groups in irregular wave fields is more challenging. The HHT may therefore be a good approach in recognising wave groups and characterising their modulation.

Furthermore, the HHT has been applied to predicting the onset of wave breaking in finite water depths by He et al. (2022). Wave breaking occurrence was investigated in terms of normalised instantaneous frequency. As the breakpoint mechanism is crucial for generating low-frequency waves on coral reefs (Pomeroy et al., 2012a), predicting the breaking of wave groups on the fore reef could be valuable.

Gaido (2019) conducted a numerical study on resonance behaviour over a schematised coral reef and found that resonance exhibits a build-up behaviour, requiring a minimum number of waves to achieve final resonant amplification. This study used regular low-frequency wave forcings. It is challenging to identify similar build-up behaviour in irregular wave fields from field data. However, analysing the duration of incoming forcing could reveal patterns in the development of resonance. Larger amplifications might be achieved through resonant modes when forced for a sufficiently long duration with the right conditions.

7.4. Broader application

Analysing data from other reefs is recommended to determine if the findings from the Roi-Namur reef apply to other reef systems or are site-specific. The Roi-Namur reef is relatively narrow and smooth, making it susceptible to resonant oscillations. Different reef geometries may influence the occurrence and duration of energetic VLF and resonant oscillations differently from the relationships observed in this dataset. Various geomorphic controls have been identified for extreme runup on reef-lined coastlines, e.g., fore reef slope, reef flat submergence, reef flat width and bed slope (e.g., Quataert et al., 2015; Pearson et al., 2017; Yao et al. (2019); Cheriton et al., 2020). Furthermore, the influence of alongshore variability on the resonance response may be investigated as well as 2D aspects of wave processes, such as angle of incidence, wave directional spread and currents.

Additionally, the HHT allows for analysis of longer time recordings, as it does not require a stationarity assumption. The analysis of longer time series could provide more insights into the durations of (resonant) VLF oscillations, which are cut short in the current 34-minute records.

References

Battjes, J., Bakkenes, H., Janssen, T., & van Dongeren, A. R. (2004). Shoaling of subharmonic gravity waves. *Journal of Geophysical Research: Oceans*, *109*(C2).

Becker, J. M., Merrifield, M. A., & Ford, M. (2014). Water level effects on breaking wave setup for Pacific Island fringing reefs. *Journal of Geophysical Research: Oceans*, *119*(2), 914–932.

Beetham, E., & Kench, P. (2018). Predicting wave overtopping thresholds on coral reef-island shorelines with future sea-level rise. *Nature communications*, *9*(1), 3997.

Bertin, X., de Bakker, A., Van Dongeren, A., Coco, G., André, G., Ardhuin, F., Bonneton, P., Bouchette, F., Castelle, B., Crawford, W. C., et al. (2018). Infragravity waves: From driving mechanisms to impacts. *Earth-Science Reviews*, *177*, 774–799.

Bosboom, J., & Stive, M. J. (2021). Coastal dynamics.

Bruch, W., Cordier, E., Floc'h, F., & Pearson, S. G. (2022). Water level modulation of wave transformation, setup and runup over la saline fringing reef. *Journal of Geophysical Research: Oceans*, *127*(7), e2022JC018570.

Buckley, M. L., Lowe, R. J., Hansen, J. E., van Dongeren, A. R., & Storlazzi, C. D. (2018). Mechanisms of wave-driven water level variability on reef-fringed coastlines. *Journal of Geophysical Research: Oceans*, *123*(5), 3811–3831.

Burke, L., & Spalding, M. (2022). Shoreline protection by the worlds coral reefs: Mapping the benefits to people, assets, and infrastructure. *Marine Policy*, *146*, 105311.

Chen, H., Jiang, D., Tang, X., & Mao, H. (2019). Evolution of irregular wave shape over a fringing reef flat. *Ocean engineering*, *192*, 106544.

Cheriton, O. M., Storlazzi, C. D., & Rosenberger, K. J. (2016). Observations of wave transformation over a fringing coral reef and the importance of low-frequency waves and offshore water levels to runup, overwash, and coastal flooding. *Journal of Geophysical Research: Oceans*, *121*(5), 3121–3140.

Cheriton, O. M., Storlazzi, C. D., & Rosenberger, K. J. (2020). In situ observations of wave transformation and infragravity bore development across reef flats of varying geomorphology. *Frontiers in Marine Science*, *7*, 351.

Cohen, L. (1995). *Time-frequency analysis* (Vol. 778). Prentice Hall PTR Englewood Cliffs.

Daqian, R., Zhaorong, W., & Gongbiao, Y. (2007). Evaluation of the EMD end effect and a window based method to improve EMD. *Manufacturing automation*, *29*(1), 21–24.

Dätig, M., & Schlurmann, T. (2004). Performance and limitations of the Hilbert–Huang transformation (HHT) with an application to irregular water waves. *Ocean Engineering*, *31*(14-15), 1783–1834.

De Bakker, A., Tissier, M., & Ruessink, B. (2014). Shoreline dissipation of infragravity waves. *Continental Shelf Research*, *72*, 73–82.

Deering, R., & Kaiser, J. (2005). The use of a masking signal to improve empirical mode decomposition. *Proceedings. (ICASSP '05). IEEE International Conference on Acoustics, Speech, and Signal Processing, 2005.*, *4*, iv/485–iv/488 Vol. 4. https://doi.org/10.1109/ICASSP.2005.1416051

Dehghan, Y., Sadrinasab, M., & Chegini, V. (2022). Empirical Mode Decomposition and Fourier analysis of Caspian Sea level's time series. *Ocean Engineering*, *252*, 111114.

Deléchelle, E., Lemoine, J., & Niang, O. (2005). Empirical mode decomposition: An analytical approach for sifting process. *IEEE Signal Processing Letters*, *12*(11), 764–767.

de Souza, U. B., Escola, J. P. L., & da Cunha Brito, L. (2022). A survey on Hilbert-Huang transform: Evolution, challenges and solutions. *Digital Signal Processing*, *120*, 103292.

Elliff, C. I., & Silva, I. R. (2017). Coral reefs as the first line of defense: Shoreline protection in face of climate change. *Marine environmental research*, *127*, 148–154.

Fabus, M. S., Quinn, A. J., Warnaby, C. E., & Woolrich, M. W. (2021). Automatic decomposition of electrophysiological data into distinct nonsinusoidal oscillatory modes. *Journal of Neurophysiology*, *126*(5), 1670–1684.

Ferrario, F., Beck, M. W., Storlazzi, C. D., Micheli, F., Shepard, C. C., & Airoldi, L. (2014). The effectiveness of coral reefs for coastal hazard risk reduction and adaptation. *Nature communications*, *5*(1), 3794.

Field, M. E., Cochran, S. A., & Evans, K. R. (2002). U.S. Coral ReefsImperiled National Treasures.

Fourier, J. B. J. (1888). *Théorie analytique de la chaleur* (Vol. 1). Gauthier-Villars.

Gaido, C. (2019). Dynamics of resonant low-frequency waves over a schematized fringing coral reef.

Gawehn, M., van Dongeren, A., van Rooijen, A., Storlazzi, C. D., Cheriton, O. M., & Reniers, A. (2016). Identification and classification of very low frequency waves on a coral reef flat. *Journal of Geophysical Research: Oceans*, *121*(10), 7560–7574.

Gerritsen, F. (1980). Wave attenuation and wave set-up on a coastal reef. In *Coastal engineering 1980* (pp. 444–461).

Grady, A., Moore, L., Storlazzi, C. D., Elias, E., & Reidenbach, M. (2013). The influence of sea level rise and changes in fringing reef morphology on gradients in alongshore sediment transport. *Geophysical Research Letters*, *40*(12), 3096–3101.

He, Y., Ma, Y., Mao, H., Dong, G., & Ma, X. (2022). Predicting the breaking onset of wave groups in finite water depths based on the Hilbert-Huang transform method. *Ocean Engineering*, *247*, 110733.

Henderson, S. M., Elgar, S., & Bowen, A. (2001). Observations of surf beat propagation and energetics. In *Coastal engineering 2000* (pp. 1412–1421).

Herbers, T., & Burton, M. (1997). Nonlinear shoaling of directionally spread waves on a beach. *Journal of Geophysical Research: Oceans*, *102*(C9), 21101–21114.

Herbers, T., Elgar, S., & Guza, R. (1995). Generation and propagation of infragravity waves. *Journal of Geophysical Research: Oceans*, *100*(C12), 24863–24872.

Ho, R., & Hung, K. (2020). A comparative investigation of mode mixing in EEG decomposition using EMD, EEMD and M-EMD. *2020 IEEE 10th Symposium on Computer Applications & Industrial Electronics (ISCAIE)*, 203–210.

Hoeke, R. K., McInnes, K. L., Kruger, J. C., McNaught, R. J., Hunter, J. R., & Smithers, S. G. (2013). Widespread inundation of Pacific islands triggered by distant-source wind-waves. *Global and Planetary Change*, *108*, 128–138.

Holthuijsen, L. H. (2010). *Waves in oceanic and coastal waters*. Cambridge university press.

Huang, N. E. (2005). *Computing instantaneous frequency by normalizing Hilbert transform* (US6901353B1).

Huang, N. E., Shen, Z., & Long, S. R. (1999). A new view of nonlinear water waves: the Hilbert spectrum. *Annual review of fluid mechanics*, *31*(1), 417–457.

Huang, N. E., Shen, Z., Long, S. R., Wu, M. C., Shih, H. H., Zheng, Q., Yen, N.-C., Tung, C. C., & Liu, H. H. (1998). The empirical mode decomposition and the Hilbert spectrum for nonlinear and non-stationary time series analysis. *Proceedings of the Royal Society of London. Series A: mathematical, physical and engineering sciences*, *454*(1971), 903–995.

Huang, N. E., Shih, H. H., Shen, Z., Long, S. R., & Fan, K. L. (2000). The ages of large amplitude coastal seiches on the Caribbean Coast of Puerto Rico. *Journal of Physical Oceanography*, *30*(8), 2001–2012.

Huang, N. E., Wu, M.-L. C., Long, S. R., Shen, S. S., Qu, W., Gloersen, P., & Fan, K. L. (2003). A confidence limit for the empirical mode decomposition and Hilbert spectral analysis. *Proceedings of the Royal Society of London. Series A: Mathematical, Physical and Engineering Sciences*, *459*(2037), 2317–2345.

Huijsmans, R., Maris, J., & Christou, M. (2012). Investigating the use of the hilbert-huang transform for the analysis of freak waves. *asme 2012 31st international conference on ocean, offshore and arctic engineering, rio de janeiro, brazil*, 1–12.

Hwang, P. A., Huang, N. E., & Wang, D. W. (2003). A note on analyzing nonlinear and nonstationary ocean wave data. *Applied Ocean Research*, *25*(4), 187–193.

Hwang, P. A., Huang, N. E., Wang, D. W., & Kaihatu, J. M. (2005). Hilbert spectra of nonlinear ocean waves. In *Hilbert-huang transform and its applications* (pp. 211–225). World Scientific.

ISS Astronaut. (2020). *Reefs of new caledonia*. NASA Earth Observatory. https://earthobservatory.nasa.gov/images/149880/reefs-of-new-caledonia

Janssen, T., Battjes, J., & Van Dongeren, A. (2003). Long waves induced by short-wave groups over a sloping bottom. *Journal of Geophysical Research: Oceans*, *108*(C8).

Klaver, S. (2018). Modelling the effects of excavation pits on fringing reefs.

Laszuk, D., Cadenas, O., & Nasuto, S. J. (2015). Objective empirical mode decomposition metric. *2015 38th International Conference on Telecommunications and Signal Processing (TSP)*, 504–507.

Lin, D.-C., Guo, Z.-L., An, F.-P., & Zeng, F.-L. (2012). Elimination of end effects in empirical mode decomposition by mirror image coupled with support vector regression. *Mechanical Systems and Signal Processing*, *31*, 13–28.

Liu, G., Hu, X., Wang, E., Zhou, G., Cai, J., & Zhang, S. (2019). SVR-EEMD: an improved EEMD method based on support vector regression extension in PPG signal denoising. *Computational and Mathematical Methods in Medicine*, *2019*.

Liu, Y., Yao, Y., Liao, Z., Li, S., Zhang, C., & Zou, Q. (2023). Fully nonlinear investigation on energy transfer between long waves and short-wave groups over a reef. *Coastal Engineering*, *179*, 104240.

Lowe, R. J., Falter, J. L., Bandet, M. D., Pawlak, G., Atkinson, M. J., Monismith, S. G., & Koseff, J. R. (2005). Spectral wave dissipation over a barrier reef. *Journal of Geophysical Research: Oceans*, *110*(C4).

Lu, C., Zheng, Z., & Wang, S. (2020). Degradation status recognition of axial piston pumps under variable conditions based on improved information entropy and gaussian mixture models. *Processes*, *8*(9), 1084.

Lv, C., Zhao, J., Wu, C., Guo, T., & Chen, H. (2017). Optimization of the end effect of Hilbert-Huang transform (HHT). *Chinese Journal of Mechanical Engineering*, *30*, 732–745.

Mandal, S., Nair, M. A., & Kumar, V. S. (2020). Hilbert-Huang transform analysis of surface wavefield under tropical cyclone Hudhud. *Applied Ocean Research*, *101*, 102269.

Mandic, D. P., Ur Rehman, N., Wu, Z., & Huang, N. E. (2013). Empirical mode decomposition-based time-frequency analysis of multivariate signals: The power of adaptive data analysis. *IEEE signal processing magazine*, *30*(6), 74–86.

Masselink, G., Tuck, M., McCall, R., van Dongeren, A., Ford, M., & Kench, P. (2019). Physical and numerical modeling of infragravity wave generation and transformation on coral reef platforms. *Journal of Geophysical Research: Oceans*, *124*(3), 1410–1433.

Merrifield, M., Becker, J., Ford, M., & Yao, Y. (2014). Observations and estimates of wave-driven water level extremes at the Marshall Islands. *Geophysical Research Letters*, *41*(20), 7245–7253.

Niu, X.-d., Lu, L.-r., Wang, J., Han, X.-c., Li, X., & Wang, L.-m. (2021). An improved empirical mode decomposition based on local integral mean and its application in signal processing. *Mathematical Problems in Engineering*, *2021*, 1–30.

NOAA. (2023). In what types of water do corals live?

NOAA. (2024). What are the three main types of coral reefs?

Nwogu, O., & Demirbilek, Z. (2010). Infragravity wave motions and runup over shallow fringing reefs. *Journal of waterway, port, coastal, and ocean engineering*, *136*(6), 295–305.

Ortega, J., & Smith, G. H. (2009). Hilbert–Huang transform analysis of storm waves. *Applied Ocean Research*, *31*(3), 212–219.

Pearson, S. G. (2016). Predicting wave-induced flooding on low-lying tropical islands using a bayesian network.

Pearson, S. G., Storlazzi, C. D., Van Dongeren, A., Tissier, M., & Reniers, A. (2017). A Bayesian-based system to assess wave-driven flooding hazards on coral reef-lined coasts. *Journal of Geophysical Research: Oceans*, *122*(12), 10099–10117.

Péquignet, A.-C., Becker, J. M., Merrifield, M., & Boc, S. (2011). The dissipation of wind wave energy across a fringing reef at Ipan, Guam. *Coral Reefs*, *30*, 71–82.

Péquignet, A.-C., Becker, J. M., & Merrifield, M. A. (2014). Energy transfer between wind waves and low-frequency oscillations on a fringing reef, Ipan, Guam. *Journal of Geophysical Research: Oceans*, *119*(10), 6709–6724.

Péquignet, A.-C., Becker, J. M., Merrifield, M. A., & Aucan, J. (2009). Forcing of resonant modes on a fringing reef during tropical storm Man-Yi. *Geophysical Research Letters*, *36*(3).

Pomeroy, A. W. M., Lowe, R., Symonds, G., Van Dongeren, A., & Moore, C. (2012b). The dynamics of infragravity wave transformation over a fringing reef. *Journal of Geophysical Research: Oceans*, *117*(C11).

Pomeroy, A. W. M., Lowe, R. J., Van Dongeren, A. R., Ghisalberti, M., Bodde, W., & Roelvink, D. (2015). Spectral wave-driven sediment transport across a fringing reef. *Coastal Engineering*, *98*, 78–94.

Pomeroy, A. W. M., Van Dongeren, A., Lowe, R., de Vries, J. v. T., & Roelvink, J. (2012a). Low frequency wave resonance in fringing reef environments. *Coastal Engineering Proceedings*, (33), 25–25.

Quataert, E., Storlazzi, C., Van Rooijen, A., Cheriton, O., & Van Dongeren, A. (2015). The influence of coral reefs and climate change on wave-driven flooding of tropical coastlines. *Geophysical Research Letters*, *42*(15), 6407–6415.

Quinn, A. J. (2022). *emd Documentation, Release 0.6.dev0*.

Quinn, A. J., Lopes-dos-Santos, V., Dupret, D., Nobre, A. C., & Woolrich, M. W. (2021). EMD: Empirical mode decomposition and Hilbert-Huang spectral analyses in Python. *Journal of open source software*, *6*(59).

Rabinovich, A. B. (2010). Seiches and harbor oscillations. In *Handbook of coastal and ocean engineering* (pp. 193–236). World Scientific.

Rey, A. (2019). Wave runup on fringing reefs with paleo-stream channels.

Riemenschneider, S., Liu, B., Xu, Y., & Huang, N. E. (2014). B-spline based empirical mode decomposition. In *Hilbert–huang transform and its applications* (pp. 69–97). World Scientific.

Rilling, G., Flandrin, P., Goncalves, P., et al. (2003). On empirical mode decomposition and its algorithms. *IEEE-EURASIP workshop on nonlinear signal and image processing*, *3*(3), 8–11.

Roeber, V., & Bricker, J. D. (2015). Destructive tsunami-like wave generated by surf beat over a coral reef during Typhoon Haiyan. *Nature communications*, *6*(1), 7854.

Rogers, J. S., Monismith, S. G., Feddersen, F., & Storlazzi, C. D. (2013). Hydrodynamics of spur and groove formations on a coral reef. *Journal of Geophysical Research: Oceans*, *118*(6), 3059–3073.

Schimmel, M., Stutzmann, E., & Gallart, J. (2011). Using instantaneous phase coherence for signal extraction from ambient noise data at a local to a global scale. *Geophysical Journal International*, *184*(1), 494–506.

Schlurmann, T. (2002). Spectral analysis of nonlinear water waves based on the Hilbert-Huang transformation. *J. Offshore Mech. Arct. Eng.*, *124*(1), 22–27.

Schlurmann, T., Bleck, M., & Oumeraci, H. (2003). Wave transformation at artificial reefs described by the Hilbert-Huang transformation (HHT). In *Coastal engineering 2002: Solving coastal conundrums* (pp. 1791–1803). World Scientific.

Senthilkumar, R., Romolo, A., Fiamma, V., Arena, F., & Murali, K. (2015). Analysis of wave groups in crossing seas using Hilbert Huang Transformation. *Procedia Engineering*, *116*, 1042–1049.

Shan, X., Huo, S., Yang, L., Cao, J., Zou, J., Chen, L., Sarrigiannis, P. G., & Zhao, Y. (2021). A Revised Hilbert-Huang Transformation to Track Non-Stationary Association of Electroencephalography Signals. *IEEE Transactions on Neural Systems and Rehabilitation Engineering*, *29*, 841–851. https://doi.org/10.1109/TNSRE.2021.3076311

Shimozono, T., Tajima, Y., Kennedy, A. B., Nobuoka, H., Sasaki, J., & Sato, S. (2015). Combined infragravity wave and sea-swell runup over fringing reefs by super typhoon Haiyan. *Journal of Geophysical Research: Oceans*, *120*(6), 4463–4486.

Stallone, A., Cicone, A., & Materassi, M. (2020). New insights and best practices for the successful use of Empirical Mode Decomposition, Iterative Filtering and derived algorithms. *Scientific reports*, *10*(1), 15161.

Storlazzi, C. D., Gingerich, S. B., Van Dongeren, A., Cheriton, O. M., Swarzenski, P. W., Quataert, E., Voss, C. I., Field, D. W., Annamalai, H., Piniak, G. A., et al. (2018). Most atolls will be uninhabitable by the mid-21st century because of sea-level rise exacerbating wave-driven flooding. *Science advances*, *4*(4), eaap9741.

Storlazzi, C. D., Reguero, B. G., Cole, A. D., Lowe, E., Shope, J. B., Gibbs, A. E., Nickel, B. A., McCall, R. T., van Dongeren, A. R., & Beck, M. W. (2019). *Rigorously valuing the role of us coral reefs in coastal hazard risk reduction* (tech. rep.). US Geological Survey.

Sun, H.-M., Jia, R.-S., Du, Q.-Q., & Fu, Y. (2016). Cross-correlation analysis and time delay estimation of a homologous micro-seismic signal based on the Hilbert–Huang transform. *Computers & geosciences*, *91*, 98–104.

Tait, R. J. (1972). Wave set-up on coral reefs. *Journal of Geophysical Research*, *77*(12), 2207–2211.

Thomson, R. E., & Emery, W. J. (2014). *Data analysis methods in physical oceanography*. Newnes.

Tissier, M., & Bonneton, P. (2020). Numerical Experiments on Bore Merging over Mildly Sloping Beaches. *AGU Fall Meeting Abstracts*, *2020*, OS038–01.

Titchmarsh, E. C. (1948). Introduction to the theory of Fourier integrals.

Torres, M. E., Colominas, M. A., Schlotthauer, G., & Flandrin, P. (2011). A complete ensemble empirical mode decomposition with adaptive noise. *2011 IEEE international conference on acoustics, speech and signal processing (ICASSP)*, 4144–4147.

Van Dongeren, A., Lowe, R., Pomeroy, A. W. M., Trang, D. M., Roelvink, D., Symonds, G., & Ranasinghe, R. (2013). Numerical modeling of low-frequency wave dynamics over a fringing coral reef. *Coastal Engineering*, *73*, 178–190.

Van Dongeren, A., Battjes, J., Janssen, T., Van Noorloos, J., Steenhauer, K., Steenbergen, G., & Reniers, A. (2007). Shoaling and shoreline dissipation of low-frequency waves. *Journal of Geophysical Research: Oceans*, *112*(C2).

Van Noort, R. (2021). Infragravity wave resonance over coral reef lined coasts.

Veldt, T. (2019). The effect of wave directional spread on coastal hazards at coastlines fronted by a coral reef.

Veltcheva, A. D., & Soares, C. G. (2007). Analysis of abnormal wave records by the Hilbert–Huang transform method. *Journal of Atmospheric and Oceanic Technology*, *24*(9), 1678–1689.

Veltcheva, A. D. (2002). Wave and group transformation by a Hilbert spectrum. *Coastal Engineering Journal*, *44*(4), 283–300.

Veltcheva, A. D., & Soares, C. G. (2004). Identification of the components of wave spectra by the Hilbert Huang transform method. *Applied Ocean Research*, *26*(1-2), 1–12.

Veltcheva, A. D., & Soares, C. G. (2016). Analysis of wave groups by wave envelope-phase and the Hilbert Huang transform methods. *Applied Ocean Research*, *60*, 176–184.

Vetter, O., Becker, J. M., Merrifield, M. A., Pequignet, A.-C., Aucan, J., Boc, S. J., & Pollock, C. E. (2010). Wave setup over a pacific island fringing reef. *Journal of Geophysical Research: Oceans*, *115*(C12).

Wang, W., Li, X., & Zhang, R. (2007). Boundary processing of HHT using support vector regression machines. *Computational Science–ICCS 2007: 7th International Conference, Beijing, China, May 27-30, 2007, Proceedings, Part III 7*, 174–177.

Wang, Y.-H., Hu, K., & Lo, M.-T. (2018). Uniform Phase Empirical Mode Decomposition: An Optimal Hybridization of Masking Signal and Ensemble Approaches. *IEEE Access*, *6*, 34819–34833. https://doi.org/10.1109/ACCESS.2018.2847634

Wilson, B. W. (1953). The mechanism of seiches in Table Bay Harbor, Cape Town. *Coastal Engineering Proceedings*, (4), 4–4.

Wu, Z., & Huang, N. E. (2009). Ensemble empirical mode decomposition: a noise-assisted data analysis method. *Advances in adaptive data analysis*, *1*(01), 1–41.

Xue, X. M., Zhou, J. Z., Zhang, Y. C., Jian, X., & Wang, X. M. (2013). An extrema extension method based on support vector regression for restraining the end effects in empirical mode decomposition. *Applied Mechanics and Materials*, *404*, 526–532.

Yao, Y., Zhang, Q., Chen, S., & Tang, Z. (2019). Effects of reef morphology variations on wave processes over fringing reefs. *Applied ocean research*, *82*, 52–62.

Yin, L., Qiao, F., & Zheng, Q. (2014). Coastal-trapped waves in the East China Sea observed by a mooring array in winter 2006. *Journal of Physical Oceanography*, *44*(2), 576–590.

Zare, M., & Nouri, N. M. (2023). End-effects mitigation in empirical mode decomposition using a new correlation-based expansion model. *Mechanical Systems and Signal Processing*, *194*, 110205.

A

EMD and HHT performance

Supplements for results

Visual inspection

This section provides examples of signal decompositions of various sifting configurations to go along with the findings for visual inspection as described in Section 4.1. Figures A.1, A.2 and A.3 present examples of inner reef signal decompositions for the various decomposition method: EMD, M-EMD, iM-EMD, EEMD and CEEMD. Figures A.4 and A.5 are examples of the decompositions of the inner, mid and outer reef signals by the M-EMD and iM-EMD respectively. Figure A.6 and A.7 provide examples of the influence of the stopping criterion, interpolation technique and boundary extensions settings on the M-EMD decomposition.

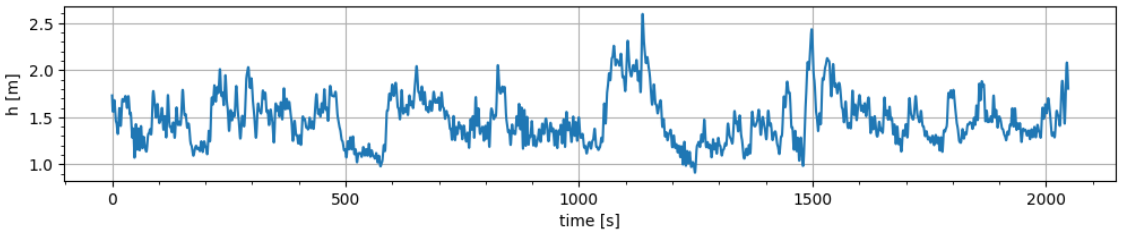

(a) Inner reef signal

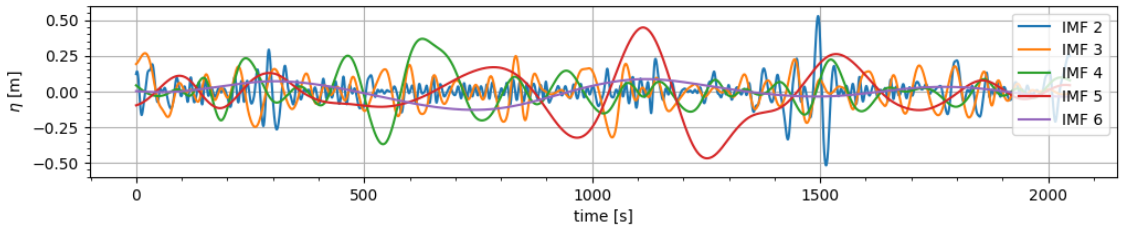

(b) EMD

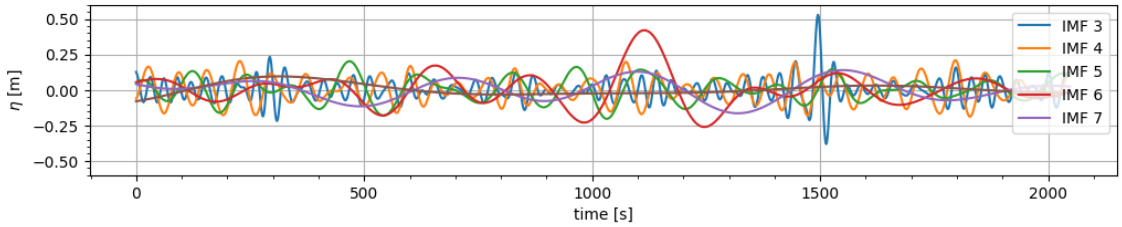

(c) M-EMD

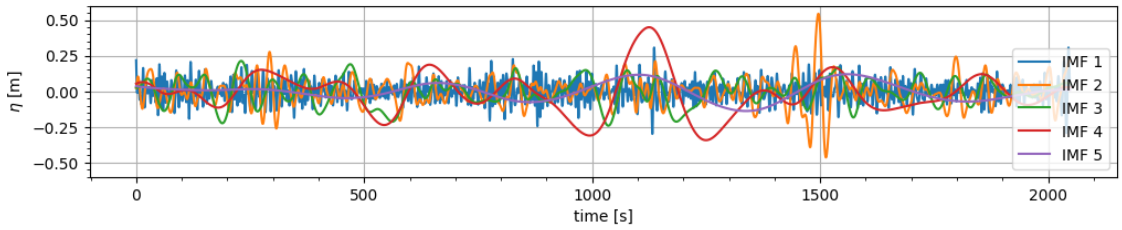

(d) iM-EMD

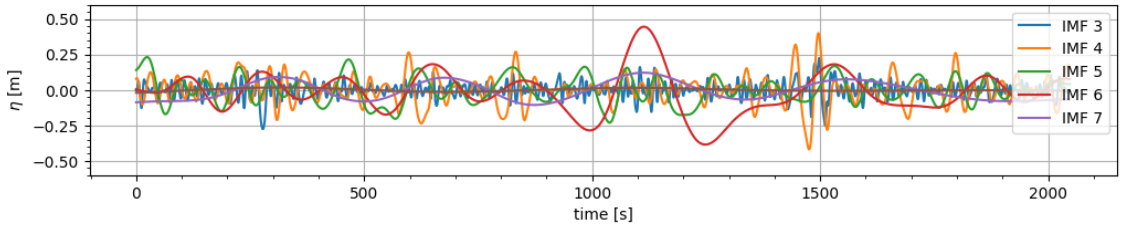

(e) EEMD

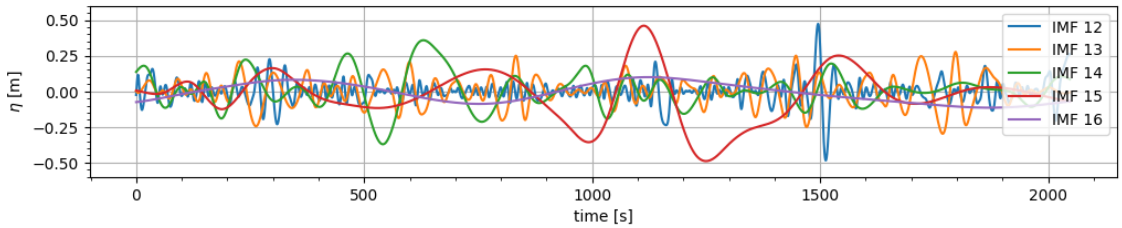

(f) CEEMD

Figure A.1: Example of an (a) inner reef signal and (b-f) its decomposition by various sifting methods. Mode mixing is observed for the EMD (b) where IMF 4 and IMF 5 both contain part of the dominant low-frequency motion (peaks at 600 s and 1100 s). The same pattern is recognized in the CEEMD (f) for IMF 14 and 15. The M-EMD (c), iM-EMD (d) and EEMD (e) perform relatively similar.

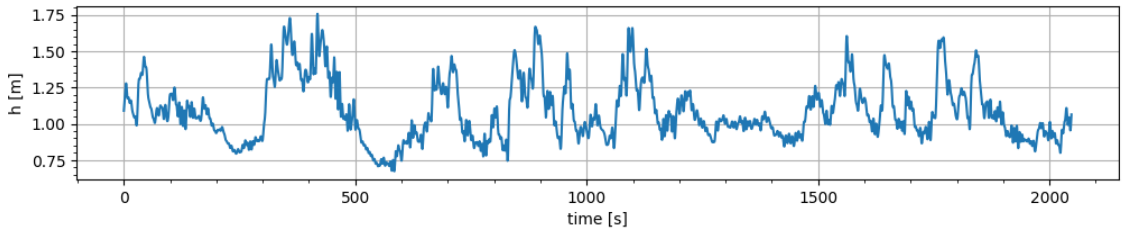

(a) Inner reef signal

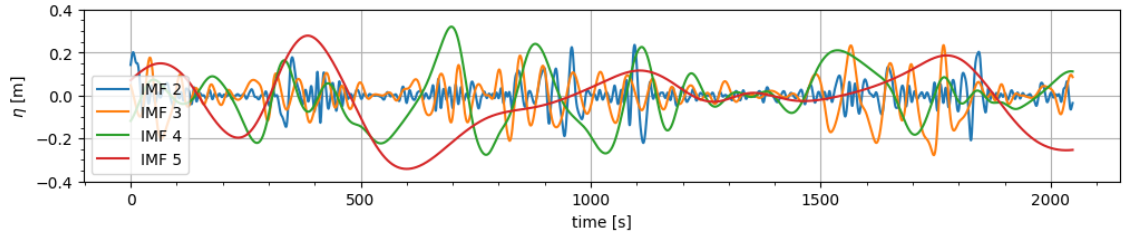

(b) EMD

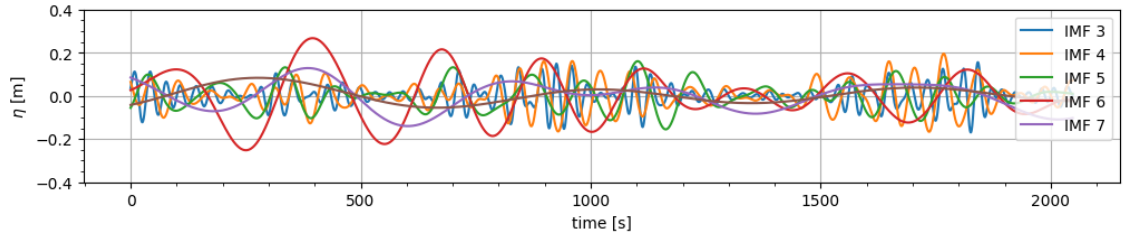

(c) M-EMD

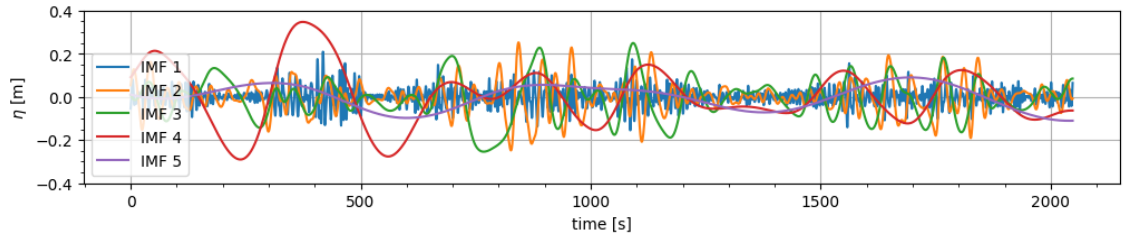

(d) iM-EMD

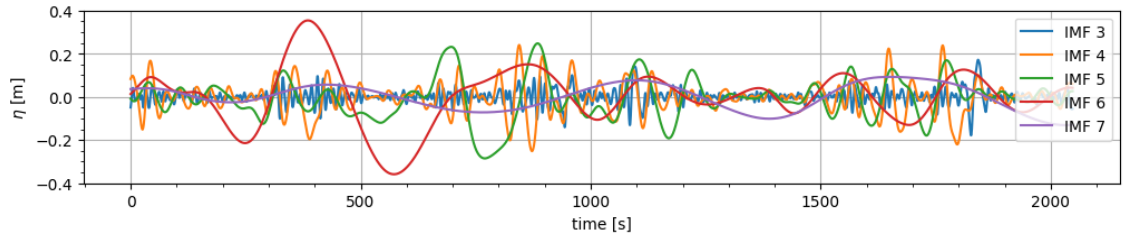

(e) EEMD

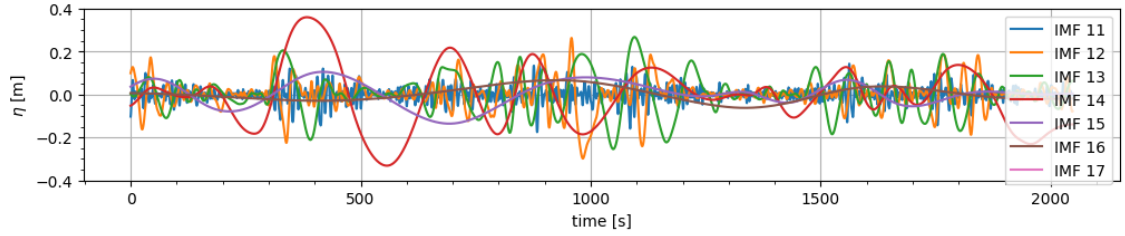

(f) CEEMD

Figure A.2: Example of an (a) inner reef signal and (b-f) its decomposition by various sifting methods. Mode mixing is observed for the EMD (b) where peaks are inconsistently extracted by IMF 4 or IMF 5. A similar pattern is observed for the EEMD (e). In the iM-EMD (d), parts of the peaks at t = 700s and 900s are captured by IMF 3 and 4. Some mode splitting is observed for the M-EMD around t = 400s, where the amplitude is split between IMF 6 and IMF 7. Otherwise, the dominant low-frequency oscillations is captured relatively well by the M-EMD. The CEEMD (f) also captures this motion well.

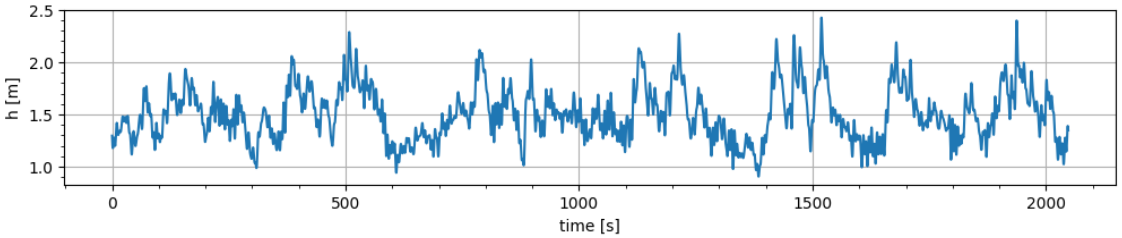

(a) Inner reef signal

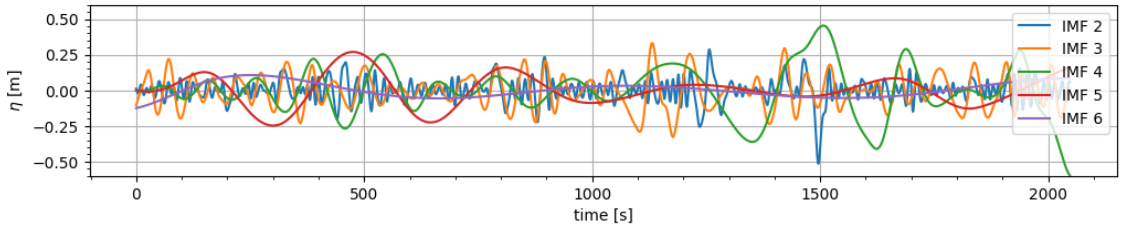

(b) EMD

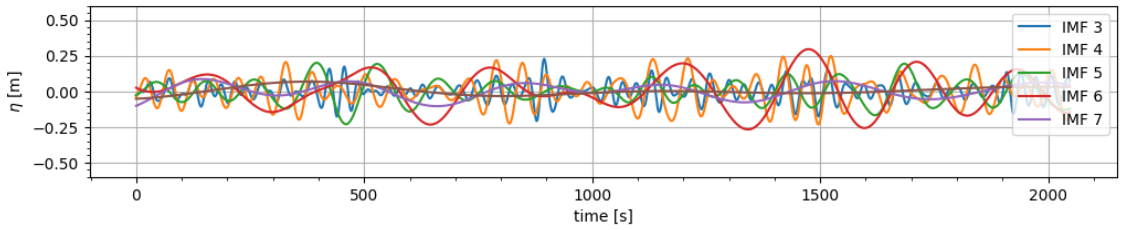

(c) M-EMD

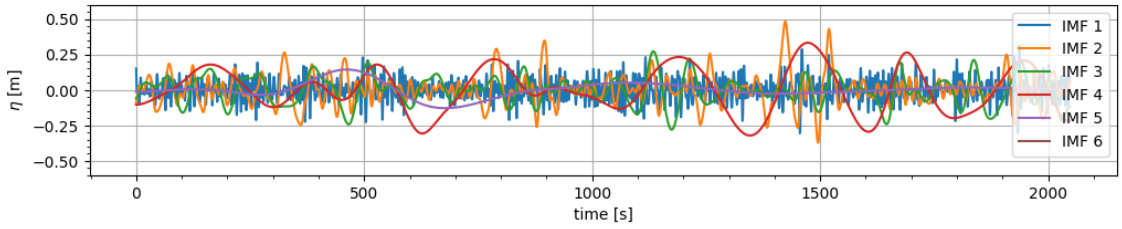

(d) iM-EMD

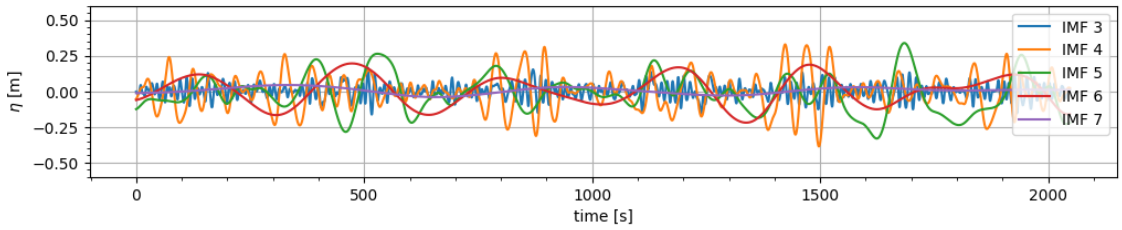

(e) EEMD

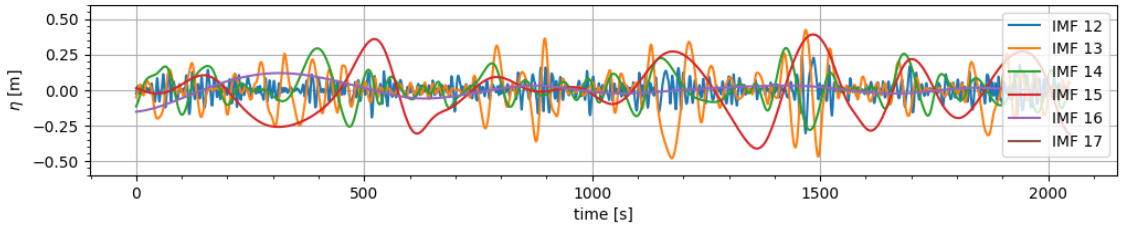

(f) CEEMD

Figure A.3: Example of an (a) inner reef signal and (b-f) its decomposition by various sifting methods. Mode mixing is observed for the EMD (b) where peaks are inconsistently extracted by IMF 4 or IMF 5. Some mode mixing is observed for the EEMD (e) around t = 520s and 1700s. Note the variation of amplitudes extracted by the different dominant LF components (red line for all decompositions)

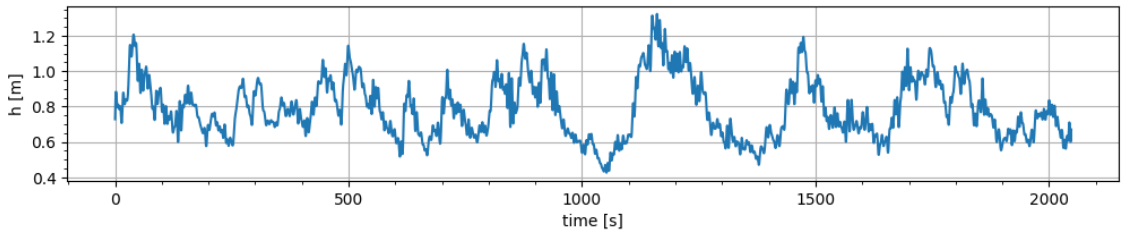

(a) Inner reef signal

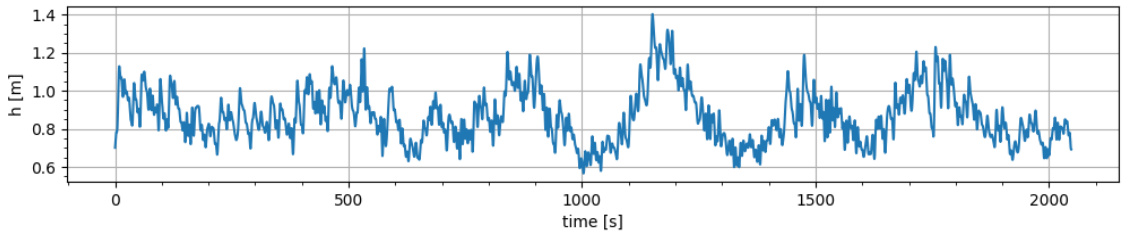

(b) Mid reef signal

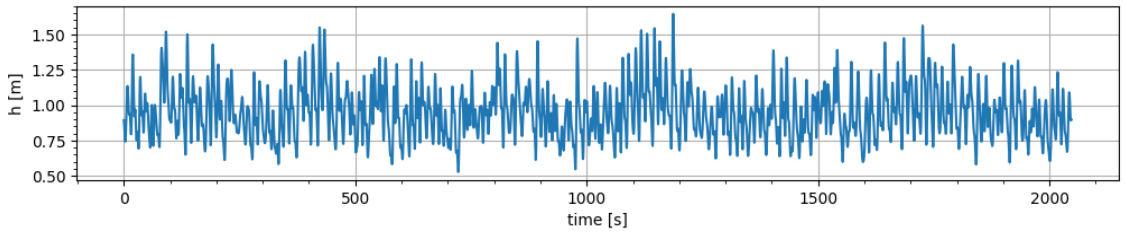

(c) Outer reef signal

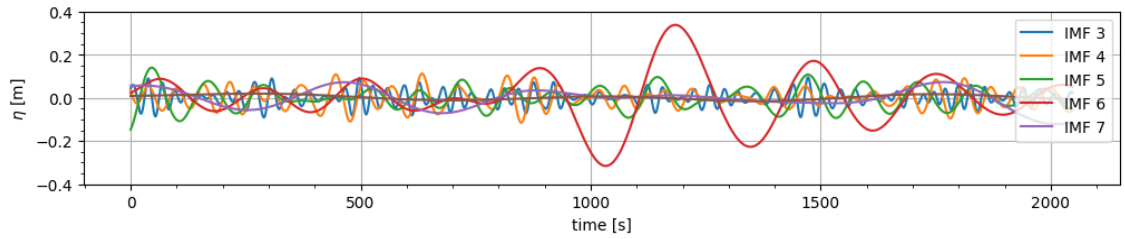

(d) M-EMD inner reef

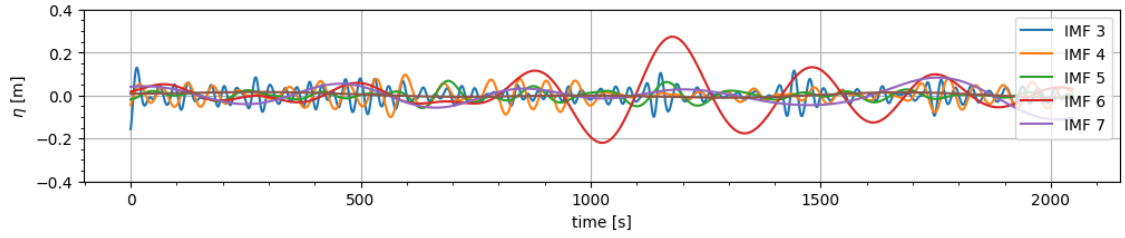

(e) M-EMD mid reef

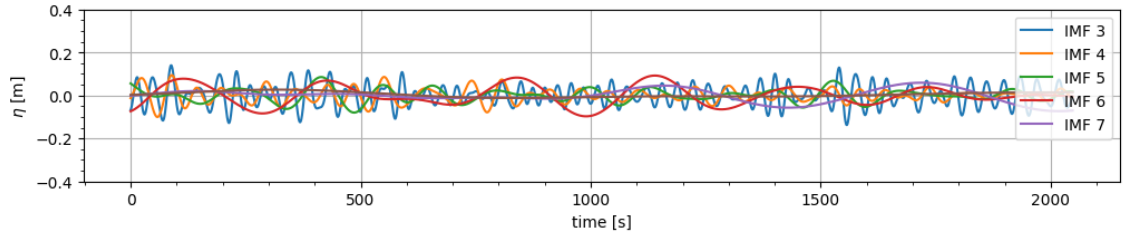

(f) M-EMD outer reef

Figure A.4: Example of an (a) inner, (b) mid and (c) outer reef signal with their respective decompositions by the M-EMD (d-f). IMF 6 (red line) seems to be of similar waveform and frequency for the inner and mif reef signal decompositions, which is important for the classification of VLF oscillations in Phase 2.

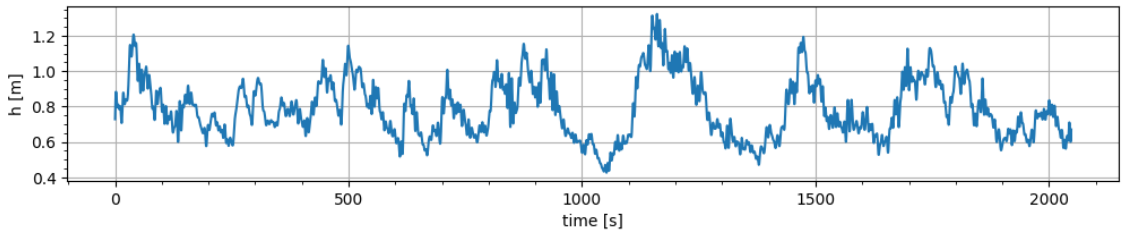

(a) Inner reef signal

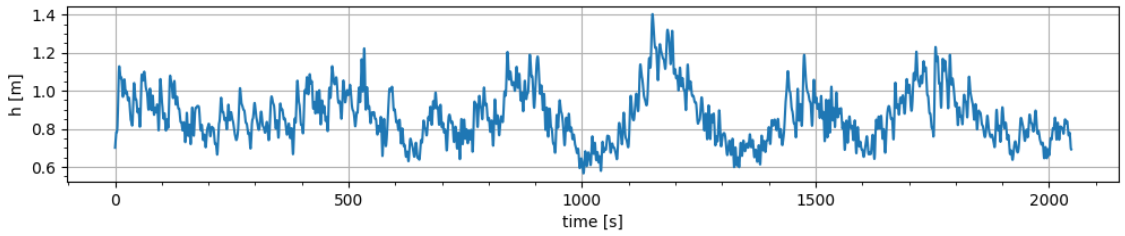

(b) Mid reef signal

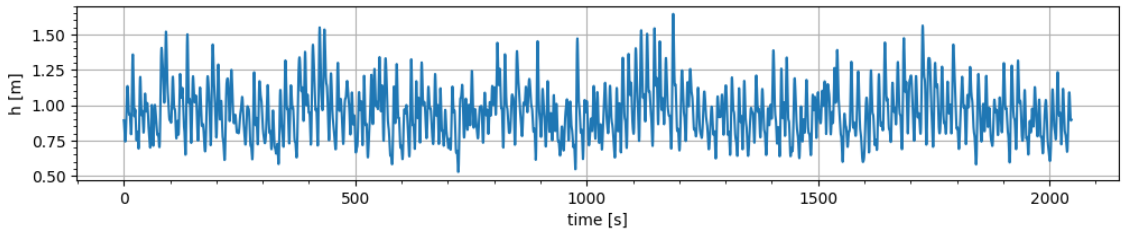

(c) Outer reef signal

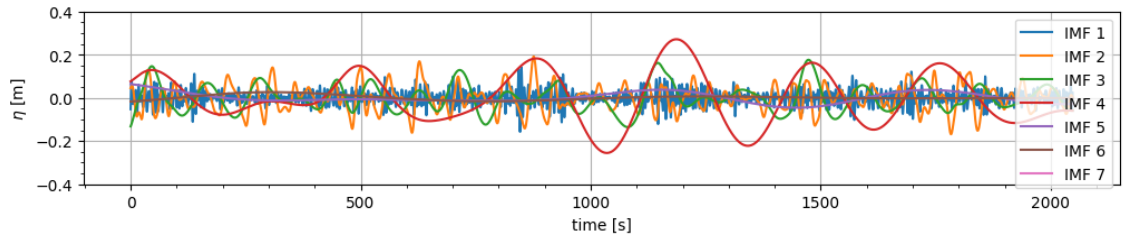

(d) iM-EMD inner reef

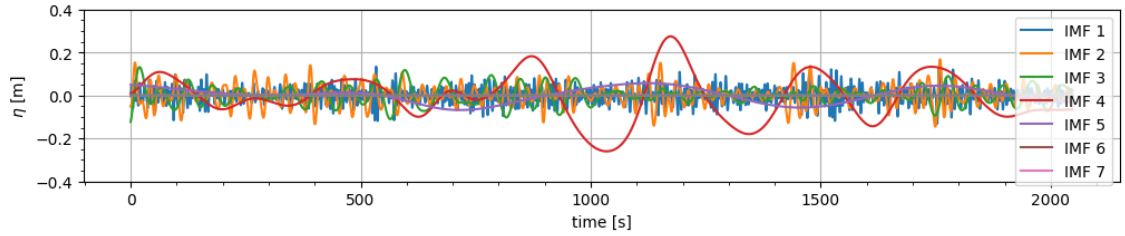

(e) iM-EMD mid reef

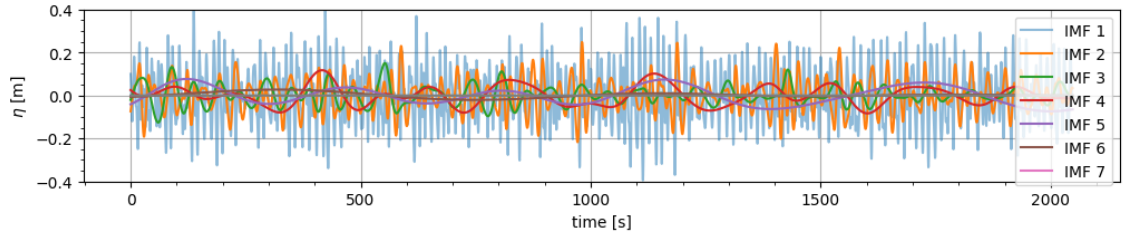

(f) iM-EMD outer reef

Figure A.5: Example of an (a) inner, (b) mid and (c) outer reef signal with their respective decompositions by the iM-EMD (d-f). IMFs 4 (red line) of the inner and mid reef decomposition have a slightly different waveform, although the waveform of their respective signal is alike.

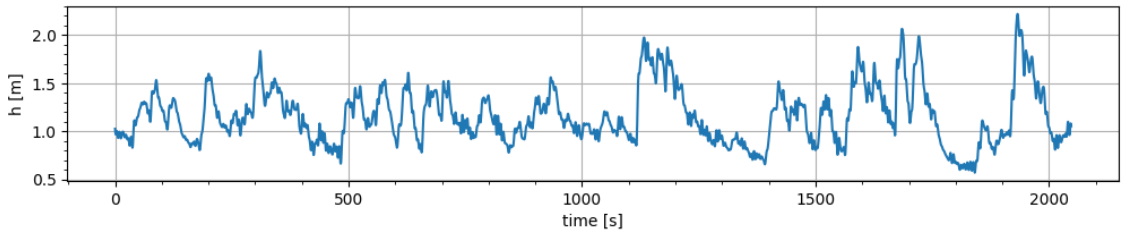

(a) Inner reef signal

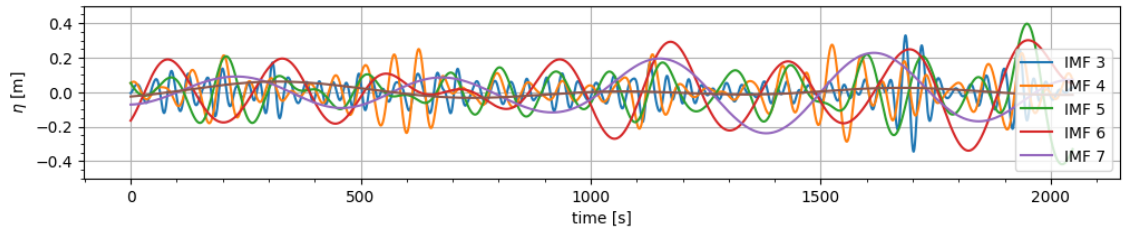

(b) Default configuration

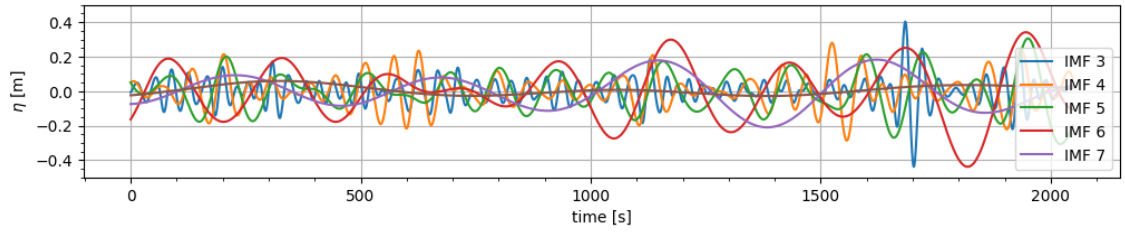

(c) Stopping criterion: SD = 0.3

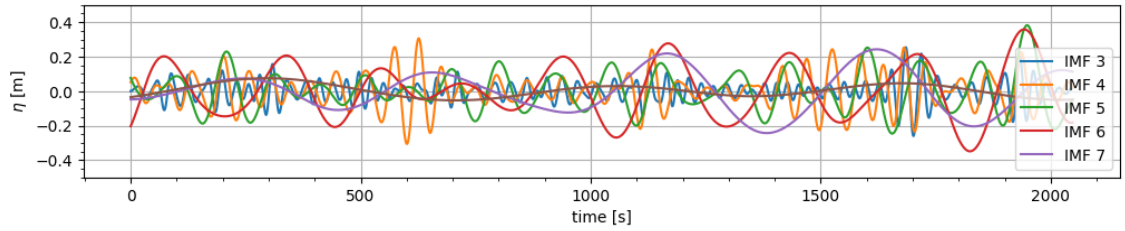

(d) Stopping criterion: Rilling

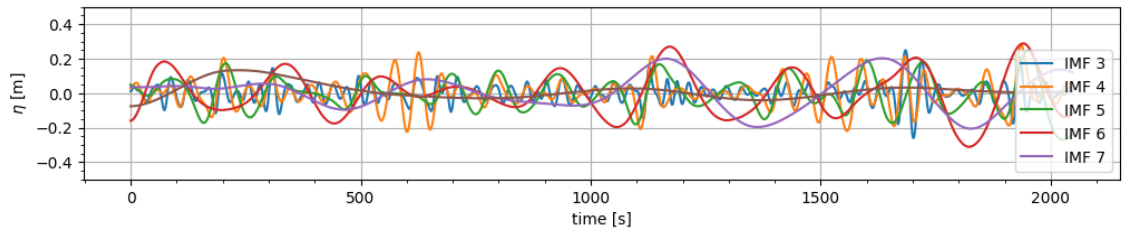

(e) Interpolation: cubic spline

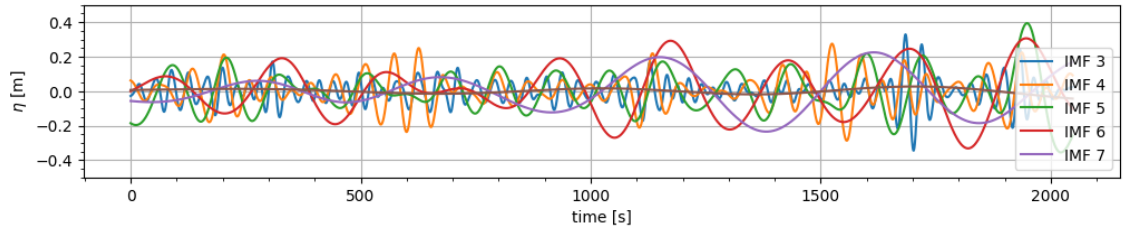

(f) Boundary extension: constant padding

Figure A.6: Example of an (a) inner reef signal and (b-f) its decomposition by various configurations of the M-EMD. Hardly any difference is observed between the stopping criterion SD = 0.2 (b) and SD = 0.3 (c). The constant padding boundary extension (f) results in a slightly different IMF 5 compared to the Rilling approach (b-e).

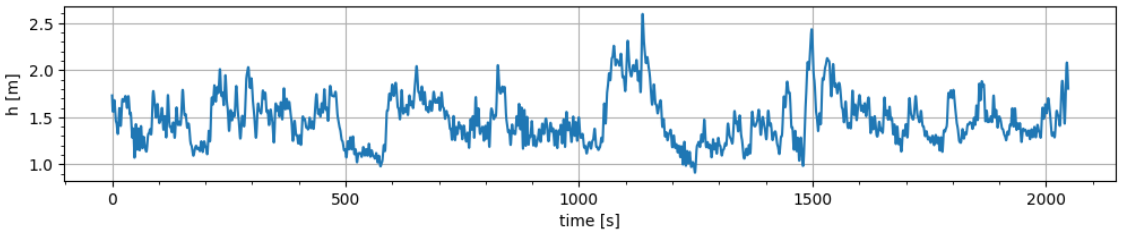

(a) Inner reef signal

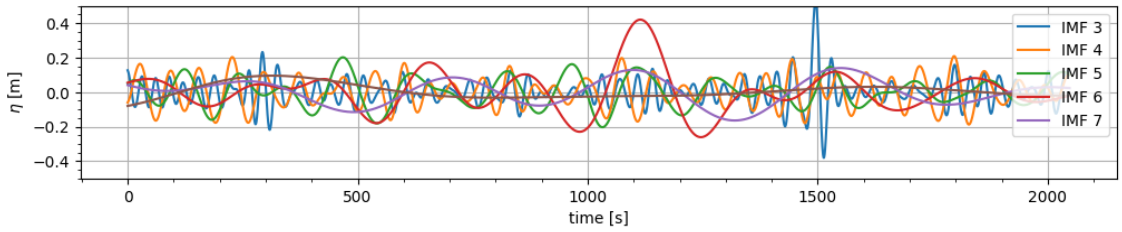

(b) Default configuration

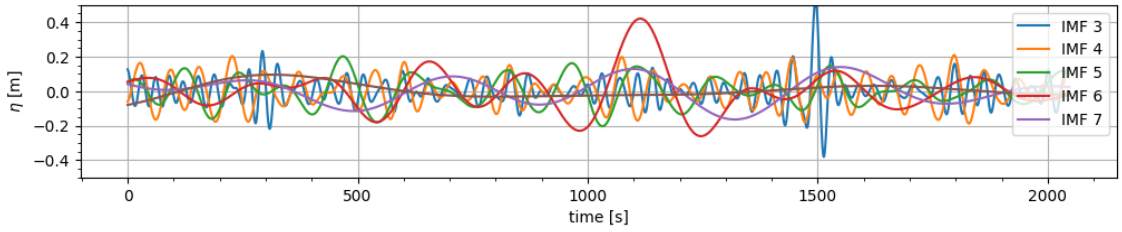

(c) Stopping criterion: SD = 0.3

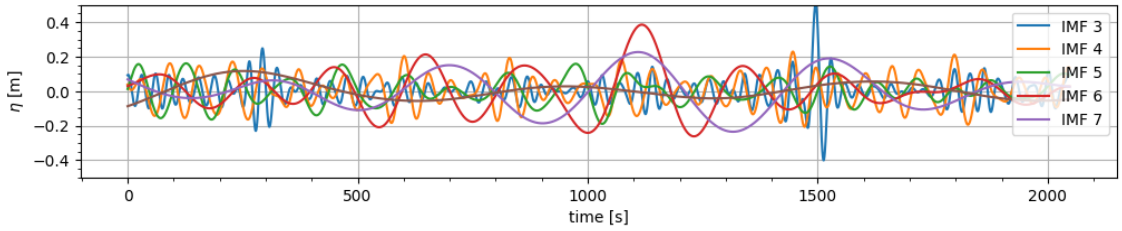

(d) Stopping criterion: Rilling

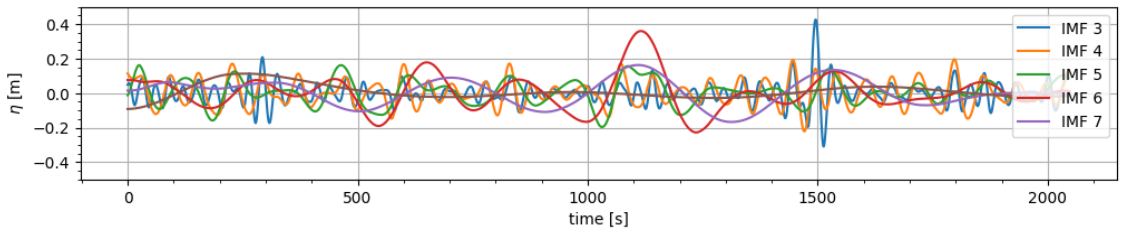

(e) Interpolation: cubic spline

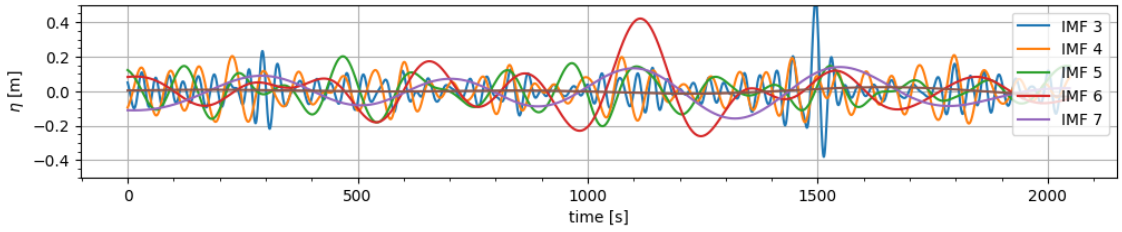

(f) Boundary extension: constant padding

Figure A.7: Example of an (a) inner reef signal and (b-f) its decomposition by various configurations of the M-EMD. Rilling's stopping criterion results in more energy being assigned to IMF 7 compared to the other configurations. Otherwise, the settings influence the decomposition minimally.

Performance of sifting configurations

This section is a supplement for Section 4.1, where the evaluation of the EMD configurations based on a set of performance metrics is described. Figure A.8 illustrates the offshore wave characteristics of the data set and the selection of records used for this analysis. A set of records is chosen which contains various values for each of the characteristics, to best represent the data.

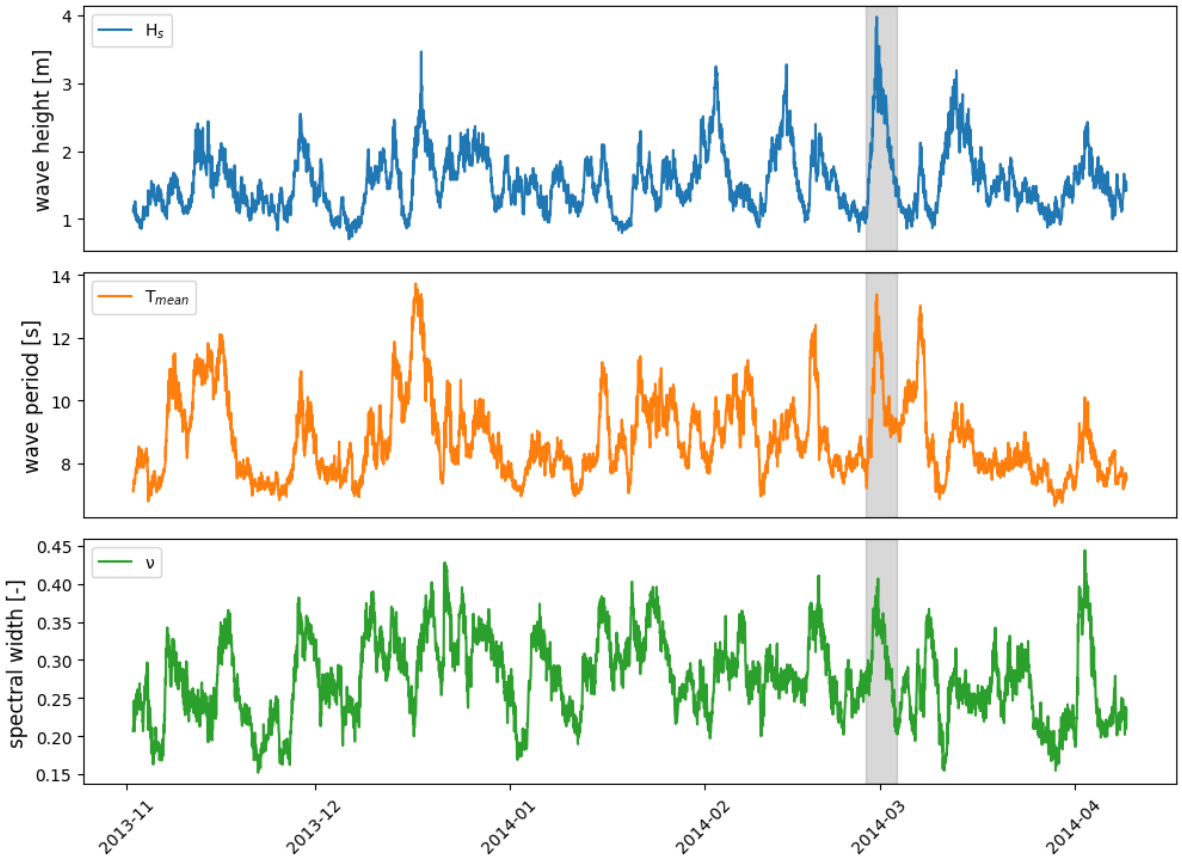

Figure A.8: (a) Significant wave height, (b) mean wave period and (c) spectral width for offshore surface elevation records. The span of records selected for the performance evaluation is indicated in grey.

The following pages include the tables with numerical values for the median and standard deviations for each of the performance indices per sifting configuration. Tables A.1 and A.2 present the global indices for the fore and inner reef decompositions respectively. Tables A.3 and A.4 present the IMF-specific metrics for the fore and inner reef decompositions respectively. In Section 4.1, these tables are summarized by Table 4.1 and 4.2 for the global and IMF-specific metrics respectively.

Table A.1: Global performance metrics for the fore reef signal decomposition of various sifting configurations. Each cell contains the median value and standard deviation of the scores of the 120 selected records.

Method	Modification aspect	detail	Evaluation metrics (median value) IO	θ	$a_{max,error}$	EI	Computation time (s)
EMD	*default*		1.8e-03 (SD: 2.0e-03)	1.1e-03 (SD: 0.19)	1.8e-15 (SD: 1.8)	0.97 (SD: 0.065)	0.02 (SD: 0.003)
	stopping criterion	SD = 0.3	1.8e-03 (SD: 2.0e-03)	1.1e-03 (SD: 0.17)	1.8e-15 (SD: 1.7)	0.97 (SD: 0.066)	0.02 (SD: 0.004)
	stopping criterion	Rilling	9.5e-04 (SD: 1.1e-03)	6.7e-04 (SD: 0.24)	1.8e-15 (SD: 2.3)	0.98 (SD: 0.044)	0.13 (SD: 0.043)
	interpolation	cubic spline	1.5e-03 (SD: 1.8e-03)	8.1e-04 (SD: 1.0e-03)	1.8e-15 (SD: 3.5e-16)	0.96 (SD: 0.069)	0.03 (SD: 0.006)
	boundary extension	constant	2.0e-03 (SD: 2.2e-03)	1.2e-03 (SD: 0.12)	1.8e-15 (SD: 1.2)	0.99 (SD: 0.089)	0.03 (SD: 0.003)
M-EMD	*default*		4.4e-03 (SD: 0.16)	2.3e-03 (SD: 0.10)	1.8e-15 (SD: 3.3e-16)	0.79 (SD: 0.036)	0.13 (SD: 0.010)
	stopping criterion	SD = 0.3	4.4e-03 (SD: 0.16)	2.3e-03 (SD: 0.10)	1.8e-15 (SD: 3.3e-16)	0.79 (SD: 0.036)	0.13 (SD: 0.009)
	stopping criterion	Rilling	4.3e-03 (SD: 0.10)	2.6e-03 (SD: 6.7e-02)	1.8e-15 (SD: 3.0e-16)	0.78 (SD: 0.046)	0.24 (SD: 0.026)
	interpolation	cubic spline	5.1e-03 (SD: 0.17)	2.1e-01 (SD: 0.12)	1.8e-15 (SD: 1.0)	0.84 (SD: 11.543)	0.13 (SD: 0.013)
	boundary extension	constant	1.7e-03 (SD: 0.18)	1.0e-03 (SD: 0.12)	1.8e-15 (SD: 0.23)	0.83 (SD: 0.081)	0.15 (SD: 0.012)
iM-EMD	*default*		1.2e-03 (SD: 2.5e-02)	7.4e-04 (SD: 1.9e-02)	1.8e-15 (SD: 8.1e-17)	0.92 (SD: 0.053)	1.10 (SD: 0.40)
	stopping criterion	SD = 0.3	1.2e-03 (SD: 1.0e-03)	7.3e-04 (SD: 6.2e-04)	1.8e-15 (SD: 0.0)	0.91 (SD: 0.052)	1.40 (SD: 0.51)
	boundary extension	constant	1.6e-03 (SD: 5.6e-02)	9.1e-04 (SD: 3.8e-02)	1.8e-15 (SD: 4.3)	0.91 (SD: 0.088)	1.83 (SD: 0.68)
EEMD	*default*		7.9e-04 (SD: 8.5e-04)	7.0e-04 (SD: 0.16)	2.5e-01 (SD: 1.5)	0.87 (SD: 0.070)	0.34 (SD: 0.03)
	stopping criterion	SD = 0.3	6.5e-04 (SD: 8.4e-04)	5.5e-04 (SD: 0.16)	2.7e-01 (SD: 1.5)	0.86 (SD: 0.056)	0.33 (SD: 0.02)
	boundary extension	constant	1.0e-03 (SD: 1.1e-03)	7.1e-04 (SD: 0.11)	2.4e-01 (SD: 1.0)	0.87 (SD: 0.078)	0.38 (SD: 0.02)
CEEMD	*default*		6.9e-04 (SD: 1.0e-03)	4.5e-04 (SD: 0.15)	1.8e-15 (SD: 1.5)	0.83 (SD: 0.039)	1.96 (SD: 0.12)
	stopping criterion	SD = 0.3	9.1e-04 (SD: 1.2e-03)	6.0e-04 (SD: 0.15)	1.8e-15 (SD: 1.5)	0.82 (SD: 0.042)	1.94 (SD: 0.12)
	boundary extension	constant	9.4e-04 (SD: 1.3e-03)	5.7e-04 (SD: 0.12)	1.8e-15 (SD: 1.2)	0.84 (SD: 0.048)	2.37 (SD: 0.14)

Table A.2: Global performance metrics for the inner reef signal decomposition of various sifting configurations. Each cell contains the median value and standard deviation of the scores of the 120 selected records.

Method	Modification		Evaluation metrics (median value)				
	aspect	detail	IO	θ	$a_{max,error}$	EI	Computation time (s)
EMD	*default*		5.0e-05 (SD: 1.4e-04)	5.1e-03 (SD: 0.13)	1.1e-16 (SD: 0.13)	0.98 (SD: 0.071)	0.03 (SD: 0.004)
	stopping criterion	SD = 0.3	5.5e-05 (SD: 1.8e-04)	5.4e-03 (SD: 8.4e-02)	1.1e-16 (SD: 6.4e-02)	0.98 (SD: 0.069)	0.02 (SD: 0.003)
	stopping criterion	Rilling	2.6e-05 (SD: 9.6e-05)	3.7e-03 (SD: 0.24)	2.2e-16 (SD: 0.27)	1.00 (SD: 0.040)	0.19 (SD: 0.127)
	interpolation	cubic spline	5.9e-05 (SD: 1.8e-04)	6.8e-03 (SD: 9.1e-03)	1.1e-16 (SD: 1.3e-16)	0.97 (SD: 0.085)	0.03 (SD: 0.005)
	boundary extension	constant	5.7e-05 (SD: 2.1e-04)	7.5e-03 (SD: 0.18)	1.1e-16 (SD: 0.15)	0.99 (SD: 0.096)	0.03 (SD: 0.004)
M-EMD	*default*		9.1e-05 (SD: 1.4e-04)	7.5e-03 (SD: 5.4e-03)	2.2e-16 (SD: 1.1e-16)	0.92 (SD: 0.095)	0.14 (SD: 0.010)
	stopping criterion	SD = 0.3	9.3e-05 (SD: 1.4e-04)	7.5e-03 (SD: 5.4e-03)	2.2e-16 (SD: 1.1e-16)	0.92 (SD: 0.095)	0.14 (SD: 0.012)
	stopping criterion	Rilling	8.1e-05 (SD: 1.2e-04)	6.5e-03 (SD: 4.4e-03)	1.9e-16 (SD: 1.1e-16)	0.94 (SD: 0.059)	0.32 (SD: 0.054)
	interpolation	cubic spline	1.3e-04 (SD: 2.0e-04)	1.5e-02 (SD: 0.11)	2.2e-16 (SD: 0.12)	0.90 (SD: 0.068)	0.16 (SD: 0.022)
	boundary extension	constant	2.2e-05 (SD: 7.5e-05)	2.5e-03 (SD: 3.7e-03)	2.2e-16 (SD: 1.1e-16)	0.96 (SD: 0.069)	0.15 (SD: 0.012)
iM-EMD	*default*		3.1e-05 (SD: 3.7e-04)	3.3e-03 (SD: 3.2e-02)	1.1e-16 (SD: 7.9e-17)	0.86 (SD: 0.119)	2.03 (SD: 0.65)
	stopping criterion	SD = 0.3	4.4e-05 (SD: 1.4e-03)	4.2e-03 (SD: 6.9e-02)	1.1e-16 (SD: 7.6e-17)	0.86 (SD: 0.116)	2.11 (SD: 0.71)
	boundary extension	constant	3.8e-05 (SD: 8.0e-04)	4.1e-03 (SD: 4.9e-02)	1.1e-16 (SD: 7.7e-17)	0.85 (SD: 0.123)	2.40 (SD: 0.66)
EEMD	*default*		3.0e-05 (SD: 1.1e-04)	4.1e-03 (SD: 0.13)	5.0e-02 (SD: 0.15)	0.87 (SD: 0.061)	0.37 (SD: 0.02)
	stopping criterion	SD = 0.3	3.6e-05 (SD: 1.4e-04)	4.8e-03 (SD: 0.17)	4.0e-02 (SD: 0.22)	0.87 (SD: 0.076)	0.35 (SD: 0.02)
	boundary extension	constant	2.8e-05 (SD: 1.3e-04)	4.1e-03 (SD: 7.2e-02)	4.1e-02 (SD: 8.3e-02)	0.88 (SD: 0.072)	0.39 (SD: 0.03)
CEEMD	*default*		3.9e-05 (SD: 1.6e-04)	4.5e-03 (SD: 0.17)	1.1e-16 (SD: 0.21)	0.88 (SD: 0.040)	2.16 (SD: 0.16)
	stopping criterion	SD = 0.3	3.6e-05 (SD: 1.4e-04)	5.2e-03 (SD: 0.12)	1.1e-16 (SD: 6.2e-02)	0.86 (SD: 0.037)	2.09 (SD: 0.15)
	boundary extension	constant	4.1e-05 (SD: 1.7e-04)	4.6e-03 (SD: 6.7e-03)	1.1e-16 (SD: 1.0e-16)	0.88 (SD: 0.042)	2.29 (SD: 0.17)

Table A.3: IMF-specific performance metrics for the fore reef signal decomposition of various sifting configurations. Each cell contains the median value and standard deviation of the scores of all IMFs for the 120 selected records.

Method	Modification		Evaluation metrics (median value)			
	aspect	detail	IO	ρ	$PMSI$	$f_{overlap}$
EMD	*default*		0.047 (SD: 0.011)	0.047 (SD: 0.011)	0.014 (SD: 0.010)	0.044 (SD: 0.014)
	stopping criterion	SD = 0.3	0.046 (SD: 0.011)	0.046 (SD: 0.011)	0.014 (SD: 0.011)	0.044 (SD: 0.014)
	stopping criterion	Rilling	0.039 (SD: 0.009)	0.039 (SD: 0.009)	0.016 (SD: 0.010)	0.045 (SD: 0.016)
	interpolation	cubic spline	0.077 (SD: 0.013)	0.076 (SD: 0.014)	0.060 (SD: 0.016)	0.087 (SD: 0.022)
	boundary extension	constant	0.047 (SD: 0.013)	0.048 (SD: 0.013)	0.014 (SD: 0.012)	0.047 (SD: 0.032)
M-EMD	*default*		0.053 (SD: 0.009)	0.048 (SD: 0.011)	0.053 (SD: 0.009)	0.059 (SD: 0.011)
	stopping criterion	SD = 0.3	0.053 (SD: 0.009)	0.048 (SD: 0.011)	0.053 (SD: 0.009)	0.059 (SD: 0.011)
	stopping criterion	Rilling	0.041 (SD: 0.006)	0.040 (SD: 0.005)	0.051 (SD: 0.008)	0.058 (SD: 0.011)
	interpolation	cubic spline	0.115 (SD: 0.021)	0.123 (SD: 0.024)	0.113 (SD: 0.018)	0.089 (SD: 0.020)
	boundary extension	constant	0.059 (SD: 0.010)	0.062 (SD: 0.010)	0.058 (SD: 0.011)	0.064 (SD: 0.016)
iM-EMD	*default*		0.066 (SD: 0.011)	0.066 (SD: 0.011)	0.042 (SD: 0.010)	0.068 (SD: 0.012)
	stopping criterion	SD = 0.3	0.066 (SD: 0.011)	0.066 (SD: 0.011)	0.042 (SD: 0.009)	0.066 (SD: 0.012)
	boundary extension	constant	0.062 (SD: 0.012)	0.063 (SD: 0.012)	0.038 (SD: 0.010)	0.069 (SD: 0.013)
EEMD	*default*		0.051 (SD: 0.008)	0.052 (SD: 0.009)	0.032 (SD: 0.010)	0.086 (SD: 0.014)
	stopping criterion	SD = 0.3	0.054 (SD: 0.010)	0.054 (SD: 0.010)	0.033 (SD: 0.012)	0.091 (SD: 0.015)
	boundary extension	constant	0.053 (SD: 0.009)	0.053 (SD: 0.009)	0.030 (SD: 0.011)	0.091 (SD: 0.020)
CEEMD	*default*		0.049 (SD: 0.003)	0.049 (SD: 0.003)	0.006 (SD: 0.004)	0.336 (SD: 0.012)
	stopping criterion	SD = 0.3	0.049 (SD: 0.003)	0.049 (SD: 0.003)	0.007 (SD: 0.005)	0.338 (SD: 0.010)
	boundary extension	constant	0.050 (SD: 0.004)	0.050 (SD: 0.004)	0.006 (SD: 0.005)	0.339 (SD: 0.013)

Table A.4: IMF-specific performance metrics for the inner reef signal decomposition of various sifting configurations. Each cell contains the median value and standard deviation of the scores of the low-frequency (median instantaneous frequency $<$ 0.04 Hz) IMFs for the 120 selected records.

Method	Modification		Evaluation metrics (median value)			
	aspect	detail	IO	ρ	$PMSI$	$f_{overlap}$
EMD	*default*		0.060 (SD: 0.023)	0.059 (SD: 0.023)	0.017 (SD: 0.017)	0.058 (SD: 0.022)
	stopping criterion	SD = 0.3	0.060 (SD: 0.023)	0.059 (SD: 0.023)	0.017 (SD: 0.015)	0.062 (SD: 0.022)
	stopping criterion	Rilling	0.047 (SD: 0.014)	0.047 (SD: 0.014)	0.018 (SD: 0.014)	0.059 (SD: 0.025)
	interpolation	cubic spline	0.097 (SD: 0.019)	0.097 (SD: 0.020)	0.069 (SD: 0.022)	0.099 (SD: 0.029)
	boundary extension	constant	0.056 (SD: 0.022)	0.058 (SD: 0.023)	0.015 (SD: 0.016)	0.057 (SD: 0.036)
M-EMD	*default*		0.061 (SD: 0.014)	0.062 (SD: 0.014)	0.079 (SD: 0.018)	0.070 (SD: 0.017)
	stopping criterion	SD = 0.3	0.062 (SD: 0.014)	0.062 (SD: 0.014)	0.079 (SD: 0.017)	0.069 (SD: 0.018)
	stopping criterion	Rilling	0.050 (SD: 0.013)	0.050 (SD: 0.013)	0.062 (SD: 0.016)	0.060 (SD: 0.016)
	interpolation	cubic spline	0.125 (SD: 0.015)	0.124 (SD: 0.015)	0.159 (SD: 0.015)	0.106 (SD: 0.025)
	boundary extension	constant	0.066 (SD: 0.014)	0.066 (SD: 0.014)	0.074 (SD: 0.016)	0.066 (SD: 0.016)
iM-EMD	*default*		0.073 (SD: 0.023)	0.073 (SD: 0.023)	0.049 (SD: 0.020)	0.080 (SD: 0.026)
	stopping criterion	SD = 0.3	0.074 (SD: 0.024)	0.075 (SD: 0.024)	0.047 (SD: 0.019)	0.079 (SD: 0.024)
	boundary extension	constant	0.072 (SD: 0.020)	0.073 (SD: 0.020)	0.047 (SD: 0.017)	0.071 (SD: 0.022)
EEMD	*default*		0.064 (SD: 0.019)	0.065 (SD: 0.019)	0.048 (SD: 0.024)	0.085 (SD: 0.024)
	stopping criterion	SD = 0.3	0.065 (SD: 0.019)	0.066 (SD: 0.019)	0.050 (SD: 0.023)	0.085 (SD: 0.023)
	boundary extension	constant	0.070 (SD: 0.019)	0.070 (SD: 0.019)	0.053 (SD: 0.022)	0.091 (SD: 0.027)
CEEMD	*default*		0.025 (SD: 0.006)	0.025 (SD: 0.006)	0.019 (SD: 0.015)	0.055 (SD: 0.019)
	stopping criterion	SD = 0.3	0.025 (SD: 0.007)	0.026 (SD: 0.008)	0.018 (SD: 0.016)	0.057 (SD: 0.027)
	boundary extension	constant	0.025 (SD: 0.008)	0.025 (SD: 0.009)	0.017 (SD: 0.017)	0.059 (SD: 0.038)

Manual masks for the M-EMD

The application of manual masks for the M-EMD based on the eigenfrequency was considered to improve the extraction of the right frequency oscillation from the signal. In the M-EMD algorithm, the first mask frequency ($f_{0,zc}$) is determined by the number of zero-crossings for the highest frequency component (determined with the EMD). For the following mask frequencies, a factor of 2 is applied between two consecutive masks. The result is that the powerful LF oscillation is typically captured in the same component (IMF 6), as is demonstrated in the examples provided in Section 4.1.1.

Would the masks be determined based on the eigenfrequency, then either the LF oscillation would be captured in a different IMF (when maintaining the factor 2 between consecutive mask frequencies), or the first mask frequency would be very inconsistent. For example, for a certain moment of recording the eigenfrequency is 0.003 Hz, and the first mask determined by the zero-crossing for the inner reef time series is $f_{0,zc} = 0.159$ Hz. Maintaining the spacing of a factor 2, the closest mask frequency to the zero-crossing mask would be 0.197 Hz, and the mask with the eigen frequency would be in IMF 7.

However, the eigenfrequency ranges from 0.001 - 0.004 Hz. If the first mask frequency should be close to $f_{0,zc}$, the oscillation with the eigenfrequency would be in a different IMF, depending on the value of the eigenfrequency at that moment. Otherwise, to have the oscillation of interest consistently in the same IMF to prevent over-splitting of components, the first mask frequency would not necessarily be close to $f_{0,zc}$. This is illustrated in Figure A.9.

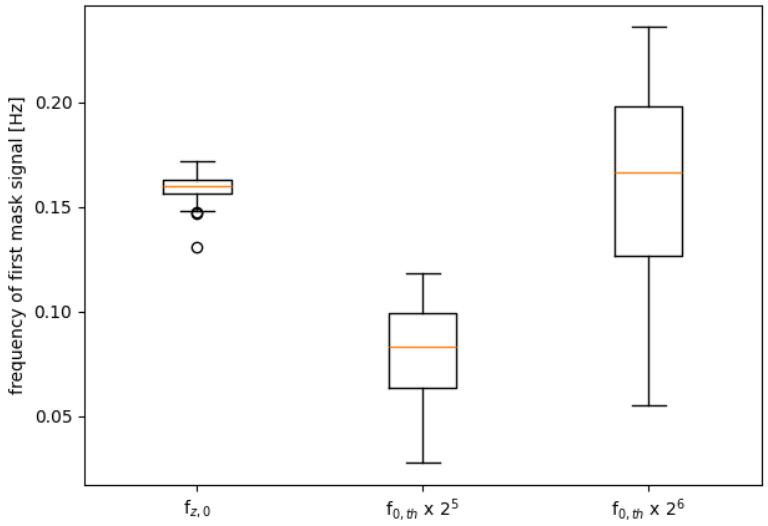

Figure A.9: Distribution of first mask frequency for the M-EMD, determined by the zero-crossing of the fastest oscillation in the signal ($f_{z,0}$) or based on a multiple of the eigenfrequency ($f_{0,th}$).

Comparison of spectra

In this section, examples of the IMF-specific marginal spectra for various sifting configurations are given and compared to the corresponding Fourier spectra. Figures A.10 and 4.2 contain the (marginal) spectra for a fore reef and inner reef signal signal respectively.

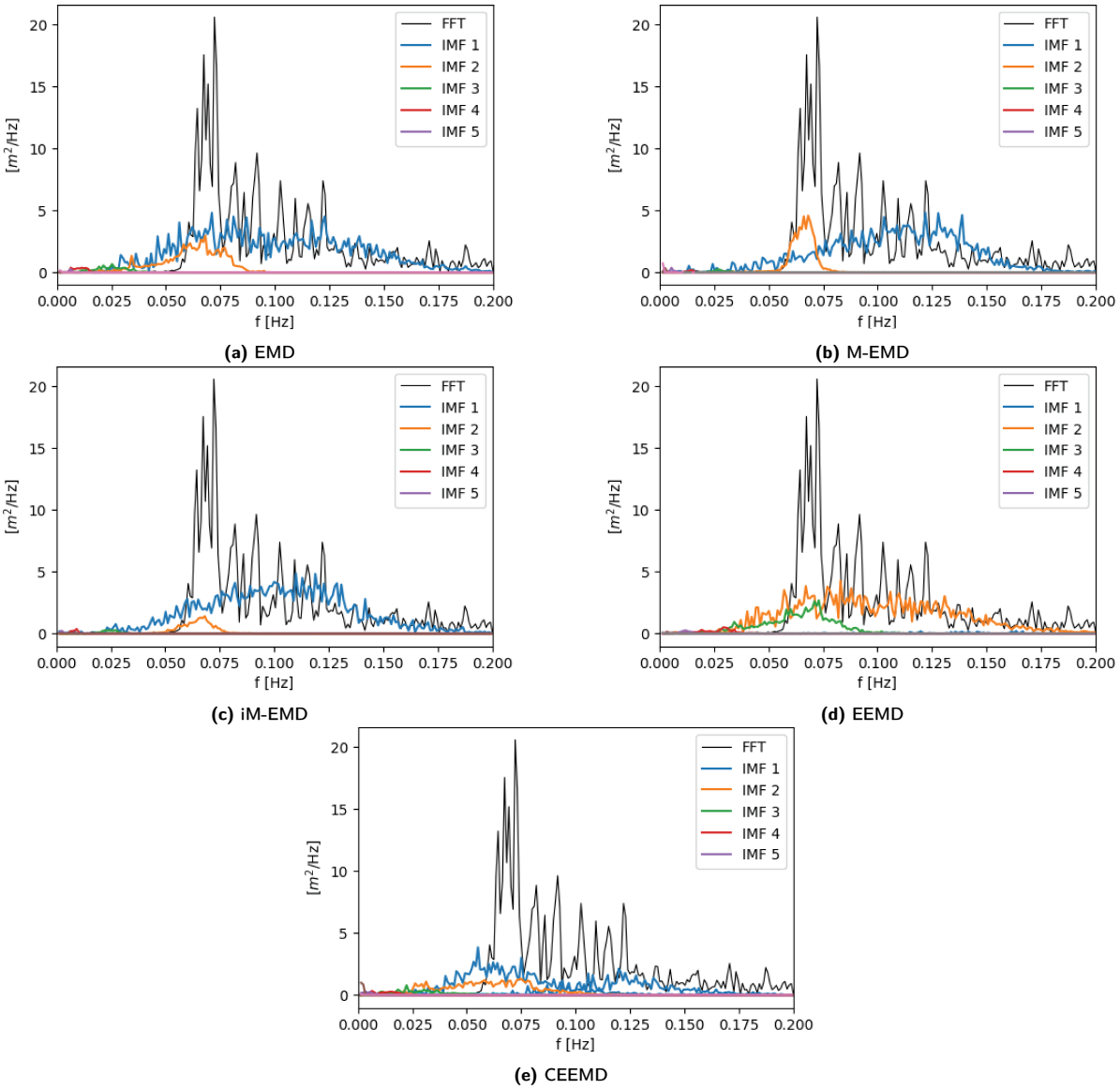

(a) EMD **(b)** M-EMD

(c) iM-EMD **(d)** EEMD

(e) CEEMD

Figure A.10: Marginal spectra per IMF with bandwidth 0.001 Hz (coloured solid lines) for the different sifting methods and Fourier spectra with bandwidth 0.001 Hz (black solid one) for a fore reef signal. The M-EMD shows the most prominent separation between IMF 1 and IMF 2.

B

VLF wave classification and resonance identification

Supplements for methodology

Time lag calculation

The time lag between stations depends on the velocity at which waves travel. On the reef flat (between the outer reef and inner reef station) the waves are relatively long compared to the water depth, allowing the use of the shallow water approximation. This assumption is confirmed by the ratio h/L that is calculated for all signals recorded at the reef stations. Wavelength L is determined with:

$$L = \frac{gT^2}{2\pi} \tanh kh \tag{B.1}$$

with wavenumber $k = 2\pi/L$. For period T the peak period T_p is used, which is derived from the Fourier spectrum. For each station, the mean water depth of a time series is used as h. For the outer, mid and inner reef the shallow water criterion ($h/L < 1/20$) is satisfied, as is illustrated in Figure B.1. Therefore, the shallow water phase velocity ($c = \sqrt{gh}$) is used in computing the time lag between these stations. The shallow water criterion is not satisfied for the fore reef (see Figure B.1), which has transitional water depths rather than shallow water.

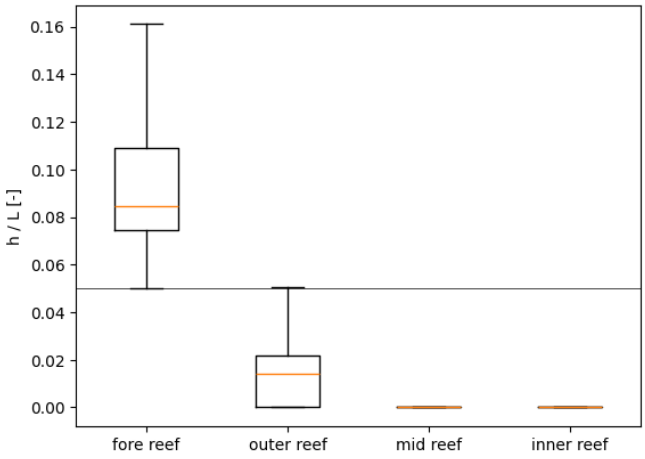

Figure B.1: Boxplots of the water depth (h) divided by the wavelength (L) at different reef stations for the complete field data. h is the mean water depth of a time series, and L is the wave length based on the peak frequency in the Fourier spectrum. The black horizontal line indicates the threshold for the shallow water approximation (0.05). All reef flat stations (inner, mid and outer reef) satisfy the shallow water criterion.

Instead of using the shallow water phase velocity, the group velocity should be used at the fore reef location.

The group velocity is defined as:

$$c_g = nc = 0.5\left(1 + \frac{2kh}{\sinh 2kh}\right) \tag{B.2}$$

With phase velocity c for transitional water depth:

$$c = \frac{gT}{2\pi}\tanh kh \tag{B.3}$$

The mean water depth at the fore reef and outer reef are determined, and linear interpolation is applied between these two stations to approximate the water depth of the intermediate x-coordinates (see Figure 3.2). The bathymetry of the Roi-Namur reef is available with a spatial resolution of 1 m.

The time lag between the fore and outer reef station is computed by both the shallow water phase velocity and the group velocity. The time lags resulting from these respective approaches are compared. The ratios are presented in Figure B.2, which shows that the ratio between these time lags is around 0.9 for the majority of the records..

As the wave group approaches more shallow water on the fore reef, the waves start breaking, after which the waves do not travel as a group anymore. It is assumed that once broken, the waves travel with $\sqrt{gh}$, since the water is relatively shallow at that point. An estimation of the location of the breaking point is made according to Miche criterion (Bosboom & Stive, 2021), namely:

$$\gamma = \frac{H_s}{h} = 0.4 - 0.5 \tag{B.4}$$

where h is the depth at which wave break for a given significant wave height $H_s = 4\sqrt{m_0}$, with m_0 the zeroth spectral moment determined with the Fourier spectrum. After estimating the breaking depth, the time lag is computed by using the group velocity up until this depth, and the shallow water phase velocity from that point to the outer reef.

Figure B.3 presents the time lag between the fore and outer reef, computed with the various methods, related to the eigenfrequency of the reef flat. For higher eigenfrequencies, the time lags are closer together. This is also illustrated in Figure B.4a, which shows the ratio between the time lag computed by the combined method and the group velocity. Situations with higher eigenfrequencies ($>$ 0.0025 Hz) are more likely to lead to powerful standing low-frequency waves at the inner reef, as is illustrated in Figure 4.16 in the results of Phase 3. In these situations, the time lag is less dependent on the use of one of the time lag computation methods, c_g or combined. Therefore, the exact location of the breaking point is not critical for an adequate approximation of the time lag between the fore and outer reef. Furthermore, when considering the complete time lag between the fore reef and inner reef, the ratio between the two methods for the fore-to-outer reef time lag roughly ranges between 0.9 and 1 with a median of 0.99. This is illustrated in Figure B.4b. Therefore, the combined method will be used to compute the time lag between the fore and outer reef stations, and the sensitivity to the exact location of the breaking point is neglected.

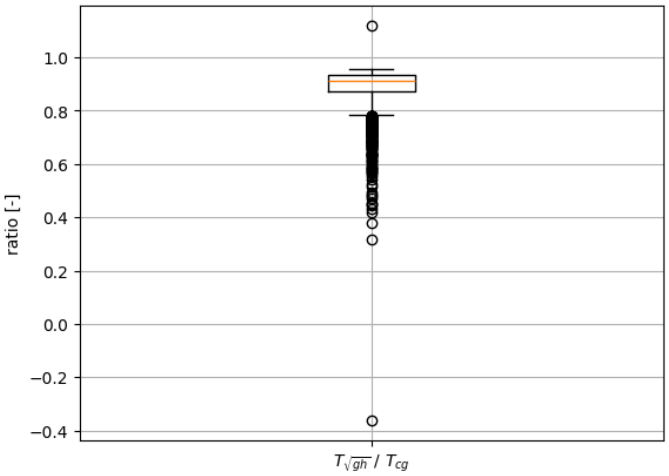

Figure B.2: The ratio between the fore-to-outer-reef time lag determined by shallow water phase velocity ($\sqrt{gh}$) and the wave group velocity (c_g) based on the peak frequency in the Fourier spectrum at the fore reef.

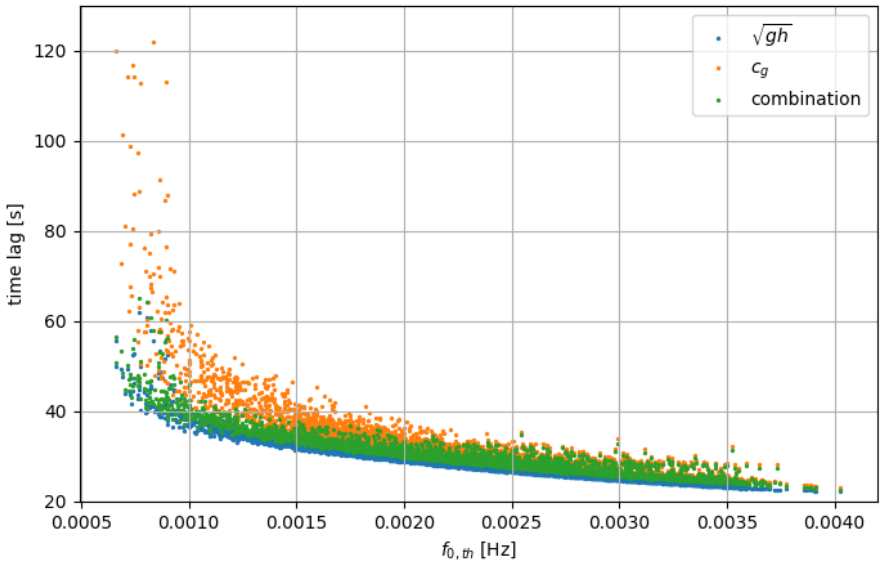

Figure B.3: Fore-to-outer reef time lag computed by group velocity (c_g), shallow water phase velocity ($\sqrt{gh}$) and a combination of these two approaches by including an estimated location for the breaking point. The time lags are displayed against the reef flat eigenfrequency ($f_{0,th}$) on the x-axis, illustrating a decreasing difference in time lags of the three methods for an increasing eigenfrequency.

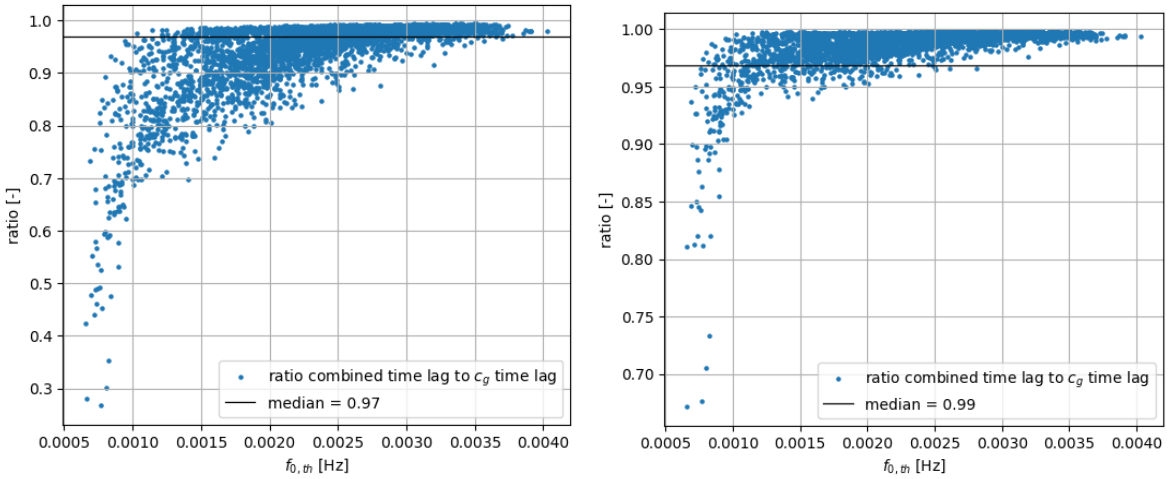

(a) Fore-to-outer reef time lag

(b) Fore-to-inner reef time lag

Figure B.4: (a) Ratio between fore-to-outer reef and (b) fore-to-inner reef time lag computed by the combined method, that considers c_g before breaking and $\sqrt{gh}$ after breaking, and the group velocity. Displayed against the reef eigenfrequency ($f_{0,th}$). The respective median ratios are indicated with a black horizontal line.

Fore reef signal and envelope

The signal at the fore reef primarily consists of short waves, often travelling in groups where wave heights vary. The varying wave height in a wave group leads to temporal variations in radiation stresses, resulting in a variation of the mean water level on a group scale (Bosboom & Stive, 2021). This low-frequency motion is referred to as the bound long wave. The bound long wave shares the length and frequency with the wave group and travels with the group (as it is bound to the wave group). A perfect bound long wave is exactly 180 degrees out of phase with the short wave group (see Figure B.5), though in reality, the correlation may vary.

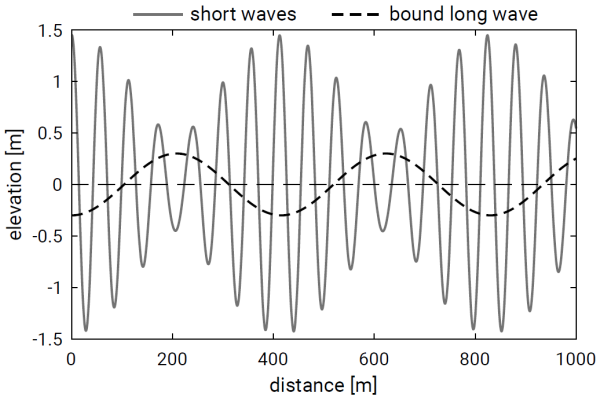

Figure B.5: A bound long wave that is 180 degrees out of phase with the wave group. (Bosboom & Stive, 2021)

Because the bound long wave is correlated to the wave group, it could be considered as an indicator for the length and amplitude of a wave group. The EMD decomposes a signal into monocomponents and may therefore be able to extract the bound long wave from the total fore reef signal. However, the small amplitude of the bound long wave relative to the short wave amplitude may disguise the bound long wave, complicating its extraction. Figure B.6 shows an example of a fore reef signal and its decomposition by the M-EMD. Figure B.6a illustrates the signal and IMF 5 (multiplied with a factor 10). At some moments, IMF 5 seems to align with the fore reef signal (with the correct phase shift), for example from t = 1600 s to the end of the time series. However, this is not always the case. It is also observed in this decomposition and others (not shown), that the first oscillation of the components show a larger amplitude than the later oscillations. This is apparent not only for IMF 5, but also the higher number of IMFs, as illustrated in Figure B.6b. This issue could be caused by the end effect, which is described in Section 2.5.2.

When investigating the relation between the low-frequency amplitude content of the fore reef signal and the fore reef envelope (computed with the Hilbert transform), a correlation is apparent (see Figure B.7). However, the pattern may be influenced by the end effect.

Additionally, it should be taken into account that the fore reef signals used in the analyses of this research contain the full signal, which is composed of both incoming and outgoing waves. While the short wave content of the fore reef signal are expected to mainly represent the incoming waves, the low-frequency oscillations may be a composite of incident and reflected waves.

Using the envelope of the fore reef signal is the preferred option as it is more reliable in describing the proper wave group amplitude and frequency and it is minimally affected by potentially outgoing waves.

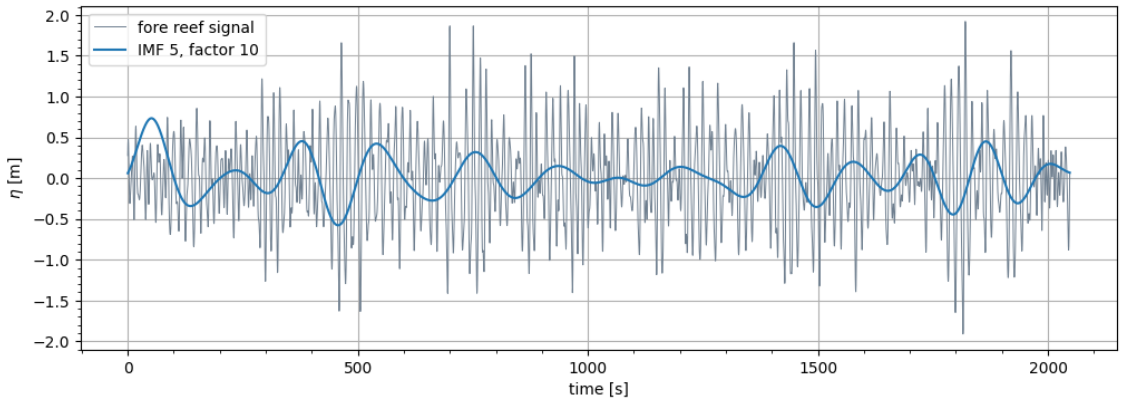

(a) Fore reef signal (grey line) and IMF 5 multiplied with a factor 10 (blue line)

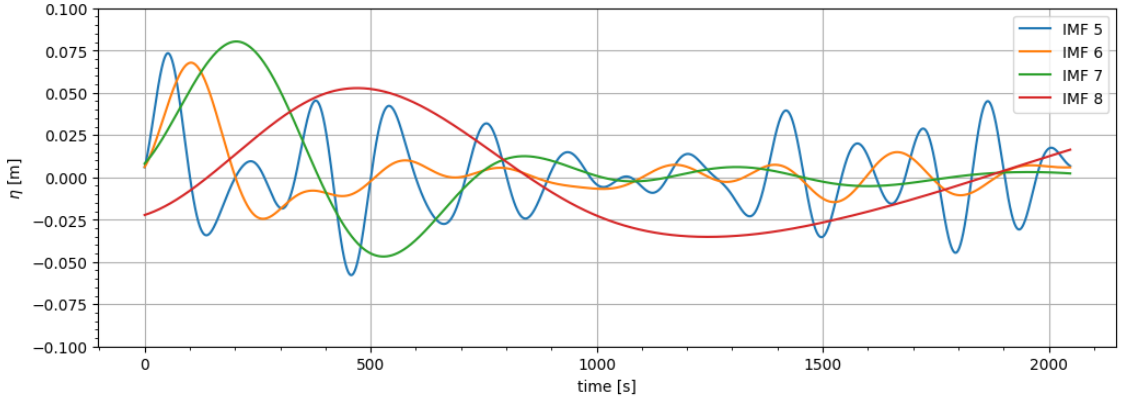

(b) Low-frequency components of fore reef signal decomposition

Figure B.6: Example of a (a) fore reef signal and (a-b) decomposition into IMFs by the M-EMD. IMF 5 sometimes aligns with wave groups in the fore reef signal (a), but not as a rule. Note that the first oscillation of the lower frequency components (b) is larger than subsequent oscillations, this could be an artefact of the end effect.

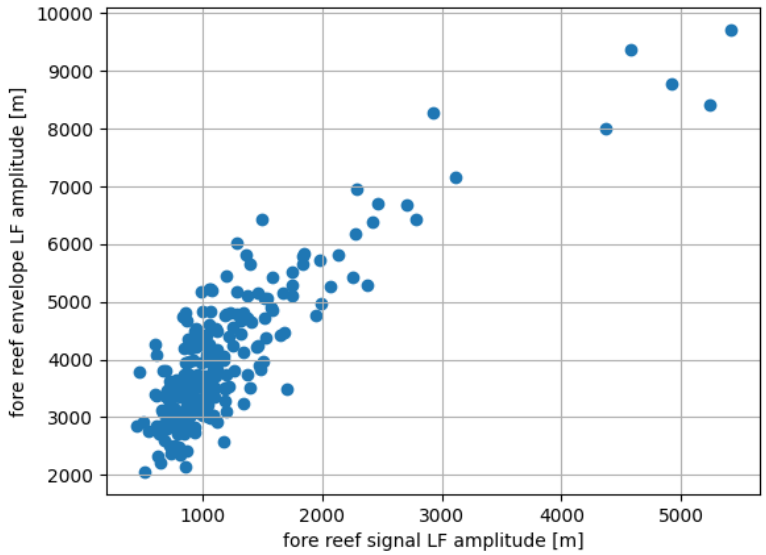

Figure B.7: The low-frequency amplitude content of the fore reef signal decomposition against fore reef envelope decomposition. The low-frequency amplitude content is described by the marginal amplitude spectra integrated from 0.001 to 0.04 Hz.

Frequency selection method for the resonance analysis

In the resonance analysis proposed by Gawehn et al. (2016) a peak transfer frequency is selected based on the maximum value of the transfer function, as described in Section 3.3.2. However, when looking at the result of this approach, the selection of $f_{p,transfer}$ may seem arbitrary in some cases. An example is given in Figure B.9a, where the transfer function H_{Axy} has a similar value around f = 0.015 Hz and f = 0.004 Hz, although slightly higher for the higher frequency. However, for f = 0.015 Hz, there seems to be an insignificant oscillation at the inner reef (denoted with the blue line in Figure B.9a). Coincidentally, the cross-product between the fore reef envelope and the inner reef signal at f = 0.015 Hz outscored the value at f = 0.004 Hz, but one may be more interested in the frequency with significant energy transfer and a significant inner reef oscillation for the purpose of this research. A new frequency selection method is therefore proposed. This method considers the frequencies for which H_{Axy} is greater than its 85th percentile, from the frequencies that satisfy that condition, the $f_{p,transfer}$ is then chosen based on the maximum value of the inner reef energy. This would result in the $f_{p,transfer}$ selection as illustrated in Figure B.9b for this example. This method is referred to as the 85th-percentile method.

Figure B.8 shows the comparison between the frequency selection by the original method and the 85th-percentile method. This figure illustrates that there is not a significant difference between the methods for the majority of the cases, but the 85th-percentile method tends to select a lower frequency (around 0.0025 Hz), where the original method selects a higher frequency.

Considering the classification of the VLF oscillations at the inner reef as determined in Phase 2 (see Sections 3.3 and 4.2, the 85th-percentile method results in a more intuitive distribution of the potential resonance cases in the resonance diagram, as is illustrated in Figure 4.9b in Section 4.3, when comparing it to Figure 4.9a.

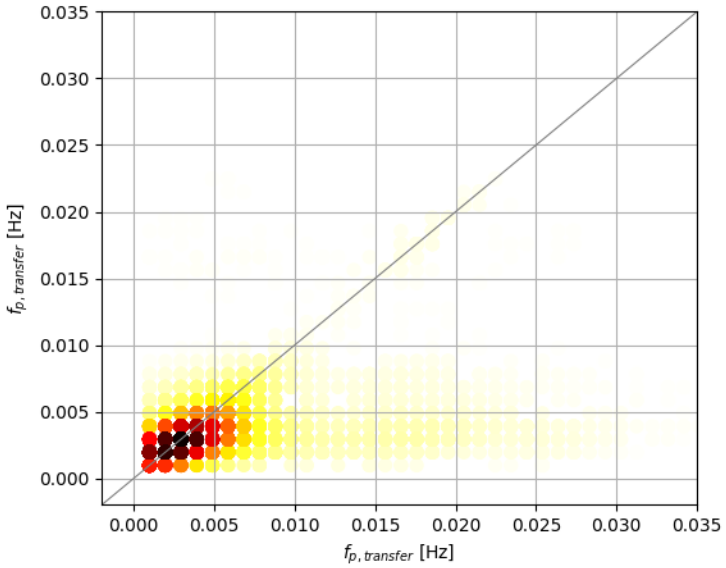

Figure B.8: A comparison of the selected $f_{p,transfer}$ in for the Fourier approach. The x-axis represents the $f_{p,transfer}$ based on the original method, the y-axis represents the $f_{p,transfer}$ based on the 85th-percentile method. The colour indicates the density of the scatter distribution, dark red denotes a high density, and light yellow a low density. The density distribution illustrates that the two methods mainly result in the same selection of frequencies, although the original frequency selection sometimes selects higher frequencies compared to the 85th-percentile method, as is illustrated by the light yellow area.

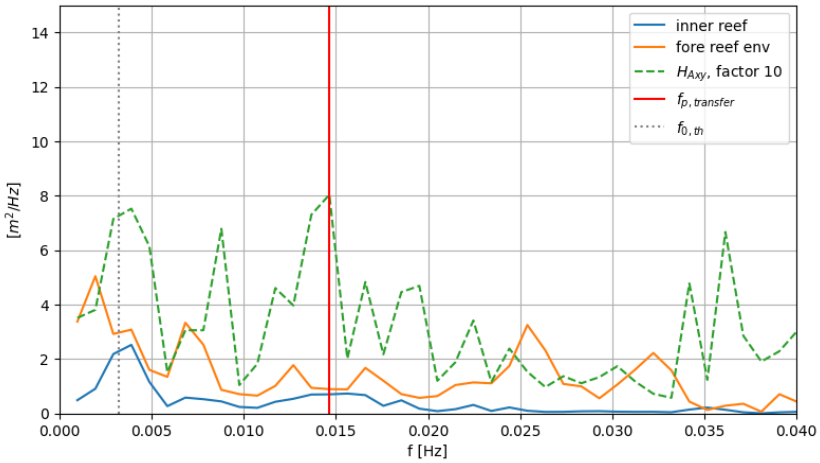

(a) frequency selection original method: maximum H_{Axy}.

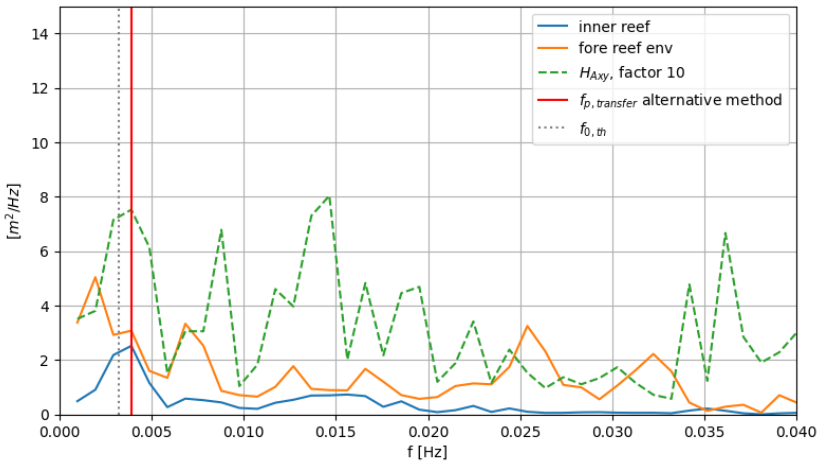

(b) frequency selection 85th-percentile method

Figure B.9: Example of (a) peak frequency selection by the original method and (b) the 85th-percentile method. The inner reef signal and fore reef envelope signal are denoted by orange and blue solid lines respectively, with the transfer function H_{Axy} as a green dashed line. The $f_{p,transfer}$ is indicated by a red vertical solid line and $f_{0,th}$ is indicated by a grey dotted line. Transfer function H_{Axy} exhibits similar values for two frequencies, f = 0.015 Hz and f = 0.004 Hz. While the original frequency selection method (a) only considers the value of H_{Axy}, the 85th-percentile method (b) aims to prioritize frequencies with significant energy transfer and notable inner reef oscillations.

Cross-spectra and energy transfer with the HHT

Despite similarities in spectral characteristics for the Fourier spectrum and Hilbert marginal spectrum, as demonstrated in previous research (e.g., Hwang et al., 2005) and Phase 1 of this study (see Section 4.1.3), special attention is required for computing the cross-spectrum.

As the Fourier transform assumes stationarity and linearity, a time series is transformed to the frequency domain, yielding a single complex number per frequency step. These complex numbers provides information about the amplitude and phase of oscillations at each specific frequency. The cross-spectrum (S_{x1x2}) between two signals, $x_1(t)$ and $x_2(t)$, is then computed by multiplying the frequency-distributed information $X_1(f)$ by the complex conjugate of $X_2(f)$:

$$S_{x1x2}(f) = \frac{X_1(f) \cdot [X_2(f)]^*}{2df} \tag{B.5}$$

where df is the frequency resolution and $[..]^*$ denotes the complex conjugate.

The Hilbert spectrum is constructed from the analytic signal (see (3.11)), which is the complex representation of a real-valued signal (or IMF), obtained by the Hilbert transform. Like the Fourier transform, the complex value describes the amplitude and phase of the oscillation. However, they serve different purposes. While the complex values of the Fourier transform represent information per frequency step, the analytic

signal provides a complex value per time step, which can be translated into instantaneous amplitude, phase, and frequency. When organized in a frequency-time distribution, the Hilbert spectrum represents the amplitude or energy, which is real-valued. The cross-spectrum cannot be computed like (B.5) because it requires the frequency-distributed complex values.

While research on the cross-spectrum for the Hilbert-Huang transform is limited, a few methods have been proposed. Sun et al. (2016) proposed the cross-marginal spectrum, which is defined as follows:

$$h_{x1x2}(\omega) = h_{x1}(\omega) \cdot [h_{x2}(\omega)]^* \tag{B.6}$$

where h_{x1} and h_{x2} are the marginal spectra of the sum of IMFs for signal $x_1(t)$ and $x_2(t)$ respectively. The marginal spectrum is defined as the real-valued Hilbert spectrum integrated over time. Since the marginal spectrum lacks an imaginary part, using the complex conjugate seems trivial. Practically, (B.6) multiplies the time-integrated frequency-distributed amplitudes of the respective signals.

Alternatively, Shan et al. (2021) propose a method similar to the Continuous Wavelet Transform (CWT) cross-spectrum. Instead of using the standard Hilbert spectrum, they define the spectrum $RHHT(t, \omega(t))$, similar to the description in (3.15).

$$RHHT(t, \omega(t)) = \sum_{j=1}^{n} a_j(t) e^{i\phi_j(t)} \tag{B.7}$$

with $a_j(t)$ and $\phi_j(t)$ the instantaneous amplitude and phase, as described by (3.12) and (3.13) respectively. The cross-spectrum between signals $x_1(t)$ and $x_2(t)$ is then defined as:

$$SH_{x1x2}(t, \omega) = \int_{t-\delta/2}^{t+\delta/2} RHHT_{x1}(\tau, \omega) \cdot [RHHT_{x2}(\tau, \omega)]^* d\tau \tag{B.8}$$

where δ is the length of the integrating range. In the context of the fore and inner reef signal, a time lag Δt would logically be included, resulting in the description:

$$SH_{xy}(t, \omega) = \int_{t-\delta/2}^{t+\delta/2} RHHT_{x1}(\tau, \omega) \cdot [RHHT_{x2}(\tau + \Delta t, \omega)]^* d\tau \tag{B.9}$$

Unfortunately, the `EMD` package offers no option to compute the complex-valued representation of the Hilbert spectrum, as described in (B.7). This is not surprising, since it is a notation not found in other research papers. However, the absolute of the cross-spectrum is utilized in the computation of the energy transfer and not the original cross-spectrum. Assuming the derivation in (3.31), the absolute cross-spectrum may be defined as the multiplication of the frequency-distributed amplitudes.

Based on the methods proposed by Sun et al. (2016) and Shan et al. (2021) and the limitations of the `EMD` package, some approaches to compute the energy transfer are compared.

Full time-integration of time series

For the initial application of the resonance criterion, the Hilbert spectra are integrated over the full time-length of the records. This way, the marginal spectra resemble the Fourier spectra, as illustrated in Section 4.1.3. Three methods are analysed for the computation of the transfer function H_{x1x2} between the fore reef envelope and the inner reef signal. These methods are based on the derivation of the Fourier based function:

$$H_{x1x2} = \frac{|G_{x1x2}|}{G_{x1}} = \frac{|X_1||X_2|/(2df)}{|X_1|^2/(2df)} = \frac{|X_2|}{|X_1|} = \frac{\sqrt{G_{x2}}}{\sqrt{G_{x1}}} \tag{B.10}$$

The following methods are applied:

1. For the first approach, the marginal energy spectra for the fore reef envelope and inner reef signal are computed through the full-time time-integration of the Hilbert energy spectrum. This method resembles the Fourier approach most since it uses the energy spectra.

$$H_{Axy,1} = \frac{\sqrt{h_{inner}(f)}}{\sqrt{h_{fore}(f)}} \tag{B.11}$$

2. The second method is similar but the marginal spectra are based on the integration of the Hilbert amplitude spectra instead of the energy spectra. This is similar to the approach by Sun et al. (2016), see (B.6).

$$H_{Axy,2} = \frac{h_{a,inner}(f)}{h_{a,fore}(f)} \tag{B.12}$$

3. Finally, a combination of these two methods is considered:

$$H_{Axy,3} = \frac{h_{a,fore}(f) \cdot h_{a,inner}(f)}{h_{fore}(f)} \tag{B.13}$$

The eventual product of the transfer function is the selection of the peak transfer frequency $f_{p,transfer}$. The 85th-percentile method is applied for the frequency selection, since this method yields more logical results (see Sections 4.2 and B). Figure B.10 shows the relation between the $f_{p,transfer}$ selected in the Fourier approach and the $f_{p,transfer}$ selected in the respective HHT approaches. This figure indicates that there is minimal difference in the selection of peak transfer frequency as a result of the various transfer function approaches. Figure B.11 shows the different H_{xy} distributions for an example. The transfer function by method 1 $H_{xy,1}$ aligns most with H_{xy} determined by the Fourier approach. An exact match between the two approaches is not expected because of the assumptions of the respective spectral analysis methods. Although it is not necessary that the scale of the H_{xy} matches the Fourier scale, the internal scaling is of importance. For example, $H_{xy,3}$ has its maximum at a lower frequency compared to the other methods. For the full time-integration approach for the resonance criterion, method 1 is used to compute the transfer function H_xy as it resembles the Fourier transfer function most in internal scaling.

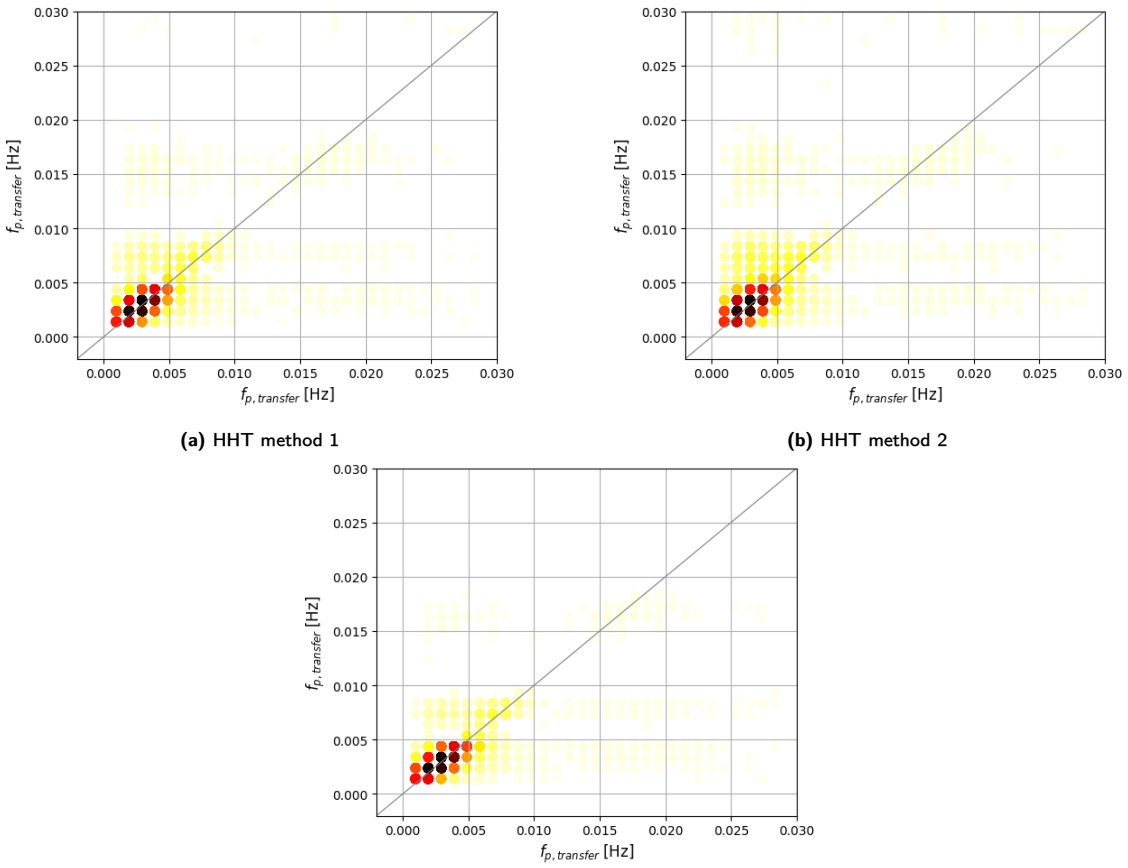

(a) HHT method 1

(b) HHT method 2

(c) HHT method 3

Figure B.10: The selected $f_{p,transfer}$ in the Fourier method and the various HHT methods. The colour indicates the density of the scatter distribution, dark red denotes a high density, and light yellow a low density. The three methods have different approaches to compute the transfer function, which are described by (B.11), (B.12) and (B.13) respectively. The 85th-percentile method is used for frequency selection.

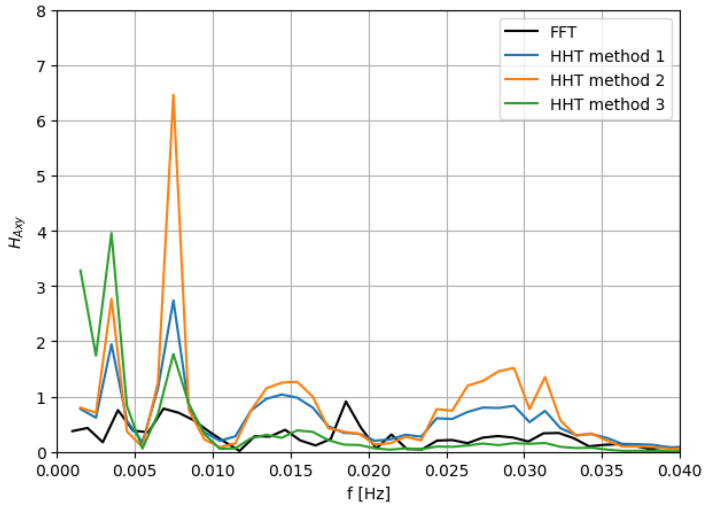

Figure B.11: Example of the transfer functions H_{Axy} computed by the different methods described by (B.11), (B.12) and (B.13) respectively for a fore reef envelope and an inner reef signal. The H_{Axy} computed with method 3 is scaled with a factor $1/800$. H_{Axy} of method 1 (blue solid line) displays internal scaling most consistent with the Fourier transfer function (black solid line).

Partly time-integration of time series

In the partly time-integration resonance analysis, the fore reef envelope and inner reef signal are compared via a time window (with a length of 600 s) and the time lag between the two signals is considered in choosing the ranges of the respective windows. The same approach as considered for the full time integration can be used but with smaller time integrations, however an approach based on (B.9) may also be relevant in this case. Only method 1 of the full-integration approach is used, as the results proved to be very similar to the other two approaches. The methods that are applied for the partly time-integration are as follows:

1. The first method is similar as previously defined, but only a partial integration is applied with the length of the time window t_w (600 seconds) and the time lag Δt is included in the time window for the inner reef Hilbert spectrum.

$$H_{xy,1}(\omega,\tau) = \frac{\sqrt{\int_{t_0}^{t_0+t_w} HS_{inner}(\omega, t+\tau)}}{\sqrt{\int_{t_0}^{t_0+t_w} HS_{fore}(\omega,t)}} \tag{B.14}$$

2. The second approach is based on (B.9). This approach multiplies the Hilbert spectra per time step, including a time lag for the inner reef spectrum. However, since the time lag is an estimate and not an exact value, the inner reef signal and fore reef envelope signal should not compared with such accuracy as the time resolution provides (0.5 s time steps). Instead, a margin is applied to the time lag by applying a moving average to the time-axis of the Hilbert spectrum. If the same margin is applied as in the analysis in Phase 2 (see Section 4.2), the range of the time lag is 0.8-1.2 times the computed time lag. For a median time lag between the fore and inner reef station of 128 s, this margin implies a range of approximately 50 seconds. A size of 50 seconds (or 100 time steps) is thus applied as moving average window, an example of a smoothed Hilbert spectrum is illustrated in Figure B.12. The transfer function is then described as:

$$H_{xy,2}(\omega,\tau) = \frac{\int_{t_0}^{t_0+t_w} \overline{HS}_{a,fore}(\omega,\tau) \cdot \overline{HS}_{a,inner}(\omega, t+\tau)dt}{\int_{t_0}^{t_0+t_w} \overline{HS}_{fore}(\omega,t)} \tag{B.15}$$

where $\overline{HS}_a$ and $\overline{HS}$ denote the smoothed Hilbert amplitude spectrum and smoothed Hilbert energy spectrum respectively.

The resulting comparison of the $f_{p,transfer}$ selection is presented in Figure B.13. It appears that these two approaches result in a very similar distribution of both diagrams. To stay consistent with the approach for the full-integration resonance analysis, method 1 is chosen for this analysis.

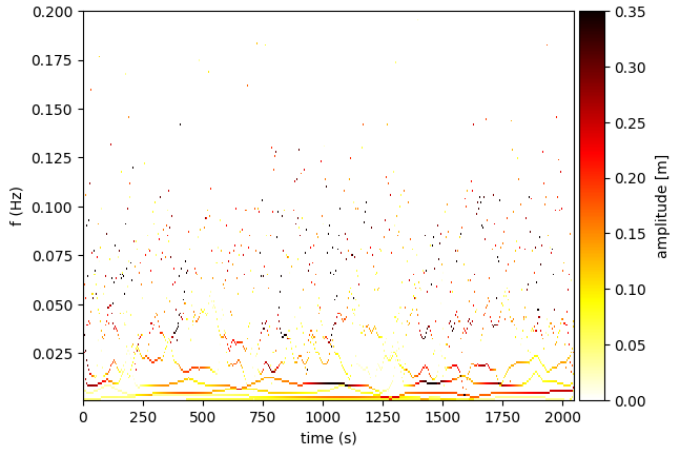

(a) Original Hilbert amplitude spectrum

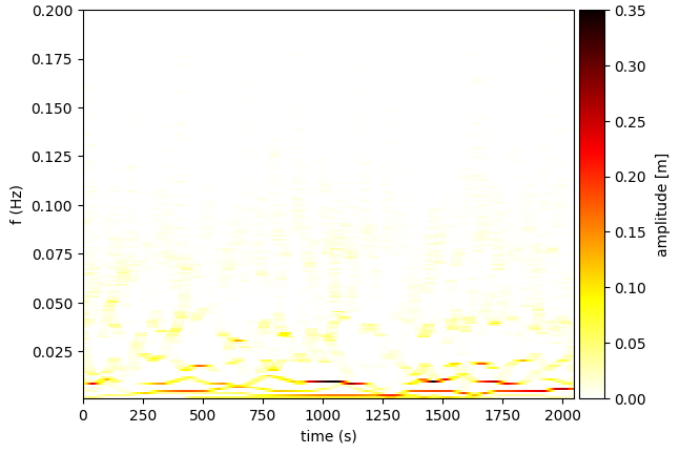

(b) Smoothed Hilbert amplitude spectrum

Figure B.12: Example of the Hilbert amplitude spectra, with (a) original time resolution and (b) smoothed with a moving window of 50 seconds (100 samples), for s fore reef envelope.

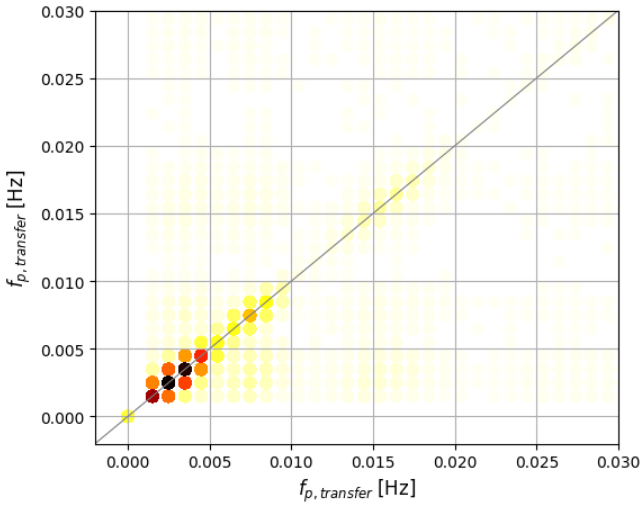

Figure B.13: A comparison of the selected $f_{p,transfer}$ in the two HHT methods for the partial-integration resonance analysis. The colour indicates the density of the scatter distribution, dark red denotes a high density, and light yellow a low density. The two methods have different approaches to compute the transfer function, which are described by (B.14) (on x-axis) and (B.15) (on y-axis) respectively. The 85th-percentile method is used for frequency selection.

Supplements for results

Classification of wave propagation type

Figures B.14 and B.15 are supplements for the classification of the propagation type, as is further elaborated in Section 4.2. Figure B.14 illustrates the phase difference between the dominant VLF component of the inner and mid reef signal decompositions in radians. The trends with their origin in 2π and -2π result from the phase transition of consecutive waves, causing jumps to 2π or -2π. These deviations are corrected by adding or subtracting 2π if the phase difference falls outside the range $-3/2\pi$ and $1/2\pi$. The result is the realigned diagram in Figure B.15. In the realigned distribution, there is are two noticeable trends for cases where the coherence is greater than 0.8. The two linear relation with a slightly different gradient are related to frequency ranges of IMF 6 and 7, which are selected for as dominant VLF component.

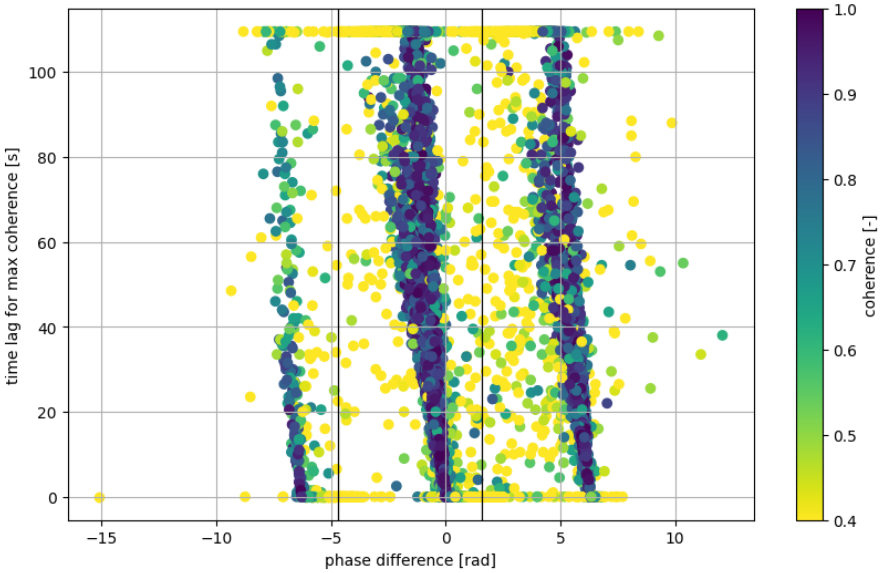

Figure B.14: Phase difference in radians versus the time lag of the maximum coherence determined with (3.23), between the mid and inner reef VLF component.

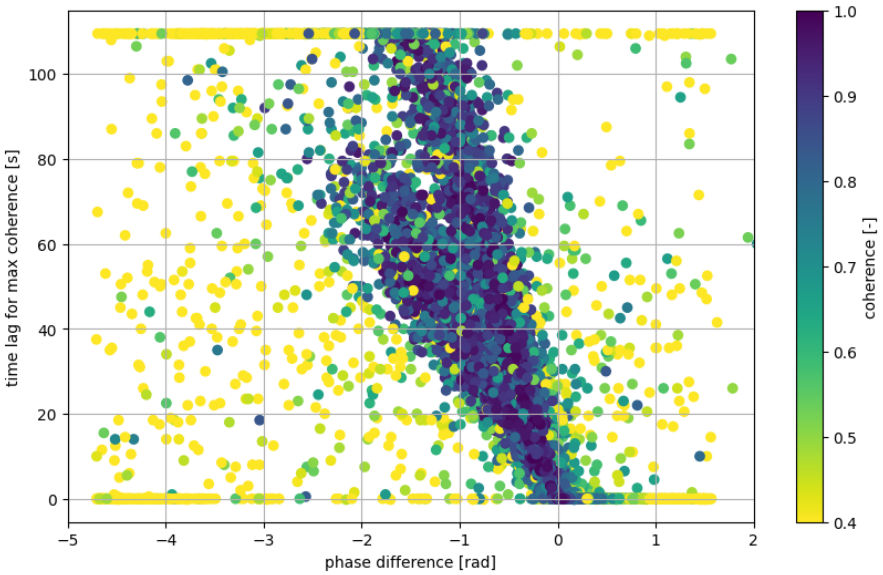

Figure B.15: Distribution of phase difference in radians to time lag for the maximum value of coherence, determined with (3.23). Every point represents a time window containing approximately one full wave. In this figure, phase differences over 2π are shifted to the origin. This figure is an adjusted version of Figure B.14.

Resonance analysis

This section is a supplement for Section 4.2.2 and contains resonance diagrams for the various resonance analysis approaches with their scatter densities indicated with histograms displayed at the top and on the right of each scatter diagram. The histograms denote the unweighted number of points per bin unless indicated otherwise. The bin width for the diagrams are 0.01 or 0.02 for $normE_{p,transfer}$ (y-axis) and 0.1 for $f_{p,transfer}/f_{0,th}$ (x-axis).

Resonance analysis with the FFT

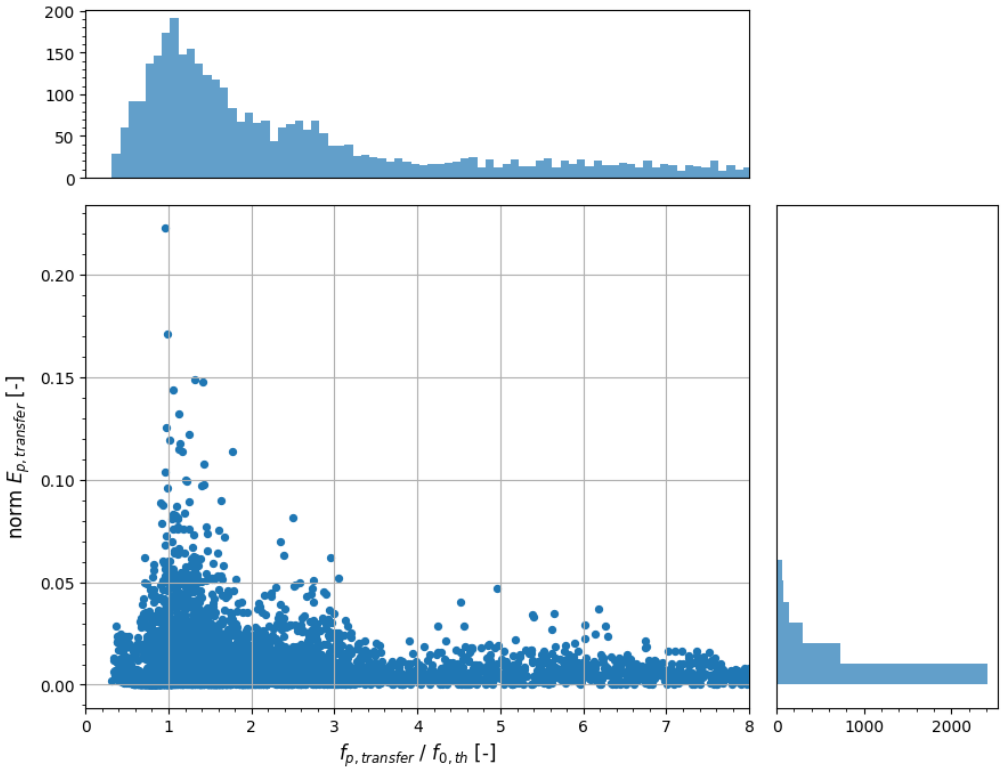

(a) FFT, original frequency selection method.

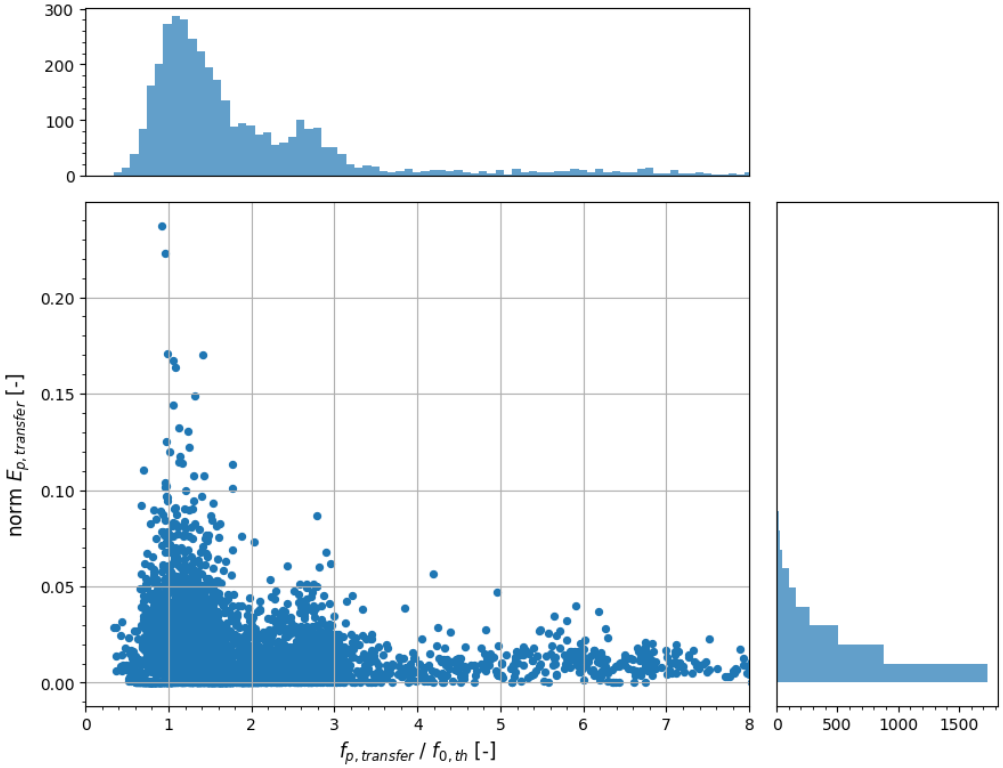

(b) FFT, 85th-percentile frequency selection method.

Figure B.16: Resonance diagram for Fourier spectra approach with the (a) original and (b) 85th-percentile frequency selection method. The histograms on the top and right of the resonance diagram indicate the scatter density.

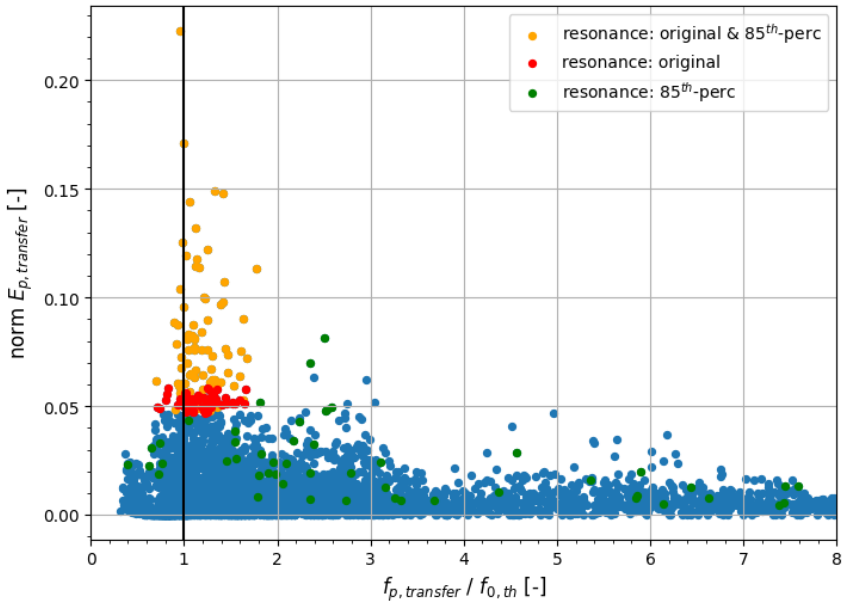

(a) FFT, original frequency selection method.

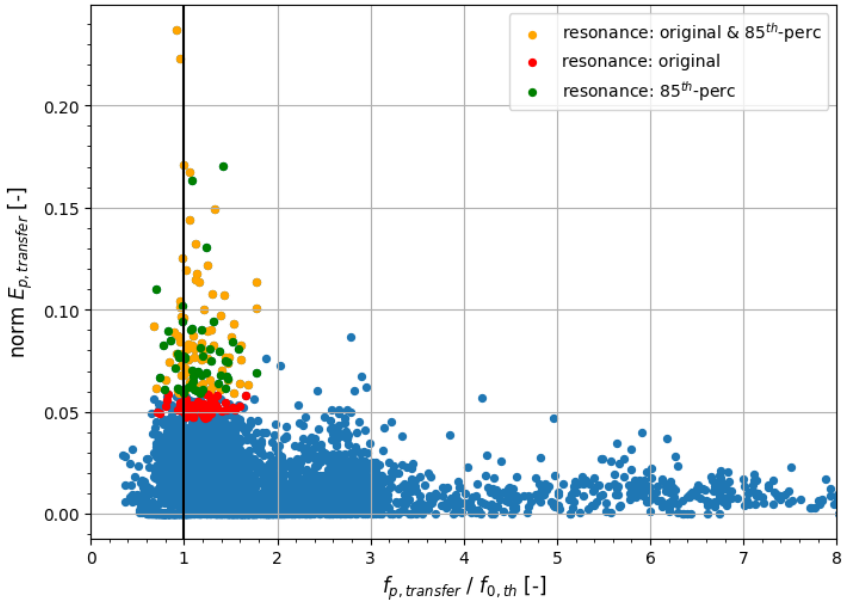

(b) FFT, 85th-percentile frequency selection method.

Figure B.17: Resonance diagram for Fourier spectra approach with the (a) original and (b) 85th-percentile frequency selection method. The colours indicate the resonance classification by the different methods: orange dots are identified as resonance by both methods, red dots are only identified by the original frequency selection method, green dots are only identified by the 85th-percentile frequency selection method. The red dots are the result of the higher threshold for the 85th-percentile method, to maintain a resonance occurrence of 3.6%.

Resonance analysis with the HHT

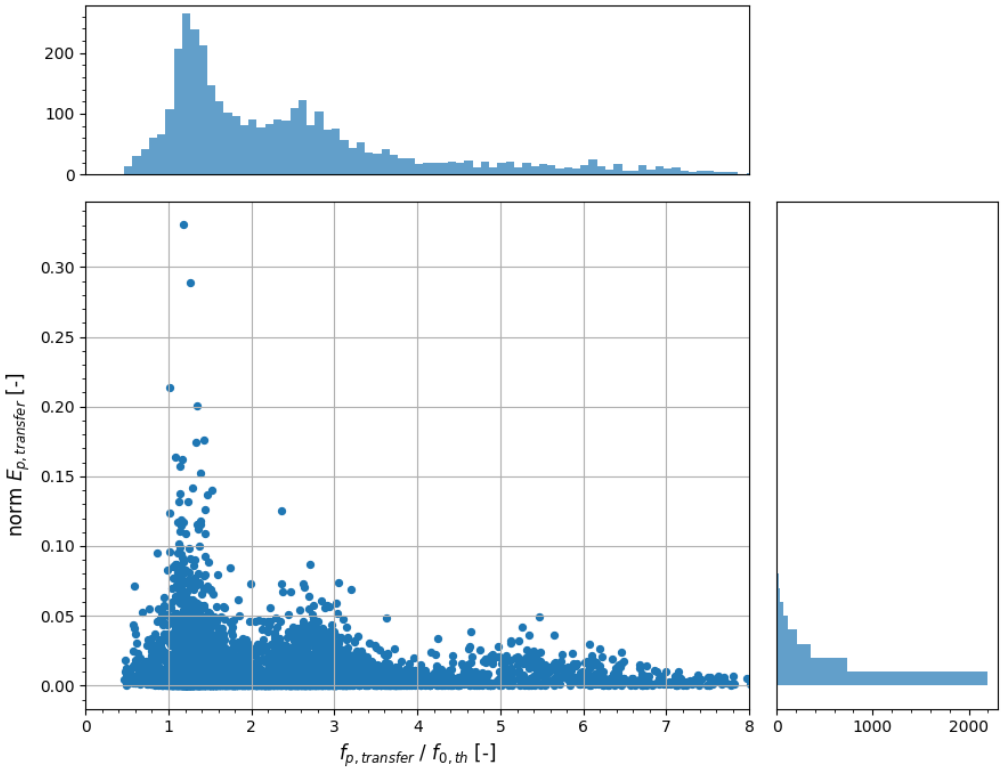

(a) HHT, original frequency selection method.

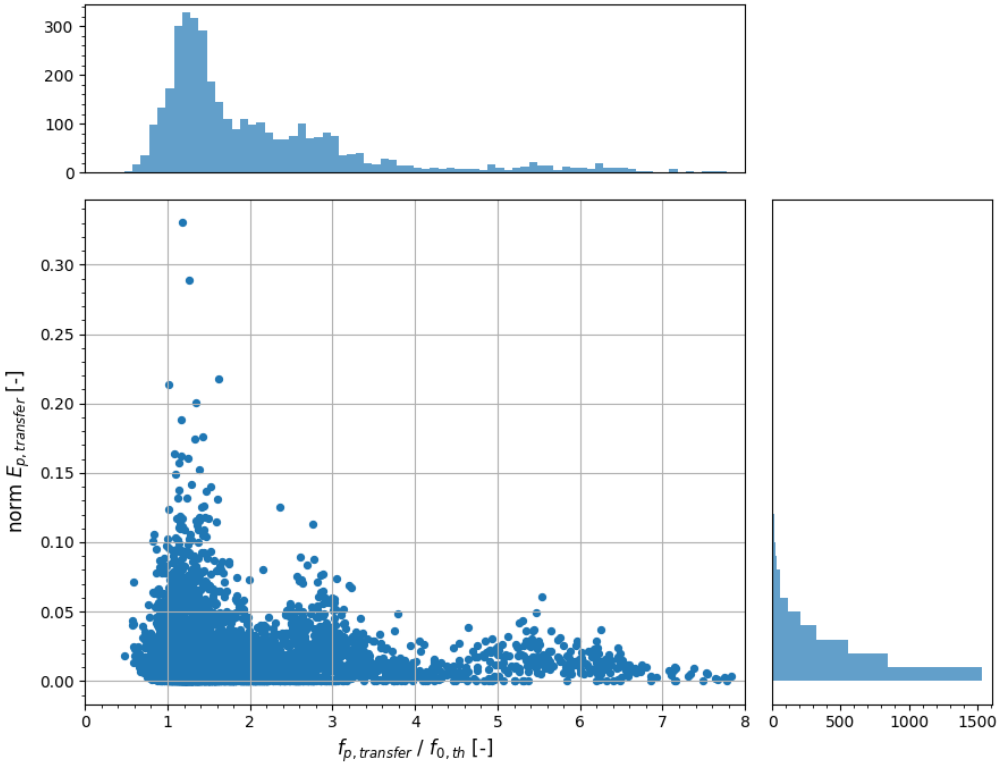

(b) HHT, 85th-percentile frequency selection method.

Figure B.18: Resonance diagram for Hilbert spectra approach with the (a) original and (b) 85th-percentile frequency selection method. The histograms on the top and right of the resonance diagram indicate the scatter density.

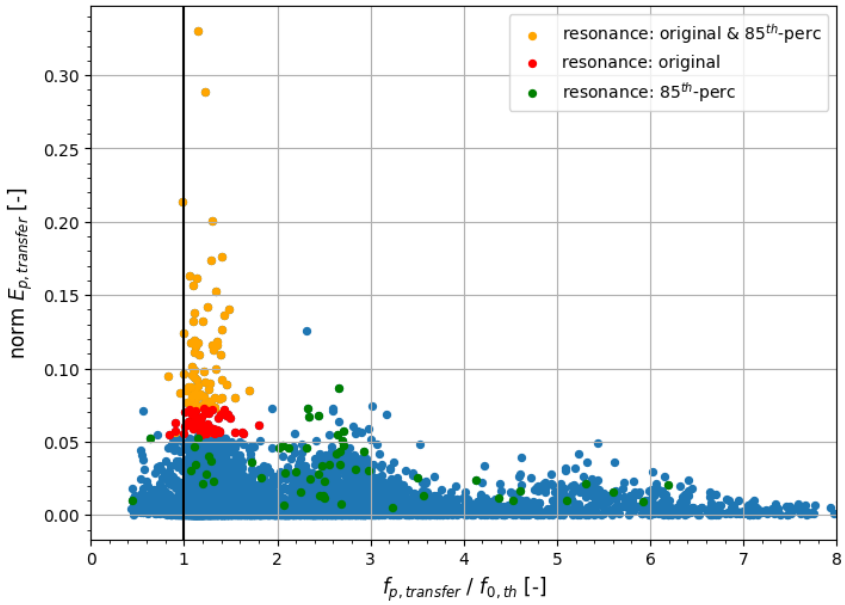

(a) HHT, original frequency selection method.

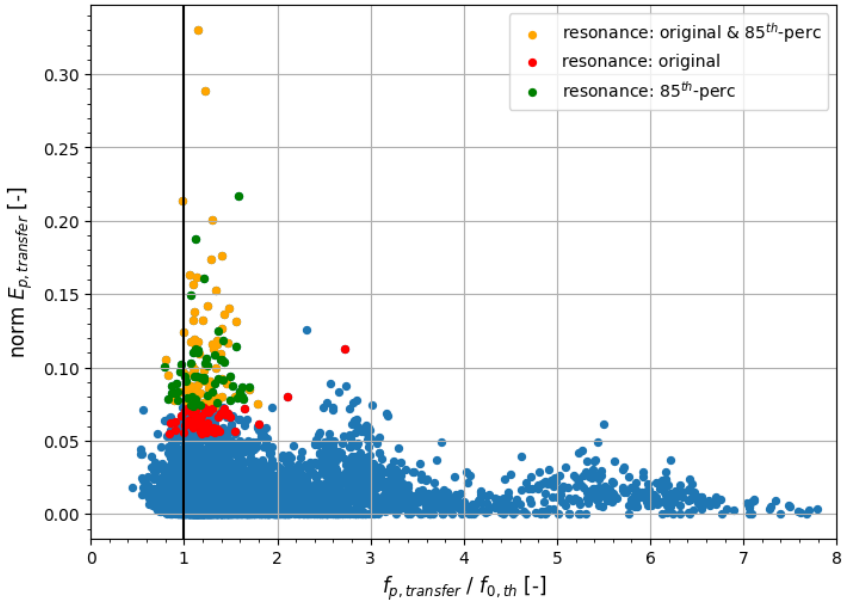

(b) HHT, 85th-percentile frequency selection method.

Figure B.19: Resonance diagram for Hilbert spectra approach with the (a) original and (b) 85th-percentile frequency selection method. The colours indicate the resonance classification by the different methods: orange dots are identified as resonance by both methods, red dots are only identified by the original frequency selection method, green dots are only identified by the 85th-percentile frequency selection method. The red dots are the result of the higher threshold for the 85th-percentile method, to maintain a resonance occurrence of 3.6%.

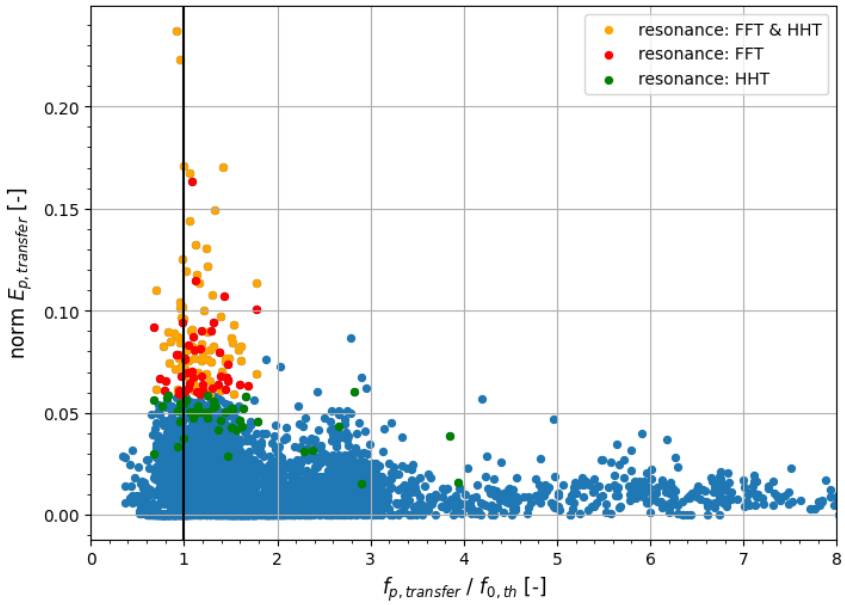

(a) FFT, 85th-percentile frequency selection method.

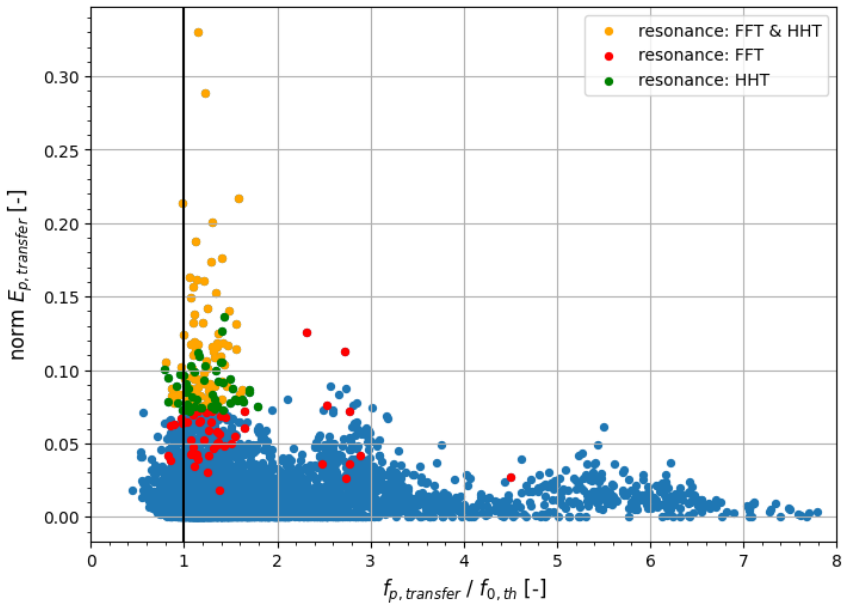

(b) HHT, 85th-percentile frequency selection method.

Figure B.20: Resonance diagrams for (a) Fourier and (b) Hilbert spectra approach with 85th-percentile frequency selection. The colours indicate the resonance classification by the different methods: orange dots are identified as resonance by both methods, red dots are only identified by the FFT method, green dots are only identified by the HHT method.

Time-varying resonance analysis with the HHT

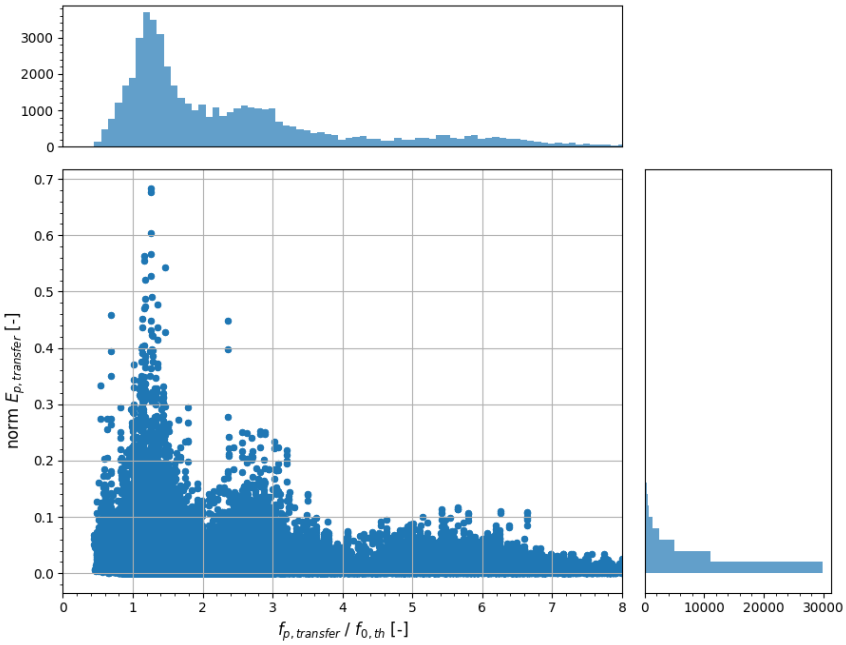

Figure B.21: Resonance diagram for time-varying Hilbert spectra approach (HHT_{temp}) with the 85^{th}-percentile frequency selection method for all signals. The histograms on the top and right of the resonance diagram indicate the scatter density.

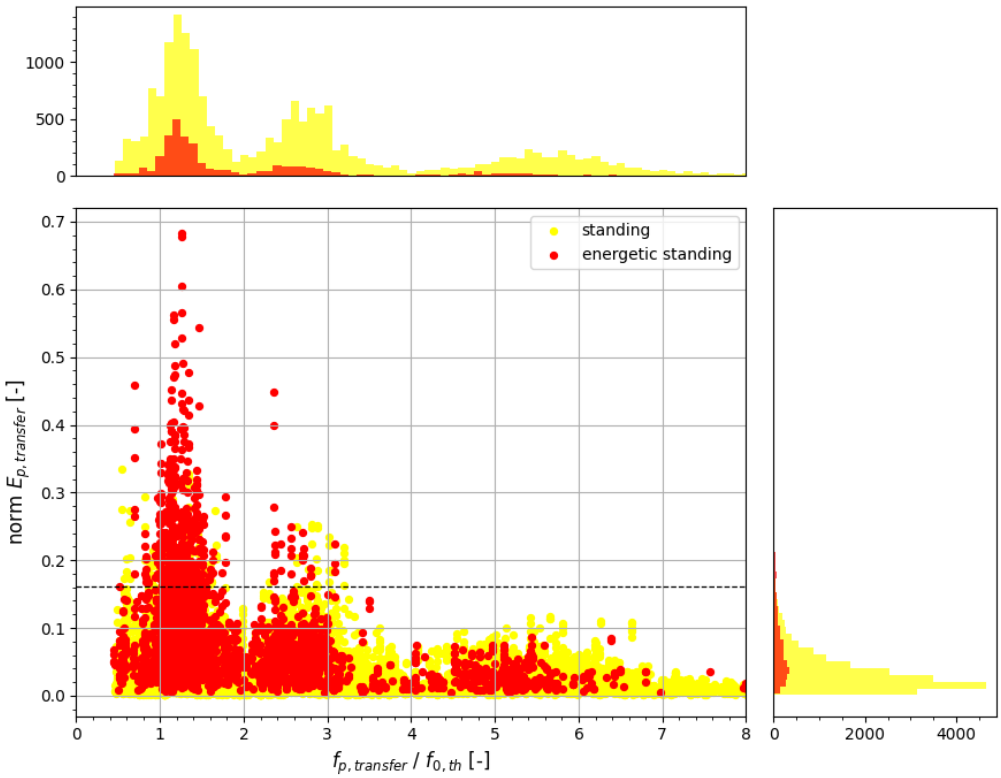

(a) Standing and powerful standing VLF wave classes.

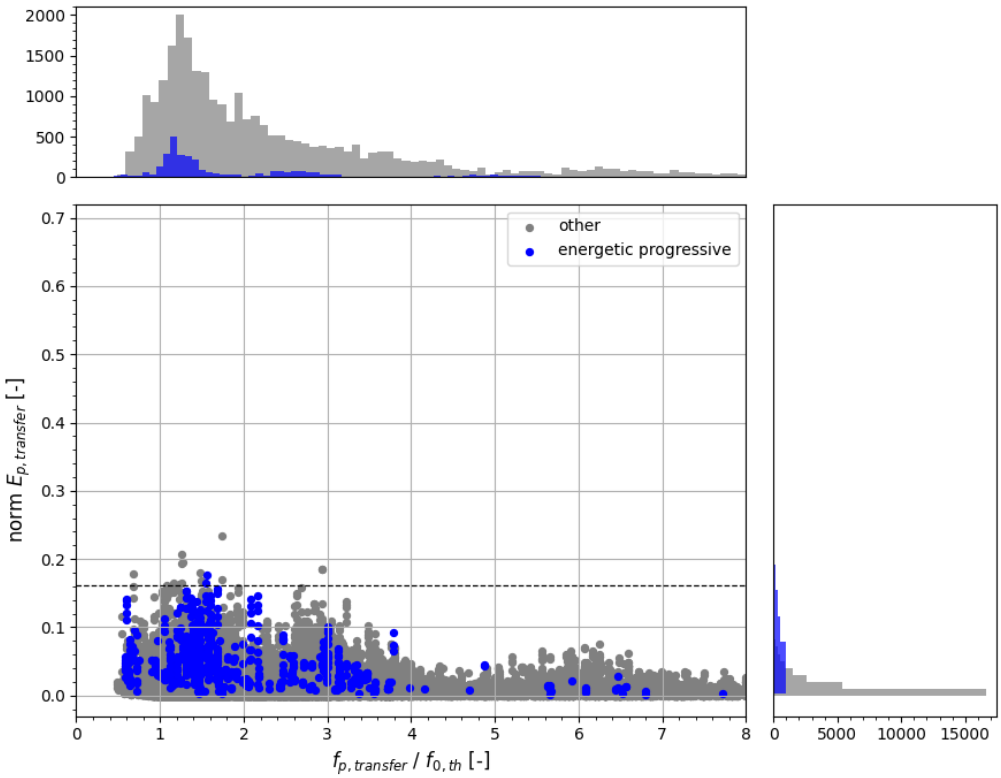

(b) Progressive and powerful progressive VLF wave classes.

Figure B.22: Resonance diagram for time-varying Hilbert spectra approach (HHT_{temp}) with the 85^{th}-percentile frequency selection method for the (a) standing VLF wave classes and (b) progressive VLF wave classes. The histograms on the top and right of the resonance diagram indicate the scatter density.

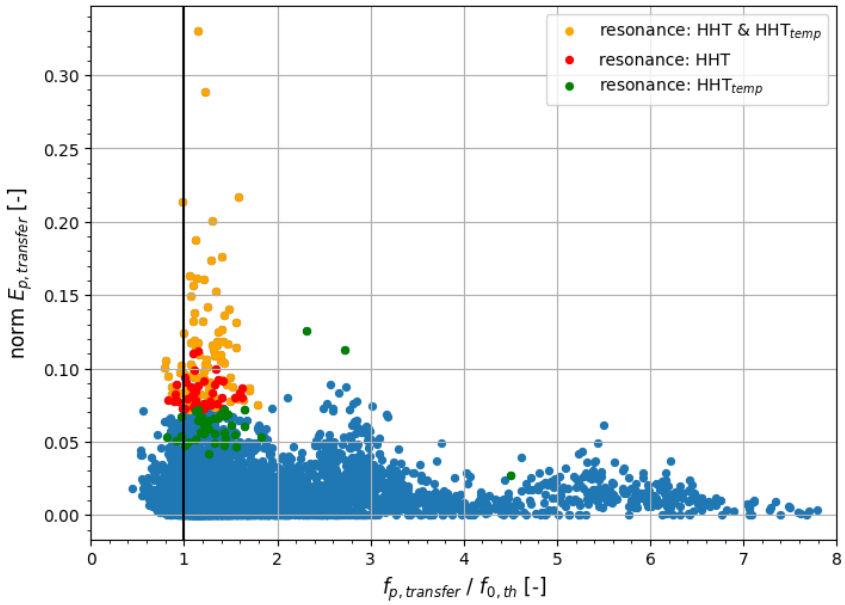

(a) HHT, 85th-percentile frequency selection method.

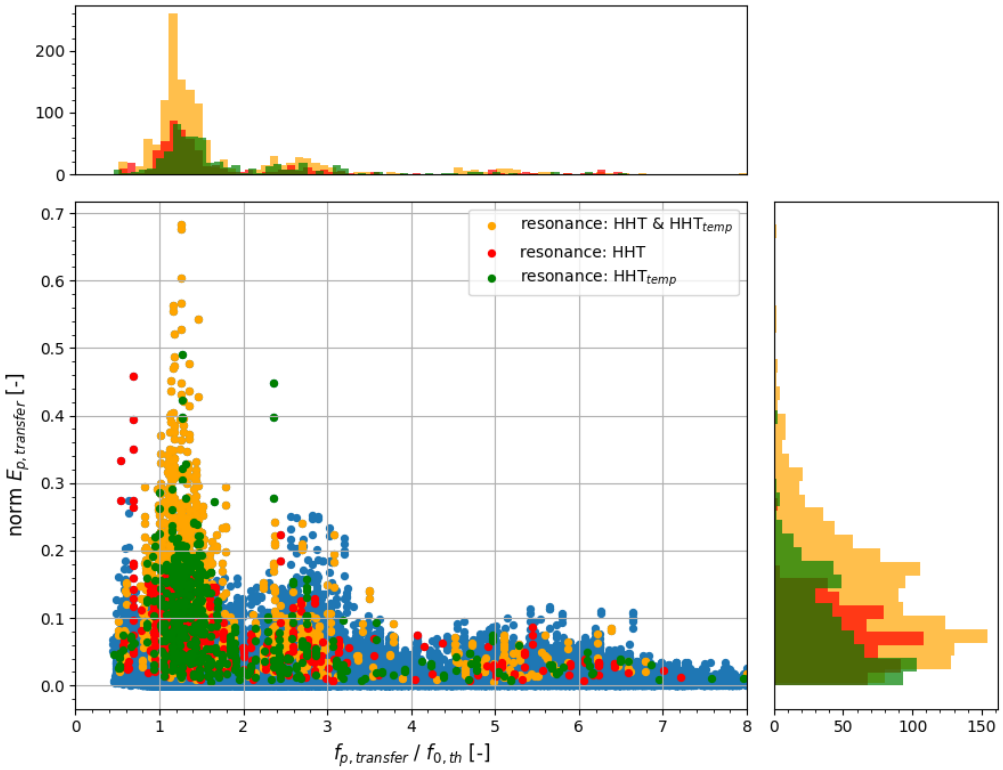

(b) HHT$_{temp}$, 85th-percentile frequency selection method.

Figure B.23: Resonance diagrams for HHT and HHT$_{temp}$ approach with the 85th-percentile frequency selection approach. The colours indicate the resonance classification by the different methods: orange dots are identified as resonance by both methods, red dots are only identified by the HHT method, green dots are only identified by the HHT$_{temp}$ method. The histograms on the top and right of the resonance diagram in (b) indicate the scatter density.

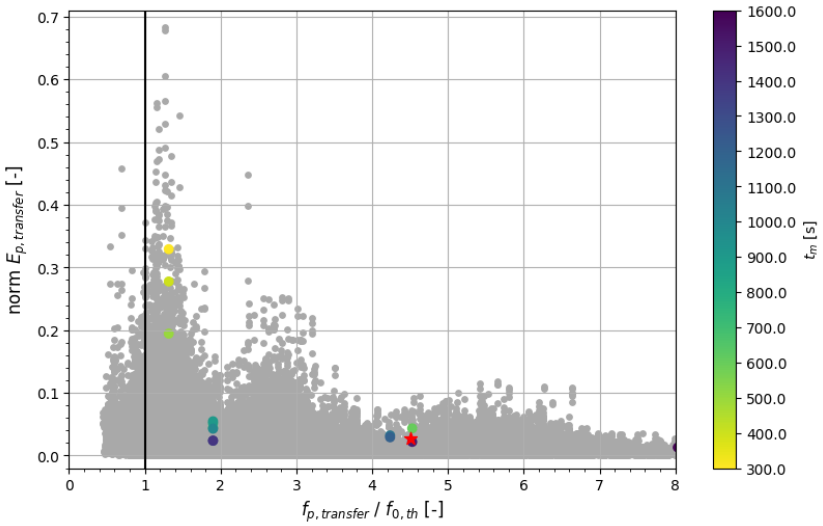

(a) resonance diagram

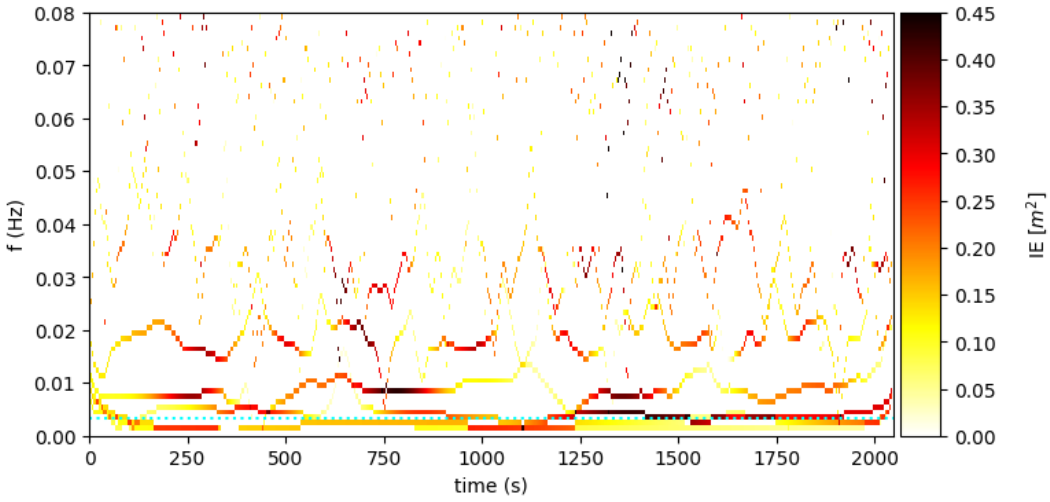

(b) Hilbert spectrum fore reef envelope

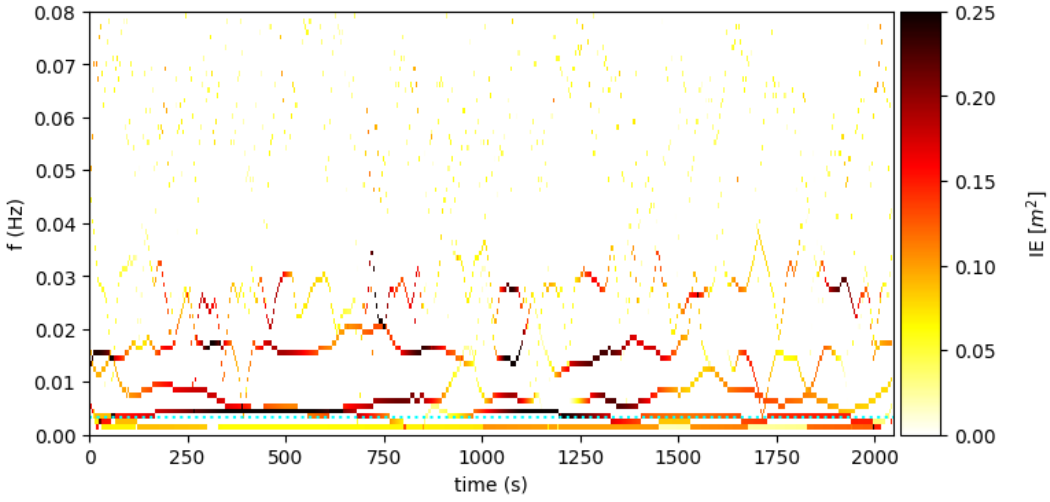

(c) Hilbert spectrum inner reef signal

Figure B.24: An example of (a) the HHT_{temp} resonance analysis, where the colour bar indicates the mean time index of a 600-second window and the red star indicates the value of the HHT resonance approach. Notice how resonance is identified by the HHT_{temp} approach in the first segments of the time series but dies out later. The HHT approach does not recognize the resonance. The fore reef envelope and inner reef signal Hilbert spectra are given in (b) and (c) respectively.

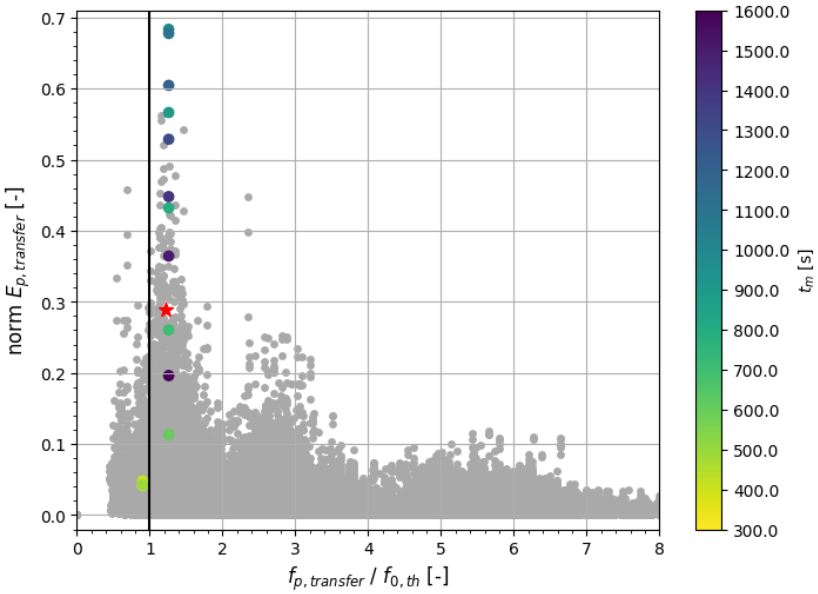

(a) HHT_{temp} resonance diagram.

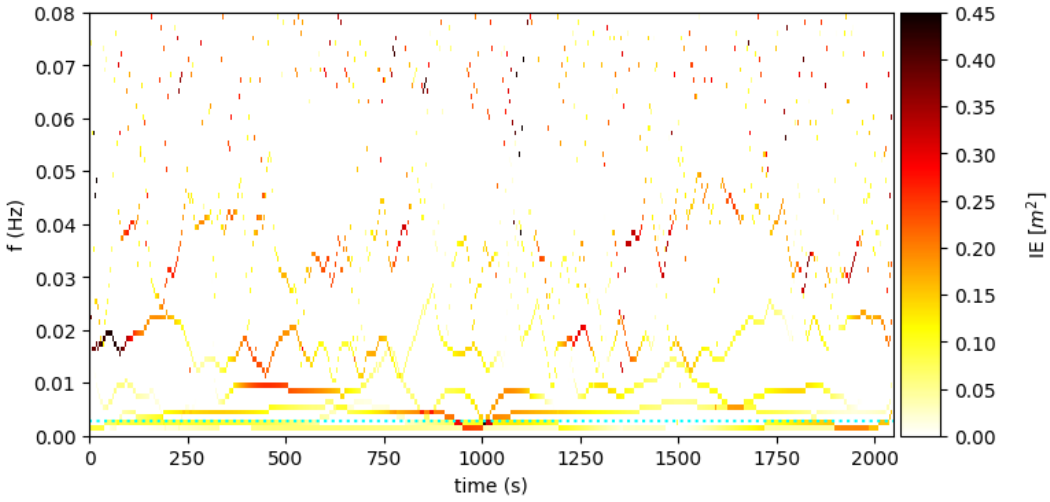

(b) Hilbert spectrum fore reef envelope.

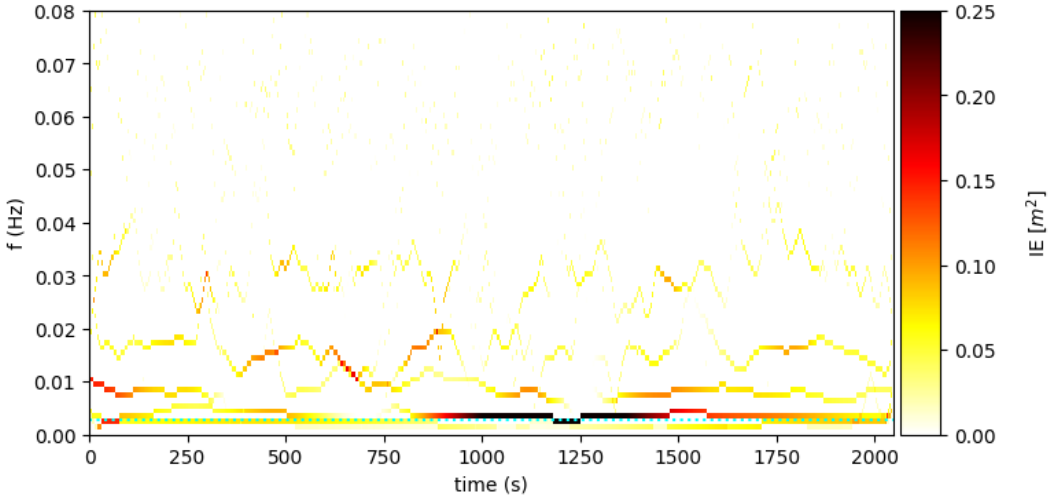

(c) Hilbert spectrum inner reef signal.

Figure B.25: An example of (a) the HHT_{temp} resonance analysis, where the colour bar indicates the mean time index of a 600-second window and the red star indicates the value of the HHT resonance approach. Notice how the resonance 'develops' over time. The fore reef envelope and inner reef signal Hilbert spectra are given in (b) and (c) respectively.

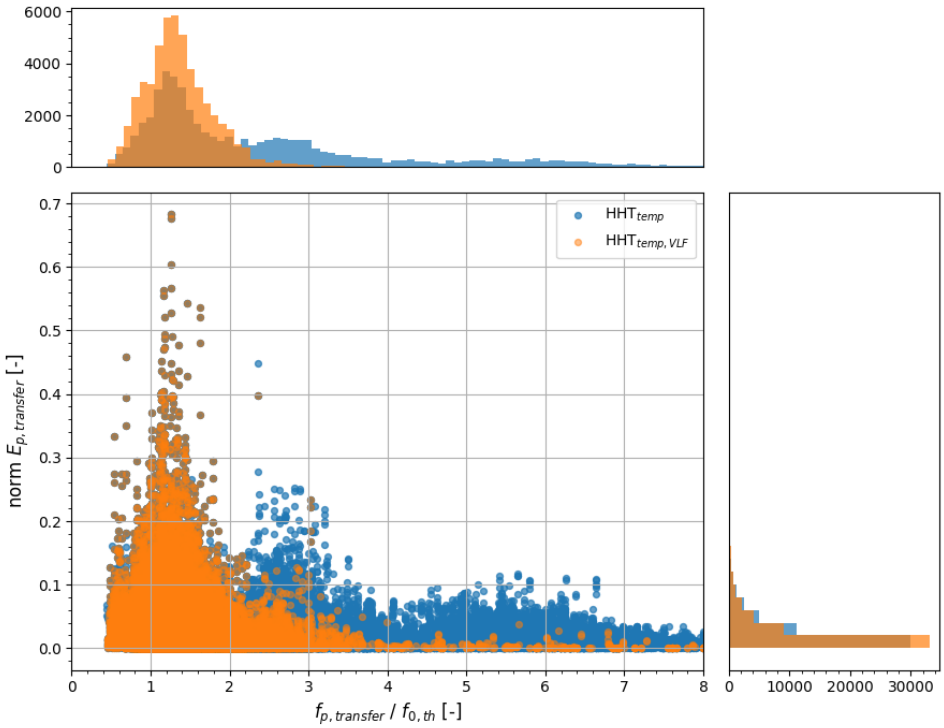

Figure B.26: Resonance diagram based on the time-varying HHT approach (HHT$_{temp}$) and HHT approach only using the dominant VLF component of the inner reef signal (HHT$_{temp,VLF}$), with the 85th-percentile frequency selection method. Time windows of 600 seconds are used. The histograms on the top and right of the resonance diagram in indicate the scatter density.

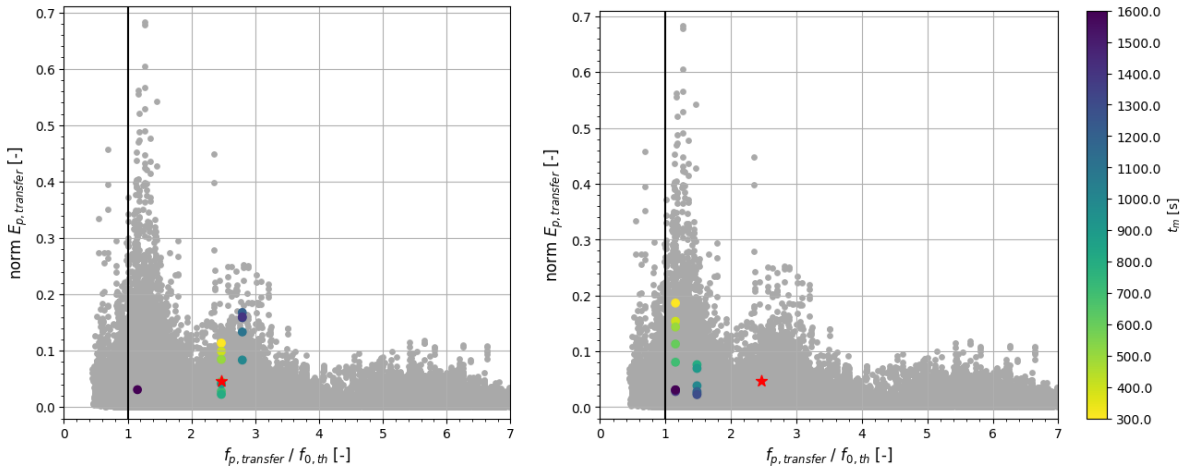

(a) HHT$_{temp}$ **(b)** HHT$_{temp,VLF}$

Figure B.27: Example of a different resonance distribution for one time series for the (a) HHT$_{temp}$ approach and (b) HHT$_{temp,VLF}$ approach. The colour bar indicates the mean time index of the 600-second windows. While in the HHT$_{temp}$ method some $f_{p,transfer}$ are selected around the first resonance mode, the HHT$_{temp,VLF}$ approaches only selects frequencies around the zeroth resonance mode, corresponding with different inner reef energies and thus different values for $normE_{p,transfer}$. This results in the HHT$_{temp,VLF}$ approach categorizing this time series as containing resonance and the HHT$_{temp}$ not.

Patterns of VLF wave classification and resonance identification

Figures B.28 to B.31 are scatter plots showing how various reef hydrodynamic parameters relate to the inner reef VLF oscillation classes and are referred to in Section 4.2.3. Additionally, Figures B.32 to B.34 show relations of the VLF wave classification and resonance identification and external factors such as tide levels and incident wave heights at the fore reef.

Relation to offshore and fore reef parameters

Analysis from Figure B.32 suggests that (energetic) standing VLF waves tend to occur at greater offshore water depths, whereas energetic progressive waves are more prevalent at the lower end of the water depth range. The influence of wave setup on reef flat water depth is depicted in Figure B.33, showing the reef flat water depth against offshore water depth. Additionally, Figure B.34 portrays the distribution of the fore reef's significant wave height ($H_{s,fore}$) and water depth. These figures show that energetic VLF oscillations, although primarily occurring for higher fore reef water levels, also occur for lower water levels in combination with a higher $H_{s,fore}$, thus also demonstrating the contribution of wave setup, this is especially apparent for energetic progressive oscillations.

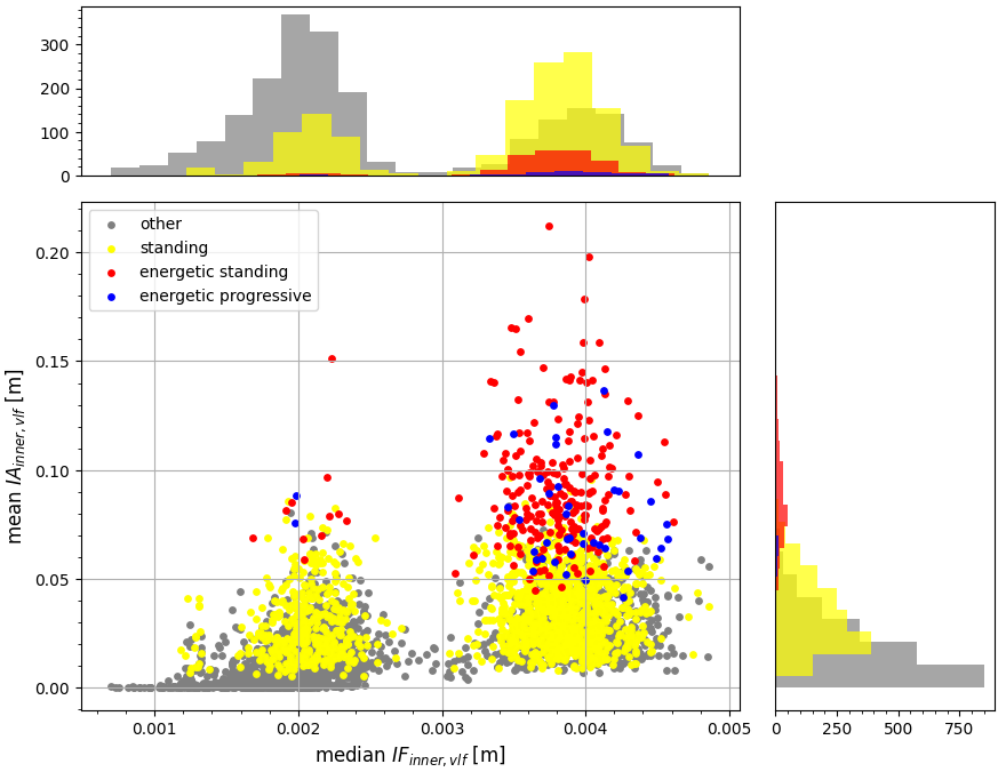

(a) Distribution for VLF wave classes.

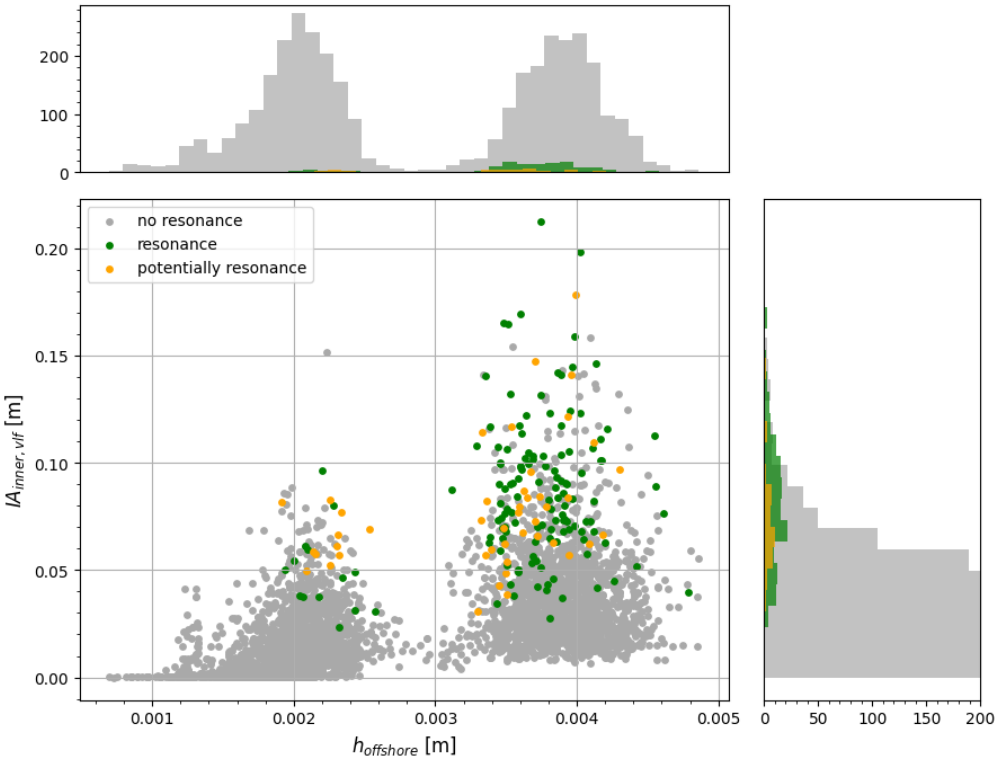

(b) Distribution for resonance occurence.

Figure B.28: The mean instantaneous amplitude of the inner reef VLF component ($IA_{inner,vlf}$) plotted against the median instantaneous frequency of the VLF component ($IF_{inner,vlf}$), with colour indicating the (a) VLF wave classes and (b) resonance. The histograms on top of and right of the diagram indicate the scatter density, the bin widths are 0.0001 Hz and 0.01 m for the x- and y-axis respectively. This figure is also displayed in Figure 4.15 in Section 4.2.

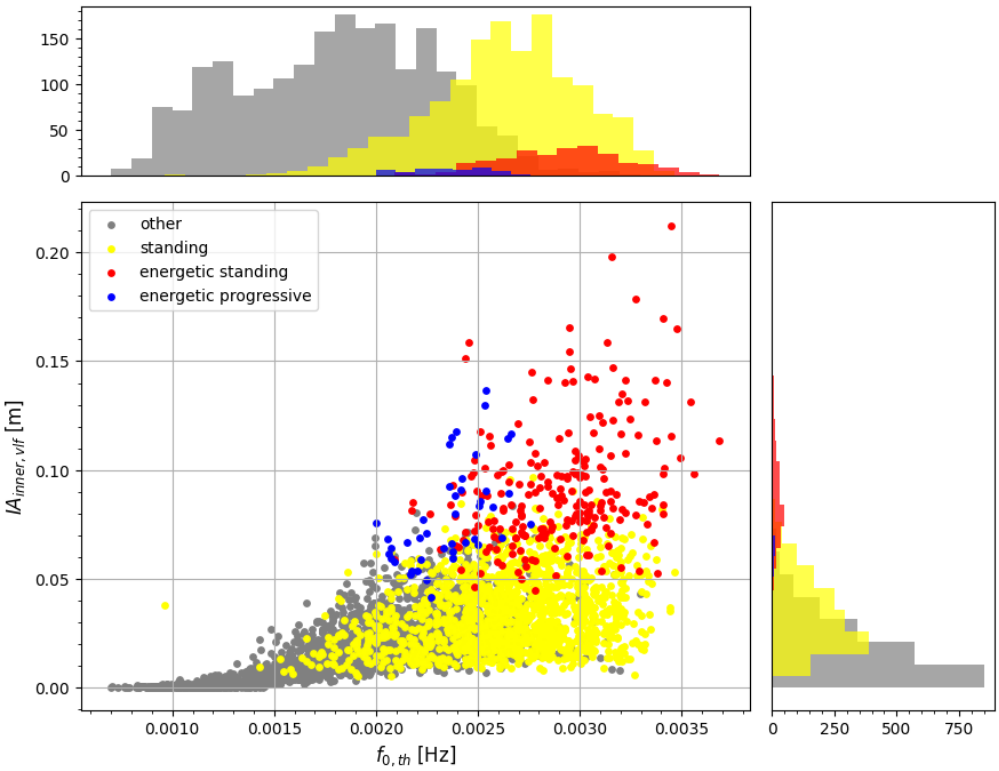

(a) Distribution for VLF wave classes.

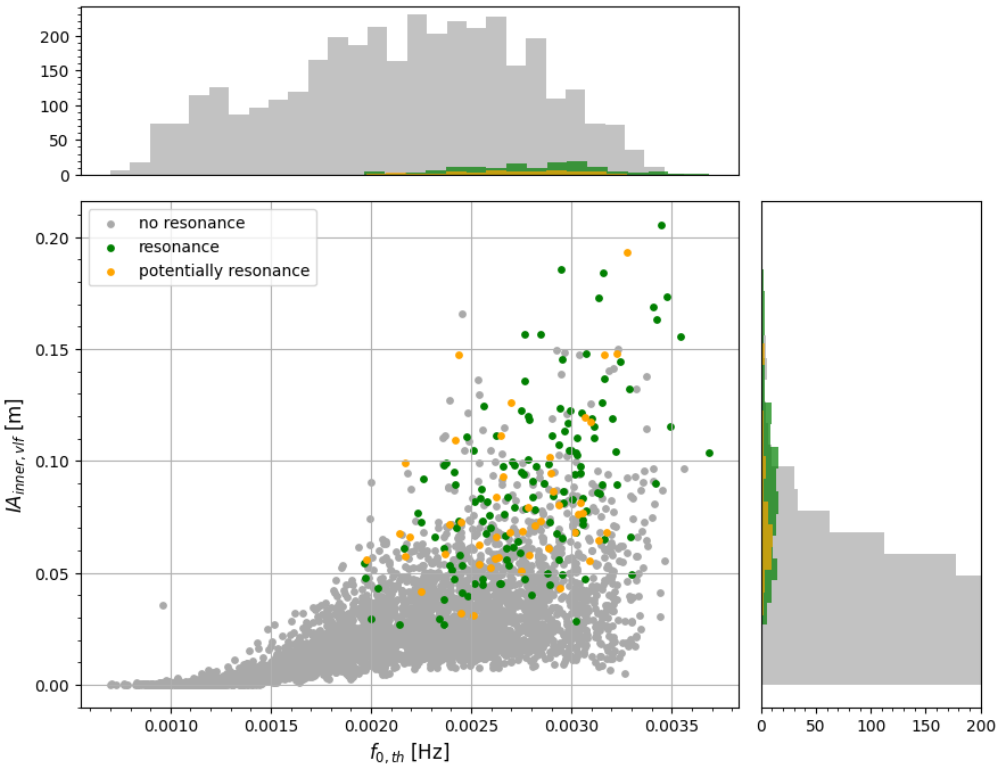

(b) Distribution for resonance occurence.

Figure B.29: The mean instantaneous amplitude of the inner reef VLF component ($IA_{inner,vlf}$) plotted against the eigenfrequency ($f_{0,th}$), with colour indicating the (a) VLF wave classes and (b) resonance. The histograms on top of and right of the diagram indicate the scatter density, the bin widths are 0.0001 Hz and 0.01 m for the x- and y-axis respectively. This figure is also displayed in Figure 4.16 in Section 4.2.

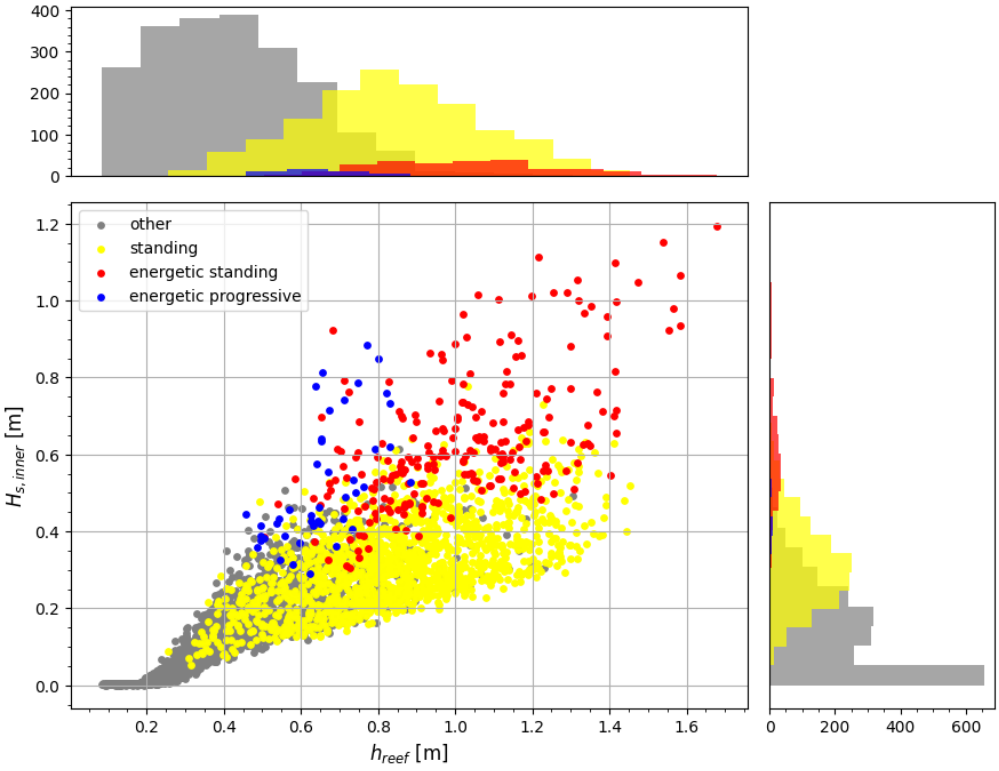

(a) Distribution for VLF wave classes.

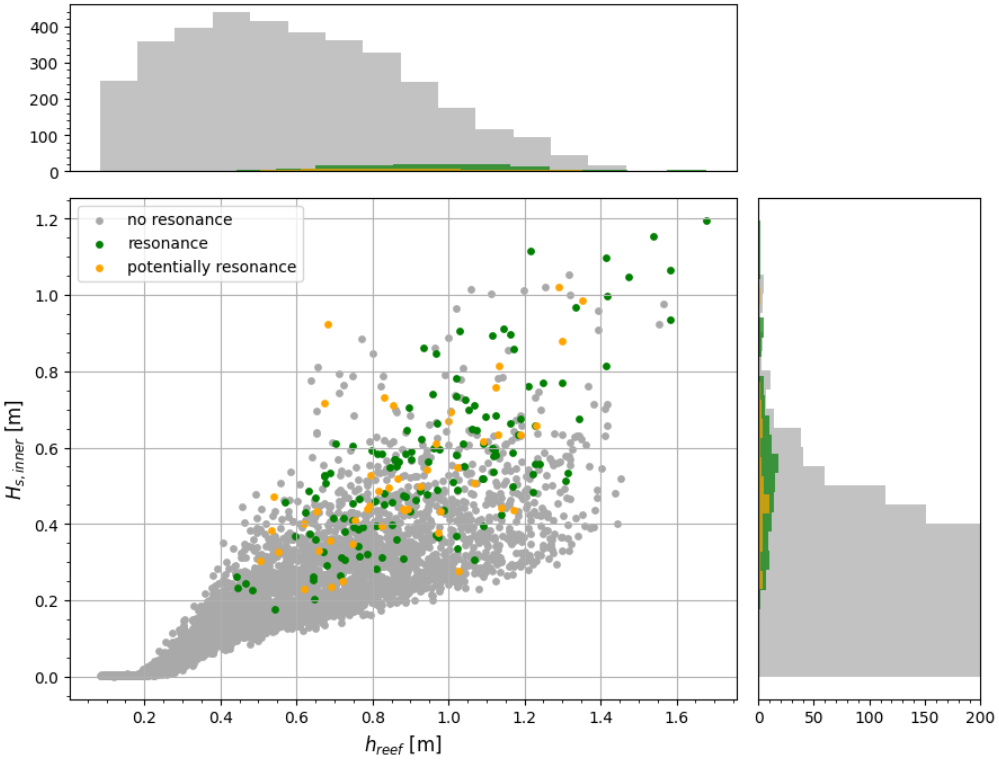

(b) Distribution for resonance occurence.

Figure B.30: The reef flat width (h_{reef}) plotted against the inner reef significant wave height ($H_{s,inner}$), with colour indicating the (a) VLF wave classes and (b) resonance. The histograms on top of and right of the diagram indicate the scatter density, the bin widths are 0.1 m and 0.05 m for the x- and y-axis respectively. This figure is also displayed in Figure 4.17 in Section 4.2.

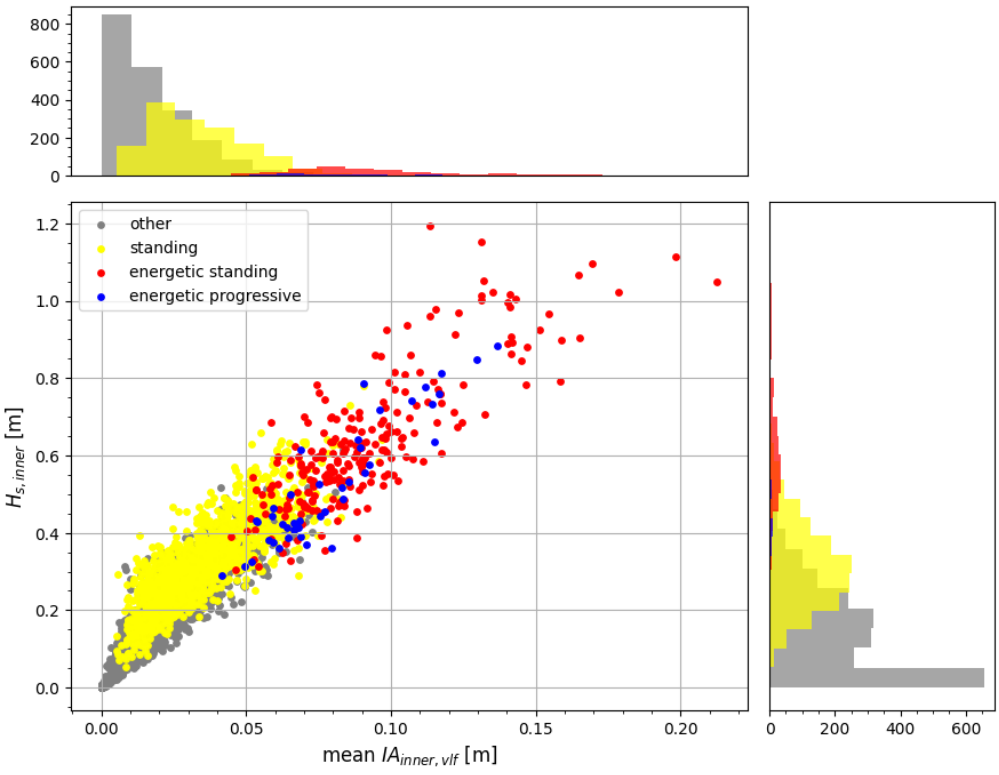

(a) $IA_{inner,vlf}$ versus $H_{s,inner}$.

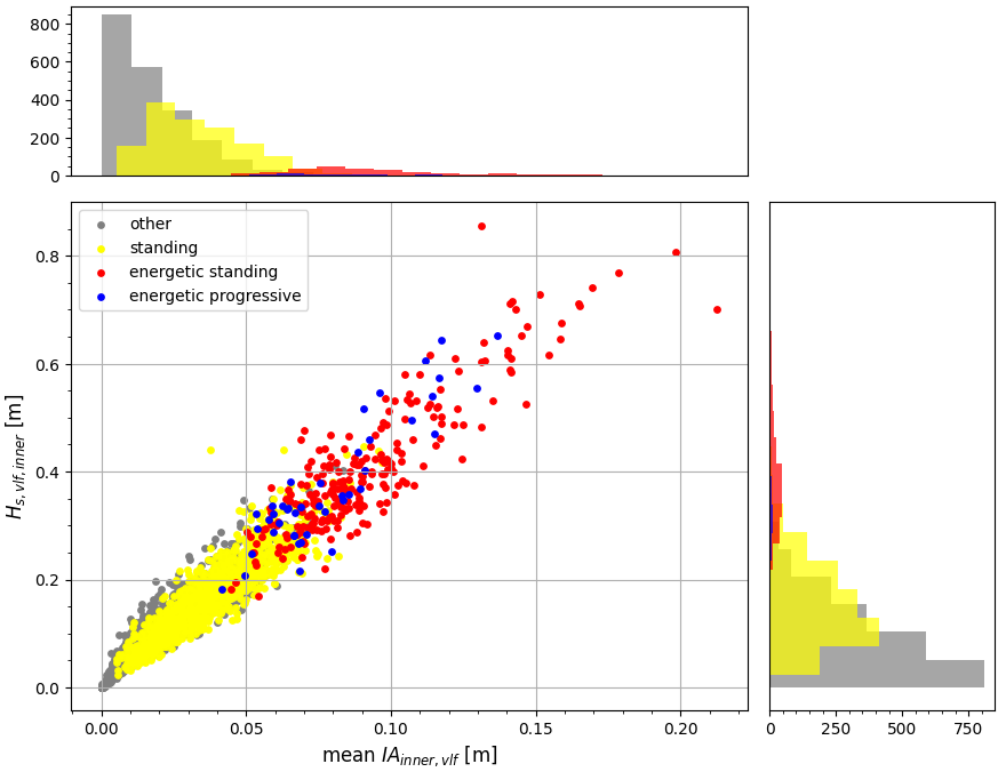

(b) $IA_{inner,vlf}$ versus $H_{s,vlf,inner}$.

Figure B.31: The mean instantaneous amplitude of the inner reef VLF component ($IA_{inner,vlf}$) plotted against the (a) inner reef significant wave height ($H_{s,inner}$) and (b) significant wave height of the VLF domain ($H_{s,vlf,inner}$), with colour indicating the VLF wave classes. Strong linear relations are visible, with respective Pearson correlation coefficients of 0.93 and 0.97. The histograms on top of and right of the diagram indicate the scatter density, the bin widths are 0.01 m and 0.05 m for the x- and y-axis respectively. This figure is also referred to in Section 4.2.

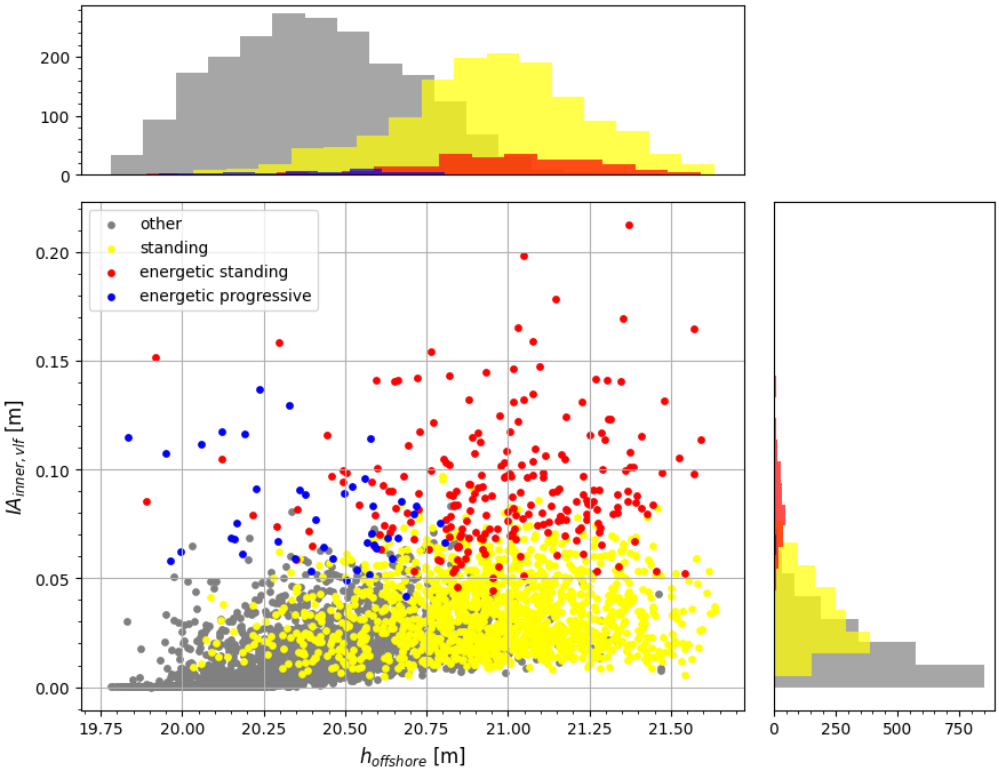

(a) Distribution for VLF wave classes.

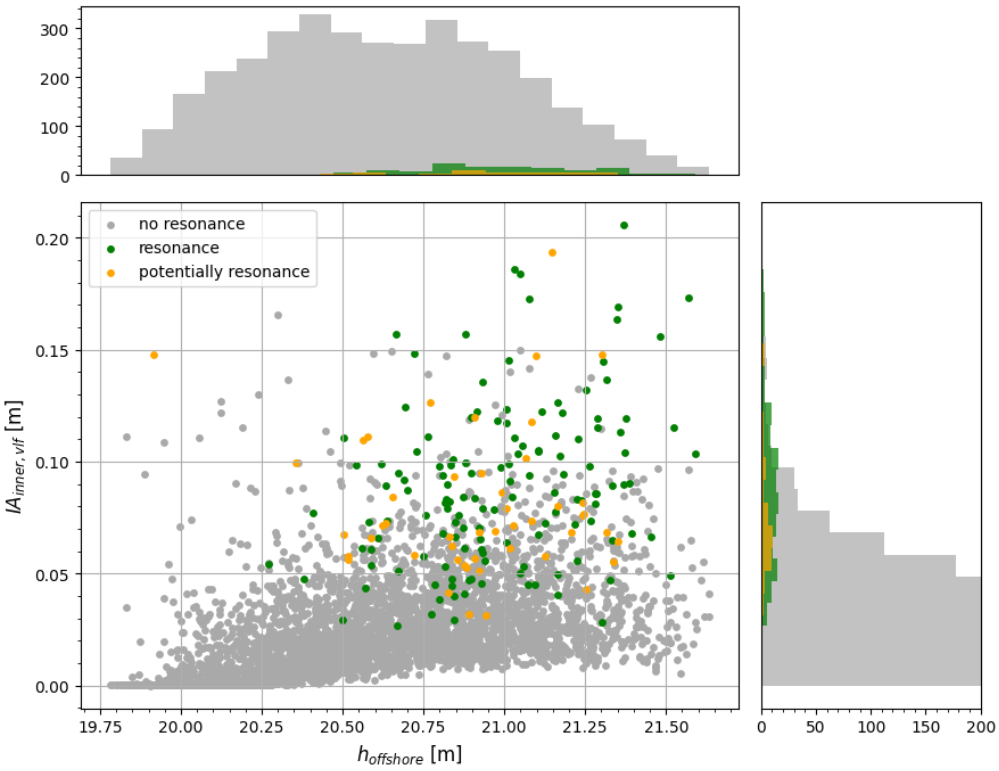

(b) Distribution for resonance occurence.

Figure B.32: The mean instantaneous amplitude of the inner reef VLF component ($IA_{inner,vlf}$) plotted against the offshore water depth ($h_{offshore}$), with colour indicating the (a) VLF wave classes and (b) resonance. The histograms on top of and right of the diagram indicate the scatter density, the bin widths are 0.1 m and 0.01 m for the x- and y-axis respectively. This figure is mentioned in Section 4.2.3. Note that in (a) the majority of progressive standing oscillations occur for a relatively high offshore water level (tide), while the progressive oscillations occur more for lower water levels. Most resonance cases (b) occur for higher tidal levels.

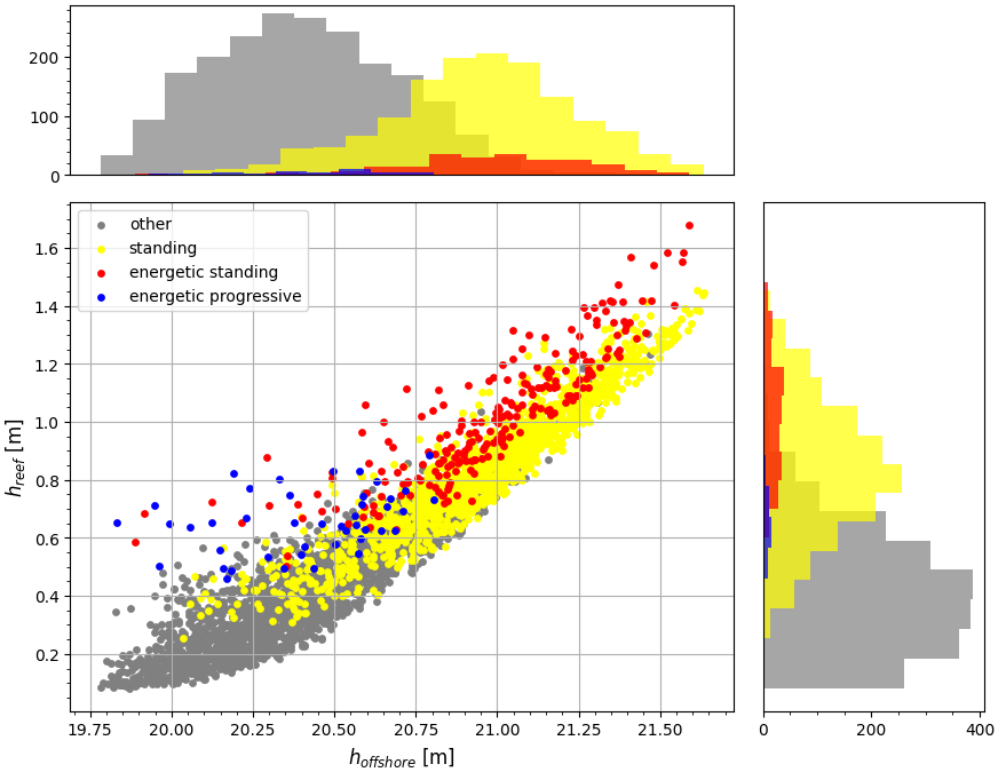

(a) Distribution for VLF wave classes.

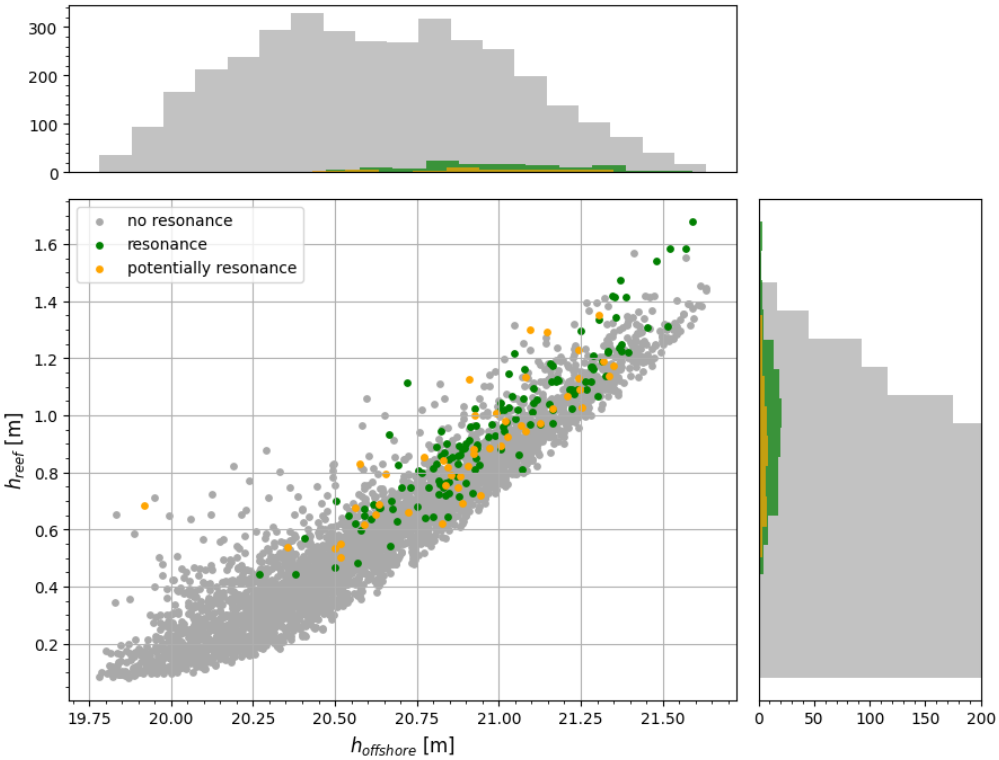

(b) Distribution for resonance occurence.

Figure B.33: The reef flat water depth (h_{reef}) plotted against the offshore water depth ($h_{offshore}$), with colour indicating the (a) VLF wave classes and (b) resonance. The histograms on top of and right of the diagram indicate the scatter density, the bin widths are 0.1 m for both axes. This figure is mentioned in Section 4.2.3. These figures illustrate the wave setup component of h_{reef} through the deviation of the strong trend between the two water depths. The powerful progressive oscillations (a) tend to occur for more significant wave setup, but during powerful standing waves wave setup is experienced as well. Most resonance cases (b) are displayed within the main trend, therefore suggesting a generally less significant contribution of wave setup.

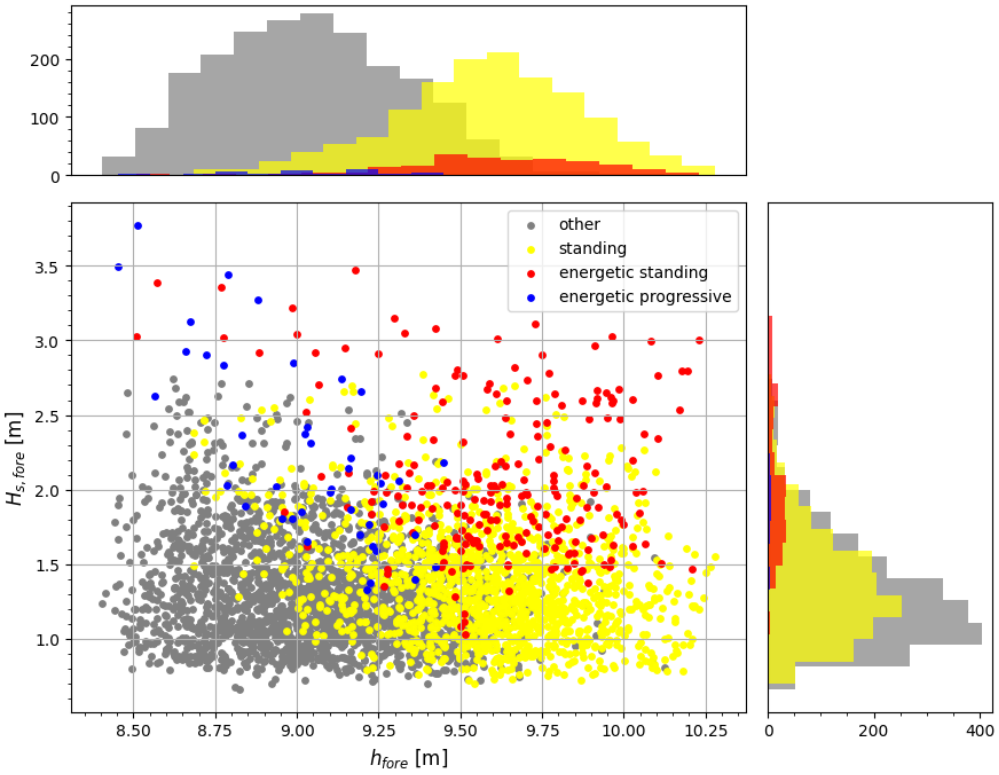

(a) Distribution for VLF wave classes.

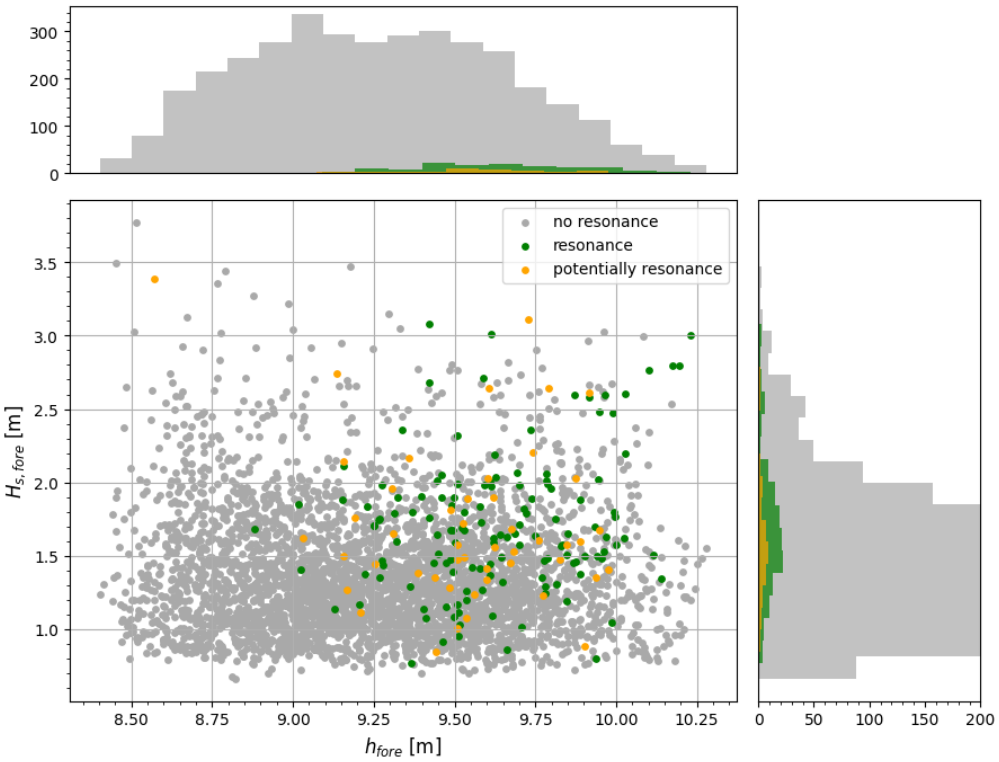

(b) Distribution for resonance occurence.

Figure B.34: The fore reef significant wave height ($H_{s,fore}$) plotted against the fore reef water depth (h_{fore}), with colour indicating the (a) VLF wave classes and (b) resonance. The histograms on top of and right of the diagram indicate the scatter density, the bin widths are 0.1 m and 0.15 m for the x- and y-axis respectively. This figure is mentioned in Section 4.2.3. The powerful progressive oscillations (a) occur for higher values of $H_{s,fore}$, confirming the contribution of wave setup, see also Figure B.33.

C

Transient characteristics of energetic and resonant VLF waves

Supplements for results

This appendix contains supplementary figures for Section 4.3.

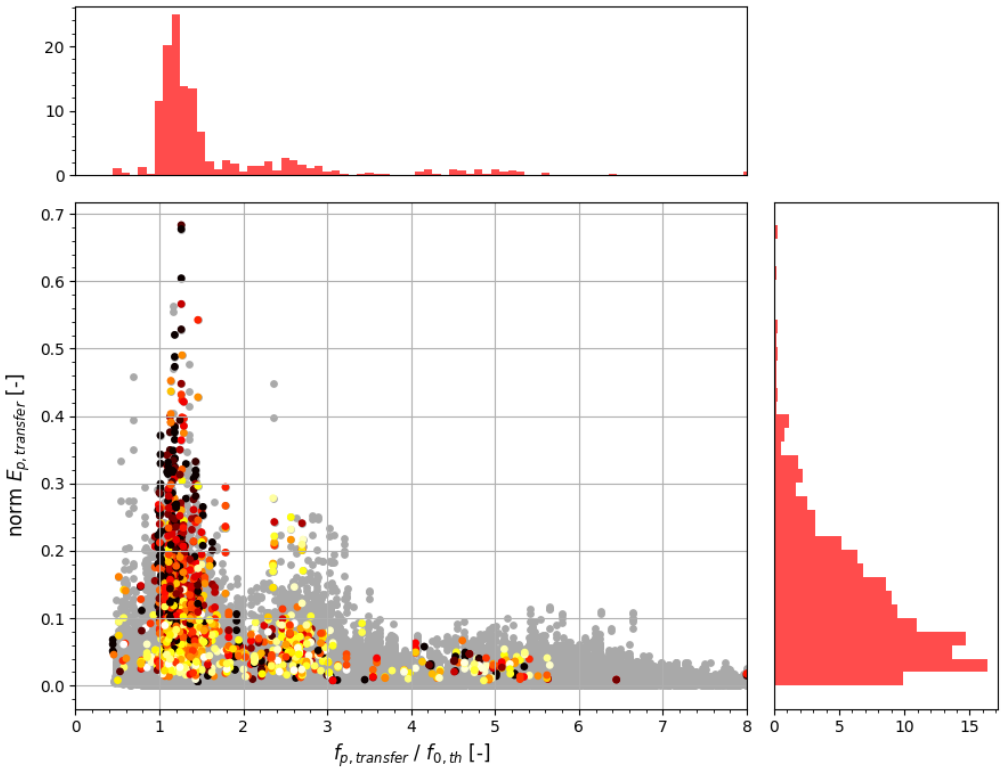

Figure C.1: Resonance diagram based on the time-varying HHT approach (HHT_{temp}) with the 85th-percentile peak selection method. Time windows of 600 seconds are used. The colour indicates the duration of a powerful VLF event in the 600-second windows, the maximum duration being 600 seconds indicated with dark red. The histograms on top of and right of the diagram indicate the scatter density, weighted with the VLF event duration. This figure is also displayed in Figure 4.24 in Section 4.3.

Energetic VLF events duration and intensity

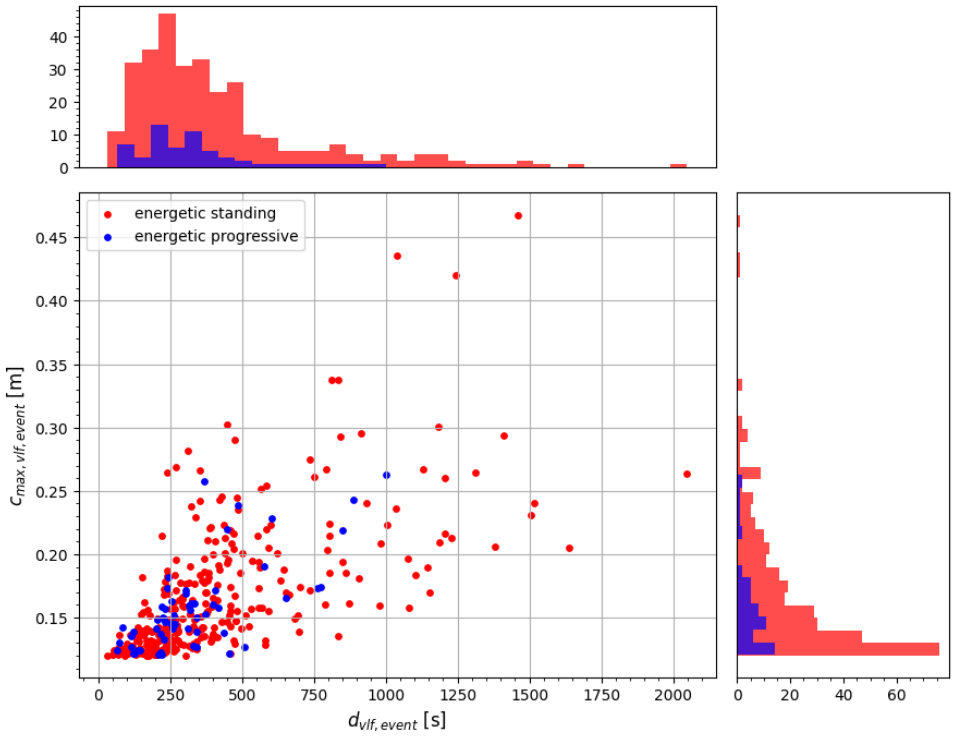

(a) Maximum peak of the powerful VLF event.

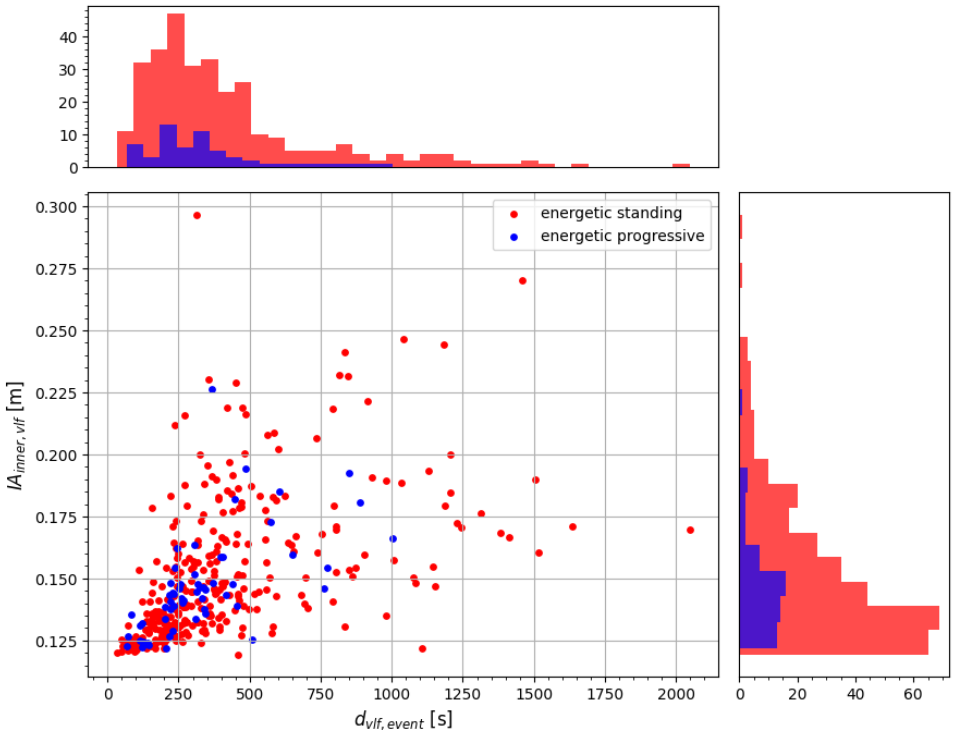

(b) Mean IA of the powerful VLF event.

Figure C.2: The powerful VLF event duration plotted against (a) the maximum peak ($c_{max,vlf,event}$) and (b) the mean instantaneous amplitude ($IA_{vlf,event}$) of the powerful VLF event. The histograms on top of and right of the diagram indicate the scatter density, the bin widths are 0.01 m and 60 seconds for the y- and x-axes respectively. This figure is also displayed in Figure 4.19 in Section 4.3.

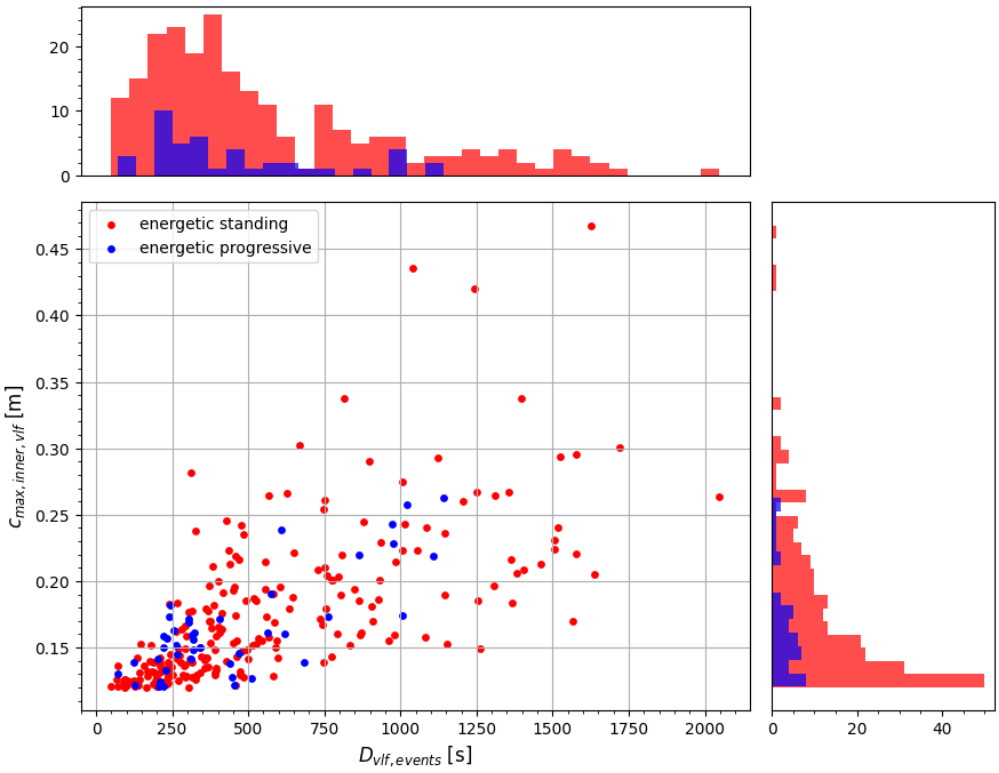

(a) Maximum peak of the powerful VLF event.

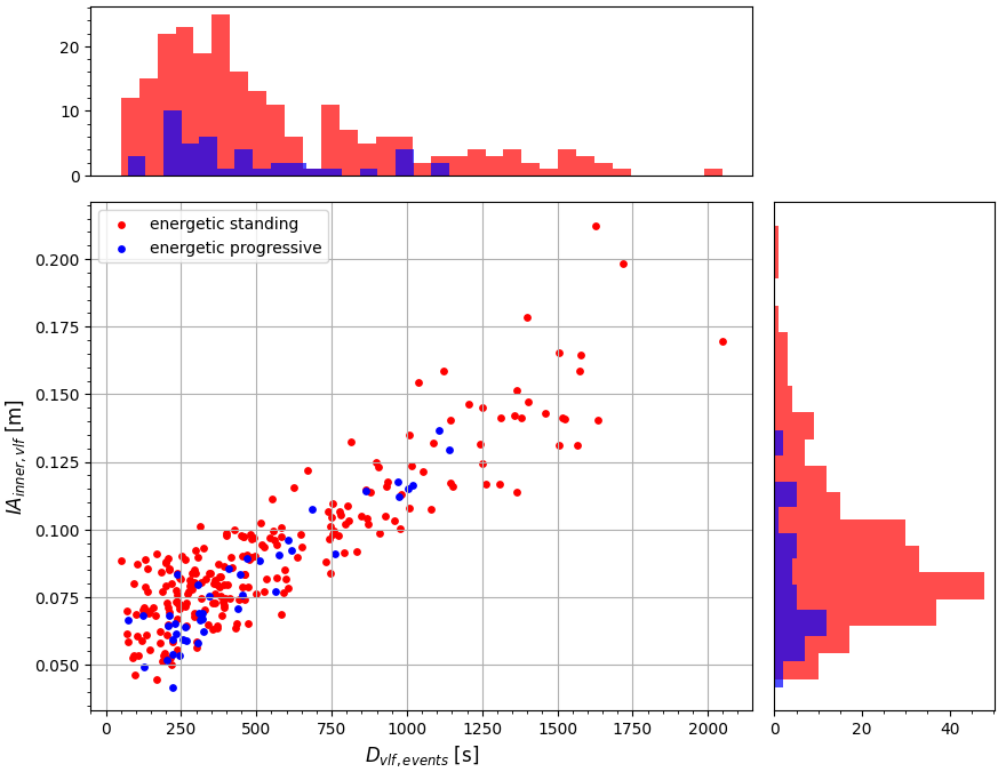

(b) Mean IA of the powerful VLF event.

Figure C.3: The sum of the duration of powerful VLF events per record plotted against (a) the maximum peak ($c_{max,inner,vlf}$) and (b) the mean instantaneous amplitude ($IA_{inner,vlf}$) of the inner reef VLF component. The histograms on top of and right of the diagram indicate the scatter density, the bin widths are 0.01 m and 60 seconds for the y- and x-axes respectively. This figure is also displayed in Figure 4.20 in Section 4.3.

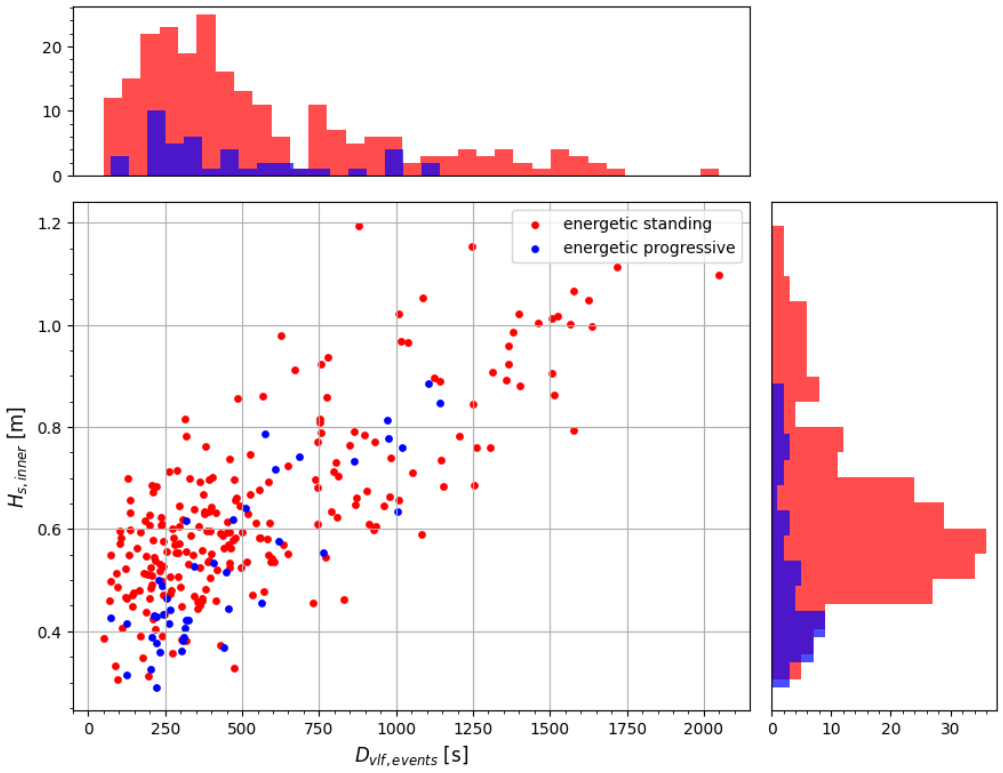

(a) Inner reef significant wave height.

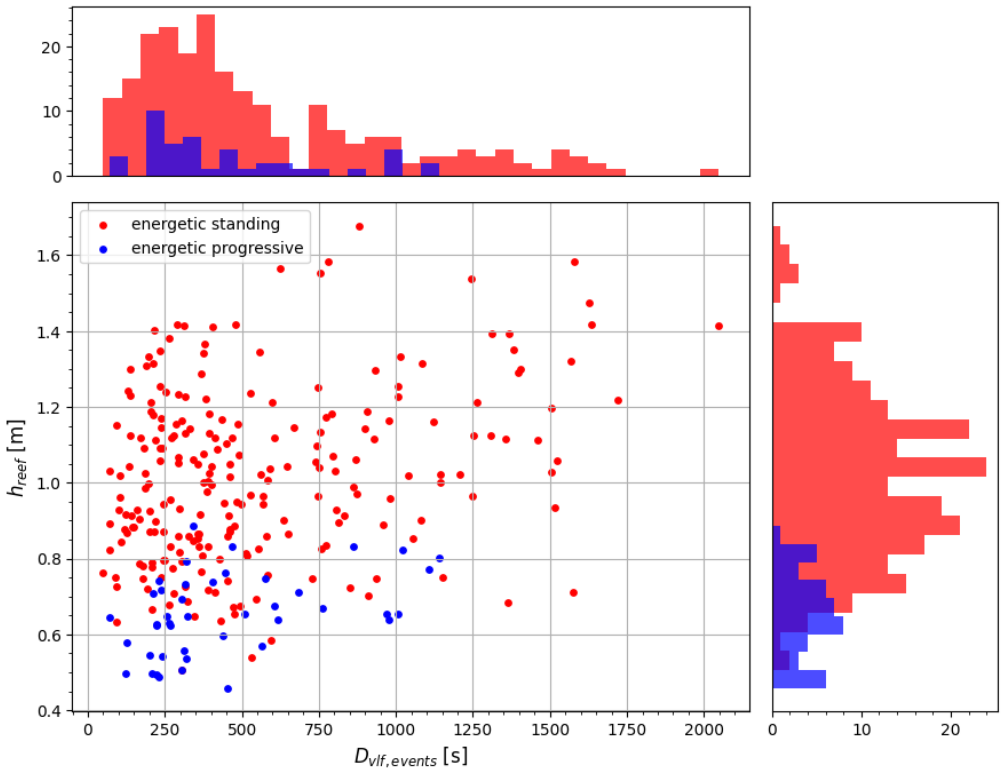

(b) Reef flat water depth.

Figure C.4: The sum of the duration of powerful VLF events per record plotted against (a) the inner reef significant wave height ($H_{s,inner}$) and (b) the reef flat water depth (h_{reef}). The histograms on top of and right of the diagram indicate the scatter density, the bin widths are 0.05 m and 60 seconds for the y- and x-axes respectively. This figure is also displayed in Figure 4.21 in Section 4.3.

Resonance events duration and intensity

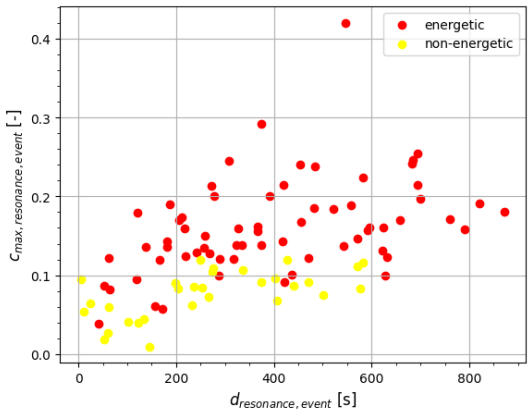

(a) Maximum peak of the resonance event.

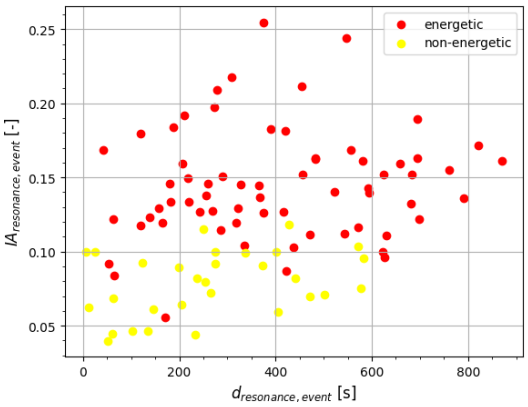

(b) Mean IA of the resonance event.

Figure C.5: Resonance event duration plotted against (a) the corresponding maximum peak ($c_{max,resonance,event}$) and (b) the mean instantaneous amplitude ($IA_{resonance,event}$) of the inner reef VLF component. The correlation coefficients for these relations are 0.52 and 0.32 respectively. These figures are referred to in Section 4.3.

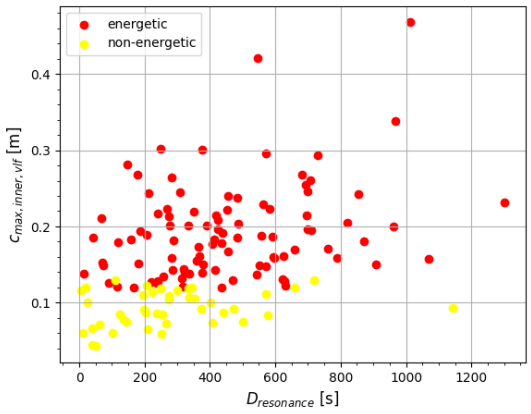

(a) Maximum peak of the VLF component.

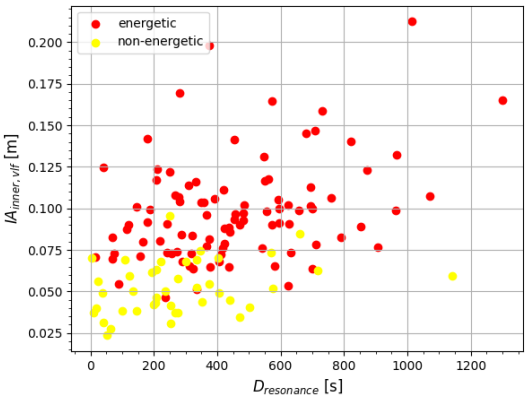

(b) Mean IA of the VLF component.

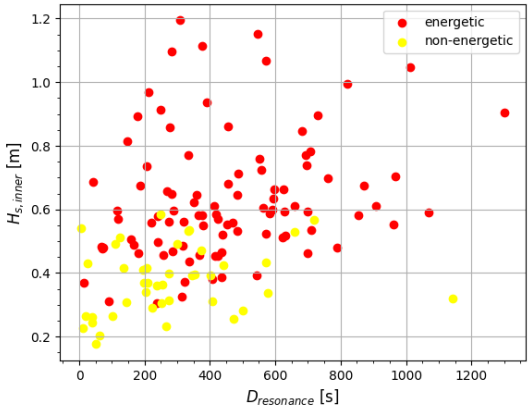

(c) Inner reef significant wave height.

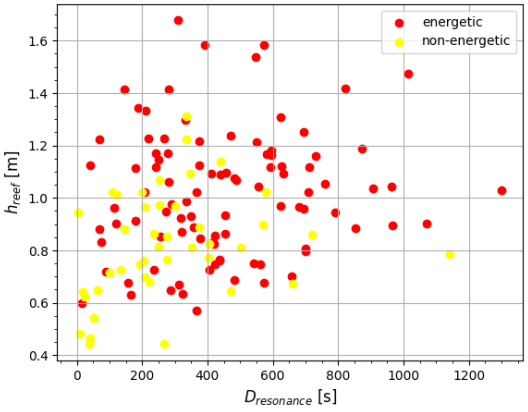

(d) Reef flat water depth.

Figure C.6: Total resonance durations plotted against the (a) maximum peak and (b) mean instantaneous amplitude of the VLF component, (c) the inner reef significant wave height ($H_{s,inner}$) and (d) the reef flat water depth (h_{reef}). The correlation coefficients for these relations are 0.40, 0.44, 0.35 and 0.25 respectively. These figures are referred to in Section 4.3.

300-second window analysis

The resonance duration is also performed using 300-second windows. The relation between the normalised resonance event duration between the 600-second window and 300-second window approach is presented in Figure C.7. Additionally, the medians and 90-percentiles for (normalised) event duration and total duration are given for both approaches in Table 4.10. Compared to the 600-second window approach, the 300-window analysis results in slightly longer resonance events on average. Figure C.9 shows an example of how this difference arises. Regarding the resonance event (with a upward and downward crossing of the resonance threshold), the 300-second window approach results in fewer normalised durations below 1 (21%) compared to the 600-second window approach (47%).

It should be noted that, because of the shorter time windows used, there may not be any energy appointed to each frequency in the inner reef and fore reef envelope HHT spectra. This may lead to a less accurate selection for $f_{p,transfer}$, as the transfer energy H_{Axy} may contain multiple NaN (Not a Number) and infinity values. In the resonance analysis, the NaN and infinity values were ignored in selecting the $f_{p,transfer}$.

Also note that for the threshold for $normE_{p,transfer}$ the same value is used for the 600-second and 300-second window approaches, because this analysis is only executed for the cases already identified as resonance, therefore a new value is not computed.

Table C.1: Resonance (normalised) event duration and total duration for 600-second and 300-second window approach, the median and 90 percentile are given.

	Event duration [s]		Normalised event duration [-]		Total duration [s]	
	50%	90%	50%	90%	50%	90%
600-second windows	308.5	627.8	1.1	2.3	359.0	714.0
300-second windows	362.5	593.6	1.3	2.2	454.0	741.9

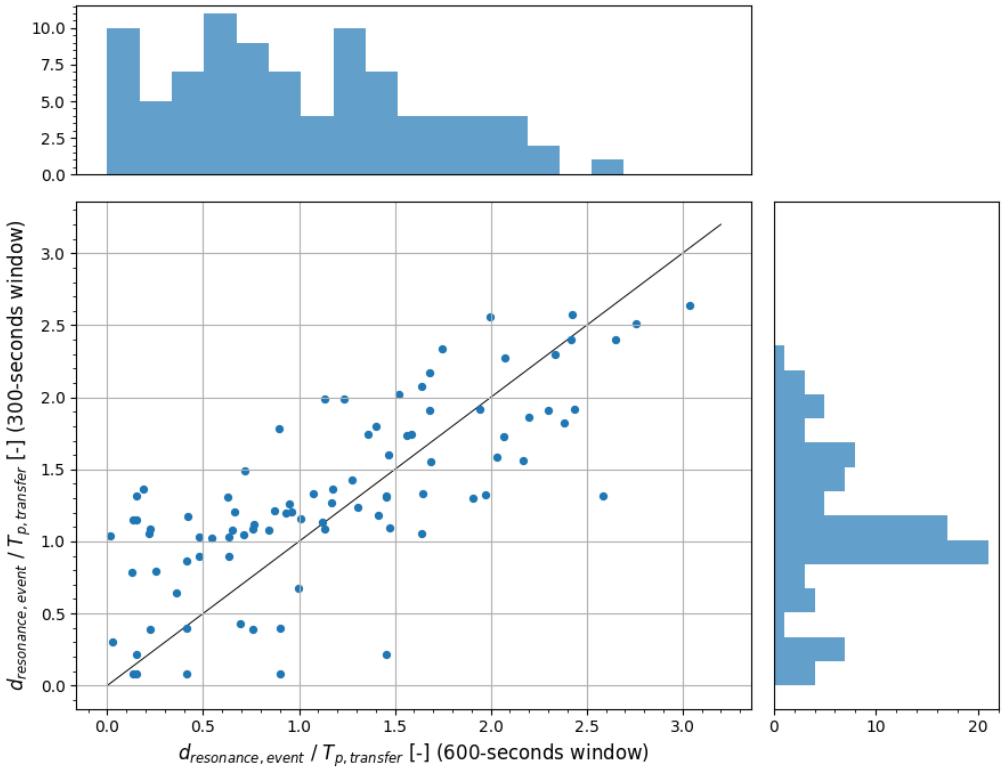

Figure C.7: Comparison of normalised resonance event duration for 600-second and 300-second window approach.

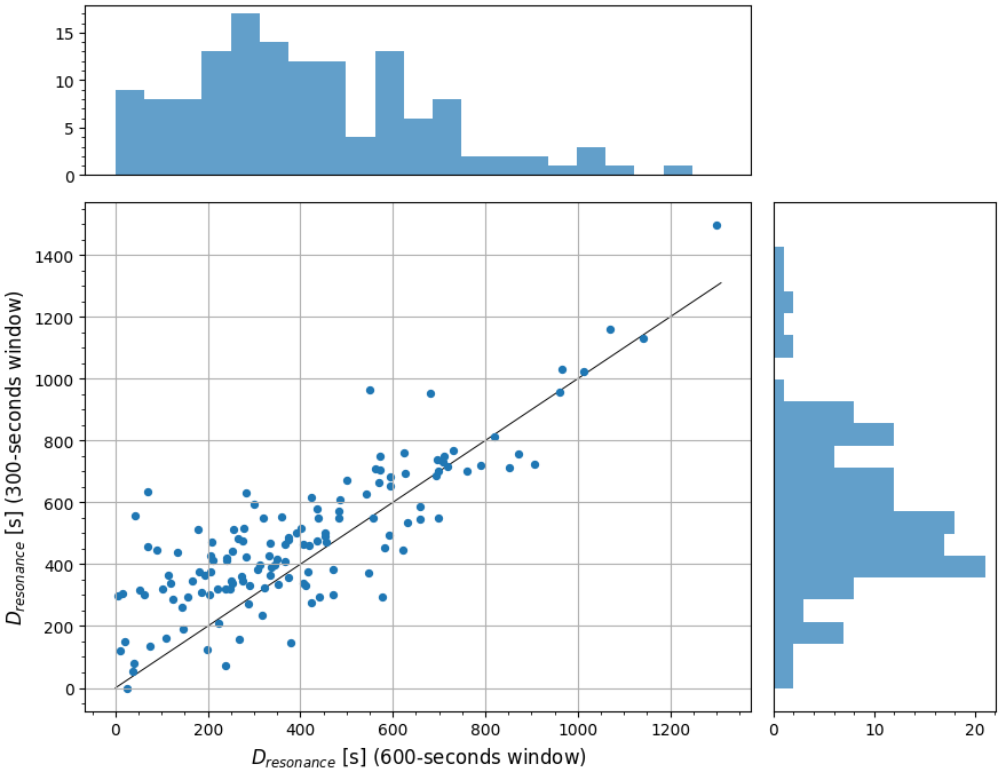

Figure C.8: Comparison of total resonance duration for 600-second and 300-second window approach.

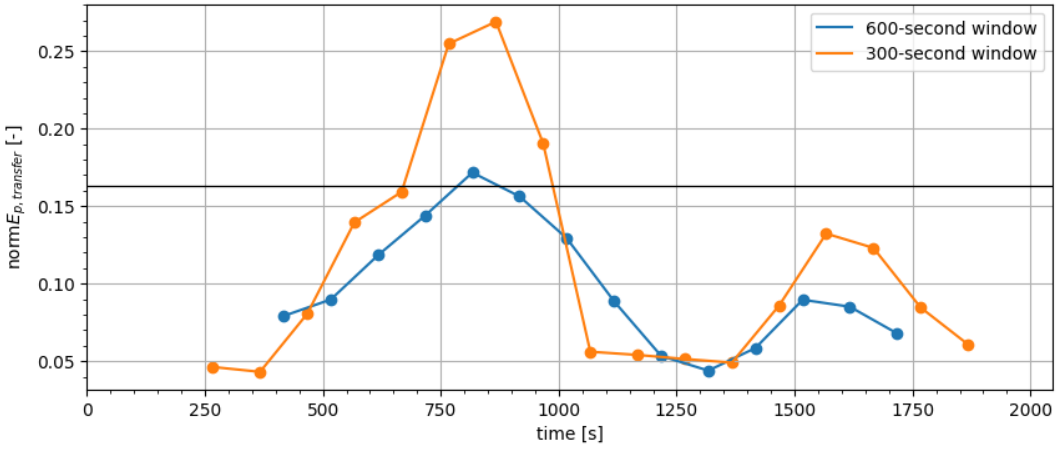

Figure C.9: Example of resonance event duration for 600-second (blue line) and 300-second (orange line) window approach. This example illustrates that the duration for the 300-second window approach is longer than that of the 600-second window approach.